

General Disclaimer

One or more of the Following Statements may affect this Document

- This document has been reproduced from the best copy furnished by the organizational source. It is being released in the interest of making available as much information as possible.
- This document may contain data, which exceeds the sheet parameters. It was furnished in this condition by the organizational source and is the best copy available.
- This document may contain tone-on-tone or color graphs, charts and/or pictures, which have been reproduced in black and white.
- This document is paginated as submitted by the original source.
- Portions of this document are not fully legible due to the historical nature of some of the material. However, it is the best reproduction available from the original submission.

JPL PUBLICATION 82-34

The Nature of Large-Scale Turbulence in the Jovian Atmosphere

Jim L. Mitchell

(NASA-CP-169138) THE NATURE OF LARGE-SCALE
TURBULENCE IN THE JOVIAN ATMOSPHERE (Jet
Propulsion Lab.) 298 p HC A13/MF A01

N82-30207

CSSL 03B

Unclass

G3/91 28446

January 15, 1982



National Aeronautics and
Space Administration

Jet Propulsion Laboratory
California Institute of Technology
Pasadena, California



JPL PUBLICATION 82-34

The Nature of Large-Scale Turbulence in the Jovian Atmosphere

Jim L. Mitchell

January 15, 1982



National Aeronautics and
Space Administration

Jet Propulsion Laboratory
California Institute of Technology
Pasadena, California

The research described in this publication was carried out by the Jet Propulsion Laboratory, California Institute of Technology, under contract with the National Aeronautics and Space Administration.

ABSTRACT

THE NATURE OF LARGE-SCALE TURBULENCE IN THE JOVIAN ATMOSPHERE

The energetics and spectral characteristics of quasi-geostrophic turbulence in Jupiter's atmosphere are examined using sequences of Voyager images and infrared temperature soundings. Using global wind measurements we quantify momentum transports associated with zonally symmetric stresses and turbulent stresses. Though a strong up-gradient flux of momentum by eddies is observed, measurements do not preclude the possibility that symmetric stresses play a critical role in maintaining the mean zonal circulation. Strong correlation between the observed meridional distribution of eddy-scale kinetic energy and available potential energy suggests coupling between the observed cloudtop turbulent motions and the upper tropospheric thermodynamics. We formulate an Oort energy budget for Jupiter's upper troposphere.

Fourier analyses of turbulent motions within zonal jets suggest that large-scale Jovian turbulence obeys a $k^{-5/3}$ power law, where k is the zonal wavenumber. This implies that the observed turbulence is two-dimensional with an up-gradient flow of kinetic energy from smaller scales (e.g., baroclinic scales). Turbulent kinetic energy generally peaks at the scale for which Rossby wave propagation begins as suggested by Rhines (1975).

The largest turbulent scales (e.g., the Great Red Spot (GRS) and the White Ovals) occur at the order of or greater than the so-called Rhines radius. Studies of the inertial transport of kinetic energy within momentum control volumes around the GRS and White Oval BC indicate that these eddies feed barotropically upon the meridional shear in the mean zonal wind and are thus maintained as shear instabilities.

The solitary Rossby wave model of Maxworthy and Redekopp (1976) is one of the few models capable of accommodating such a barotropically forced perturbation. Using the observed temperature profile in the atmosphere ambient to the GRS, we compute a perturbation temperature profile based upon numerical solution of the eigenvalue problem governing the vertical structure of a soliton. For choices of eigenvalue appropriate for the observed meridional shear of the ambient mean zonal wind we obtain eigenfunctions which match the observed perturbation temperature profile above the GRS. This suggests the validity of the solitary wave model for describing the largest turbulent scales.

Refer to Chapter 6 for a brief summary.

PREFACE AND ACKNOWLEDGEMENTS

This report represents an attempt to unify several pieces of related research to produce a consistent scenario as to the nature of large-scale, quasi-geostrophic turbulence in the atmosphere of Jupiter. To a large extent this technical report is a re-issue of the author's Ph.D. dissertation at the University of Southern California (December, 1981) in a form which makes the work more accessible to the interested scientific community.

The author is greatly indebted to a host of co-investigators working as part of the Voyager imaging and infrared radiometer experiments, most particularly to Drs. Mike Allison (Goddard Institute for Space Studies), Reta Beebe (New Mexico State University), and Andy Ingersoll (California Institute of Technology). The bulk of the imaging processing necessary to complete this research would have been impossible without the hard-work provided unselfishly by Glenn Garneau at the Image Processing Laboratory at JPL. The constant support provided by the Voyager Project, most particularly by Andy Collins, Candy Hansen, and Anne Bunker, made this long term effort possible. NASA's Office of Space Sciences and Dr. Henry Brinton provided generous sponsorship for the research herein described. Much of the stimulus for this work came from the suggestions and kind advice of Drs. Tony Maxworthy and Larry Redekopp. Their faith in the scientific worth of this effort is directly responsible for its completion.

Jim L. Mitchell

DEDICATION

To the memory of Seymour L. Hess who introduced both the world and the author to the study of the atmospheric dynamics of other planets by application of his keen scientific intuition to groundbased and spacecraft observations and eventually to the first in situ weather measurements from another world.

TABLE OF CONTENTS

	Page
CHAPTER 1. AN INTRODUCTION	1-1
1.1 The Role of Large-Scale Eddies in Earth's Atmosphere.....	1-3
1.2 Observational Resources Provided by Voyager.....	1-10
1.2.1 The Voyager Imaging Experiment and the AMOS System.....	1-11
1.2.2 Voyager Infrared Spectrometer and Imaging Radiometer (IRIS).....	1-14
1.3 A Review of the Theoretical Resources at Our Disposal	1-15
1.3.1 The Classical Model of the Jovian Circulation	1-15
1.3.2 Possible Mechanisms Driving the Mean and/or Eddy Flow	1-18
1.3.2.1 Convective Models	1-20
1.3.2.1.1 Shallow Convective Models	1-21

TABLE OF CONTENTS (Continued)

	Page
1.3.2.1.2 Deep Convective Models	1-24
1.3.2.1.3 Latent Heat Dependent Convection and CISK	1-33
1.3.2.2 Baroclinic Models	1-35
1.3.2.2.1 Inertial Baroclinic Instabilities	1-36
1.3.2.2.2 Conventional Baro- clinic Instabilities.	1-40
1.3.2.3 Wave Driven Jets	1-48
1.3.2.4 Barotropic Instabilities	1-50
CHAPTER 2. GLOBAL ENERGETICS	2-1
2.1 Introduction	2-1
2.2 The 2-Dimensional Kinetic Energy Equation	2-1
2.2.1 Derivation of the 2-Dimensional Mean Zonal Kinetic Energy Equation	2-2
2.2.2 The Operational Scheme	2-8
2.2.3 Interpretation of the Terms in the Kinetic Energy Equation	2-12
2.3 Eddy Transports and Previous World Map Studies	2-25

TABLE OF CONTENTS (Continued)

	Page
2.4 Observed Global Transport Processes	2-32
2.4.1 Results of the Extended Voyager 2 World Map	2-33
2.4.2 Problems in Interpretation of the Results .	2-38
2.5 Comparisons with IRIS: Energy Budget of the Upper Troposphere	2-40
 Chapter 3. THE LARGE-SCALE TURBULENT SPECTRUM	 3-1
3.1 Introduction	3-1
3.1.1 The Coupling of Thermodynamics and Dynamics	3-1
3.1.2 Two-Dimensional and Three-Dimensional Turbulence	3-3
3.2 Three-Dimensional, Isotropic Turbulence	3-5
3.3 Two-Dimensional or Geostrophic Turbulence	3-9
3.4 Large-Scale Jovian Turbulence	3-17
3.4.1 Measurement of the Turbulent Kinetic Energy Power Spectrum	3-18
3.4.2 Interpretation of the Jovian Turbulent Spectrum	3-19

TABLE OF CONTENTS (Continued)

	Page
CHAPTER 4. KINEMATICS AND ENERGETICS OF THE GREAT RED SPOT	4-1
4.1 Introduction	4-1
4.2 The Velocity and Vorticity Field of the GRS	4-5
4.3 Energetics of the Great Red Spot	4-34
4.3.1 Deduced Energetics for a Closed Momentum Control Volume	4-34
4.3.2 Asymmetry and Eddy Stress	4-35
4.3.3 Evaluation of the GRS-Mean Flow Interaction	4-43
4.3.4 A Preliminary and Cautious Error Analysis .	4-49
4.3.4.1 The Effects of Our Smoothing Schemes	4-55
4.3.4.2 The Effects of Error in North-Angle	4-59
4.3.4.3 The Pressure Torque Term	4-65
4.3.4.3.1 An Estimate of the Radial Pressure Gradient of the GRS .	4-65
4.3.4.3.2 An Estimate of the Ageostrophic Pressure Gradient ...	4-67

TABLE OF CONTENTS (Continued)

	Page
4.3.4.3.3 The Asymmetry Associated with Ageostrophic Flow ...	4-69
4.4 Eddy Stresses Associated with White Oval BC	4-71
4.5 The Role of Eddy Stresses in Maintaining the GRS ..	4-72
4.5.1 Nature of the Observed Stresses	4-73
4.5.2 The Barotropic Stability of the Mean Shear.	4-78
4.5.3 Theoretical Implication of the Observed Stresses	4-82
 CHAPTER 5. THE VERTICAL STRUCTURE OF SOLITARY ROSSBY WAVES	 5-1
5.1 Solutions to the Quasi-geostrophic Potential Vorticity Equation	 5-1
5.2 Observed Stratification Profiles and Vertical Eigenfunctions	 5-6
5.3 Some Conclusions and Suggestions	5-17
 CHAPTER 6. SUMMARY	 6-1
 REFERENCES	 7-1

Not without art, but yet to nature true.

Charles Churchill
in "The Rosciad"

CHAPTER 1. AN INTRODUCTION

We investigate the nature of large-scale Jovian ($\sim 10^2$ - 10^4 km) turbulent eddies and the role they play in the global circulation of the atmosphere of Jupiter. In Chapters 2 and 3 we use time sequences of Voyager images and Voyager Infrared Radiometer and Imaging Spectrometer (IRIS) data to obtain information relating to the dynamics and energetics of the Jovian atmosphere. In Chapter 2 we examine the role of various observable energy reservoirs and transport processes in maintaining the mean zonal circulation. In Chapter 3 we examine the large-scale turbulent spectrum. The second segment of our report begins in Chapter 4 with a detailed examination of the role played by stresses in maintaining the largest Jovian eddy, the Great Red Spot. We then turn to an investigation of the validity of the solitary Rossby wave model for the Great Red Spot as suggested by Maxworthy and Redekopp (1976). Based upon observed IRIS vertical temperature profiles we examine the vertical structure of an atmospheric soliton in Chapter 5 and compare our results to IRIS observations of the temperature structure of the Red Spot.

Chapter 1 is a rather detailed introduction to our thesis. We begin with a brief discussion of the role played by large-scale turbulence in Earth's atmosphere. Our dependence upon Voyager imaging and IRIS data throughout this investigation dictates a very brief discussion of the hardware and methods used to obtain measurements of Jovian

wind speeds and turbulence. Chapter 1 ends with a review of theoretical models which have been developed to explain the Jovian circulation.

The basic geometry used in our study will be that familiar to geophysical fluid dynamicists as the mid-latitude beta-plane. We generally follow notation much like that of Holton (1972). We may establish a spherical coordinate system with origin at Jupiter's center from which we measure r radially outward. We measure longitude by λ (positive westward) and latitude by θ_c (positive northward). For an oblate spheroid like Jupiter we may define an oblate or planetographic latitude by unsubscripted θ as,

$$\theta = \tan^{-1} \left[\left(\frac{r_{JE}}{r_{JP}} \right)^2 \tan \theta_c \right]$$

where,

- r_{JE} = equatorial radius of Jupiter
- r_{JP} = polar radius of Jupiter
- θ_c = angle measured about Jupiter's center from equatorial plane, i.e., the so-called planetocentric latitude.

Unless otherwise explicitly stated all latitudes referenced in our work will be planetographic.

On the large, so-called quasi-geostrophic, scale curvature terms are generally neglected in the governing equations. Hence, we will typically replace λ , θ , and r by their local Cartesian equivalents x , y , and z , where x is measured positive eastward, y is measured positive northward, and z is measured positive upward. The velocity

components along these three Cartesian axes are given by the total time derivatives of x , y , and z and are represented symbolically as u , v , and w .

All other symbols will be explicitly defined as they initially appear in the context of our investigation. Unless otherwise noted a symbol will retain its meaning throughout the entire body of this work. We have (with very few exceptions) avoided the redundant use of a single symbol for two different parameters even though the parameters may appear in very different contexts.

1.1 The Role of Large-Scale Eddies in Earth's Atmosphere

The global circulation of any planetary atmosphere is driven by the atmosphere's attempt to minimize available potential energy. This minimization generally involves the even redistribution of unevenly distributed heat. In Earth's atmosphere incoming heat is unevenly distributed from equator to pole and subsequent attempts by the atmosphere to move cold air equatorward and warm air poleward drive the global circulation. The redistribution of heat can take place over a wide spectrum of spatial scales so that the definitive measurement of energy transport rates associated with the redistribution is quite complicated. The simplest approach to take regarding these spatial scales is bimodal and is obtained by performing a decomposition of the global circulation into zonally-averaged components and fluctuations from these zonal averages or "eddy" components. Thus, the zonal wind component (u) becomes,

$$u = \bar{u} + u'$$

where,

\bar{u} = zonally averaged component

u' = deviation or eddy component.

This so-called Reynolds decomposition (after Reynolds, 1895) raises the question: on which scale (mean or eddy) does the redistribution of heat take place? Original attempts to explain the global circulation of Earth's atmosphere (Halley, 1686; Hadley, 1735) were based upon the notion that the redistribution took place on the zonal mean scale. The so-called "Hadley cell" circulation, representing a redistribution on the mean scale, formed the basis for most general circulation models for the next 200 years or so (Ferrel, 1889; Thomson, 1857). Models based upon mean scale redistribution met with only limited success, and understanding of the general circulation of Earth's atmosphere seemed to stagnate.

Jeffreys (1926) instigated the modern era of general circulation studies with his investigation of the angular-momentum balance of our atmosphere. His work suggested that eddy-scale motions must play an important role in any model of the global circulation. Starr and White (1951) and Lorenz (1955) subsequently showed that at mid-latitudes eddies with length scales of 10^3 km were responsible for the bulk of the heat transport in the terrestrial atmosphere. Hence, in Earth's atmosphere eddies represent a critical link in the north-south redistribution of potential energy.

A useful context in which to look at the global circulation is that provided by the Oort Energy Budget Diagram (Oort, 1964; see

Lorenz, 1967 for a detailed treatment). The approach is to divide the total energy contained in the atmospheric system into 4 reservoirs: zonal mean and eddy available potential energy (\bar{P} and P') and zonal mean and eddy kinetic energy (\bar{K} and K'). The dynamics of the global circulation may be described in terms of the energy transport processes which link the four reservoirs. In Figure 1.1 we present an Oort diagram for Earth's troposphere. Following Lorenz (1967) the magnitude of the energy contained in each reservoir may be expressed approximately as,

$$\bar{P} = \frac{1}{2} \int_V \rho \frac{R^2 \bar{T}^2}{H^2 N^2} dV \quad (1.1)$$

$$P' = \frac{1}{2} \int_V \rho \frac{R^2 T'^2}{H^2 N^2} dV \quad (1.2)$$

$$\bar{K} = \frac{1}{2} \int_V \rho (\bar{u}^2 + \bar{v}^2) dV \quad (1.3)$$

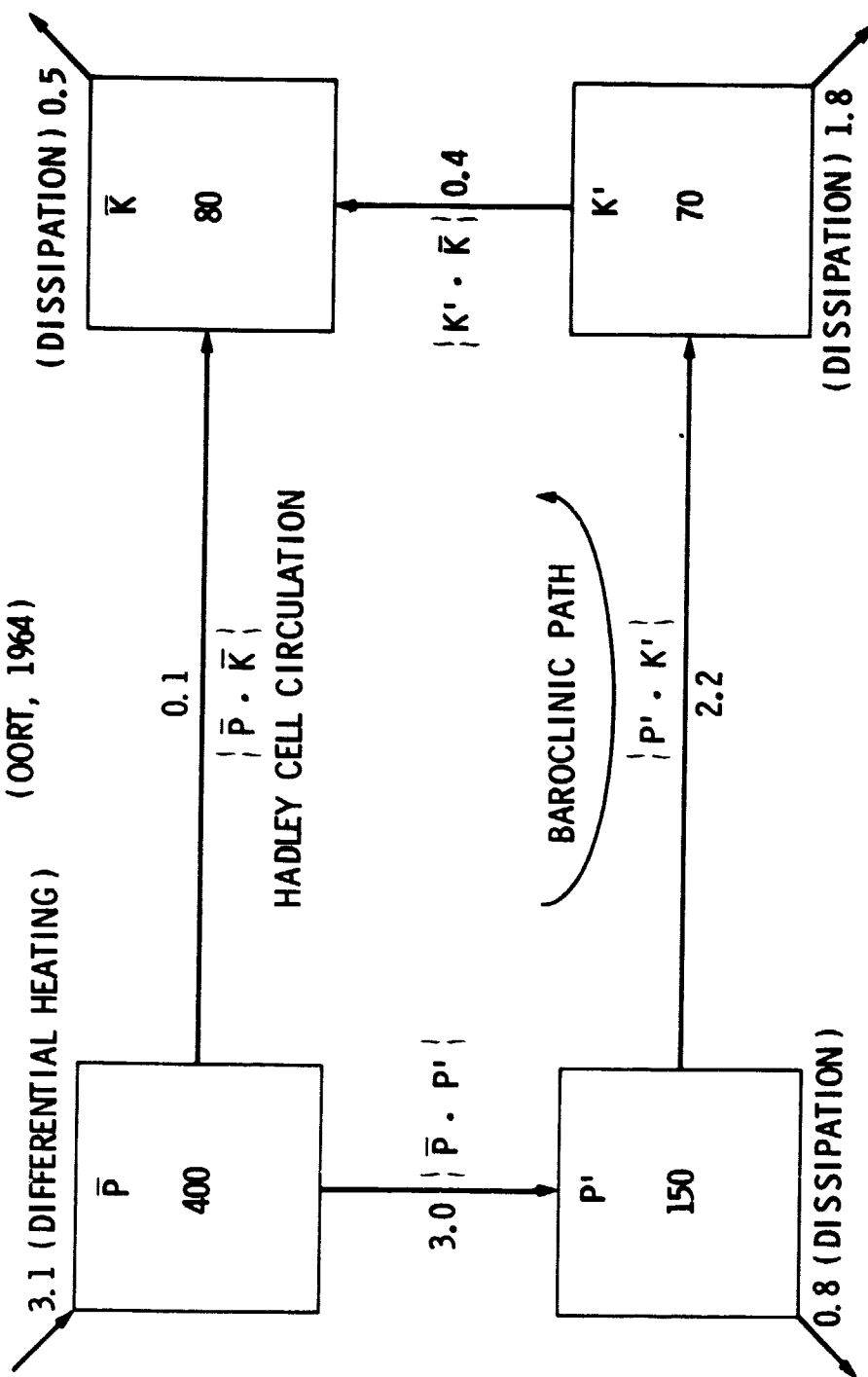
$$K' = \frac{1}{2} \int_V \rho (u'^2 + v'^2) dV \quad (1.4)$$

where,

- ρ = mass density
- R = gas constant
- H = pressure scale height

Figure 1.1. Oort Energy Budget Diagram for the terrestrial troposphere. Zonally symmetric differential solar heating establishes a reservoir of mean available potential energy (\bar{P}) in a process which is about 2% efficient. Roughly 20% of this mean available potential energy is converted into zonal flow by direct Hadley cell overturning mostly in the tropics. Nearly 80% of the forcing for Earth's general circulation is provided by mid-latitude baroclinic eddies which ultimately pump the bulk of their momentum into the mean zonal flow.

ENERGY BUDGET OF THE TERRESTRIAL TROPOSPHERE (OORT, 1964)



QUANTITIES WITHIN RESERVOIRS HAVE UNITS OF 10^{-4} joules kgm^{-1} .
TRANSPORT QUANTITIES HAVE UNITS OF 10^{-4} watts kgm^{-1} .

PRECEDING PAGE BLANK NOT FILMED

- N = Brunt-Väisälä frequency
 \bar{T} = zonally averaged temperature deviation from global mean
 T' = eddy temperature deviation from global mean
 \bar{u}, \bar{v} = zonal mean of zonal and meridional wind component
 u', v' = eddy zonal and meridional wind component

and $\int_V () dV$ indicates integration over a volume of atmosphere.

The redistribution of atmospheric energy involves transport processes linking the four reservoirs. These transport processes may be written as (Holton, 1975):

$$\{\bar{P} \cdot \bar{K}\} = + \int_V \frac{R}{H} \bar{w} \bar{T} dV \quad (1.5)$$

$$\{\bar{P} \cdot P'\} = - \int_V \rho \frac{R^2}{H^2 N^2} \left(\overline{v' T'} \frac{\partial \bar{T}}{\partial y} + \overline{w' T'} \frac{\partial \bar{T}}{\partial z} \right) dV \quad (1.6)$$

$$\{P' \cdot K'\} = + \int_V \rho \frac{R}{H} \overline{w' T'} dV \quad (1.7)$$

$$\begin{aligned} \{K' \cdot \bar{K}\} = & + \int_V \rho \left(\overline{u' v'} \frac{\partial \bar{u}}{\partial y} + \overline{u' w'} \frac{\partial \bar{u}}{\partial z} + \overline{v'^2} \frac{\partial \bar{v}}{\partial y} + \overline{v' w'} \frac{\partial \bar{v}}{\partial z} \right. \\ & \left. + \bar{u} \overline{u' v'} \frac{\tan \theta}{r_J} - \overline{u'^2} \frac{\bar{v} \tan \theta}{r_J} \right) dV \end{aligned} \quad (1.8)$$

where,

\bar{w} , w' = zonal mean and eddy vertical velocity component

r_J = Jovian radius

$H = \frac{R\bar{T}}{g}$ = pressure scale height

θ = latitude.

Note that the above expressions are geostrophic, as we have made the substitution,

$$\frac{\partial \phi}{\partial z} = \text{geopotential thickness} \approx \frac{R\bar{T}}{H}.$$

Overbars represent zonal mean values, while the symbolism $\{A \cdot B\}$ describes energy transport from reservoir A to reservoir B. In Earth's atmosphere the processes responsible for maintaining a supply of energy in the K' reservoir relate to the baroclinicity (see Section 1.3.2.2.2) of our atmospheric system. Later in this chapter we will review those processes which have been proposed as being responsible for maintaining \bar{K} and K' in Jupiter's atmosphere. In Chapter 2 we shall set up an Oort diagram for Jupiter's atmosphere and comment on its powerful implications.

1.2 Observational Resources Provided by Voyager

The two Voyager flybys of Jupiter in March and July, 1979 provided a wealth of information relating to the dynamics and energetics of Jupiter's atmosphere. In our observational studies we are dependent

upon time sequences of Voyager images to obtain measurements of the Jovian cloudtop motions. Thus, a brief description of the Voyager imaging system and the methods used to deduce wind speeds from observed cloud motions is in order. The interested reader is referred to Smith et al. (1977) and Snyder (1979) for a more detailed description of the hardware.

1.2.1 The Voyager Imaging Experiment and the AMOS System

Each Voyager spacecraft is equipped with identical television camera systems, consisting of boresighted narrow-angle and wide-angle vidicon cameras with focal lengths of 1500 mm and 200 mm respectively. The fields-of-view provided by the two camera systems are respectively a square $0^{\circ}424$ and $3^{\circ}209$ on the side. The active imaging area on the vidicon faceplate consists of a square array of 800×800 picture elements or pixels. Thus, the approximate angular resolutions of the narrow-and wide-angle cameras are respectively 1.060×10^{-3} degrees/pixel pair and 8.024×10^{-3} degrees/pixel pair. This corresponds to a spatial resolution of 150 km/pixel pair and 1050 km/pixel pair at a range from Jupiter to the spacecraft of approximately 8.1×10^6 km. This is roughly the range and resolution associated with the global data sets used in Chapters 2 and 3.

Each camera is fitted with an eight position filterwheel which allows for monochromatic imaging through a series of filters (which for the narrow-angle camera range from an "orange" filter centered at 5700A to an "ultraviolet" filter at 3250A). Though it is possible that images through different filters might allow limited vertical discrimination of the data, we shall not concern ourselves with a possible

relation between color and altitude. Data comprising the Voyager 1 global data set (or "world map") was obtained through a narrow-angle orange filter, while the Voyager 2 world map utilized a series of narrow-angle violet images (centered at 4000Å).

Shading is encoded in an eight-bit format so that there are a total of 256 gray levels which can be assigned to each pixel in the frame. Subsequent ground-based "stretching" of the encoding can be used to enhance detail which might otherwise be lost. Such enhancement was performed on almost all of the frames used in this study.

The truly unique character of Voyager imaging data is realized in a time series of frames in which motions of small cloud features are used to deduce a measure of the wind speed at the cloudtop level. As pointed out by Maxworthy (1973) it is risky to assume that cloudtop motions represent the movement of atmospheric mass and not the phase speeds of atmospheric waves. However, we note that over a wide range of spatial scales (10^1 to 10^3 km) the observed wind speeds in any one region of the planet do not appear to be a function of wavelength (at least in the sense anticipated for motions representing phase velocities). Based upon this observation and with some faith, we shall assume that the observed cloud motions represent mass advection or "wind".

At the Image Processing Laboratory (IPL) of the Jet Propulsion Laboratory a special computer interactive facility has been set up to convert measurements of cloud motions into data sets of wind velocities. The system makes use of IPL's IBM 360/65 and PDP-11 front end processor with a set of software known as Atmospheric Motion Study

(AMOS). It is probably inappropriate and certainly time consuming for us to discuss the AMOS process in too much detail, hence, the interested reader is referred to Yagi et al. (1978). Positions in the 2-dimensional "image space" of a Voyager frame are converted into planetographic coordinates on Jupiter's "surface" (i.e., latitude and longitude). This conversion is based upon several navigational input parameters taken from the spacecraft's Science and Engineering Data Record (SEDR). The process is not, however, precisely deterministic as it requires that the limb of a Jovian map grid be fit in a least squares sense to the optical limb of Jupiter. Following the conversion from image space to map space a pair of frames separated by a known interval of time are displayed side by side on a video monitor. Using a trackball operated cursor the user cross-identifies individual cloud features in the two frames. The observed motion of these features through map space is automatically converted into a measure of u and v , the feature's zonal and meridional speed. Under the assumption that the observed velocity is advective the method provides measures of ambient wind speed. The author and others (see Beebe et al., 1980; Ingersoll et al., 1981) have estimated the total error in velocity measurement due to the sum of limb fitting, navigational parameter, and user identification errors to be approximately $\pm 1.5 \text{ m sec}^{-1}$ at a spatial resolution of roughly 150 km/pixel pair (i.e., "world map" resolution).

1.2.2 Voyager Infrared Spectrometer and Imaging Radiometer (IRIS)

Reference to Equations 1.3, 1.4, and 1.8 indicates that wind measurements with the AMOS system allows the computation of \bar{K} , K' , and portions of $\{K' \cdot \bar{K}\}$ at the cloudtop level. The computation of \bar{P} and P' and the energy conversions from potential to kinetic energy requires a spatially resolved measure of zonal mean and eddy temperature deviations, represented by \bar{T} and T' respectively. Measurements of temperature as a function of both spatial location (x and y) and pressure (p) are provided by the IRIS instrument (see Hanel et al., 1977, for a complete description of the hardware and the method of data analysis).

The IRIS instrument consists of a pair of Michelson interferometers and a boresighted radiometer. The interferometers are used to obtain measurements of radiance within absorption bands of minor atmospheric constituents. Provided the mixing ratio (assumed constant with depth) and the absorption coefficients of these constituents are known, the optical depth as a function of pressure can be computed for each frequency in the absorption band. Selection of a set of spectral intervals with a range of opacities allows one to deduce $T(p)$, the temperature as a function of pressure (Gautier and Courtin, 1979). Naturally, the presence of clouds will lead to error, and below the cloud top level deduced vertical profiles are questionable. The vertical resolution in the range from 1000 to 10 mb varies between 1 and 3 pressure scale heights. Horizontal spatial resolutions obtainable with IRIS are roughly 2000 to 4000 km for the highest resolution set of data used to compute \bar{P} and P' globally.

1.3 A Review of the Theoretical Resources at Our Disposal

Having briefly examined the nature of the Voyager data set at our disposal, it is also necessary that we provide our reader with a review of past theoretical treatments and models of the Jovian circulation. Such a background is no less a valuable resource than the rich Voyager data set. We divide this review into two sections. The first provides a brief qualitative description of what we shall later refer to as the "classical" or Hess-Panofsky model for the mean zonal circulation. The second section deals with several more detailed mechanisms which have been suggested to explain both the mean and eddy circulation.

1.3.1 The Classical Model of the Jovian Circulation (Hess and Panofsky, 1951; Ingersoll and Cuzzi, 1969)

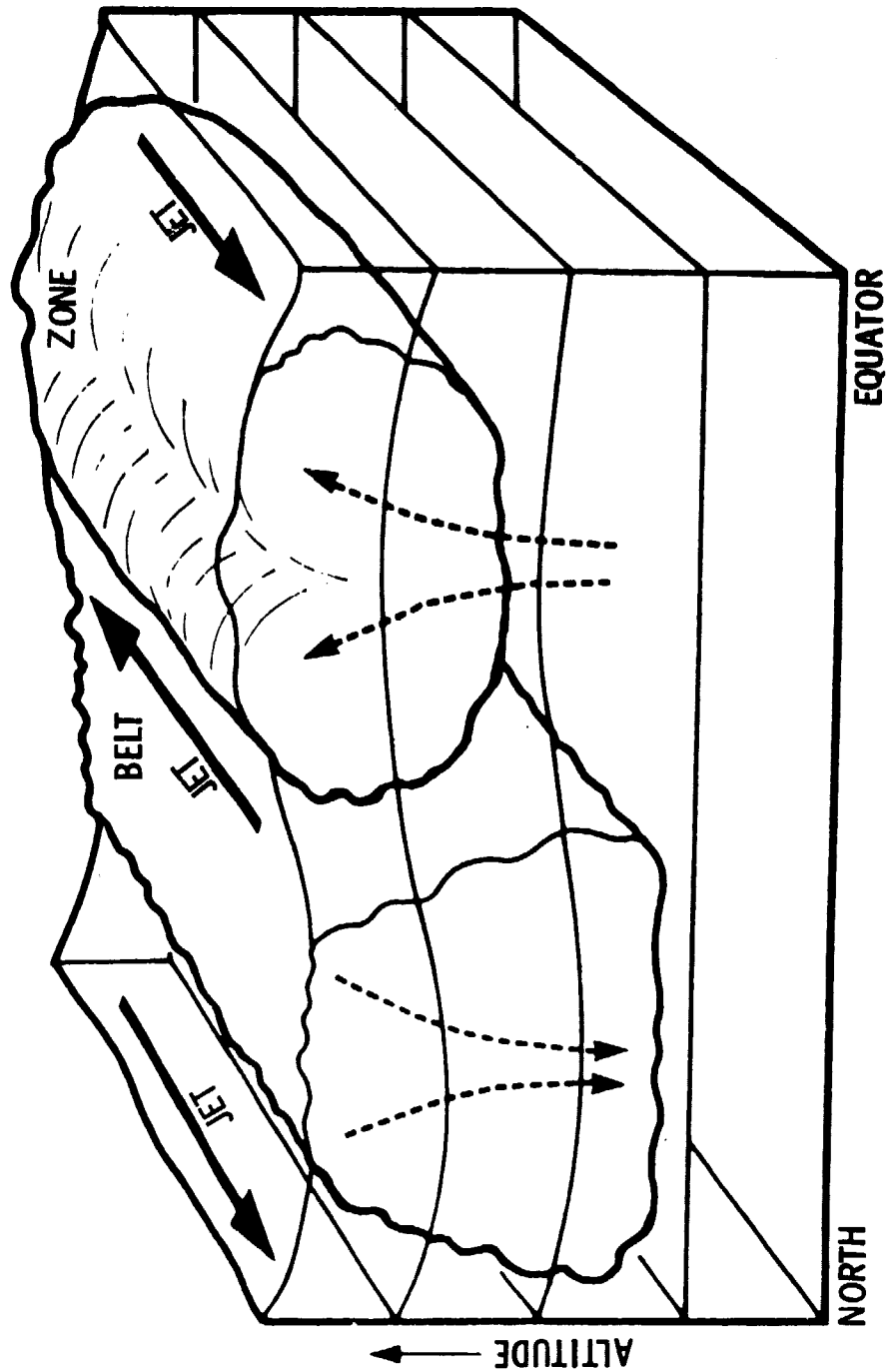
Based upon historical observations of mean zonal velocity as a function of latitude ($\bar{u}(\theta)$) Hess and Panofsky (1951), noting the cyclonic relative vorticity associated with belts (darker bands) and the anticyclonic vorticity of zones (lighter bands), first suggested that the observed cloudtop vorticity was coupled to horizontal fields of divergence (zones) and convergence (belts) through the strong constraints of geostrophy. The basic notion was that rising motion beneath the cloudtops in the zones resulted not only in the observed anticyclonic vorticity, but also in the freezing out of some atmospheric constituent (probably ammonia). They presumed that this process gave zones their brighter albedo. They suggested that sinking motion in belts led not only to cloud level convergence, but to clearing, rendering darker underlying clouds visible (see Figure 1.2).

Figure 1.2. The Hess-Panofsky mechanism for driving Jovian zonal jets.

The jets arise from the Coriolis deflection of cloudtop divergence in zones and convergence in belts, thus maximum zonal velocities occur at the belt/zone interfaces.

ORIGINAL PAGE IS
OF POOR QUALITY

CIRCULATION OF BELTS AND ZONES
(HESS - PANOFSKY)



Ingersoll and Cuzzi (1969) extended this "classical" concept of Jovian circulation to argue that the thermal wind relation constrained zones to be warmer regions beneath the cloudtops and belts to be colder regions. Thus, in this classical concept of the Jovian circulation zones were analogous to terrestrial anticyclones and belts to terrestrial cyclones. The unavoidable connotation was that the zonal mean circulation was driven by a zonally symmetric temperature distribution. This resulted in a zonally symmetric vertical motion field like that of an equator to pole series of Hadley cells. We shall henceforth refer to this classical or Hess-Panofsky model for Jupiter's mean zonal circulation as the HP model. Due to its simple eloquence, this basic model has remained nearly unchallenged in popular explanations of the Jovian circulation.

1.3.2 Possible Mechanisms Driving the Mean and/or Eddy Flow

The simple or "classical" HP model is dynamically limited only to the extent that planetary rotation is required to produce Coriolis deflections in a mean meridional wind. The mean meridional motions are assumed to be driven by an associated zonally symmetric vertical motion field. The classical model does not specify the mechanism energetically responsible for these vertical motions. More detailed theoretical treatments are necessary if we are to appeal to specific mechanisms capable of supplying energy to the mean and eddy motions. In this section we will provide a brief, yet hopefully complete, review of more detailed treatments which have appeared in the literature. We discuss only those mechanisms which currently seem to be viable. At this point we will intentionally neglect the solitary Rossby wave model

of Maxworthy and Redekopp (1976) as this model is not tied to any specific energy mechanism. Chapter 5 is devoted to a detailed investigation of the solitary wave model. In this section we examine three mechanisms which seem viable as explanations for the Jovian mean and/or eddy flow: the convective, baroclinic, and barotropic mechanisms.

Stone (1976) in a highly recommended review article looks at the mechanisms we call "convective" and "baroclinic" as manifestations of the same phenomenon: the sinking of dense fluid and the rising of light fluid so that available potential energy is reduced. He envisions this process as taking place over a wide spectrum of Richardson number (Ri) where we choose to write Ri in a form given by,

$$Ri = \frac{T\Omega^2}{g} \frac{\frac{\partial \Theta}{\partial z}}{\left(\frac{\partial T}{\partial y}\right)^2}$$

where,

Ω = planetary rotational frequency = $1.76 \times 10^{-4} \text{ sec}^{-1}$ for
Jupiter

g = gravitation acceleration

T = temperature

$\Theta \equiv T(p/p_0)^{-R/c_p} = \text{potential temperature}$

with,

p = pressure

p_0 = reference pressure

R = gas constant

c_p = specific heat at constant pressure

$\frac{\partial T}{\partial y}$ = typical meridional gradient temperature

$\frac{\partial \theta}{\partial z}$ = potential temperature lapse rate.

Notice that the Richardson number represents in some sense a measure of the ratio of the non-adiabatic lapse rate to the horizontal temperature gradient. Thus, the Richardson number can be used to classify an atmosphere as convective (at low or negative values of Ri) or as baroclinic (at larger and positive values of Ri). At negative values of Ri (i.e., a statically unstable fluid) most of the heat transport takes place vertically, and the flow is said to be convective. As Ri increases the plane of heat transport reorients to the horizontal and at a critical value of $Ri = 1/4$ (at which even forced convection ceases) the flow becomes baroclinic (Drazin and Howard, 1966). Thus, we might take the view that baroclinicity is little more than "sideways" convection.

Both convective and baroclinic instabilities involve vertical gradients of temperature, coupled in the latter case with horizontal temperature gradients. Unfortunately, it remains likely that both the vertical and the horizontal spatial resolution obtainable with the Voyager IRIS instrument is inadequate for a definitive observational treatment of either subject. We nevertheless, begin with a review of Jovian circulation models which employ these mechanisms.

1.3.2.1 Convective Models

A logical extension of the classical HP model is one in which vertical motions are driven by some form of convective instability

associated with the belts and zones. Thus, convective models have often been used to describe not only the nonaxisymmetric (eddy), but the axisymmetric (mean) Jovian features as well. We designate as convective those models which depend essentially upon unstable vertical density (i.e., temperature) gradients and note that they may be divided into three categories: those for which convective motions are shallow relative to the planetary radius, those for which convective motions are deep relative to this radius, and those which involve a convective feedback mechanism driven by latent heat release or a Conditional Instability of the Second Kind (CISK; note that this CISK mechanism is convective rather than wave induced).

1.3.2.1.1 Shallow Convective Models (Williams and Robinson, 1973)

Williams and Robinson (1973) examine both the linear and nonlinear problem of spherical, rotating Bénard convection for a "semi-shallow" atmosphere (one for which "deep" atmospheric effects due to curvature terms in the equation of motion become active while remaining secondary). From the linear theory of rotating Bénard convection they point out that with the assumption that the Prandtl number (σ) is of order unity,

$$\sigma = \frac{K_e}{\kappa} \sim O(1)$$

where,

K_e = total eddy viscosity coefficient

κ = eddy thermal diffusivity,

the convective eddy geometrical aspect ratio (horizontal wavelength to depth) is given by $2\pi\mu^{1/2} Ta_0^{-1/4}$, where $Ta_0 = (Ta \sin^2 \theta)$ is a local

Taylor number at latitude θ , and $Ta = 4\Omega^2 d^4 / K_{eV}^2$ is the Taylor number (for atmospheric depth d and vertical eddy viscosity coefficient K_{eV}). The dimensionless parameter μ is just the ratio of horizontal (K_{eH}) to vertical (K_{eV}) eddy viscosities where,

$$K_e^2 = K_{eV}^2 + K_{eH}^2$$

and

$$\mu = K_{eH} / K_{eV}.$$

Hence, if L_0/d represents a measure of the local planetary aspect ratio (where L_0 = local horizontal length scale) then,

$$\mu = \frac{Ta_o^{1/2}}{4\pi^2} \left(\frac{L_0}{d} \right)^2.$$

The Rayleigh number (Ra) measures the ratio of the buoyant force to the product of the viscous drag and the rate of heat diffusion. For the Jovian atmosphere Ra is given by,

$$Ra = g \beta \Delta T \frac{d^3}{K_{eV} \kappa_V}$$

where,

g = gravitational acceleration

$\beta = \frac{df}{dy}$ = gradient of planetary vorticity

$\Delta T = T_L - T_U$ with T_L and T_U respectively the lower and upper boundary temperatures

κ_V = vertical thermal diffusivity.

Williams and Robinson assume that Ra in the Jovian atmosphere is given by the critical value for the onset of convection,

$$Ra_c = 4\pi^2 \nu Ta_0^{1/2}$$

in order to arrive at the relation,

$$d\Delta T = \frac{4\Omega^2}{g} L_0^2 \sin^2 \theta.$$

Using the equatorial westerly jet to fix the value of L_0 and θ they argue that the product $d\Delta T$ is a constant, indicating that for a given depth scale there is only one free parameter, K_{ev} , the vertical eddy viscosity. For parametric inputs of d and K_{ev} (i.e., Ra and Ta respectively) they generate numerical solutions to the linear problem (i.e., profiles of u , w , and T in the vertical-meridional plane, where u is the zonal velocity, w is the vertical velocity, and T is the temperature). They find that linear rotating Bénard convection is capable of maintaining an equatorial jet of the observed width, shape, and magnitude if the active atmosphere is relatively shallow ($d < 500$ km). Convective activity is a maximum at the equator. The latitudinal range of convective activity seems determined by $Ra/Ta^{1/2}$, while Ra determines the amplitude of the convection.

An important distinction between the baroclinic and forced convective instability mechanisms is that the former is independent of the characteristics of the resulting turbulent field (and in that sense linear to first order), whereas the latter depends upon the eddy

viscosities associated with the turbulence (and is hence a nonlinear mechanism). Thus, Williams and Robinson are compelled to parameterize the eddy viscosities according to mixing-length theory for shear-driven turbulence (Deardorff, 1971). The numerical solutions of the nonlinear case have axisymmetric modes which yield a zonal wind profile remarkably like Jupiter's. The associated vertical velocity field yields a pattern of increasingly narrow belts and zones progressing poleward. As in the HP model, belts and zones are regions of cyclonic and anti-cyclonic mean shear. Poleward of approximately 45° latitude convective activity ceases. Williams and Robinson thus speculate that the mean zonal wind profile and associated belts and zones can be represented as 2-dimensional (i.e., "flat") Bénard convection cells with fairly large aspect ratios ($L_0/d \geq 15$).

They conclude their investigation by performing a numerical stability analysis in which the axisymmetric flow of both the linear and nonlinear model is subjected to longitudinal perturbations. Thus, they represent the observed cloudtop eddies as perturbations on the zonally symmetric Bénard cells. The resulting 3-dimensional cells in the velocity and temperature fields grow at a slow rate, indicating that the turbulence lies close to the transition point from 3- to 2-dimensional flow (i.e., from large to fairly small aspect ratios).

1.3.2.1.2 Deep Convective Models (Busse, 1976; Ingersoll and Pollard, 1981)

Williams and Robinson found that for Rayleigh numbers near Ra_c the dominant convective mode consists of 2-dimensional cells which are symmetric in the vertical-meridional plane. However, for small values

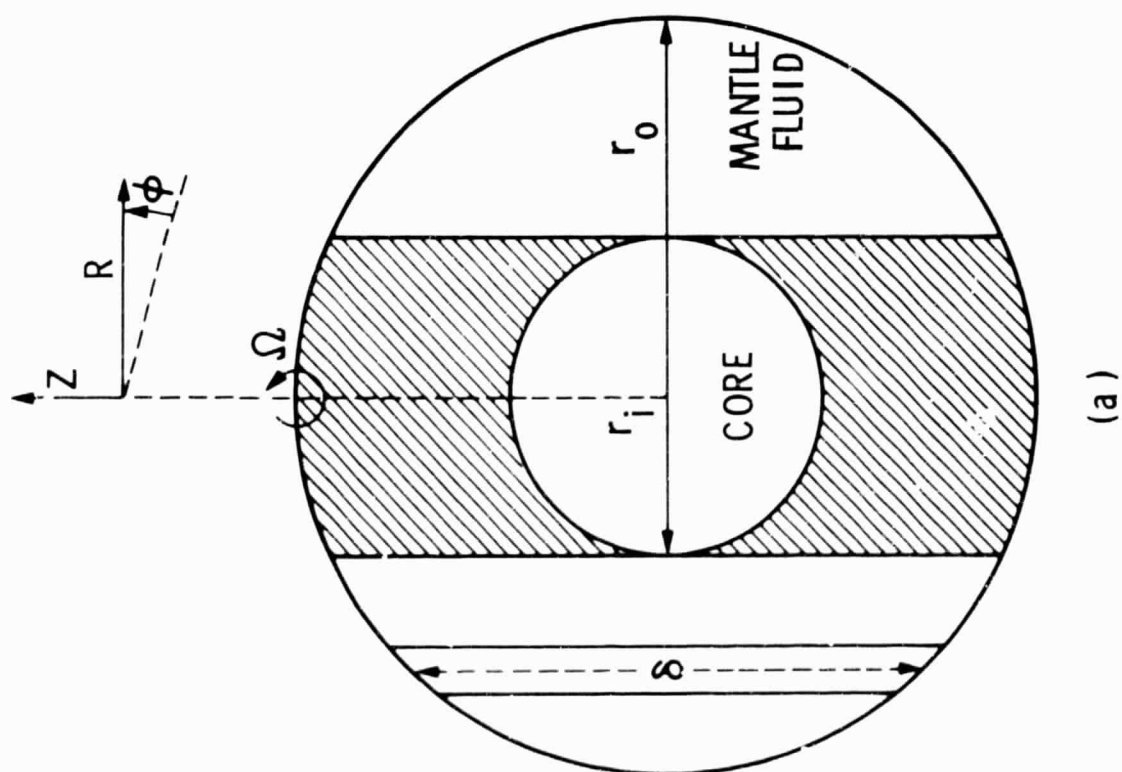
of Taylor number (i.e., small rotation effects) the convective cells become deep in the sense that the depth scale (d) of the atmosphere is constrained to values of order 1000 km or more. The linear theory for such low Taylor number cases is examined by Busse (1970a) and thereafter extended to describe the motions within the solar (Busse, 1970b) and Jovian (Busse, 1976) atmospheres.

Busse examines the case of 3-dimensional turbulence in a self-gravitating, rotating spherical shell of inner radius (r_i) and outer radius (r_o) with uniform heating on the inner sphere. For the case where turbulent viscosity is important in the interior, non-boundary layer flow (i.e., low Taylor numbers or high Ekman numbers) he is able to obtain expressions for both the critical radius and critical Rayleigh number for the onset of convection as both functions of Ekman number ($E \equiv K_e/\Omega L^2$, essentially an inverse Taylor number), Prandtl number ($\sigma \equiv K_e/\kappa$) and latitude (θ). These expressions, as well as the solutions to the governing Boussinesq equations, are obtained on the basis of a perturbation expansion in the parameter n , where n is the variation in the length of the fluid cylinder in a direction parallel to the axis of rotation. The linear analysis requires that $n/\delta \ll 1$, where δ is a typical cylinder length in the fluid shell (see Figure 1.3a). Busse found that in the Jovian case, where $r_i \approx 50,000$ km (for the metallic hydrogen core; see Podolak and Cameron, 1974) and $r_o \approx 70,000$ km, the inviscid flow at latitudes less than that defined by the intersection of a tangent to the core at the equator with the outer surface at r_o is governed by the Taylor-Proudman constraint to lowest order in n . Even in the

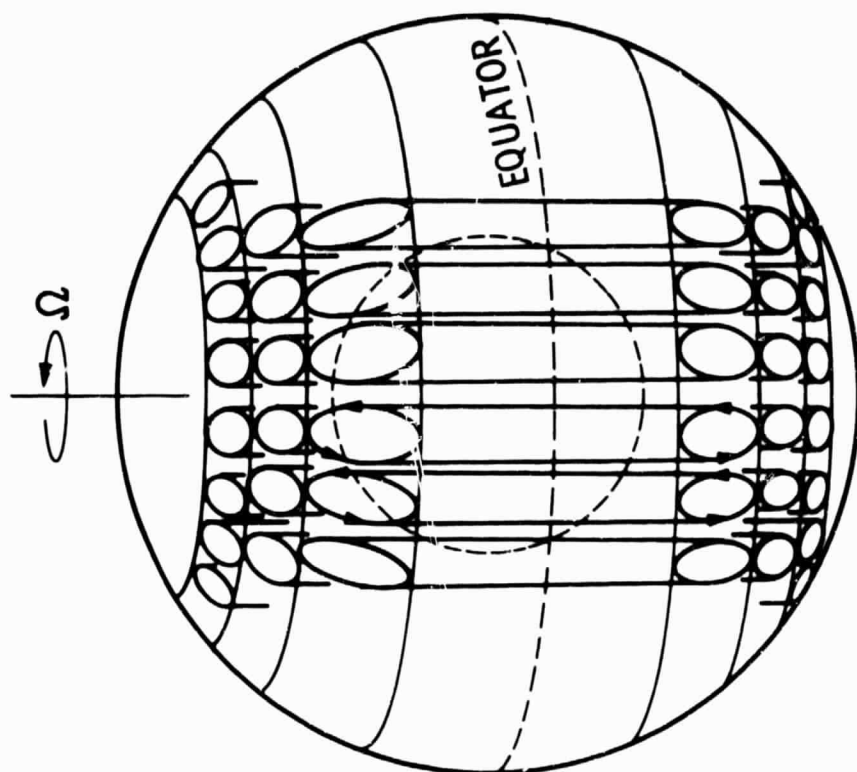
Figure 1.3.(a) Schematic cross-sectional view of the deep convective cylinders of Busse (1976). The Taylor-Proudman cylinders extend through the fluid mantle with their long axis parallel to the rotational axis of Jupiter. The solid core casts a "shadow" at polar latitudes and prevents the formation of cylinders.

(b) 3-dimensional sketch of Busse cylinders. Busse (1976) suggests that eddy stresses, arising from the vorticity associated with the cylinders, drive the observed mean zonal circulation at the level of the cloudtops.

ORIGINAL PAGE IS
OF POOR QUALITY



(a)



(b)

turbulently viscous case the instabilities in the temperate and tropical regions take the form of deep convective rolls oriented parallel to the rotational axis (see Figure 1.3b). Busse (1970a) found close agreement between his results and the nonlinear numerical results for the so-called "even" mode of Roberts (1968), which is remarkable in that the linearity condition ($\tau/\delta \ll 1$) is clearly violated for such deep cells. The flow at latitudes higher than the "critical" value (i.e., about 45° latitude for Jupiter) corresponds to the so-called "odd" mode and is characterized by convective cells like those found in a plane layer, rotating about a vertical axis and heated from below (Chandrasekhar, 1961). Busse (1976) uses the fact that there are five observed zones in each hemisphere of Jupiter, and presumably five layers of convective columns, to deduce a turbulent Ekman number and corresponding eddy viscosity coefficient of $K_e = 1.2 \times 10^6 \text{ m}^2 \text{ sec}^{-1}$.

A key point to note regarding the shallow model of Williams and Robinson and the deep model of Busse is the essential difference between the mechanism giving rise to the mean zonal flow. In the model of Williams and Robinson the mean zonal flow is the result of the Coriolis deflection of mean meridional motions produced by 2-dimensional Bénard convection cells which are most active in the equatorial regions. This mechanism is identical to that maintaining the mean flow in the classical HP model. In the model of Busse the mean zonal flow is inertially driven through the nonlinear advection of momentum by eddy stresses associated with the giant convective cells which are presumably hidden beneath the Jovian cloudtops in the temperate and tropical regions.

Busse's Taylor-Proudman cylinders correspond to the so-called "geostrophic mode" of Greenspan (1968) in which the inner flow between two concentric cylinders remains constant in directions parallel to the axis of rotation. Ingersoll and Pollard (1981) perform a linear stability analysis of mean zonal flow in this geostrophic mode. The driving mechanism for the flow itself is not specified; however, forced convection in Busse-like cylinders would be one consistent mechanism. Ingersoll and Pollard describe the differential rotation of the coaxial geostrophic cylinders with a zonal velocity profile given by $\bar{u}(R)$ where \bar{u} is the mean zonal velocity in the azimuthal direction (ϕ), and R is the radial direction in a cylindrical coordinate system with a Z -axis corresponding to the planet's rotational axis (see Figure 1.3). Note that $R = r_J \cos \theta_c$, where r_J is the Jovian radius and θ_c is the planetocentric latitude. Ingersoll and Pollard (1981) perform a linear stability analysis of the radial profile $\bar{u}(R)$. They find that for low azimuthal wavenumber disturbances (i.e., x , the distance measured to the east on a spherical surface is scaled by $L_0 = r_J \cos \theta_c$, whereas R , the radial distance toward the rotational axis is scaled by a length $L \ll L_0$) differential rotation associated with the geostrophic cylinders obeys a modified form of the barotropic vorticity equation given by,

$$\frac{d\omega}{dt} - B \frac{dR}{dt} = 0$$

where,

$$\omega = \hat{e}_z \cdot \nabla \times \vec{V} = \text{axial component of relative vorticity in cylindrical coordinates}$$

and,

$$B \equiv \frac{2\Omega}{M} \frac{dM}{dr}$$

with,

$$M(R) \equiv \int_{-h}^{+h} \rho(R, Z) \, dZ,$$

$$h = \sqrt{r_J^2 - R^2} = \text{one-half the length of the geostrophic cylinder.}$$

Note that in the above vorticity equation B takes the usual role of $-\beta$, where $\beta \equiv df/dy$ is the gradient of planetary vorticity.

Ingersoll and Pollard find that the stability of the differential azimuthal rotation $\bar{u}(R)$ with respect to a perturbation of the form $\psi(R) \exp[ik(x-ct)]$ is governed by the equivalent of the barotropic stability equation in which $-B$ replaces β and is given by,

$$(u - c)\psi_{RR} + (B - \bar{u}_{RR})\psi = 0$$

where,

$\psi = \psi(R)$ = amplitude of the disturbance streamfunction

c = disturbance phase speed in the azimuthal direction.

The azimuthal index of the disturbance, which must be small, is given by $m = kr_J \cos \theta$ and the growth rate by the product kc_i , where c_i is the imaginary part of the azimuthal phase speed. Numerically, Ingersoll and Pollard find that a sufficient condition for c to be complex is that the quantity $(B - \bar{u}_{RR})$ must reverse sign somewhere within the domain (note the similarity with the classical barotropic stability criterion; see Section 1.3.2.4). One would expect violations of their modified barotropic stability criterion to occur at the latitudes of the eastward jets (i.e., where $(B - \bar{u}_{RR}) \gtrsim 0$) in analogy with the classical barotropic stability criterion for which violations are anticipated at the latitudes of the westward jets (i.e., where $(B - \bar{u}_{yy}) \lesssim 0$).

They assume that $\bar{u}(R)$ manifests itself in the observed cloudtop profile ($\bar{u}(y)$), and examine the stability of the observed profile of differential rotation $\bar{u}(R)$ on Jupiter. According to their modified barotropic stability criterion the deduced profile of $\bar{u}(R)$ is stable to low wavenumber, linear perturbations. There is the suggestion (see their figure 2) that one eastward jet at $+23^\circ$ latitude might be unstable, but they argue that the overall stability of the $\bar{u}(R)$ profile favors a mean zonal wind which is driven by the differential rotation of geostrophic cylinders. Their numerical results indicate that if the modified barotropic stability criterion is violated, the disturbance phase lines will slope eastward with increasing R away from the centers

of the eastward jets. This implies that the disturbance is extracting kinetic energy from the mean zonal flow given by $\bar{u}(R)$, and they conclude that the amplitude of the mean zonal wind profile on Jupiter is limited by their modified stability criterion such that the mean flow remains marginally stable.

On this basis they fail to explain why the amplitudes of the eastward jets are for the most part far below the stability limit. They argue that the classical barotropic stability criterion, which holds for a shallow atmosphere, is violated by the observed westward jets. Hence, their reader is led to the conclusion that many of the observed cloudtop eddies are manifestations of barotropic instability in a shallow, stratified upper layer of the atmosphere. On the other hand the mean zonal flow of Ingersoll and Pollard is controlled by the differential rotation of the geostrophic mode cylinders and is thereby decoupled from the observed cloudtop eddies. They point to long term constancy of the zonal flow (Chapman, 1969) and the hemispheric symmetry of $\bar{u}(y)$ as observations supporting their view.

If the model of Ingersoll and Pollard is accepted, we will be able to deduce little from the cloudtop kinematics which is meaningful on the level of the planetary scale energetics. That is, if the observed mean and eddy flows are decoupled, we will not be able to represent the atmosphere's energy budget by a closed Oort energy diagram, as the observed reservoirs of eddy energy have little relevance to the observed mean energy reservoirs (see our diagram in Section 2.5). Ingersoll and Pollard do not address the ultimate question of what mechanism drives the differential rotation.

We shall later see that at least at some latitudes the observations are at best marginal for deducing violations of the classical barotropic stability criterion. More importantly, on the global mean the deduced direction of kinetic energy transport associated with the cloudtop eddy advection of momentum is opposed to that anticipated for barotropic instability.

1.3.2.1.3 Latent Heat Dependent Convection and CISK (Barcilon and Gierasch (1970); Gierasch, Ingersoll, and Williams (1973))

Barcilon and Gierasch (1970) proposed that the mean zonal flow observed at the cloudtop level is driven by the latent heat of water vapor which condenses in the Jovian zones. Thus, unlike the deep convective cells of Busse their convective activity is shallow. Unlike the shallow convection of Williams and Robinson, the mechanism driving the convection is not tied to a uniformly heated lower boundary (presumably due to the presence of a deep internal heat source), but rather to local thermodynamics at the level of the clouds. Their mean zonal flow is driven by geostrophic constraints, in this case coupled to the mean meridional motion via an induced meridional temperature gradient and subsequent thermal wind field. Their treatment is valid only for small Ekman numbers (where $E = K_{eV}/fH_0^2 =$ Ekman number at the tropopause, with vertical eddy viscosity K_{eV} , Coriolis parameter f , and a pressure scale height H_0 at the tropopause level). The condition that $E < 10^{-2}$ holds for $K_{eV} < 10^3 \text{ m}^2 \text{ sec}^{-1}$. For typical Jovian velocity scales the resulting Richardson number (Ri) is 3.7×10^{-3} , clearly indicative of forced convection in which the turbulence becomes 2-dimensional (i.e., the horizontal scales of motion become much larger than the vertical scales; see Priestly, 1959).

In the model of Barcilon and Gierasch the stress-free interface at the tropopause gives rise to an Ekman layer of order E . Subsequent Ekman pumping implies an $O(E)$ mean meridional flow dependent upon the vertical gradient of meridional temperature differences. Their meridional temperature differences, characterized by a meridional gradient $\partial T_0 / \partial y$ (where T_0 = temperature at the tropopause level), are maintained as a result of a net flux of condensate (i.e., water vapor) into the zones. The subsequent release of latent heat increases the temperature in cloudy regions (zones). Thus, their meridional temperature gradient applies not on the equator to pole scale, but rather on the zone to adjacent belt scale.

The order E mean meridional motions advect entropy away from the zones. They parameterize this loss of entropy with a linear function in $T_0(y)$, which, if balanced by diminished radiation loss to space due to the blocking effect of the clouds within the zone, leads to a vertically integrated statement of energy conservation which takes the form of a non-linear, inhomogeneous second-order differential equation in $T_0(y)$. The inhomogeneity is related to the water vapor flux entering the zones.

Their solutions indicate that higher temperatures can be maintained in the zones due to an increased water vapor concentration there. Unfortunately, their model does little more than simply defer the ultimate question which now becomes: how does water vapor become concentrated in the zones in the first place? They speculate that perhaps the zonally symmetric baroclinic instabilities of Stone (1966) are ultimately responsible for this concentration.

A more pleasing argument results if we explain the water vapor concentration in zones on the basis of lower level convergence in the zones. In such a case the release of latent heat drives increased vertical motions which through continuity of mass drive more vigorous mean meridional motions. These meridional motions increase the influx of water vapor, which, through the increased release of latent heat, drives more vigorous vertical motions. Such an inherently unstable mechanism is one example of a Conditional Instability of the Second Kind (the CISK mechanism). In subsequent work Gierasch, Ingersoll, and Williams (1973) suggest that a greenhouse effect associated with the cloudy zones is responsible for local warming which leads to increased vertical motion, more condensation, and subsequently more cloudiness; the mechanism is of the CISK type. A major criticism is levelled against a mean zonal flow ultimately maintained through the CISK mechanism by Williams and Robinson who point out that a direct analogy with terrestrial CISK mechanisms requires that the downwelling regions (belts) cover approximately five times the horizontal area of the upwelling regions or zones (see Charney, 1970). Such a belt/zone asymmetry is not observed on Jupiter.

1.3.2.2 Baroclinic Models

We have already remarked that in a sense baroclinic instabilities represent horizontal or "sideways" convection (see Pedlosky, 1979, pg. 451 for a discussion of "Eady Angle convection") hence, a "baroclinic" atmosphere is characterized by horizontal heat transport rather than large vertical heat transport as in a "convective" atmosphere. As pointed out by Stone (1976), the baroclinic mechanism tends to

stabilize the vertical temperature gradient of an atmosphere leading to higher values of temperature lapse rate ($\partial T / \partial z$) and higher values of Richardson number. Thus, in Stone's Richardson number spectrum baroclinic instabilities occur in the $Ri > 1/4$ regime. The basic instability mechanism can be of two types: a so-called inertial instability ($1/4 < Ri < 1$) and the conventional baroclinic instability ($Ri > 1$). Both forms of instability are "baroclinic" in the sense that they depend upon vertical shear induced by the thermal wind relation in the mean zonal wind (as opposed to "barotropic" mechanisms which depend upon the horizontal shear in the mean wind). The ultimate source of this vertical shear is, of course, the available potential energy stored in a field for which isopycnics (lines of constant density) and isobars (lines of constant pressure) do not coincide ($\nabla \rho \times \nabla p \neq 0$). We shall find that conventional baroclinic instabilities draw their energy directly from the mean available potential energy, whereas the inertial instability feeds upon the mean zonal kinetic energy which is driven by the symmetric conversion of \bar{P} into \bar{K} .

1.3.2.2.1 Inertial Baroclinic Instabilities (Stone, 1966; Stone, 1967; Stone, 1971)

Stone (1966) introduces the inertial instability mechanism by considering the simplest baroclinic model, that of Eady (1949). The reader is referred to Pedlosky (1979, pg. 456) for a discussion of this basic model. The approach is to perturb a basic baroclinic state given by

$$U = Z$$

$$V = W = 0$$

$$\Theta = z - \frac{y}{Ri}$$

where U , V , and W are the zonal, meridional, and vertical dimensionless velocities of the basic state; x , y , and z are now respectively the zonal, meridional, and vertical dimensionless coordinates; $\Theta = \Theta(y, z)$ is now the dimensionless potential temperature; and Ri is the Richardson number. The complete form of the perturbation, which is dependent upon x , y , and z , is given by,

$$w = N(z) \exp [i(\sigma t + kx + \lambda y)]$$

where,

w = dimensionless perturbation vertical velocity

N = dimensionless Brunt-Väisälä frequency

σ = dimensionless perturbation complex frequency

k = dimensionless perturbation zonal wavenumber

λ = dimensionless perturbation meridional wavenumber.

The linear problem reduces to a stability analysis of the characteristic equation (as written by Stone, 1966),

$$[1 - (\sigma + kz)^2] \frac{d^2 w}{dz^2} - \left[\frac{2k}{\sigma + kz} - 2i\lambda \right] \frac{dw}{dz} - \left[Ri(k^2 + \lambda^2) + \frac{2ik\lambda}{\sigma + kz} \right] w = 0$$

with rigid lid and flat bottom boundary conditions,

$$w = 0 \quad \text{when} \quad z = 0, 1.$$

The basic state is unstable to the linear perturbation if σ has a negative complex component, a situation which is determined in the characteristic equation entirely by the magnitude of Ri . Perturbations for which $\lambda = 0$ are in general zonally asymmetric. The case for $\lambda = 0$ and $Ri > 1$ has been studied extensively (Eady, 1949; Arnason, 1963) and represents the conventional baroclinic instability. Taking Ri as a free parameter, Stone (1966) examines perturbation growth rates in the λ, k domain (see his figure 5 for a good summary of the results). The analysis near the zonally symmetric axis ($k = 0$) indicates maximum perturbation growth rates for $1/4 < Ri < 1$ and $\lambda = \infty$. These rapidly growing baroclinic instabilities take the form of a series of long zonal rolls, a geometry clearly suggestive of Jovian belts and zones.

For a strongly stratified atmosphere ($Ri > 1$) the perturbation vertical velocities are of the order of the Rossby number and thus, in a quasi-geostrophic (zeroth order in Rossby number) model vertical eddy stresses of the form $\overline{w'u}$ may be neglected in the resulting perturbation energy equation. Hence, in conventional (zonally asymmetric) baroclinic instabilities the only source of energy which the perturbation can tap is the available potential energy of the mean state. On the other hand, the relatively low values of Richardson number associated with the zonally symmetric instabilities imply diminished static stability and hence, an increase in the magnitude of w , the perturbation vertical velocity. Subsequently, vertical eddy stresses may not be neglected (hence, the instability is sometimes referred to as a "nongeostrophic" baroclinic instability), and, in fact, represent the

major energy transport mechanism available to the instability which is able to feed inertially off of the kinetic energy of the mean state (hence, the term "inertial instability").

The simple Eady model neglects the effects of curvature and treats compressibility through Boussinesq equations, it is thus not readily applicable to a deep atmosphere such as Jupiter's. In later work Stone (1967) extends his analysis of inertial instabilities to a deep atmosphere and finds that the results are nearly identical to those obtained for a shallow atmosphere. Only the magnitude of the smallest unstable wavelength (L_c , the "cutoff wavelength") shows a marked change. Unlike the results for a shallow atmosphere, L_c seems to depend strongly upon the meridional temperature gradient. A lack of knowledge as to appropriate values for the meridional gradient thus leads to increased uncertainties in L_c . If curvature terms are taken into account, Stone (1971) finds that the meridional perturbation velocity (v) displays amplitude oscillations whose wavelength is a function of latitude (θ), decreasing as θ increases. Thus, the meridional widths of the inertial rolls decrease as one moves away from the equator in a way similar to Jovian belts and zones (see Figure 5 in Stone, 1976).

A major weakness of Stone's inertial model is that it can give solutions only in terms of the so-called Eady baroclinic modes (those for which $\beta = df/dy \equiv 0$ as in the original model of Eady). In the next section we shall consider models which also allow for Green mode solutions (for which $\beta \neq 0$; see Green, 1960).

In closing, a key point to make regarding Stone's symmetric, inertial instabilities is that the mean zonal wind is induced through the thermal wind relation and hence represents the effect of the Coriolis deflection of mean meridional motions associated with Hadley-like cells. This is quite in keeping with the classical HP-model for Jupiter. It has also been suggested by Gierasch and Stone (1968) that horizontal eddy stresses associated with the zonally symmetric cells can induce zonal motions by means of a horizontal up-gradient momentum transport only in eastward zonal jets (see our discussion in Section 2.4).

1.3.2.2 Conventional Baroclinic Instabilities (Williams, 1979; Gierasch, Ingersoll, and Pollard, 1979; Conrath, Gierasch, and Nath, 1981)

If the static stability is increased, vertical motions associated with the linear perturbation of a baroclinic basic state are strongly damped so that the perturbation itself becomes quasi-geostrophic. For $Ri > 1$ we have already noted that the only energy source accessible to the perturbation is then the available potential energy of the basic state. Stone (1966) found that for values of $Ri > 1$ growth rates are a maximum for instabilities lying on the asymmetric axis (i.e., $\lambda = 0$; see Figure 4 in Stone, 1966). These instabilities are therefore zonally asymmetric and represent the conventional baroclinic instabilities originally studied by Eady (1949) and Green (1960).

As applied to the Jovian atmosphere we may divide models of the conventional baroclinic instability into two categories: shallow models (Williams, 1979a) and deep models (Gierasch, Ingersoll, and

Pollard, 1979; Conrath, Gierasch, and Nath, 1981). Unlike our classification of convective models, we do not define the "depth" of a model by how deep the instability extends relatively to the planetary radius. Rather, shallow baroclinic models are those for which the lower boundary is rigid and can support stresses (giving rise to a viscous drag in a surface Ekman layer). Deep baroclinic models are those for which no rigid lower boundary exists. The major effect associated with deep models is that the growth rates of the asymmetric instabilities are greatly diminished due to the loss of energy to the lower layers of the atmosphere (McIntyre, 1972; Gierasch, Ingersoll, and Pollard, 1979). Otherwise the results remain qualitatively much the same in both deep and shallow models.

Following the suggestion of Stone (1972), Williams (1979a) applies a shallow baroclinic model to Jupiter's atmosphere. Williams carries out his parametric investigation using the 2-level quasi-geostrophic, β -plane model of Phillips (1956). This model yields time-dependent solutions for the 2-dimensional flow within each layer in the multi-parameter space defined by L_x , L_y , f , β , $\partial\theta/\partial z$, H , τ_D , τ_I , and K_e (where the parameters are respectively, the typical zonal length scale for the motion, the corresponding meridional length scale, Coriolis parameter, gradient of planetary vorticity, static stability, diabatic heating rate function (generally specified as $H = H(y)$), time constant for the lower boundary Ekman drag, time constant for the interface drag, and eddy viscosity coefficient for horizontal diffusion due to subgrid scale eddies). Williams points out that the major unknown parameters of dynamical significance are $\partial\theta/\partial z$, H , and τ_D .

In his case J1, Williams estimates the stratification ($\partial\theta/\partial z$) by the minimum value required for the onset of linear instability according to the analysis of Phillips (1954). Williams uses a latitudinal heating function $H(y)$ which is linear in y with an amplitude of 4×10^{-16} watts kgm^{-1} . For the case J1 he neglects entirely the effects of lower Ekman layer and interface drag. Williams describes in detail the time evolution of the case J1 as it spins up from an unstable zonally symmetric state for which the equator to pole temperature difference $\Delta T = 29.4$ K, $u = \pm 2.3$ m sec^{-1} in the upper and lower layers respectively, and $\bar{w} = 3 \times 10^{-3}$ m sec^{-1} (where $|\bar{w}|$ is the magnitude of a zonal mean vertical velocity associated with a weak equator to pole Hadley cell). During the initial period (from 0 to 316 terrestrial days) this zonally symmetric flow gives way to a nonuniform momentum distribution due to the β vortex pairing process of Kuo (1951). This leads to the motion of cyclonic eddies up the planetary vorticity gradient (that is, poleward) and of anticyclonic eddies equatorward. The redistribution of vorticity implies a change in the zonal mean velocity given by,

$$\frac{\partial \bar{u}}{\partial t} = \bar{v\zeta},$$

where overbars indicate zonal averages and,

u = zonal velocity component

v = meridional velocity component

ζ = vertical component of relative vorticity = $(\partial v / \partial x) - (\partial u / \partial y)$.

Thus, mean eastward velocities ($\bar{u} > 0$) will increase due to the upgradient momentum advection associated with the eddy stresses (see Williams, 1979b). By the 178th day most of the momentum advection is due to wave propagation rather than eddy stress related and is subsequently diminished in rate. At the end of this initial period only about 20% of the total kinetic energy is eddy in nature and the mean, zonal flow consists of five jet pairs (easterlies and westerlies) with a typical velocity scale $\bar{u} = 25 \text{ m sec}^{-1}$. During the period from 316 to 1210 terrestrial days the flow remains almost stable with the first of the so-called "gyres", long neutral baroclinic waves with warm, high-pressure centers, becoming prominent. The period from 1200 to 1500 terrestrial days sees the onset of a second instability which begins at high latitude and spreads equatorward. Not only do the baroclinic eddies continue to pump momentum into the zonal jets, but frontogenesis begins to occur with the subsequent release of vast amounts of mean available potential energy. By the 1500th day the typical mean velocity scale has risen to 77 m sec^{-1} . The second major stable period sets in at about 1600 days. The mean circulation then consists of four eastward and two westward jets. Superimposed on this mean flow is a large permanent gyre (referred to by Williams as the "Gyre"), which Williams compares with the Great Red Spot. The results of the model are obviously intricate (Williams goes on to examine the effects of changing the various input parameters) and, more importantly, are quite unique among global circulation models for Jupiter in that they allow evaluation of a time history of eddy-mean flow energy reservoirs (\bar{K} , k' , \bar{P} , and P') as well as the associated transport mechanisms linking these reservoirs.

Note that the baroclinic model of Williams differs substantially from the classical HP model for Jupiter in several respects. The key difference is, of course, that the conversion from zonal mean available potential energy to zonal mean kinetic energy does not take place directly in the symmetric or Hadley sense. Rather in Williams' model (as in subsequent deep baroclinic models discussed below) zonal mean available potential energy is first broken down into smaller eddy-sized packets of available potential energy (P') in regions of baroclinic instability. Eddy motions feed upon these smaller packets of potential energy, a process resulting in the conversion of P' into eddy kinetic energy (K'). The roundabout path representing baroclinicity is completed by the upgradient transport of momentum by the eddies. The reader is referred back to Figure 1.1 for a better understanding of the process.

Recall that in the HP model the mechanism is basically convective, i.e., relating to rising motion in zones and sinking motion in belts. Williams, however, maintains that the clouds are induced by horizontal variations in mechanical pressure. Thus, in a region of higher pressure (relative to the surroundings) clouds resembling terrestrial cirrostratus will form. The corresponding correlation between cloudiness and anticyclonic vorticity is as observed on Jupiter.

As pointed out by Stone (1976), shallow baroclinic models are likely to give good results only if the deeper atmosphere is as statically stable (or more so) as the atmosphere at the cloudtop level, for then instabilities will damp out quickly with depth. However, if the stability of the cloudtop atmosphere is greater than that of the

deep atmosphere (a situation which applies for an adiabatic, deep atmosphere like Jupiter's) deep models are likely to give more realistic results. Gierasch, Ingersoll, and Pollard (1979) and Conrath, Gierasch, and Nath (1981) describe such deep models.

Gierasch, Ingersoll, and Pollard (1979) formulate a 2-level model consisting of an upper continuously stratified layer (above 5 bars) in which they apply the original Eady model (1949) and a massive, nearly adiabatic lower layer (below 5 bars) with a quiescent basic state. In agreement with McIntyre (1972) they find that growth rates of linear instabilities are substantially reduced due to the energy sink represented by the lower layer. They examine both cases for lower layer perturbations which are hydrostatic and nonhydrostatic and find that though growth rates are greatly reduced in either case, only those wavelengths much longer than the Rossby deformation radius ($L_D \equiv NH/f$; see our discussion in Section 3.1) are unstable in the hydrostatic case. Nonhydrostatic effects destabilize all wavelengths with a maximum growth rate for those wavelengths near L_D . A fundamental problem with their model is that it only allows for the existence of Eady modes for which $\beta = 0$.

Conrath, Gierasch, and Nath (1981) have recently extended the deep baroclinic model to include "Green mode" solutions (for which $\beta \neq 0$). The first baroclinic stability analyses to include the effects of β were the models of Charney (1947) and Kuo (1952). For Earth's atmosphere they considered the realistic problem of a fluid bounded below, but unbounded above. The results of their stability analyses indicated that for $(\partial \bar{u} / \partial z) > 0$ and $\beta > 0$ baroclinic

instabilities were possible. Eady (1949) had considered the problem of a fluid bounded by rigid flat surfaces at the top and the bottom for which $\beta = 0$ and found that a different class of instabilities were possible (the so-called "Eady modes"). As pointed out by Green (1960), it is clear that the presence of β and rigid lids greatly affects the results of the stability analysis, for if the rigid lid in Eady's model or the planetary vorticity gradient in Charney's model is removed, all waves are rendered baroclinically neutral. In the Eady model computation of complex phase speed (c) as a function of zonal wavenumber (k) yields a pair of solutions for single values of k . This pair corresponds to amplifying or decaying perturbations traveling with the mean zonal velocity of the basic state. The perturbations show amplitudes which are vertically symmetric about two so-called "steering levels" at which $\bar{u}(z) = \Re\{c\}$ and which are located at equal distances above and below the mid-level of the fluid. As $k \rightarrow \infty$, that is, for very short waves, all the solutions are stable. On the other hand, if $\beta \neq 0$, the stability analysis of Charney and Kuo yields monotonic solutions for $c(k)$. As well, there is no shortwave cutoff to instability, and there exists only one steering level which is located below the mid-level for all values of k .

A major difference between the $\beta = 0$ and $\beta \neq 0$ case is that in the latter the absolute vorticity changes due to meridional motion ($v\beta$) must be balanced by vortex stretching $\left(f \frac{\partial w}{\partial z}\right)$ in the absence of relative vorticity advection (which is negligible for a linear perturbation). Thus, at the steering level,

$$v\bar{b} = f \frac{\partial w}{\partial z} . \quad (1.9)$$

Green (1960) considers the case for $\beta \neq 0$ in a fluid bounded by flat surfaces at the top and bottom boundaries (a hybrid of the model of Eady and that of Charney). In Green's model, as in Charney's, there is only one steering level and instabilities can exist only for $\partial \bar{u} / \partial z > 0$. If we apply the terrestrial lower boundary condition that $w = 0$ at $z = 0$ and if w is a slowly varying function of z , then at a steering level located near the lower boundary we find that $w > 0$ and $(\partial w / \partial z) > 0$. Application of equation 1.9 then requires that $v > 0$, and hence, the vertical eddy stress $\bar{v}w$ must be positive at the steering level. Positive values of $\bar{v}w$ are consistent with perturbation parcel trajectories which lie along an angle between isentropic and horizontal surfaces for $\partial \bar{u} / \partial z > 0$. Thus if $\bar{u} = 0$ at $z = 0$, the release of mean available potential energy through the "Green modes" can occur only in the vicinity of eastward jets.

Conrath, Gierasch, and Nath apply the basic Green model to Jupiter by selecting the boundary condition most appropriate to the deep Jovian atmosphere, namely, that $w = 0$ at the top of the atmosphere. Applying Green's agreement they find that at an upper steering level $(\partial w / \partial z) < 0$, and hence, by Equation 1.9, $v < 0$. Thus, $\bar{v}w$ is now negative and the release of available potential energy can only occur if $\partial \bar{u} / \partial z < 0$, that is, in the vicinity of westward jets if the lower boundary condition remains $\bar{u} = 0$ at $z = 0$. Thus, Conrath, Gierasch, and Nath's model predicts that baroclinicity and the subsequent upgradient momentum flux due to eddy motions can occur only in westward jets.

As we shall see in the next section barotropic or shear instabilities are likely to occur if $d^2\bar{u}/dy^2$ exceeds β . This can only occur in strong, narrow westward jets. Since the baroclinic modes described by Conrath, Gierasch, and Nath are operative only in westward jets, they are obliged to consider the hybrid baroclinic-barotropic instability for which the basic state is sheared meridionally as well as vertically. The results of their numerical model (designed to explore the behavior of solutions as functions of jet width), indicate that in the narrow jet limit the instabilities are basically barotropic, while in the wide jet limit the instabilities are almost purely baroclinic.

1.3.2.3 Wave Driven Jets (Maxworthy, 1975)

Mean flow in most baroclinic models of the Jovian circulation is driven by the horizontal transport of momentum into the regions of zonal jets. Maxworthy (1975) proposes that the equatorial jet can be explained on the basis of the vertical transport of momentum by Kelvin and gravity-Rossby waves. As the Kelvin wave mode can be excited only near the equator, the model cannot be specifically applied to the zonal jets observed at temperate latitudes, but the model is nevertheless important as it underscores the possibility that the vertical propagation of lower tropospheric waves may well be quite important. If such is the case, the remarks made on the work of Ingersoll and Pollard again apply, and there is little hope that an analysis of cloudtop eddy motions and upper tropospheric thermodynamics can be entirely relevant to a study of the global energetics of the mean zonal flow.

Based upon the parameterization of Lindzen (1971), Maxworthy models the observed equatorial jet as the steady state solution to a momentum balance between vertical momentum diffusion (controlled through Newtonian cooling) and vertical eddy stress dissipation (controlled through a vertical eddy viscosity and vertical wind shear). This balance is assumed to hold at each level of the atmosphere, hence numerical integration of the balance equation gives profiles of $\bar{u}(z)$. The vertical wind shear is assumed positive ($\partial\bar{u}/\partial z > 0$) and the resulting $\bar{u}(z)$ -profile gives high westerly jet speeds in the lower stratosphere. The model might be criticized on the basis of the large number of free parameters available; however, this cannot be avoided based upon our limited knowledge of the Jovian atmosphere. The specific value of the Brunt-Väisälä frequency employed by Maxworthy is quite reasonable at the tropopause (namely, $N^2 = 3.3 \times 10^{-4} \text{ sec}^{-2}$; see our discussion of observed vertical structure in Chapter 5). Based upon current observation two major criticisms arise:

- a) As we shall later see meridional temperature profiles in the upper troposphere indicate that the vertical wind shear is negative ($\partial\bar{u}/\partial z < 0$);
- b) Estimates of cloudtop heights place them near the 500 mb level for which $N^2 \approx 1 \times 10^{-4} \text{ sec}^{-2}$, the diminished stability allowing less vertical momentum transport by the propagating wave.

With regards to our second criticism we note that there is some evidence that in the equatorial region clouds (and the inferred velocities) lie higher in the atmosphere (West and Tomasko, 1979). The first criticism remains, however, and indicates that a model based upon a balance between vertical momentum diffusion and vertical eddy stress dissipation alone will not allow for an increase in momentum dissipation with increasing altitude if $\partial \bar{u} / \partial z < 0$. The problem can be resolved if, as suggested by Maxworthy, we include the effects of horizontal eddy diffusion. However, we know little about the vertical structure of horizontal diffusion so that the complete problem becomes hopelessly entangled in a mass of undetermined parameters. Nevertheless, the possibility that momentum deposited by vertically propagating waves, which are perhaps generated by the CISK mechanism (but in general could be coupled to any mechanism in a stably stratified atmosphere), plays an important role in the upper atmospheric energetics remains and renders our attempt at a global energy budget analysis a preliminary one.

1.3.2.4 Barotropic Instabilities

The instability of a 2-dimensional flow with horizontal shear on a β -plane was originally examined by Kuo (1949). His linear stability analysis revealed that a necessary condition for the existence of an instability within a zonal jet bounded at $y = y_1, y_2$ is that,

$$\int_{y_1}^{y_2} (\beta - d^2 \bar{u} / dy^2) dy = 0 .$$

This condition can be met only if the above integrand changes algebraic sign somewhere within the interval between y_1 and y_2 . For a prograde rotating planet (like Jupiter) $\beta > 0$, thus this integrand can change sign only if $d^2\bar{u}/dy^2 > \beta$. As already remarked (see previous section) this is possible only in strong, narrow westward jets.

One might rightly conclude that evaluation of $\bar{u}(y)$ through the use of Voyager image sequences should provide irrefutable evidence either for or against the possibility of barotropic instability. There are two approaches one can take to determine the algebraic sign of $(\beta - d^2\bar{u}/dy^2)$. Based upon measured profiles for $\bar{u}(y)$, the value of $d^2\bar{u}/dy^2$ can be computed using finite differences and the result compared to the magnitude of β ; such an analysis indicates that many, if not all, of the observed westward jets are barotropically unstable (see Figure 4 in Ingersoll et al., 1981). The second approach is to compute the profile of $\bar{u}(y)$ which would result in neutral stability (i.e., $\beta = d^2\bar{u}/dy^2$) and compare the width of the neutral profile at a particular latitude (θ_0) to the actual observed jet width at the same latitude. The equation for such a neutral profile is,

$$\bar{u}(y) = (\Omega \cos \theta_0) r_J (\theta - \theta_0)^2 \left(\frac{\pi}{180}\right)^2 + u(\theta_0) \quad (1.10)$$

where,

- r_J = Jovian radius
- $u(\theta_0)$ = maximum westward velocity in observed jet
- θ_0 = latitude of maximum westward velocity.

Note that the neutral profile for $\bar{u}(y)$ strictly applies only at $\theta = \theta_0$. We feel that the second method of analysis is the better one because it does not depend upon finite differences computed over a substantial fraction of the actual jet width. The results of the second analysis seem to suggest the possibility of barotropic instabilities in the westward jets (see Figure 2 in Ingersoll et al., 1979), though the interpretation is marginal at best. In Chapter 4 we are concerned with the stability of the westward jet in which the Great Red Spot is located. We shall see that while the results of a finite difference calculation of $d^2\bar{u}/dy^2$ indicate instability, the results of a stability profile analysis seems to indicate marginal stability. The energetics of barotropic instabilities require that the associated eddy stresses allow the perturbation to feed upon the ambient mean zonal kinetic energy. In our global analysis of the role played by eddy stresses (see Section 2.3) we shall see that on average the stresses tend to feed the mean zonal flow. We can only conclude that barotropic instability cannot be responsible for the bulk of the observed eddy motions. This does not preclude the barotropic mechanism in the vicinity of some of the westward jets, where one might anticipate a reduction in the deduced eddy to mean energy transport rates.

CHAPTER 2: GLOBAL ENERGETICS

2.1 Introduction

In this chapter we examine the global energetics of the Jovian circulation using measured cloudtop motions and IRIS temperature soundings to assemble the first Oort energy budget for the general circulation of the atmosphere of another planet. We will also attempt to contrast the role played by zonally symmetric (mean) and asymmetric (eddy) motions in the energy transport processes linking the Oort energy reservoirs.

2.2 The 2-Dimensional Kinetic Energy Equation

The zonally symmetric conversion of available potential to kinetic energy involves a zonally symmetric vertical velocity field which cannot be directly measured (see equation 1.5). In contrast the conversion of K' into \bar{K} involves the momentum transport associated with horizontal eddy stresses ($\overline{u'v'}$) which can be deduced from measurements of cloudtop motions (see equation 1.8). If we are to contrast the relative importance of the two processes given by $\{\bar{P} \rightarrow \bar{K}\}$ and $\{K' \rightarrow \bar{K}\}$, we must relate the symmetric conversion process $\{\bar{P} \rightarrow \bar{K}\}$ to the observed horizontal flow.

Fortunately, the relationship between horizontal motion and kinetic energetics at a given level in the atmosphere is relatively straight-

forward provided that on observable scales the kinetic energy associated with vertical motions is small and may be neglected. We proceed to derive an equation relating the observed 2-dimensional motions to the atmospheric energetics.

2.2.1 Derivation of the 2-Dimensional Mean Zonal Kinetic Energy Equation

In this section we derive an expression for the time rate of change of the mean zonal kinetic energy in a motion field consisting of a mean flow upon which are superimposed eddy or perturbation motions. Earth-based (Peek, 1958) and Voyager observations (Ingersoll et al., 1979) make it clear that most of the mean kinetic energy in the Jovian atmosphere is associated with alternating eastward and westward zonal jets. Hence, the mean kinetic energy associated with the mean meridional motions is small and we need only consider those energy transport processes relating to changes in the mean zonal motions in order to evaluate the relative importance of zonally symmetric and asymmetric energy transports.

As noted, we must neglect the effects of vertical motion which we are unable to evaluate in time sequences of Voyager images. We treat the flow as incompressible, that is we will freely move ρ on either side of any differentiation (the 2-dimensional, subsonic flow behaves as if it were incompressible) to write the momentum flux form of the zonal momentum equation as:

$$\frac{\partial \rho u}{\partial t} + \frac{\partial \rho u u}{\partial x} + \frac{\partial \rho u v}{\partial y} = - \frac{\partial p}{\partial x} + \rho f v \quad (2.1)$$

where,

x = zonal spatial coordinate, positive eastward

y = meridional spatial coordinate, positive northward

u = dx/dt = zonal wind component, positive eastward

v = dy/dt = meridional wind component, positive northward

p = pressure

ρ = mass density

f = $2\Omega \sin \theta$ = Coriolis parameter

Ω = Jovian rotational frequency = $1.75 \times 10^{-4} \text{ sec}^{-1}$

θ = Jovian planetographic latitude

If we average (integrate) equation 2.1 over some interval in x we have:

$$\int_x \frac{\partial \rho u}{\partial t} dx + [\rho u u]_x + \int_x \frac{\partial \rho u v}{\partial y} dx = - [p]_x + \int_x \rho f v dx \quad (2.2)$$

where the terms in square brackets represent perfect differentials evaluated over the limits on x .

Our concept of mean and eddy motion fields is embodied in a Reynolds-type decomposition where the assumption is made that each of the observed zonal and meridional wind speeds consists of a zonally averaged or mean component (represented by an overbar) and an eddy component (represented by a prime) so that,

$$\begin{aligned} u &= \bar{u} + u' \\ v &= \bar{v} + v' \end{aligned} \quad (2.3)$$

where,

$$(\overline{\quad}) = \frac{1}{L} \int_x (\quad) dx = \text{longitudinal mean component}$$

$$L = \int_x dx$$

$$(\quad)' = (\quad) - (\overline{\quad}) = \text{eddy component.}$$

Upon performing a Reynolds decomposition our zonal momentum equation becomes:

$$\begin{aligned} \int_x \frac{\partial \rho(\bar{u} + u')}{\partial t} dx + [\rho(\bar{u}\bar{u} + 2\bar{u}u' + u'u')]_x \\ + \int_x \frac{\partial \rho(\bar{u}\bar{v} + \bar{u}v' + u'\bar{v} + u'v')}{\partial y} dx = [-p]_x \\ + \int_x \rho f(\bar{v} + v') dx. \end{aligned} \quad (2.4)$$

Noting that all longitudinal averages involving cross products of mean and eddy components will by definition go to zero upon integration over our averaging interval in x and similarly, that u' and v' vanish from

the first and last terms of our equation, as does $[\rho \bar{u} \bar{u}]_x$, we are left with,

$$\begin{aligned} & \int_x \frac{\partial \rho \bar{u}}{\partial t} dx + [\rho(2\bar{u}u' + u'u')]_x + \int_x \frac{\partial \rho(\bar{u}\bar{v} + u'v')}{\partial y} dx \\ & = [-p]_x + \int_x \rho f \bar{v} dx. \end{aligned} \quad (2.5)$$

Noting that our limits on x are time invariant, we pull the partial differentiation with respect to time out from under the x -integral and multiply our equation by \bar{u} to obtain:

$$\begin{aligned} & \frac{\partial}{\partial t} \int_x \frac{1}{2} \rho \bar{u}^2 dx + [\bar{u}] [\rho(2\bar{u}u' + u'u')]_x + \int_x \bar{u} \frac{\partial \rho(\bar{u}\bar{v} + u'v')}{\partial y} dx \\ & = [-\bar{u}p]_x + \int_x \rho f \bar{u} \bar{v} dx. \end{aligned} \quad (2.6)$$

We desire an expression for the total time rate of change of mean zonal kinetic energy, thus we must also average over some meridional channel

ORIGINAL PAGE IS
OF POOR QUALITY

width in y and depth in z (this assumes the observed cloudtop
kinematics represent the mean in an atmospheric column) to obtain:

$$\begin{aligned} \frac{\partial}{\partial t} \int_z \int_y \int_x \frac{1}{2} \rho \bar{u}^2 dx dy dz = & - \int_z \int_y [\bar{u} \rho (2\bar{u} u' + u' u')]_x dy dz \\ & - \int_z \int_y \int_x \rho \bar{u} \frac{\partial (\bar{u} \bar{v} + u' v')}{\partial y} dx dy dz \quad (2.7) \\ & - \int_z \int_y [\bar{u} \rho]_x dy dz + \int_z \int_y \int_x \rho \bar{u} \bar{v} dx dy dz . \end{aligned}$$

We integrate the second term on the right side of our equation by parts
as:

$$\begin{aligned} - \int_z \int_y \int_x \rho \bar{u} \frac{\partial (\bar{u} \bar{v} + u' v')}{\partial y} dx dy dz = & - \int_z \int_y \int_x \rho \bar{u} d(\bar{u} \bar{v} + u' v') dx dz \\ = & - \left\{ \int_z \int_y \int_x \rho \bar{u} [\bar{u} \bar{v}]_y dx dz - \int_z \int_y \int_x \rho \bar{u} \bar{v} \frac{d\bar{u}}{dy} dx dy dz \right. \quad (2.8) \\ & \left. + \int_z \int_x \rho \bar{u} [u' v']_y dx dz - \int_z \int_y \int_x \rho u' v' \frac{d\bar{u}}{dy} dx dy dz \right\} . \end{aligned}$$

We make the assumption that our longitudinal averaging region is cyclic in x for the quantity u' in order to get rid of the first term on the right side of our energy equation. Hence, we may write symbolically,

$$\frac{\partial \bar{K}}{\partial t} = \{\bar{K} \cdot \bar{K}\} + \{K' \cdot \bar{K}\} + \{p \cdot \bar{K}\} + \{f\bar{K} \cdot \bar{K}\} \quad (2.9)$$

where,

$$\frac{\partial \bar{K}}{\partial t} = \frac{\partial}{\partial t} \int_z \int_y \int_x \frac{1}{2} \rho \bar{u}^2 dx dy dz \quad (2.10)$$

= time rate of change of mean zonal kinetic energy inside an averaging volume or momentum control volume.

Each of the energy "transport" terms on the right side of the equation is given by:

$$\{\bar{K} \cdot \bar{K}\} = + \int_z \int_y \int_x \rho \bar{u} \bar{v} \frac{d\bar{u}}{dy} dx dy dz - \int_z \int_x \rho \bar{u} [\bar{u} \bar{v}]_y dx dz \quad (2.11)$$

= Mean Meridional Transport Term; change in mean zonal kinetic energy due to transport of mean zonal momentum across latitude circles by the mean meridional wind.

$$\{K' \cdot R\} = + \int_z \int_y \int_x \rho u'v' \frac{d\bar{u}}{dy} dx dy dz - \int_z \int_x [\rho \bar{u} u'v']_y dx dz \quad (2.12)$$

= Eddy Transport Term; change in mean zonal kinetic energy due to transport of mean zonal momentum across latitude circles by eddies.

$$\{p \cdot \bar{K}\} = - \int_z \int_y \bar{u} [p]_x dy dz \quad (2.13)$$

= Pressure Torque Term; change in mean zonal kinetic energy due to east/west pressure difference (i.e., constant pressure gradient) across the region.

$$\{f\bar{K} \cdot \bar{K}\} = + \int_z \int_y \int_x p f \bar{u} \bar{v} dx dy dz \quad (2.14)$$

= Hadley or Symmetric Overturning Term; change in mean zonal kinetic energy due to conversion of mean meridional motions into mean zonal motions through Coriolis deflection.

For a more complete interpretation of these terms see Section 2.2.3.

2.2.2 The Operational Scheme

From time sequences of Voyager images we have observations of both the zonal (u) and the meridional (v) cloudtop wind speeds. We wish to use this observed horizontal flow field at the cloudtop level in order

to evaluate the terms in equation 2.9. This observational data set is easily linked to the terms in our mean zonal kinetic energy equation if we represent derivatives and integrals by finite differences and summations respectively. For conceptual ease and so that we may refer to earlier work (Beebe et al., 1980; Ingersoll et al., 1981) we may express each of the terms in equation 2.9 in units of energy per time per horizontal unit area (watts m^{-2}). In order to do this we note that the horizontal area of our control volume is $2YL$ (where the volume extends from $-Y$ to $+Y$ in the meridional dimension, i.e., the channel width is $2Y$). Dividing equation 2.9 by the quantity $2YL$ thus gives the average time rate of change of mean zonal kinetic energy per unit horizontal area inside our momentum control volume. With the assumption that the observed cloudtop kinematics represent the mean in a column of atmosphere we may pull the mass density (ρ) outside our integral in z by simply representing $\int_z \rho dz$ as ρ^*D where D is the depth scale of the atmosphere ($\sim 10^5\text{m}$; Divine, 1971) and $\rho^* = 1/D \int_z \rho dz$ is the mass per horizontal area in a column of depth D ($\sim 10^4 \text{ kgm m}^{-2}$; Divine, 1971).

In order to perform the summation and finite differencing necessary for the evaluation of each of our kinetic energy transport terms, we divide the observed horizontal flow field into zonal strips of constant width (Δy) in latitude. The zonal extent of each strip or bin (as each shall hereafter be called) is just L . Thus, our

ORIGINAL PAGE IS
OF POOR QUALITY

"operational" expression for evaluating the time rate of change of mean, zonal kinetic energy per unit horizontal area becomes:

$$\frac{a\bar{k}}{a\bar{t}} = \{\bar{k} \cdot \bar{k}\} + \{k' \cdot \bar{k}\} + \{p \cdot \bar{k}\} + \{f\bar{k} \cdot \bar{k}\} \quad (2.15)$$

where in finite difference form,

$$\bar{k} = \frac{\sum_{i=1}^N \left(\frac{1}{2} \rho^* \bar{u}^2 \right)_i}{N} \quad (2.16)$$

Each of the transport terms becomes,

$$\{\bar{k} \cdot \bar{k}\} = \frac{\sum_{i=1}^N \left(\rho^* \bar{u} \bar{v} \frac{d\bar{u}}{dy} \right)_i}{N} - \left[\frac{(\rho^* \bar{u} \bar{u} \bar{v})_{i=N} - (\rho^* \bar{u} \bar{u} \bar{v})_{i=1}}{N \Delta y} \right] \quad (2.17)$$

= Mean Meridional Transport Term,

$$\{k' \cdot \bar{k}\} = \frac{\sum_{i=1}^N \left(\rho^* \bar{u}' \bar{v}' \frac{d\bar{u}}{dy} \right)_i}{N} - \left[\frac{(\rho \bar{u} \bar{u}' \bar{v}')_{i=N} - (\rho^* \bar{u} \bar{u}' \bar{v}')_{i=1}}{N \Delta y} \right] \quad (2.18)$$

= Eddy Transport Term,

$$\{p \cdot \bar{k}\} = - \left(\frac{D}{L} \right) \frac{\sum_{i=1}^N (\bar{u} \Delta p)_i}{N} \quad (2.19)$$

= Pressure Torque Term,

where,

$\Delta p \equiv p_{\text{EAST}} - p_{\text{WEST}}$ = pressure difference in x across control volume

and,

$$\{f\bar{K} \cdot \bar{K}\} = \frac{\sum_{i=1}^N (\rho \cdot f \bar{u} \bar{v})_i}{N} \quad (2.20)$$

= Hadley or Symmetric Overturning Term.

Notice that we index the average value of a quantity in each zonal averaging bin by i, where N is the total number of latitude bins and i increases as one moves northward (i.e., with increasing values of y). Since Δy is the bin width in a constant latitude increment we must be careful to perform the actual summation $\sum_{i=1}^N ()_i$ as an area weighted summation.

The meridional shear of the mean zonal wind is approximated by its centered finite difference equivalent given by,

$$\left(\frac{d\bar{u}}{dy} \right)_i = \frac{(\bar{u})_{i+1} - (\bar{u})_{i-1}}{2\Delta y} \quad (2.21)$$

2.2.3 Interpretation of the Terms in the Kinetic Energy Equation

Note that equation 2.9 contains only inertial terms with the exception of the horizontal pressure torque term. The three inertial terms representing $\{\bar{K} \cdot \bar{K}\}$, $\{K' \cdot \bar{K}\}$, and $\{f\bar{K} \cdot \bar{K}\}$ involve only the transport of pre-existing kinetic energy within or into the control volume. The pressure torque term is the only true kinetic energy generation term in our energy equation and, of course depends upon a pressure differential which cannot be directly observed in any Voyager data set. Also, we have completely neglected any explicit vertical motions as they are unobservable in Voyager imaging sequences. It is these vertical motion terms which are in fact ultimately responsible for the conversion of both eddy and mean available potential energy into eddy and mean kinetic energy (see equations 1.5 and 1.7).

The four terms included in equation 2.9 do, however, allow us to contrast the role of eddy motions and mean, zonally symmetric, meridional motion. The explicit effects of eddy motion can be analyzed through the use of the $\{K' \cdot \bar{K}\}$ term, whereas the effects of Hadley overturning can be quantified through the evaluation of those terms containing \bar{v} , namely $\{\bar{K} \cdot \bar{K}\}$ and $\{f\bar{K} \cdot \bar{K}\}$.

The argument for relating the energy transports associated with mean meridional motions to mean vertical velocities is a simple one. Vertical temperature profiles of the Jovian atmosphere indicate a tropopause near the 140 mb level (Hanel et al., 1979). The sharp increase in static stability near the tropopause (see our Figure 5.1) effectively acts as a rigid lid inhibiting any vertical motions near this level. Zonal mean vertical motions are thereby converted into zonal

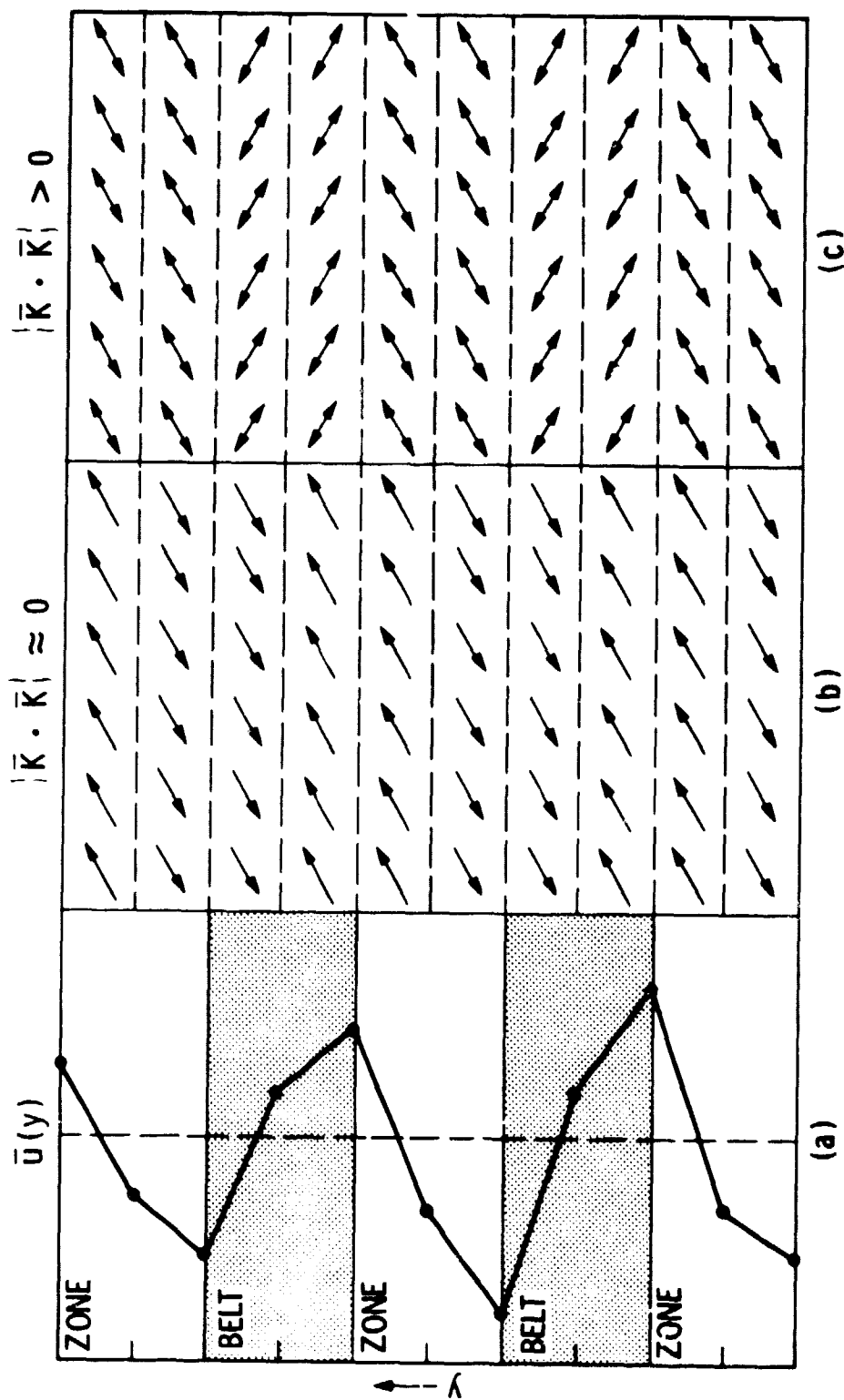
mean meridional motions through the divergence required by mass continuity near the tropopause level. The resulting \bar{v} can transport kinetic energy only by means of the two processes $\{\bar{K} \cdot \bar{K}\}$ and $\{f\bar{K} \cdot \bar{K}\}$. Thus, the measured energy transports associated with $\{\bar{K} \cdot \bar{K}\}$ and $\{f\bar{K} \cdot \bar{K}\}$ effectively amount to a measure of the $\{\bar{P} \cdot \bar{K}\}$ transport which in a strict sense involves the correlation between zonal mean vertical velocities and zonal mean temperature deviations as in equation 1.5. Since the cloudtops (and inferred velocities) lie near the 500 mb level, while the tropopause lies near the 140 mb level, estimates of transport rates associated with $\{\bar{P} \cdot \bar{K}\}$ based upon observed values of $\{\bar{K} \cdot \bar{K}\}$ and $\{f\bar{K} \cdot \bar{K}\}$ are likely to be low, i.e., the bulk of the divergence may be taking place in the clear, uppermost troposphere. We proceed to give an intuitive and physical explanation of each of the terms in equation 2.9.

The "mean meridional transport term" (symbolically represented by $\{\bar{K} \cdot \bar{K}\}$) represents the transport of kinetic energy (momentum) by zonally symmetric eddy stresses. A full physical interpretation of this term is complicated by the nonlinearity in \bar{u} ; however, as seen in Figure 2.1 a positive correlation between the zonally symmetric stress ($\bar{u}\bar{v}$) and the meridional shear of zonal wind ($d\bar{u}/dy$) is one for which the stresses lean with the ambient shear so as to enhance the mean shear. On the other hand, in a negative correlation region the stresses lean against the ambient shear so as to diminish it. Notice that according to the Hess-Panofsky Model of diverging zones and converging belts (see Figure 2.1b) the anticipated sign of the mean

Figure 2.1. Zonally symmetric stresses at the cloudtop level according to Hess and Panofsky (1951 (see Figure 2.1(b)). Figure 2.1(c) illustrates stresses for which the resulting energy transport leads to the growth of the magnitude of the mean Jovian zonal wind with a profile shown by the connected points in Figure 2.1(a).

ORIGINAL PAGE IS
OF POOR QUALITY

HESS-PANOFSKY

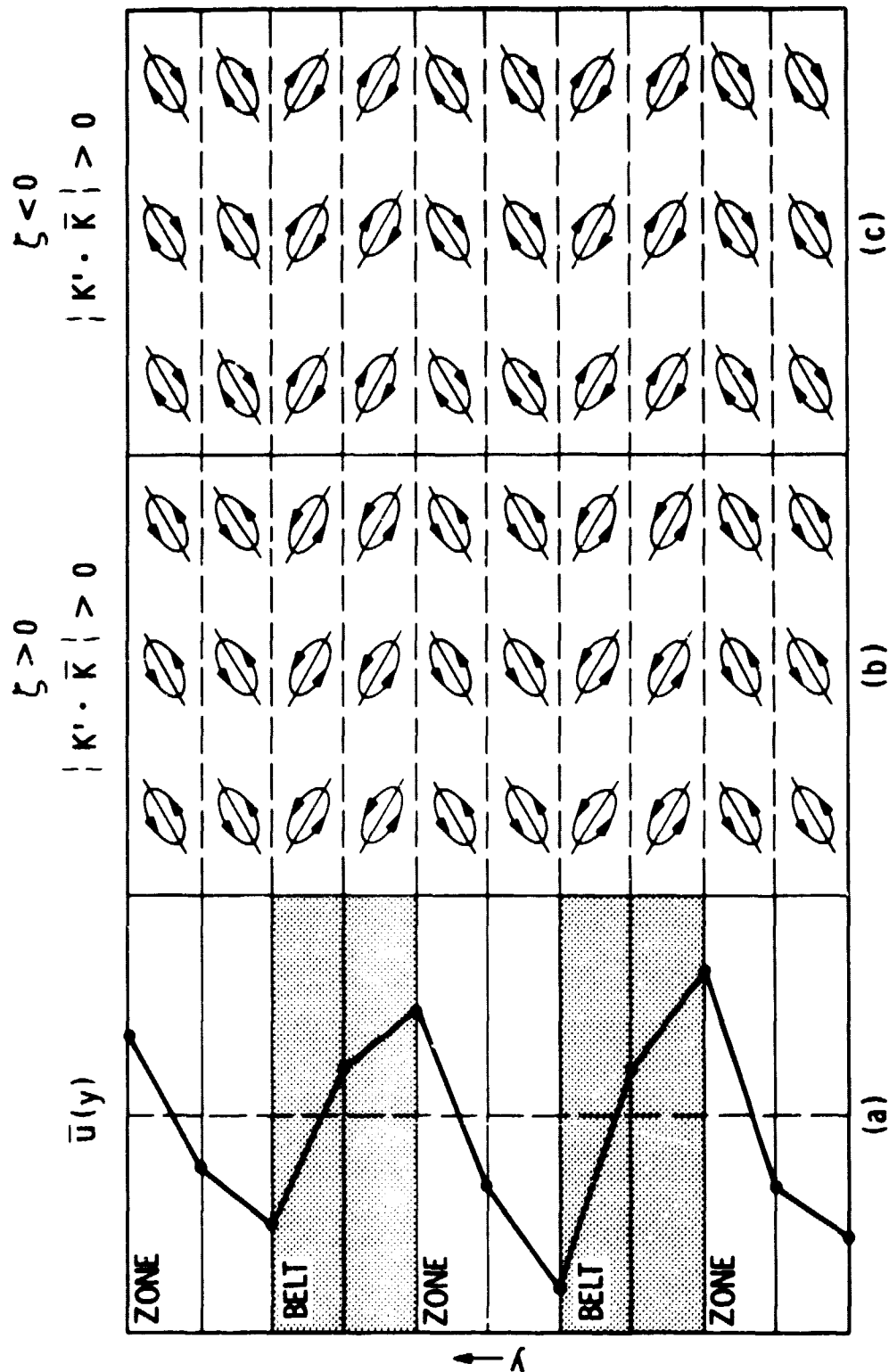


stress shows a correlation with $d\bar{u}/dy$ resulting in $\{\bar{K} \cdot \bar{K}\}$ positive for zones, but an anticorrelation in belts, such that $\{\bar{K} \cdot \bar{K}\}$ is negative. Thus, in the HP model the shear in belts is diminished by the mean stresses resulting from convergence, whereas the shear in zones is enhanced by the mean stresses. As the total area of the belts i.e., regions of convergence) and of the zones (i.e., regions of divergence) are approximately equal, we expect that the term given by $\{\bar{K} \cdot \bar{K}\}$ will be very small when taken as a global average. On the other hand, Figure 2.1c illustrates symmetric stresses for which the net contribution to $\{\bar{K} \cdot \bar{K}\}$ is a positive. Notice that the actual direction of the velocity associated with the stress is irrelevant (as represented by the double-headed arrows), only the algebraic sign of the symmetric stress $\bar{u}v$ is relevant in the correlation with the ambient shear g_1 by $d\bar{u}/dy$. On the other hand, Gierasch and Stone (1968) suggest that zonally symmetric stresses associated with inertial (zonally symmetric baroclinic) instabilities will deposit momentum only into mean eastward jets (see their Figure 1).

The "eddy transport term" (symbolically represented by $\{K' \cdot \bar{K}\}$) represents the kinetic energy transport due to zonally asymmetric eddy stresses. Reference to Figure 2.2 illustrates that a series of eddies whose major axes are aligned with the meridional shear in the mean zonal wind will pump momentum (hence kinetic energy) into the mean zonal flow. As with the symmetric stresses, notice that the algebraic sign of the vorticity associated with the eddies is irrelevant (compare Figure 2.2b with Figure 2.2c), rather, only the algebraic sign of the eddy stress $u'v'$ is relevant in the correlation with the ambient shear. We have

Figure 2.2. Eddy stresses at the cloudtop level giving rise to net energy transport into the observed mean flow illustrated in Figure 2.2(a). As can be seen by comparing Figure 2.2(b) and 2.2(c) the algebraic sign of the eddy relative vorticity (ζ) is irrelevant. Only the algebraic sign of the net stresses, represented by the direction of the eddy tilt, is relevant to the associated energy transport process.

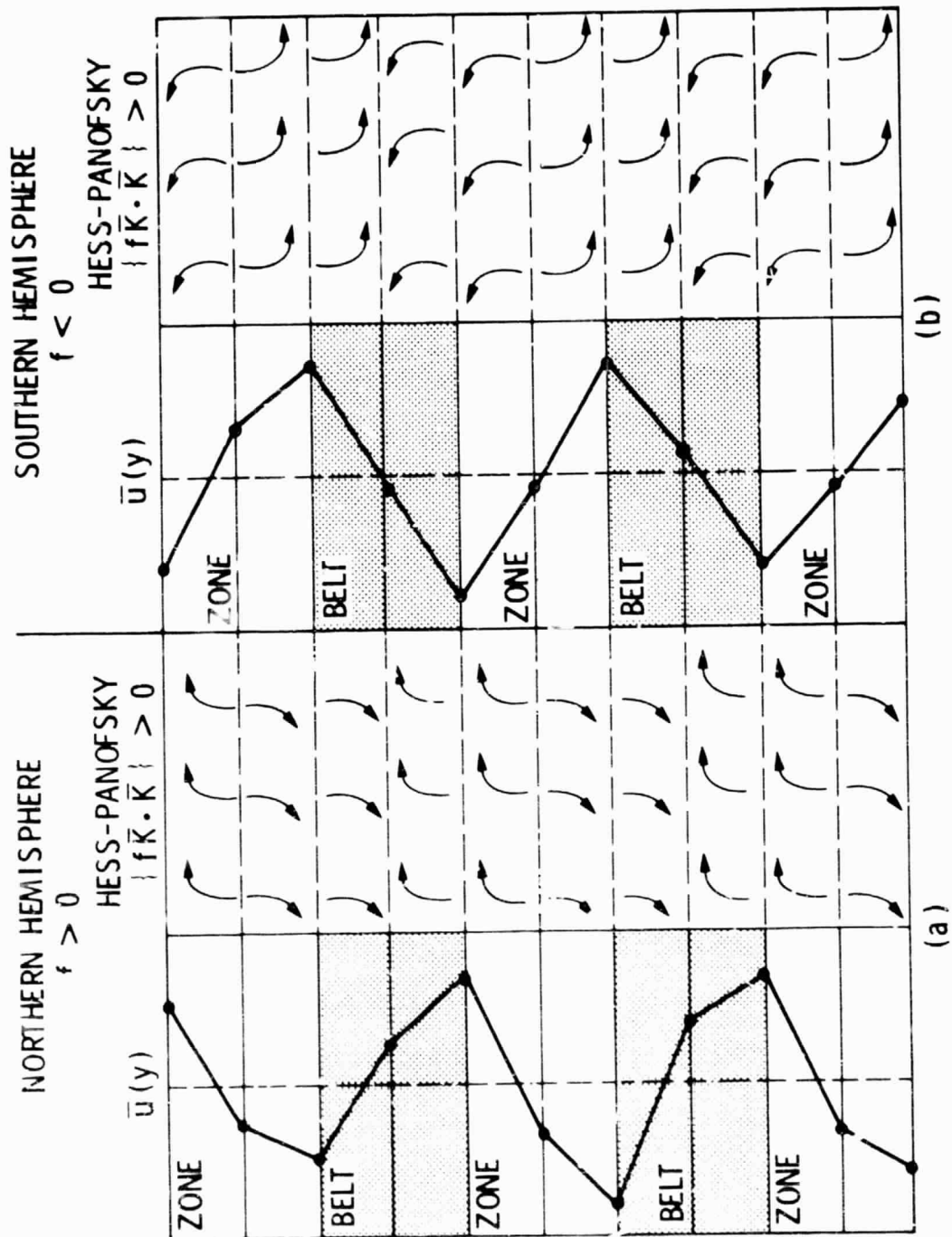
ORIGINAL PAGE IS
OF POOR QUALITY



chosen to represent a net eddy stress by a wholesale tilt of the individual major axes of the eddies in Figure 2.2. See Section 4.3.3 for a more detailed discussion of the geometries associated with the production of net eddy stress. It is this term which is responsible in Earth's atmosphere for the bulk of the momentum transfer from equator to pole. In the shallow baroclinic model of Williams (1979a) this eddy momentum transport is responsible for maintaining the mean zonal flow. Thus, quantification of the $\{K' \cdot \bar{K}\}$ term is important for a consideration of the global energetics of Jupiter's atmosphere. We shall turn to a full discussion of past work involving measurements of $\{K' \cdot \bar{K}\}$ in the next section.

The "Hadley, symmetric overturning term" (symbolically represented by $\{f\bar{K} \cdot \bar{K}\}$) represents the deflection of mean meridional flow into mean zonal flow by Coriolis forces. The process represented by this term lies at the heart of the HP model of Jovian circulation. As seen in Figure 2.3 the cloudtop divergence associated with zones gives rise to mean meridional flow northward (southward) along the northern (southern) portion of zones. We anticipate a mean meridional flow southward (northward) along the northern (southern) portion of converging belts. In the northern hemisphere the Coriolis deflection to the right will convert this mean meridional flow into a westward mean zonal flow along the northern (southern) edges of belts (zones) and into an eastward mean zonal flow along the southern (northern) edges of belts (zones). In the southern hemisphere the Coriolis deflection to the left will convert the mean meridional flow into a westward mean zonal flow along the southern (northern) edges of belts (zones) and into an eastward

Figure 2.3. Zonally symmetric stresses predicted by Hess and Panofsky (1951) which led to the growth of the illustrated mean zonal flow. Coriolis deflection to the right in the northern hemisphere (see Figure 2.3(a)) and to the left in the southern hemisphere (see Figure 2.3(b)) provides for a Hadley cell overturning which maintains anti-cyclonic zones and cyclonic belts.



mean zonal flow along the northern (southern) edges of belts (zones). Thus, anticyclonic zones (and cyclonic belts) yield positive correlations between \bar{u} and \bar{v} in the northern hemisphere and negative correlations between \bar{u} and \bar{v} in the southern hemisphere, so that the term $\{f\bar{K} \cdot \bar{K}\}$ remains positive.

The "pressure torque term" (symbolically represented by $\{p \cdot \bar{K}\}$) represents the generation of mean kinetic energy through the effects of stresses arising from net pressure differences maintained across the longitudinal extent of our averaging bin. Pressures are not directly observable by the Voyager spacecraft. The form of the term is such that if a higher net pressure exists on the eastern side of the bin ($\Delta p > 0$) a mean acceleration to the west will be maintained such that the total mean kinetic energy of an eastward (westward) flow will diminish (increase) with time. The opposite will occur if $\Delta p < 0$. If the averaging bin extends over 360° of longitude, the pressure torque term will go to zero provided there are no discontinuities on surfaces of constant pressure, as the term then becomes the integral of a perfect differential over a cyclic region. Discontinuities can be maintained in an atmosphere only if pressure surfaces intersect a solid object such as a mountain. On Earth approximately half the total mass of the atmosphere lies below the summits of the higher mountain ranges, thus the effects of the pressure torque term, or the "mountain torque term" as the terrestrial analogue is called, are considerable. In a classical study of the mountain torque effect White (1949) found that Earth's mountain ranges, particularly the Rockies and the Asiatic ranges, do indeed release angular momentum from the mid-latitude

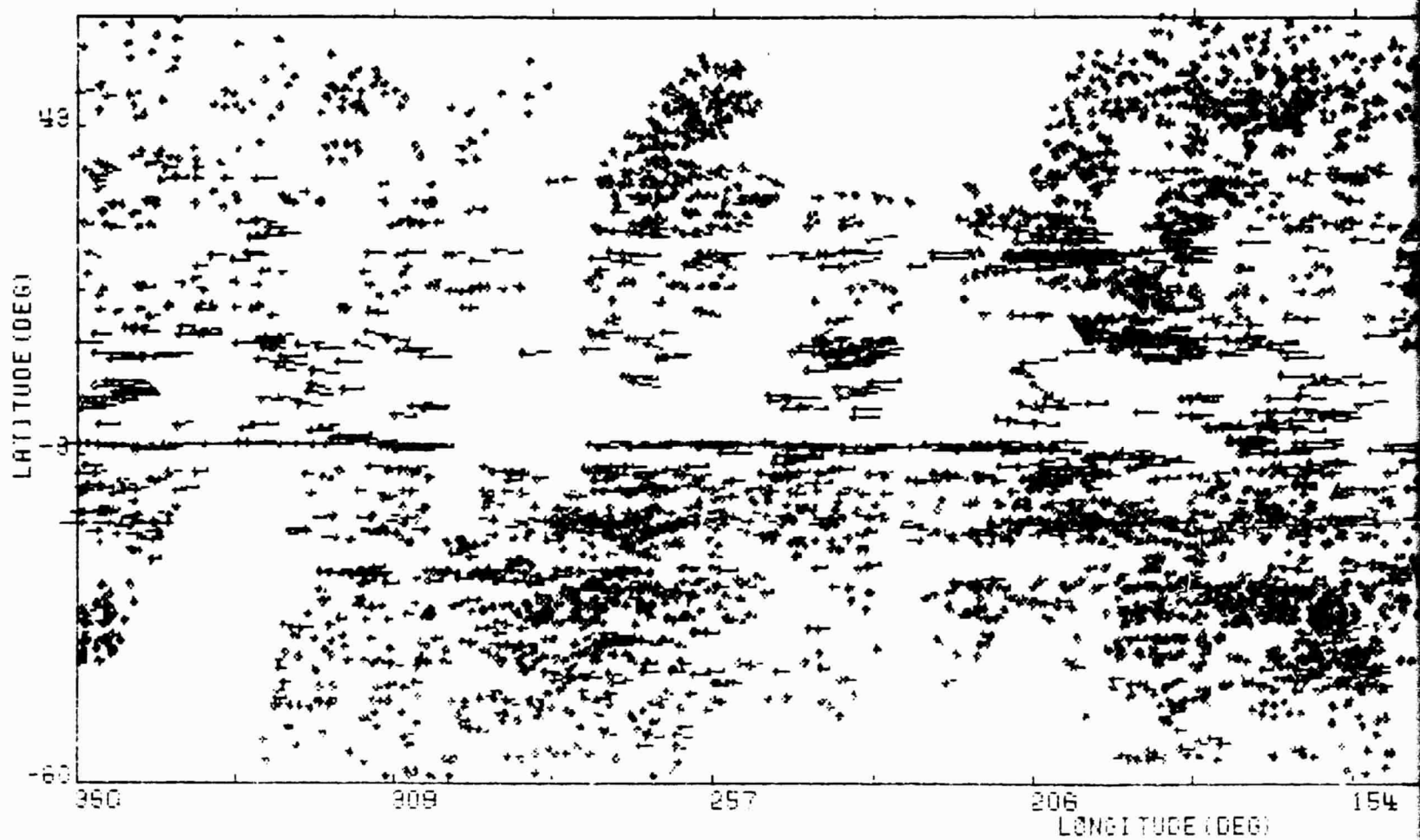
atmosphere at a rate comparable to that due to surface friction. In the tropics the mountain torque effect plays a reverse role and is a major source of atmospheric angular momentum. In our studies of the global kinetic energetics of Jupiter's atmosphere we shall hereafter make the reasonable assumption that mountains do not play a major role in the atmospheric energy cycle. The pressure torque term is not easily laid to rest and will reappear in an unwelcome way in our study of an isolated, closed momentum control volume (see Chapter 4).

2.3 Eddy Transports and Previous World Map Studies

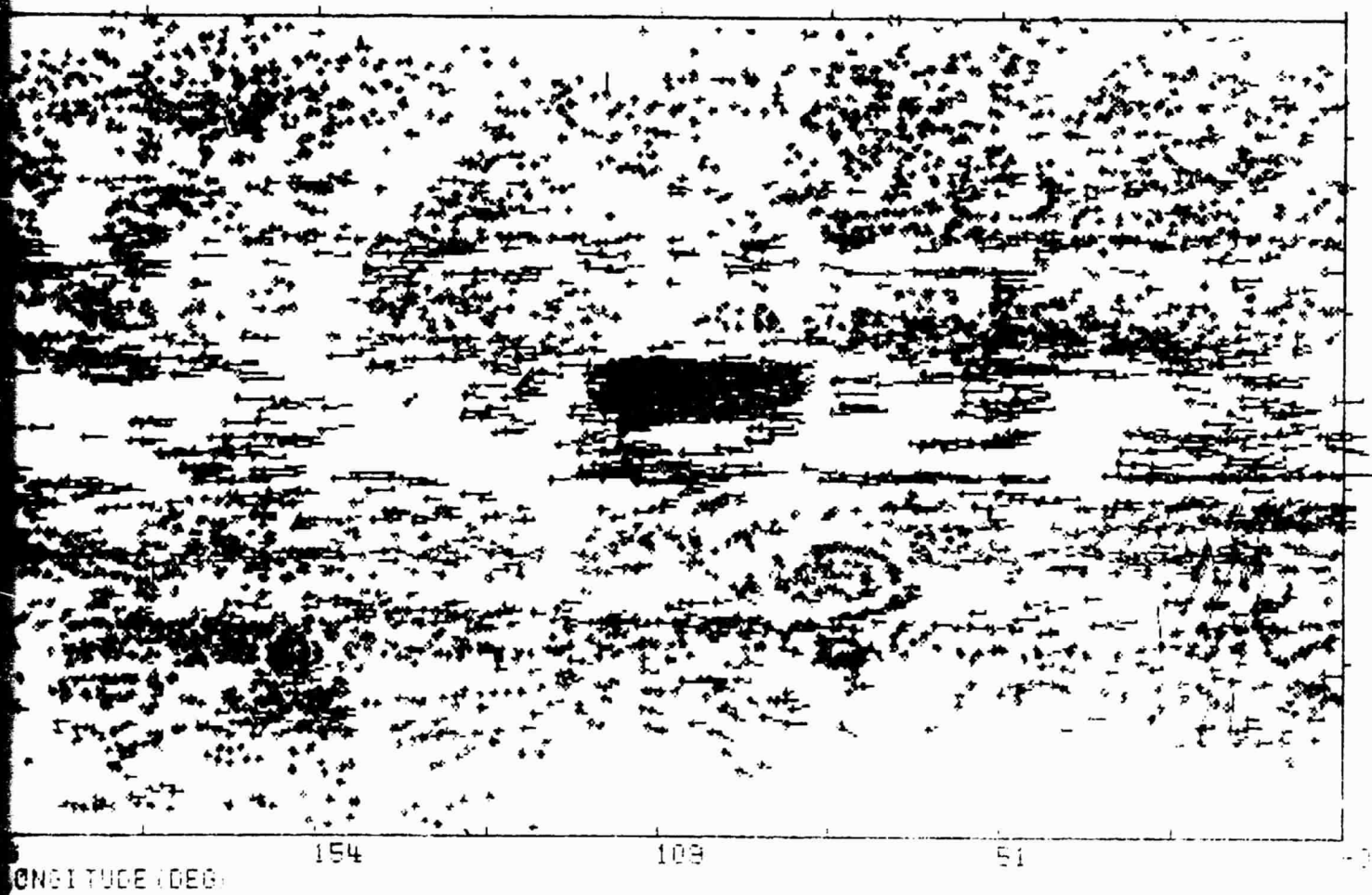
Previous collaborative work by the author regarding the nature of the eddy momentum transport term as deduced from global wind measurements made from series of Voyager 1 images (Beebe et al., 1980) and Voyager 2 images (Ingersoll et al., 1981) served as the stimulus for the subsequent observational work reported in the remainder of Chapter 2 as well as in Chapters 3 and 4. In both collaborative efforts a series of narrow-angle camera frame pairs was used to cover the globe of Jupiter during one 30-hour interval of time. This global set of measurements will subsequently be referred to as a "world map". The Voyager 1 and 2 world maps are shown on Figures 2.4 and 2.5.

The above referenced work proceeds with the longitudinal averaging bin scheme described in Section 2.2.2. The key procedural difference between these efforts and the work described in Section 2.4 is that though the zonal wind component is assumed to consist of a mean and eddy component (i.e., $u = \bar{u} + u'$), the meridional wind component is assumed to be entirely eddy in nature ($v = v'$). The reason for this

Figure 2.4. Plot of actual tiepoints comprising the Voyager 1 "world map". Latitudes are planetographic, while longitudes are measured in System III (1967.0), the conventional radio-defined system of longitude. Lengths of vectors are proportional to wind speed. Points lie at initial observed positions of cloud tracers.



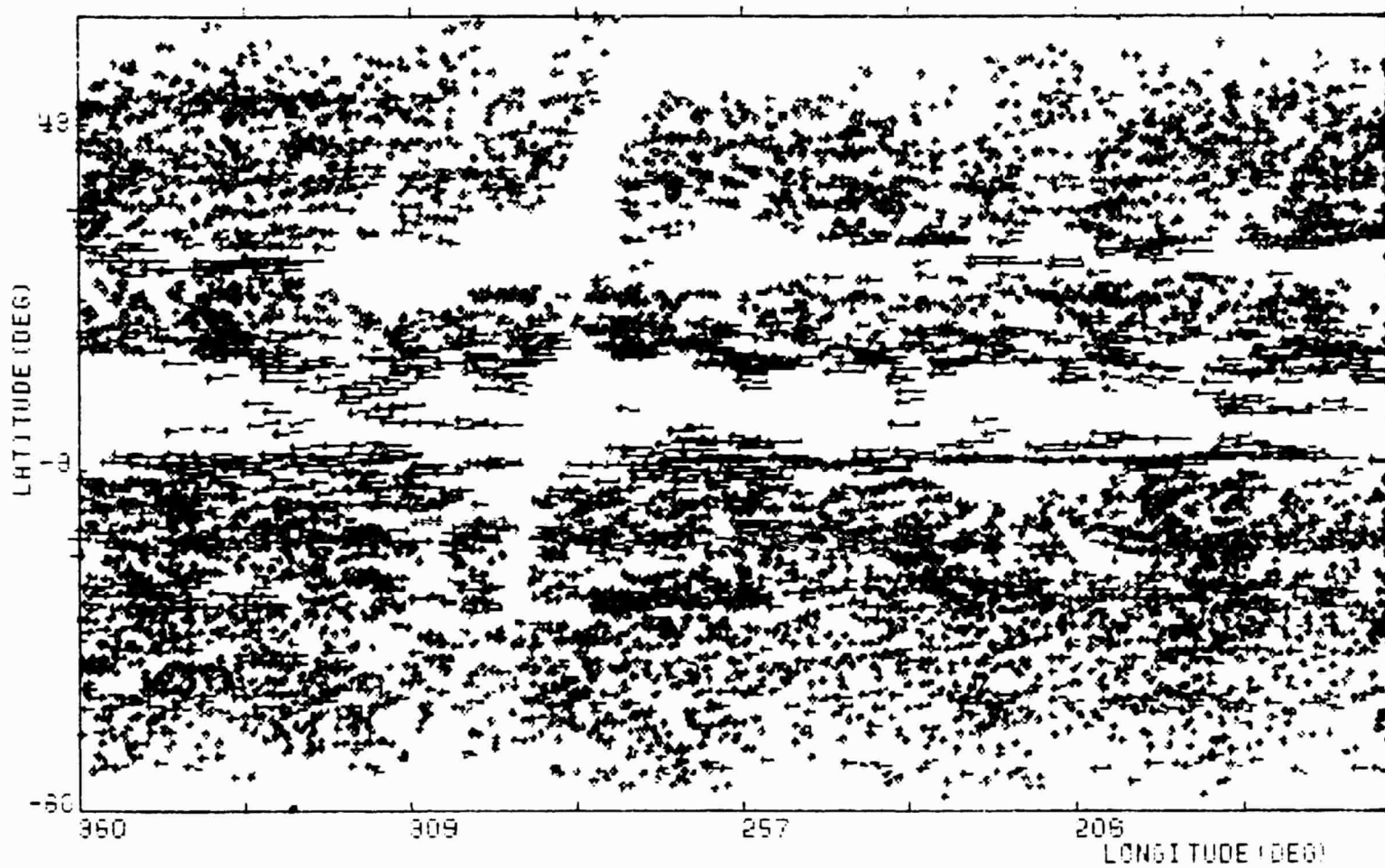
FOLDOUT FRAME



2

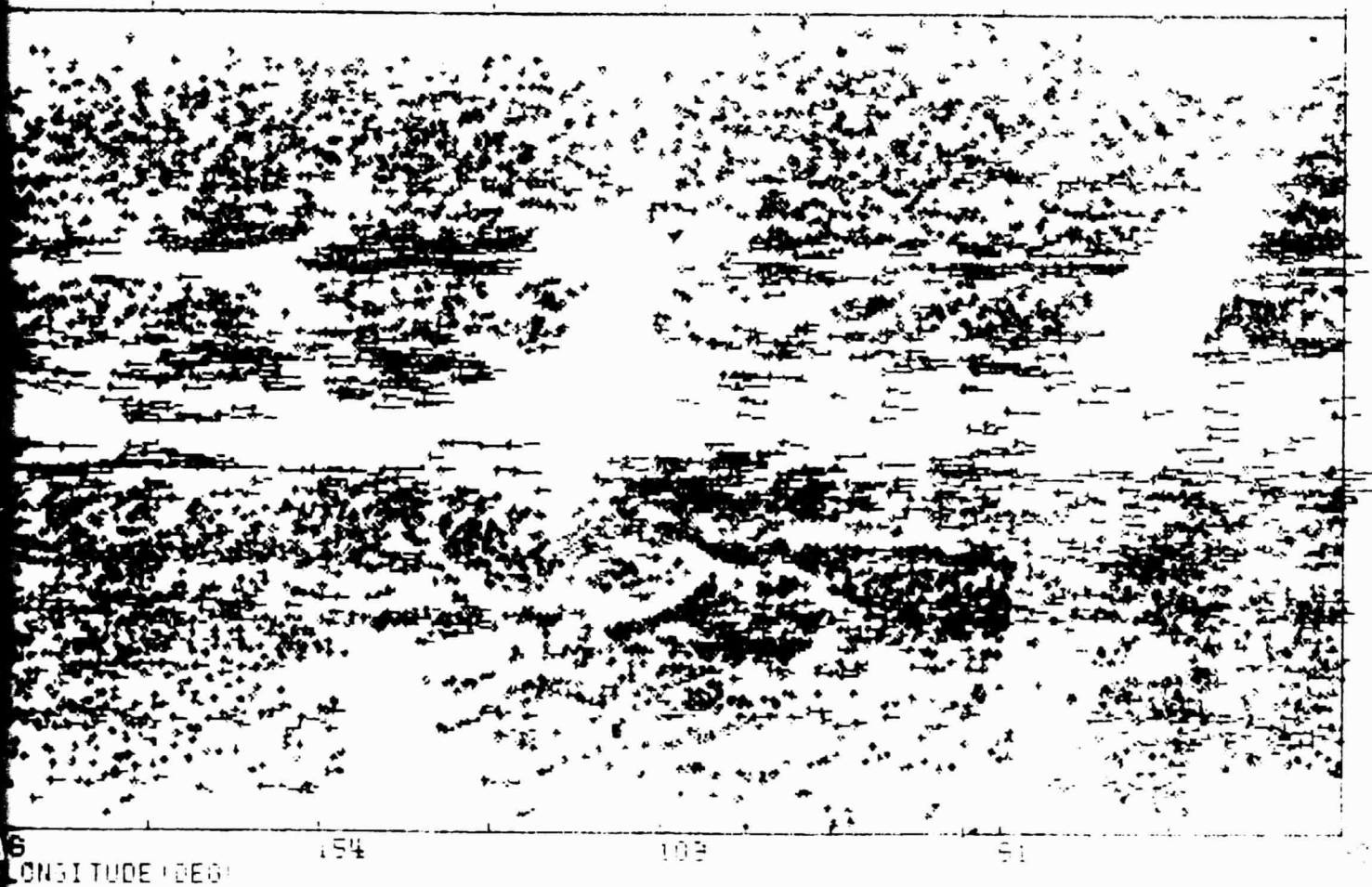
Figure 2.5. Plot of actual tiepoints comprising the Voyager 2 "world map". Latitudes are planetographic, while longitudes are measured in System III (1967.0), the conventional radio-defined system of longitude. Lengths of vectors are proportional to wind speed. Points lie at initial observed positions of cloud tracers. It is this data set which is used for the remaining discussions in Chapter 2 and the spectral analyses of Chapter 3.

ORIGINAL PAGE IS
OF POOR QUALITY



FOLDOUT FRAME

ORIGINAL PAGE IS
OF POOR QUALITY



2

simplifying assumption is two-fold: first, if the mean meridional component is by definition zero ($\bar{v} \equiv 0$) then both the mean meridional transport term ($\{\bar{K} \cdot \bar{K}\}$) and the Hadley overturning term ($\{f\bar{R} \cdot \bar{R}\}$) will disappear from the mean zonal kinetic energy equation 2.9. Secondly, relative errors in measured values of \bar{v} are likely to be much higher than similar relative errors associated with \bar{u} , u' , and v' simply because \bar{v} is typically the smallest of the four wind components. We shall find in Section 2.4 that neglect of \bar{v} has very little impact upon the deduced eddy momentum transport rate.

Treating the world maps as a fully global data set (actually the world maps extend only to $\pm 60^\circ$ latitude and have some gaps in longitude coverage) allows us to write a mean kinetic energy equation which possesses only the eddy transport term on its right-hand side. Beebe et al. and Ingersoll et al. make the assumption that the cloudtop kinematics extend over an atmospheric column containing 10^4 kgm m^{-2} to write the observed global mean eddy kinematic transport rate as $+3.0 \text{ watts m}^{-2}$ for Voyager 1 (Beebe et al., 1980) and $+1.5 \text{ watts m}^{-2}$ for Voyager 2 (Ingersoll et al., 1981). More precisely their results may be written as $+3.0 \times 10^{-4} \text{ watts kgm}^{-1}$ for Voyager 1 and $+1.5 \times 10^{-4} \text{ watts kgm}^{-1}$ for Voyager 2. Such transport rates could imply that eddy motions play a key role in maintaining the global circulation of Jupiter (at least at the cloudtop level). In fact, the observed rates are capable of resupplying the mean zonal kinetic energy in only a few months (again based upon the assumption that the cloudtop kinematics extend through an appreciable column of atmosphere). The tight linear correlation between the eddy stresses ($\overline{u'v'}$) and the

ambient meridional shear of the zonal wind ($d\bar{u}/dy$) is typified by linear correlation coefficients of approximately $r = 0.5$, which for over 100 degrees of freedom indicates a meaningful correlation at better than the 99 percent level (see Figure 8 in Ingersoll et al.). The Prandtl mixing-length concept assumes that the transfer of momentum between eddy and mean motions takes place linearly over some mixing-length (λ') given by,

$$\overline{u'v'} = - |u'\lambda'| d\bar{u}/dy \quad (2.4)$$

where,

λ' = mixing-length or "mean free path" of momentum

u' = typical scale of eddy wind speed.

Most often the product given by $- |u'\lambda'|$ is referred to as the eddy viscosity coefficient (K_e) and plays a role similar to the kinematic viscosity coefficient (ν) in laminar flow (the latter relates to the effects of random molecular motions, while the former relates to the effects of much larger-scale turbulent motions). Ingersoll et al. give estimates of 200 km for λ' based upon typical values of u' of 10 m sec^{-1} and an observed eddy viscosity coefficient of approximately $-2 \times 10^6 \text{ m}^2 \text{ sec}^{-1}$.

The work of Beebe et al. and Ingersoll et al., though admittedly incomplete from the standpoint of contrasting the relative importance of mean, symmetric overturning and eddy motions in maintaining the global circulation, indicates that eddies are capable of transporting mean kinetic energy in the Jovian atmosphere at a rate of up to 10% of the incoming infrared energy flux (Ingersoll et al., 1981; Hanel et al.,

1981). Such a notion runs counter to the classical model of the mean Jovian circulation provided by HP (see the discussion by the author in Smith et al., 1981). It behooves us, therefore, to examine the nature of the other kinematic transport terms in equation 2.9.

2.4 Observed Global Transport Processes

In this section we attempt to extend the global studies of Beebe et al., 1980 and Ingersoll et al., 1981 to include an evaluation of all the inertial transport terms in equation 2.9. We have seen that both the symmetric stress transport $\{\bar{K} \cdot \bar{K}\}$ and the Hadley overturning transport $\{f\bar{K} \cdot \bar{K}\}$ depend upon a measure of zonally averaged or mean meridional motions given by \bar{V} . We have extended AMOS measurements to acquire a new world map consisting of approximately 11,000 tiepoints using pairs of Voyager 2 frames. The process was one of carefully "filling in" the sparse and unevenly distributed data samples used by Ingersoll et al., 1981. The improved data density and even distribution allows a better determination of \bar{V} which we anticipate to be quite small. However, even with the vastly improved data sampling the attempt to contrast zonally symmetric and asymmetric transport is at best marginal.

The operational scheme was to divide the global data set into zonal averaging strips of 1° width in latitude. Each of the transport quantities was then computed and tabulated as a function of latitude by Dr. Reta Beebe at New Mexico State University according to the algorithms provided by the author. The interpretations which follow are entirely those of the author.

The observed mean meridional velocities are typically of the same magnitude as the error associated with AMOS measurements ($\pm 1.5 \text{ m sec}^{-1}$). In an attempt to improve the statistical quality of $\bar{v}(y)$ this quantity, as deduced from the extended Voyager 2 world map, was correlated linearly with $\bar{v}(y)$ as deduced from the original more sparsely sampled Voyager 1 world map. A similar correlation of $\bar{u}(y)$ showed a tight linear relation indicating no substantial change in the $\bar{u}(y)$ profile in the 4 month interval between the two flybys. We selectively disregard those latitude bins containing less than 10 tiepoints and those for which the correlation between the Voyager 1 and extended Voyager 2 world map are poor. This amounts to disregarding approximately 30 latitude bins out of 120 in the extended Voyager 2 world map.

Bins neglected because of poor correlations between \bar{v} in the Voyager 1 and 2 world maps were at latitudes of -53° , -43° , -42° , -6° , $+5^\circ$, $+23^\circ$, $+24^\circ$, $+25^\circ$, $+26^\circ$, and $+27^\circ$. Each of these bins is correlated with an increase in eddy kinetic energy which probably leads to increased errors in the determination of \bar{v} . The equatorial region from -5° to $+4^\circ$ latitude inclusive was neglected because of the small number of data points in this region. Latitudes near $+23^\circ$ correspond to a high speed anomalous eastward jet.

2.4.1 Results of the Extended Voyager 2 World Map

Table 2.1 summarizes the results of computing each of the inertial terms in equation 2.9. Units on transport terms are 10^{-4} watts kgm^{-1} . Also tabulated are the mean and eddy kinetic energies in units of 10^{-4} joules kgm^{-1} . We choose not to confuse our analysis at

Table 2.1. Kinetic Energetics of the Extended Voyager 2 World Map

	Area (m^2)	\bar{K}	K'	$\{f\bar{K} \cdot \bar{K}\}^*$	$\{f\bar{K} \cdot \bar{K}\}^*$	$\{K' \cdot \bar{K}\}$
Global	4.4×10^{16}	1250.2	62.9	+0.22 (+12.11)	+2.66 (-3.14)	+2.24 (+2.24)
Westward Jets	1.4×10^{16}	275.3	59.0	+0.06	-0.27	+1.34
Eastward Jets	3.0×10^{16}	1705.1	64.7	+0.31 (+18.75)	+4.27 (-4.72)	+2.73 (+2.72)

Units on energy reservoirs are 10^{-4} joules kgm^{-1} .

Units on conversions are 10^{-4} watts kgm^{-1} .

*The presence of the high speed, anomalous jet at $+23^\circ$ latitude has a tremendous impact upon the determination of the symmetric transports because of the large values of \bar{u} and \bar{v} associated with this jet (see values in parentheses). We ascribe the large values of \bar{v} to noise associated with the particular difficulty of identifying tiepoints in this region. Higher spatial resolution measurements over the eastward jet are needed.

this point by multiplying through by the column density $\rho^* = 10^4 \text{ kgm m}^{-2}$. Values listed for transports are based upon neglecting the previously mentioned latitudes which gave poor correlations in $\bar{v}(y)$ between the Voyager 1 and 2 world maps. If we include all latitudes, the transports take on the alternate values given in parentheses. The vast difference in the resulting global and eastward jet values for the zonally symmetric transports is a reflection of the high noise level associated with our measurement of $\bar{v}(y)$. We fear that the true value of these zonally symmetric transports is lost in the noise associated with $\bar{v}(y)$. Nevertheless, it is crucial to note that transports associated with zonally symmetric stresses could well be several times larger than those associated with eddy stresses.

The tabulations present global mean values as well as the mean values observed in eastward and westward jets. This facilitates comparison with the models reviewed in Section 1.3 on the following basis:

- (a) According to the classical barotropic stability criterion we might anticipate an increase in K' in the vicinity of westward jets. The fact that $K' = 0$ in eastward jets indicates that the turbulence there cannot be barotropic.
- (b) The eddy stresses of the Green mode baroclinic instabilities examined by Conrath, Gierasch, and Nath (1981) are capable of transporting momentum up-gradient only in the vicinity of westward jets. We would thereby anticipate the quantity $\{K' \cdot \bar{K}\}$ to be positive only in westward jets. However, the eddy stress transport is observed to be largest and positive in the

vicinity of eastward jets. This asymmetry is statistically significant with linear correlation coefficients of $r = 0.5$ for the correlation between $\overline{u'v'}$ and $d\overline{u}/dy$ in both eastward and westward jets. Similar analysis of the Voyager 1 world map yields,

$$\{K' \cdot \overline{K}\} = +1.33 \times 10^{-4} \text{ watts kgm}^{-1} \text{ in westward jets and}$$

$$\{K' \cdot \overline{K}\} = +5.53 \times 10^{-4} \text{ watts kgm}^{-1} \text{ in eastward jets.}$$

- (c) The zonally symmetric instabilities of Stone (1966) are capable of transporting kinetic energy into eastward jets through the resulting zonally symmetric stresses. We have already remarked that this mechanism has been suggested as that which maintains the equatorial jet (Gierasch and Stone, 1968). Tabulated values of $\{\overline{K} \cdot \overline{K}\}$ do indeed indicate an increase in mean eastward kinetic energy transport in the region of eastward jets due to observed symmetric stresses. Note that failure to neglect those latitudes suspected of having very noisy values of $\overline{v}(y)$ leads to the opposite result, so we must be extremely cautious in our interpretation.
- (d) The classical HP model of a mean flow driven by diverging zones and converging belts leads us to anticipate positive values of the Hadley overturning term given by $\{f\overline{K} \cdot \overline{K}\}$. The results summarized in Table 2.1 seem to indicate that symmetric overturning could be as important a process in maintaining the mean zonal flow as is the up-gradient transport due to eddies. The HP model would also anticipate the symmetric stress term given by $\{\overline{K} \cdot \overline{K}\}$ to be positive in

zones and negative in belts and hence nearly zero on the global average. However, our observations do not yield $\{\bar{K} \cdot \bar{K}\} = 0$.

We noted above a meaningful difference in the magnitude of the $\{K' \cdot \bar{K}\}$ transport associated with eastward and westward jets. The increased efficiency of the $\{K' \cdot \bar{K}\}$ process in regions of mean eastward flow apparently runs counter to the model of Conrath, Gierasch, and Nath which predicts feeding in westward jets. Their analysis is based upon a mean zonal eastward wind which increases with altitude ($\partial \bar{u} / \partial z > 0$). This is consistent with a thermal wind generated by warm, upwelling zones and cold, downwelling belts. Allison (private communication, 1981), using IRIS observed temperatures in the upper troposphere, finds that zones appear colder, while belts appear warmer at these upper levels. Such a thermal reversal is typical in the terrestrial upper troposphere. Assuming that the vertical shear of the observed mean zonal wind (\bar{u}) is controlled by the thermal wind relation, the implied shear is one which diminishes the mean eastward flow with altitude ($\partial \bar{u} / \partial z < 0$).

In discussion with Conrath and Gierasch the author has concluded that reversing the algebraic sign of the thermal wind shear in the model of Conrath, Gierasch, and Nath results in instabilities which are capable of transporting momentum up-gradient only in regions of mean eastward flow. Our reader may convince himself of this by reference to Section 1.3.2.2.2. The argument involving vortex tube stretching and advection of planetary vorticity at the steering level remains the same except that we replace the condition that $\bar{u} = 0$ at $z = 0$ by $\bar{u} = 0$ at $z = \infty$.

2.4.2 Problems in Interpretation of the Results

The problem in making definitive statements as to the relative importance of zonally symmetric and eddy processes based upon Table 2.1 remains the large relative noise in \bar{v} . This noise is reflected in the relatively poor linear correlations of products used in the evaluation of $\{\bar{K} \cdot \bar{K}\}$ and $\{f\bar{K} \cdot \bar{K}\}$. The results of a simple, unweighted linear correlation of the terms \bar{u} (as independent variable) and $f\bar{v}$ (as dependent variable), which comprise the Hadley transport $\{f\bar{K} \cdot \bar{K}\}$, and of $d\bar{u}/dy$ (as independent variable) and $\bar{u}\bar{v}$ (as dependent variable), which comprise the symmetric stress transport $\{\bar{K} \cdot \bar{K}\}$, are presented in Table 2.2. Values of linear correlation coefficient (r) are all quite small. The resulting confidence level in the correlation appears high only under the assumption that values of quantities are statistically independent from one latitude bin to the next so that the number of bins truly represents the number of degrees of freedom. This assumption is not likely to be entirely valid.

More disturbing than the low values of r in Table 2.2 is the fact that attempts to compute the global mean value of $\{f\bar{K} \cdot \bar{K}\}$ and $\{\bar{K} \cdot \bar{K}\}$ using the sparser Voyager 1 world map yield results that are substantially different from those presented in Table 2.1. This, of course, casts further doubt on the validity of our evaluation of $\{f\bar{K} \cdot \bar{K}\}$ and $\{\bar{K} \cdot \bar{K}\}$.

Finally we note that the globally averaged value of \bar{v} is approximately $+1.0 \text{ m sec}^{-1}$ rather than identically zero. We believe this to be due to a systematic error in our measured values of \bar{v} rather than indicative of any exotic dynamical process.

Table 2.2. Linear Correlation of Variable x against Variable y for N Degrees of Freedom

x	y	r	N	Confidence Level
\bar{u}	$\bar{f}\bar{v}$	0.06	92	80%
	Global			
	Westward Jets	0.26	33	80%
	Eastward Jets	0.02	59	70%
$d\bar{u}/dy$	$\bar{u}\bar{v}$	0.14	92	85%
	Global			
	Westward Jets	0.12	33	70%
	Eastward Jets	0.24	59	85%
$d\bar{u}/dy$	$\overline{u'v'}$	0.47	92	90%
	Global			
	Westward Jets	0.45	33	88%
	Eastward Jets	0.49	59	91%

In closing we note that the large relative noise in \bar{v} prevents a straightforward evaluation of the roles played by symmetric and asymmetric transport processes. We remain hopeful, however, that further attempts to eliminate sources of noise in \bar{v} will allow the eloquent simplicity of equation 2.9 to be applied to a global data set. At present we only note that on the basis of Voyager global data sets we may not safely conclude that eddy motions play the major role in driving the mean zonal flow.

2.5 Comparisons with IRIS: Energy Budget of the Upper Troposphere

We have seen that the Voyager imaging experiment provides us with measures at the cloudtop level of $u(x,y)$ and $v(x,y)$, which can be decomposed into $\bar{u}(x,y)$, $\bar{v}(x,y)$, $u'(x,y)$, and $v'(x,y)$. The IRIS experiment is capable of yielding measures of $\bar{T}(x,y,p)$, $T'(x,y,p)$, and $N^2(x,y,p)$. Ideally, only the lack of a measure of \bar{w} and w' renders a full evaluation of the Oort energy quantities (equations 1.1 - 1.8) impossible.

Realistically, any comparison of imaging and IRIS data is also limited by the extent to which we are able to identify the level in the atmosphere at which a measurement applies. Ground-based photometry in the 6190 to 8900 Å bands of methane indicates that the cloudtop features observed by Voyager lie very roughly at the 500 mb level (West and Tomasko, 1979; West, private communication, 1981). On the other hand, inversions of the broad IRIS weighting functions allow temperature measurements at several levels in the 200 to 300 mb region. We will compare global measurements of velocity and those of temperature

in the 200 to 300 mb region in order to compute \bar{K} , K' , \bar{P} , and P' for the upper troposphere of Jupiter.

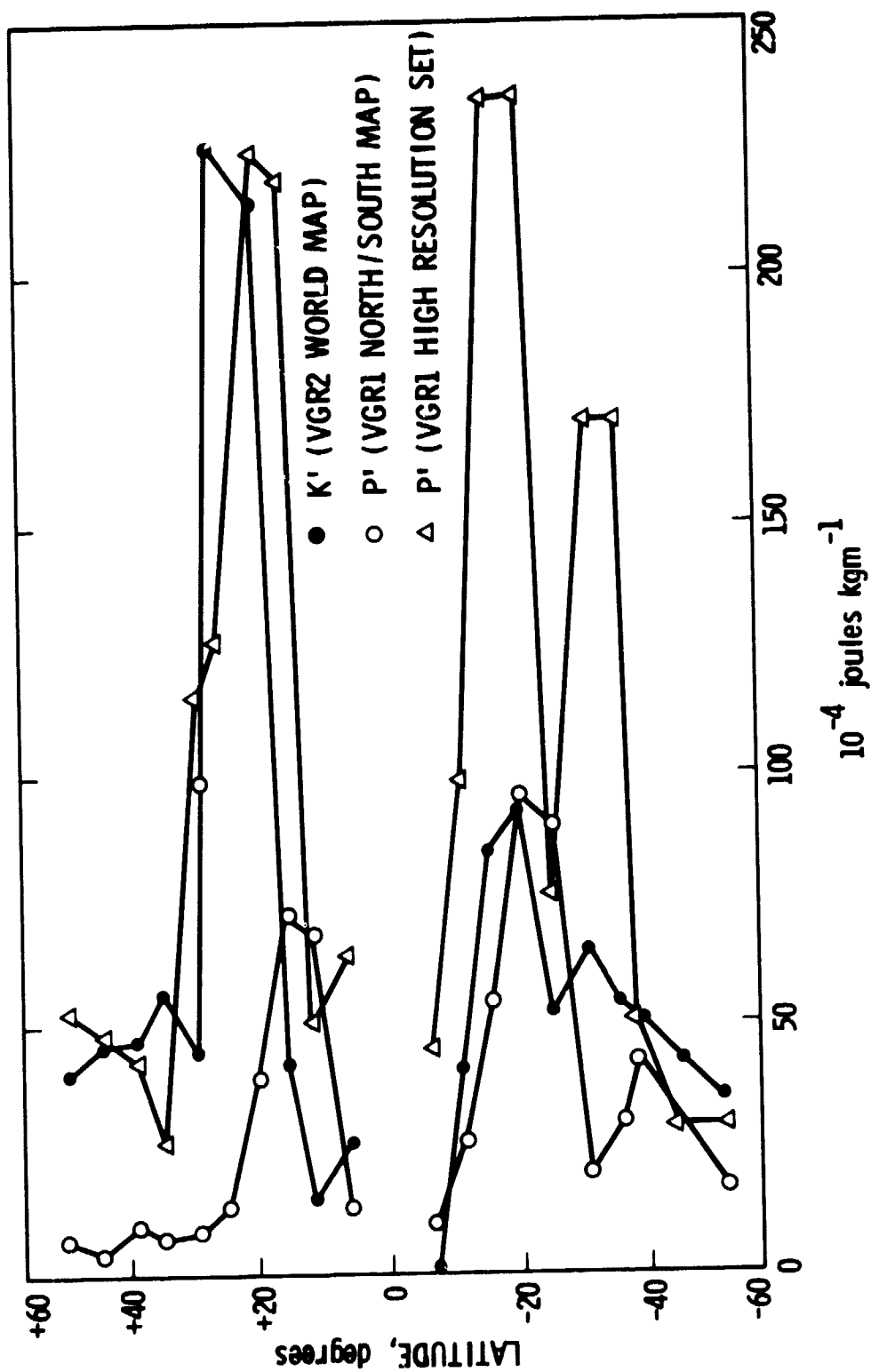
Observed belt to zone temperature differences in the upper troposphere (500 to 140 mb) generate a mean zonal wind profile which is remarkably consistent with that actually observed (Allison, private communication, 1981). This suggests a coupling of the observed cloud-top dynamics and the upper tropospheric thermodynamics with a mean zonal wind which is either driven by the thermal wind or is at least despun with increasing altitude by the thermal wind relation.

In collaboration with Allison, who provided the analysis of the IRIS temperature inversions, we compare our observations of K' , the eddy kinetic energy, with P' , the eddy available potential energy, as functions of latitude in Figure 2.6 (see equations 1.2 and 1.4 for definitions). Units on K' and P' are 10^{-4} joules kgm^{-1} . The excellent correlation between the eddy kinetic and eddy available potential energies clearly indicates a coupling between our observed cloudtop eddy motions and the temperature perturbations observed by IRIS. The profiles of P' are based upon two separate IRIS data sets. The so-called North/South Map data set is global in coverage with a field-of-view roughly 12,000 km across. The High Resolution data set, though not entirely global in coverage, has a greatly improved spatial resolution given by a field-of-view roughly 2000 km across.

The profiles of P' shown in Figure 2.6 are based upon a static stability and temperature perturbations observed for the 196 mb level. Allison and the author find that the tight correlation between P' and K' is maintained at both the 267 and 365 mb levels, though the

Figure 2.6. Meridional profile of observed cloudtop eddy kinetic energy (K') from the Voyager 2 world map and observed IRIS distributions of eddy available potential energy (P') at the 196 mb level from the Voyager 1 north/south map and so-called high resolution data sets.

ORIGINAL PAGE IS
OF POOR QUALITY



PRECEDING PAGE BLANK NOT FILMED

amplitudes on P' are considerable larger at the 267 mb level. It may be that this level represents a steering level; certainly it would be interesting to compare the model of Conrath, Gierasch, and Nath with the vertical structure observed in P' .

The coupling between IRIS thermodynamics and imaging observation of the dynamics allows us to construct an Oort energy budget diagram which we consider appropriate for the upper troposphere (see Figure 2.7). Values associated with each of the energy reservoirs are area weighted mean values for temperate and tropical latitudes (from -56° to -6° and $+5^{\circ}$ to $+55^{\circ}$ latitude). Reference to both Figure 2.7 and the schematic diagram illustrated in Figure 2.8 allows several comments.

In the Jovian diagram we note that the energy stored in the \bar{P} , P' , and K' reservoirs are roughly equal. In the terrestrial case a diminishing amount of energy is stored in each of these reservoirs respectively (see Figure 1.1). In Earth's atmosphere the energy storage in and flows through each of these reservoirs are associated with the baroclinic process. The energy budget for Jupiter suggests an extremely efficient baroclinic process. We might expect such an increased efficiency simply on the basis of a diminished radiative loss of P' due to long thermal relaxation times in the Jovian atmosphere (Gierasch and Goody, 1969) and of diminished frictional loss of K' due to the absence of a rigid lower boundary.

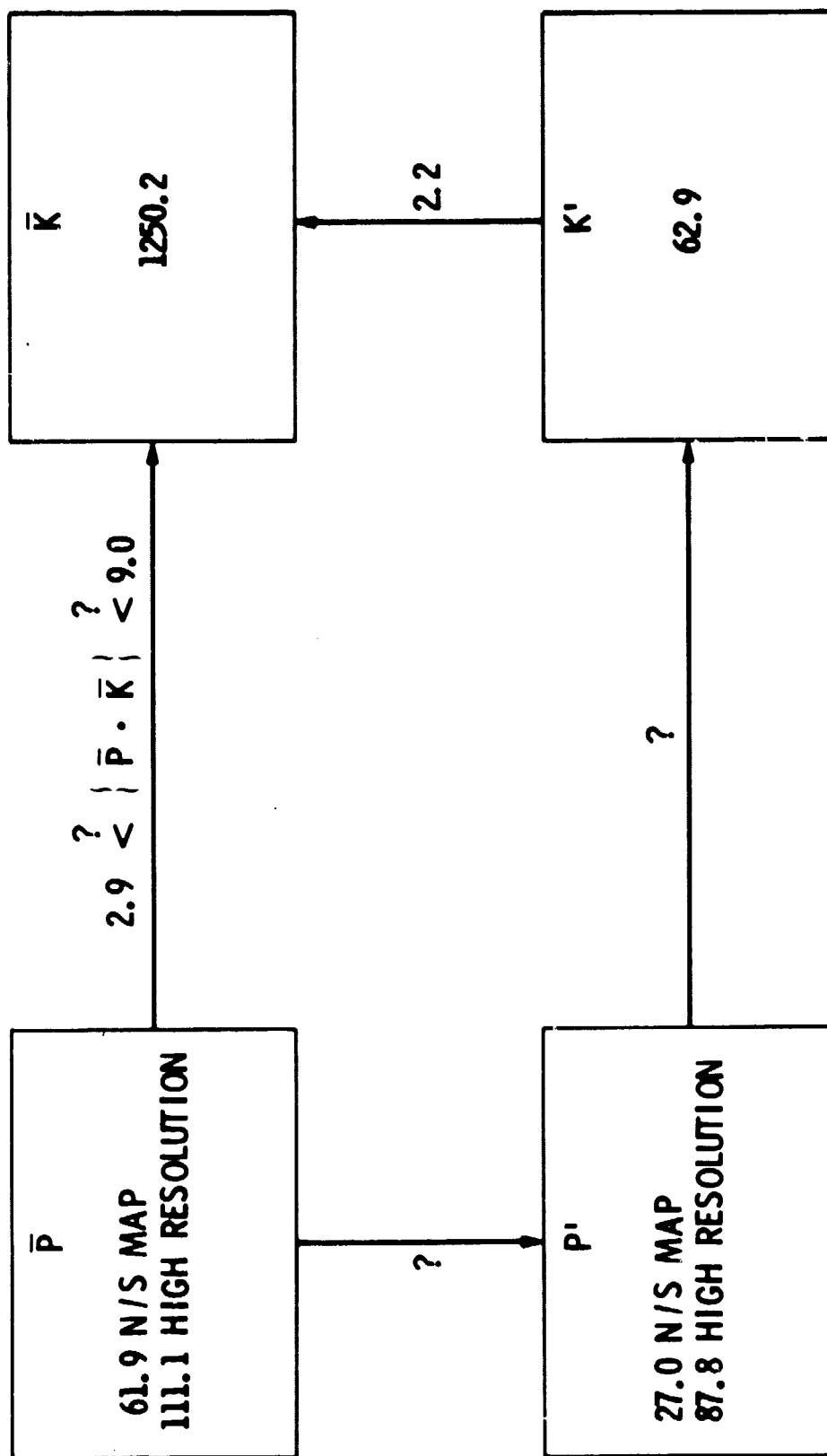
Reference to Figure 2.6 seems to suggest a diminished efficiency in the baroclinic conversion of P' into K' in the southern hemisphere relative to that observed in the north. Such an inefficiency may be due to the presence of the Great Red Spot at -22° latitude and the

Figure 2.7. Oort energy budget diagram of the Jovian upper troposphere.

Potential energies (\bar{P} and P') are evaluated using IRIS observed temperatures at the 196 mb level. Kinetic energies (\bar{K} and K') are evaluated using observed cloudtop motions in the Voyager 2 world map data set.

Uncertainties in measured values of \bar{v} result in the indicated uncertainties in the symmetric conversion of \bar{P} into \bar{K} .

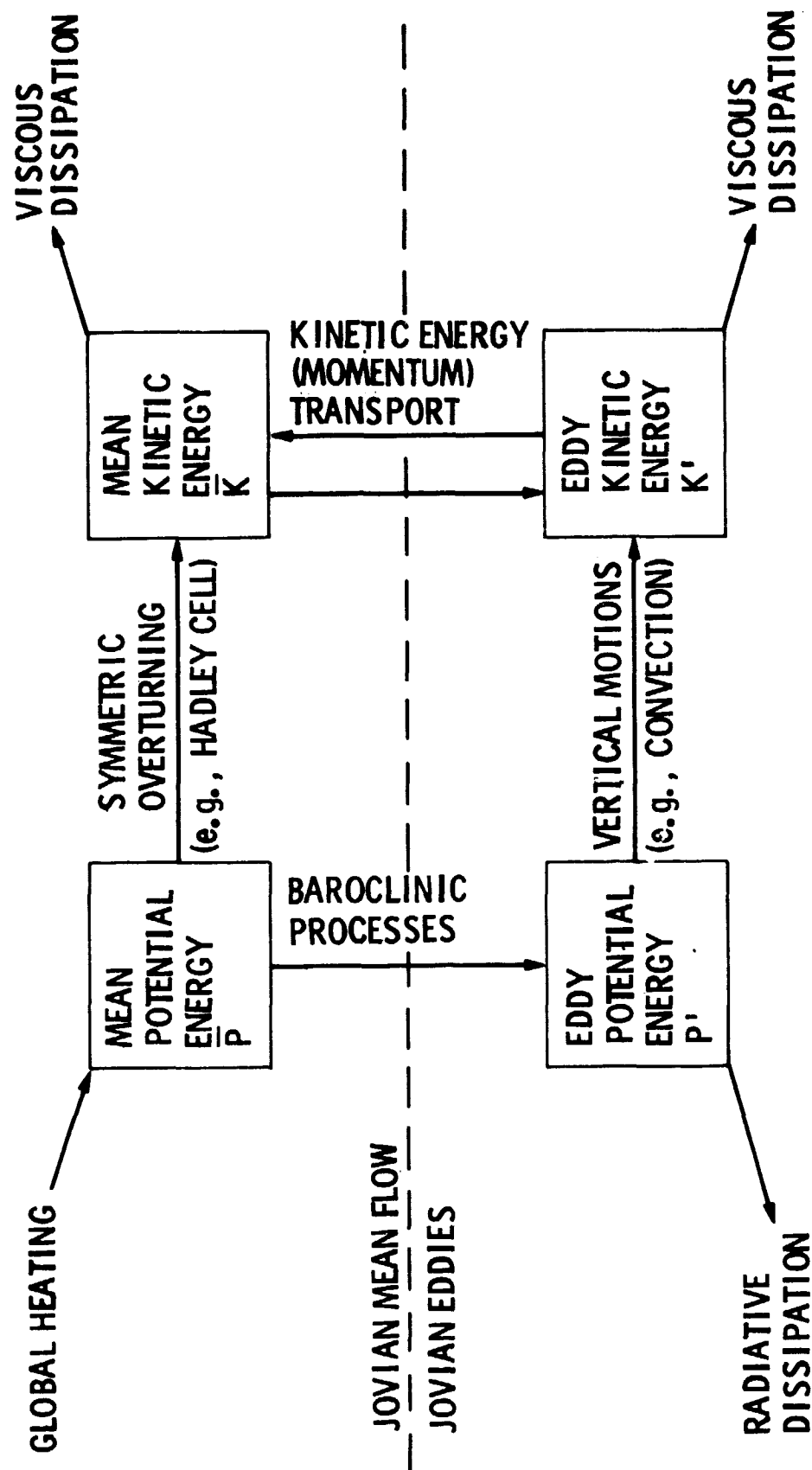
ENERGY BUDGET OF THE JOVIAN UPPER TROPOSPHERE



QUANTITIES WITHIN BOXES HAVE UNITS OF 10^{-4} joules kgm^{-1} .
 TRANSPORT QUANTITIES HAVE UNITS OF 10^{-4} watts kgm^{-1} .

Figure 2.8. Schematic Oort Energy Budget Diagram for Jupiter's atmosphere. Comparison with Figure 2.7 indicates processes observed in the Jovian upper troposphere. Viscous dissipation acts as a dissipation of \bar{K} and K' and presumably arises due to unobservable vertical eddy stresses.

ENERGY BUDGET OF THE JOVIAN ATMOSPHERE



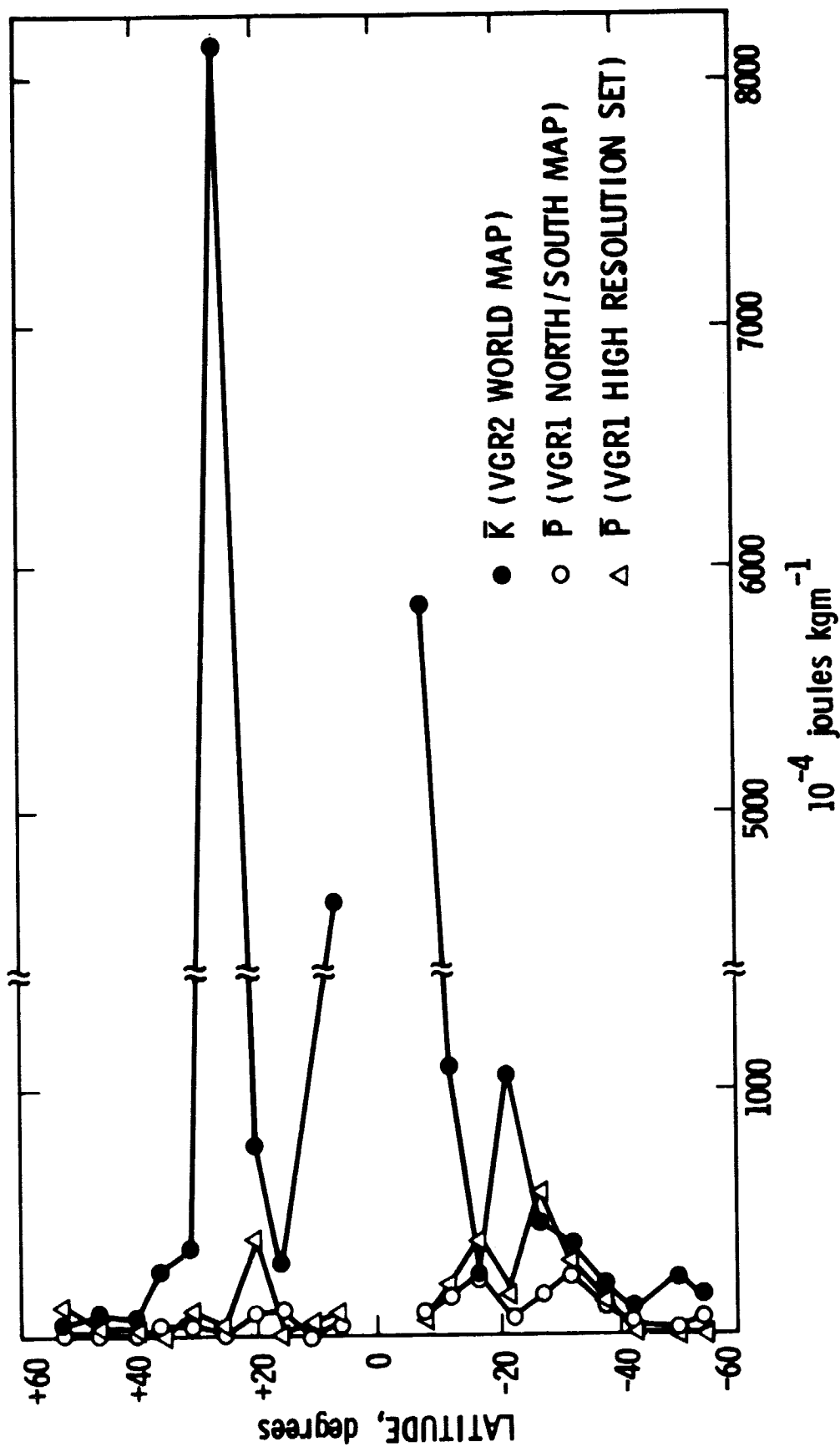
White Ovals at -34° latitude. Studies presented in Chapter 4 indicate that these features feed barotropically on the mean flow. Exactly how this barotropic feeding relates to diminished efficiency into the $\{P' \cdot K'\}$ process is not clear.

An examination of the distribution of \bar{P} and \bar{K} as functions of latitude (see Figure 2.9) indicates little correlation between these two quantities. Thus, there is little evidence for a symmetrically driven mean zonal circulation even though the conversion $\{\bar{P} \cdot \bar{K}\}$ can be large for very small values of \bar{v} . The vast quantity of energy stored in the \bar{K} reservoir may be explained in one of three ways:

- (a) Long radiative relaxation times and low dissipations (due to greatly diminished vertical eddy stresses in the bottomless Jovian atmosphere) allow the atmosphere to baroclinically spin-up, energy being efficiently passed from \bar{P} to P' to K' and then transported up-gradient by the $\{K' \cdot \bar{K}\}$ process to be ultimately stored in the \bar{K} reservoir. If vertical eddy stress dissipation is weak, the \bar{K} reservoir can then grow proportionally very large before a steady state is reached.
- (b) As suggested by Ingersoll and Pollard energy stored in \bar{K} may be deep-seated, the observed mean zonal velocity extending to vast depths. This in turn would decouple the \bar{K} reservoir from the remainder of the Oort diagram.
- (c) Upward propagating waves could deposit substantial amounts of energy into \bar{K} as suggested by Maxworthy (1975). Again, the \bar{K} reservoir might thereby be decoupled from the remainder of the Oort diagram.

Figure 2.9. Meridional profile of observed cloudtop mean kinetic energy (\bar{K}) from the Voyager 2 world map and observed IRIS distributions of mean zonal available potential energy (\bar{P}) at the 196 mb level from the Voyager 1 north/south map and high-resolution data sets. Note the seeming lack of correlation which could indicate a mean zonal flow driven by processes other than those giving rise to observable cloudtop stresses.

ORIGINAL PAGE IS
OF POOR QUALITY



In summary, our analysis of cloudtop stresses has produced the following results:

- (a) We have verified the up-gradient momentum flux due to eddy stresses as reported by Beebe et al. (1980) and Ingersoll et al. (1981) using a data set with nearly twice the number of samples as these earlier reports. As all the actual measuring on the AMOS system collected in our extended Voyager 2 world map was performed by only two individuals, we feel that our results are more likely to be free from systematic errors than these earlier reports. The Voyager 1 world map used by Beebe et al. is a collection of measurements made by a much larger team of investigators. We feel that systematic errors give rise to the apparent differences in the global average eddy stress transport between the three global analyses.
- (b) Very small values of \bar{v} can give rise to high values of symmetric transports. Within the measurement error associated with our determination of \bar{v} it is entirely feasible that symmetric stress transport could entirely outweigh the observed eddy stress transport.

In Chapter 3 we shall use the spectral characteristics of the observed large-scale turbulence in an attempt to better assess the nature of the large-scale turbulent eddies.

CHAPTER 3. THE LARGE-SCALE TURBULENT SPECTRUM

3.1 Introduction

In the Jovian atmosphere large-scale turbulent motions occur over a range of spatial scales from tens to tens of thousands of kilometers. In Chapter 2 we performed a bimodal decomposition of the velocity field and represented the zonally asymmetric or eddy motions by the velocities u' and v' . The estimate of a 10^2 to 10^3 km global mixing length (see Section 2.3) did little to improve our understanding of the length scales associated with the large-scale turbulence. In this chapter we present a brief investigation of the spectral characteristics associated with the large-scale Jovian turbulence. Such an investigation is important in at least two regards:

- a) The nature of the coupling between thermodynamics and dynamics in a fluid system depends upon the length scales associated with the dynamics.
- b) The shape of the turbulent kinetic energy spectrum provides a method for probing the vertical structure associated with the turbulence.

3.1.1 The Coupling of Thermodynamics and Dynamics

A major problem in attempting to formulate a consistent picture of the global dynamics arises from the coupling of the atmospheric thermodynamics to the dynamics through the stratification of the atmosphere. This coupling is apparent in the dynamical governing equation, the quasi-geostrophic potential vorticity equation, given by,

$$\frac{d}{dt} \left[v^2 \psi + \frac{\partial}{\partial z} \left(K^2 \frac{\partial \psi}{\partial z} \right) \right] + \beta \frac{\partial \psi}{\partial x} = 0 \quad (3.1)$$

where,

t = time

$$v^2 = \frac{\partial^2}{\partial x^2} + \frac{\partial^2}{\partial y^2}$$

$$\beta = \frac{df}{dy} \quad (f = 2\Omega \sin \theta)$$

$$K^2 = \frac{f^2 L^2}{N^2 H^2} = \text{stratification parameter}$$

with,

$$N^2(z) = \frac{g}{T_0(z)} \left[\frac{\partial T_0(z)}{\partial z} + \frac{g}{c_p} \right]$$

H = depth of atmosphere .

The static temperature profile ($T_0(z)$) and its gradient $dT_0(z)/dz$ determine the value of the Brunt-Väisälä frequency ($N(z)$) and hence the value of the stratification parameter ($K^2(z)$).

The stratification parameter can be written more simply as,

$$K^2 = \frac{L^2}{L_D^2}$$

where $L_D = NH/f$ = Rossby radius of deformation.

Thus, for length scales (L) much greater than the deformation radius (L_D), and provided $N^2(z)$ does not vary rapidly in z , the thermodynamics (i.e., the thickness or temperature field) couples simply with the dynamics through vortex stretching (i.e., the second term in Equation 3.1). Conversely, if $L < L_D$, the thermodynamics is more intricately coupled to the dynamics (i.e., the coupling involves vertical stresses) and the simplifications made in Equation 3.1 do not hold. Large-scale Jovian turbulence occurs in the regime $L \gtrsim L_D$, so that in general the dynamics and thermodynamics are coupled through vortex stretching.

3.1.2 Two-Dimensional and Three-Dimensional Turbulence

In Chapter 2 we attempted to use global velocity measurements to estimate the rates of various zonally symmetric and asymmetric kinetic energy transport processes occurring in the Jovian atmosphere. In Section 1.3 we hinted at a matrix scheme for classifying models of the Jovian circulation based upon those transport process and the effective depth of the observed circulation. We present such a classification scheme as Table 3.1. Coupled with the results of Chapter 2 a measure of the effective depth of the atmosphere could provide a means for discriminating among the various models of the Jovian circulation.

Voyager can observe motions in essentially a single horizontal plane (that of the cloudtops). Nevertheless, the shape of the kinetic energy power spectrum over a wide range of observable wavelengths

Table 3.1. A Classification Scheme for Jovian Circulation Models

TRANSPORT PROCESSES DRIVING MEAN ZONAL CIRCULATION

	Gegstrophy (e.g., Coriolis deflected Hadley Cells; thermal wind)	Zonally Symmetric Eddy Stresses	Zonally Asymmetric Eddy Stresses
Shallow Active Atmosphere ($d \ll L$)	Barcilon & Gierasch (1970) Williams & Robinson (1973) Stone (1966)		Williams (1979) Conrath, Gierasch, & Math (1981) [only in westward jets] Maxworthy (1975) [vertical stresses]
Deep Active Atmosphere ($d \gtrsim L$)	Stone (1967) Stone (1971)		Busse (1976) [Differential Rotation of Convective Cells also important, see Ingersoll & Pollard, 1981]
No Depth Restriction	Hess & Panofsky (1951) Ingersoll & Cuzzi (1969)	Gierasch & Stone (1968) [only in eastward jets]	

provides a method for probing the dimensionality of the turbulence and hence, an effective depth over which the atmosphere extends. In the next two sections we briefly review the nature of 3-dimensional and 2-dimensional turbulence.

3.2 3-Dimensional, Isotropic Turbulence

Notice that we wrote the dynamical governing Equation (3.1) in a form which neglected the effects of vertical eddy stresses. This is permissible only under the assumption that the length scales associated with the vertical stresses are much smaller than those associated with the horizontal dynamics (see Section 3.3). Turbulence which gives rise to non-negligible and equal stresses in all directions over all length scales is said to be isotropic and 3-dimensional. In this section we briefly review the well-known characteristics of isotropic turbulence. The reader may refer to Tennekes and Lumley (1972; see Chapter 8) for a more detailed treatment.

In this chapter we will examine the nature of the longitudinal turbulent energy spectrum given by,

$$\int_{-\infty}^{\infty} E(k_i) dk_i \quad \text{for } i = 1, 2, 3 \quad (3.2)$$

where,

k_1 = longitudinal wavenumber

k_2 = meridional or transverse wavenumber

k_3 = vertical wavenumber

and,

$$E(k_1) = \frac{1}{2} \oint \phi_{jj}(k_1) d\sigma \quad (3.3)$$

where $d\sigma$ is the surface element of a spherical shell of radius k .

The spectrum tensor ϕ_{ij} is just the 3-dimensional Fourier transform of the correlation tensor R_{ij} given by,

$$R_{ij} \equiv \overline{u_i(x, t) u_j(x + \Delta x, t)} \quad (3.4)$$

where,

$u_1 = u' =$ zonal turbulent velocity component

$u_2 = v' =$ meridional turbulent velocity component

$u_3 = w' =$ vertical turbulent velocity component

and the overbar signifies a time average in this case.

The longitudinal spectrum $F_{11}(k_1)$ is defined by,

$$R_{11}(\Delta x) \equiv \int_{-\infty}^{\infty} \exp(ik_1 \Delta x) F_{11}(k_1) dk_1 \quad (3.5)$$

that is, $F_{ij}(k_1)$ is the one-dimensional Fourier transform of the correlation tensor.

The relationship between ϕ_{ij} and F_{11} is generally quite

complicated. Thus, it is difficult to relate $F_{11}(k_1)$, which can be measured in a global data set, to $E(k_1)$, the 3-dimensional energy spectrum. For isotropic turbulence, however, the relationship can be given as (Batchelor, 1953),

$$E(k_1) = k_1^3 \frac{d}{dk_1} \left(\frac{1}{k_1} \frac{dF_{11}}{dk_1} \right). \quad (3.6)$$

Our energy spectrum representation (Equations 3.2 and 3.3) is strictly valid only for continuous waves not for isolated, hence, multi-component, eddies. Nevertheless, this representation has been found useful in predicting some of the characteristics of a truly turbulent field consisting of isolated eddies (see Lumley, 1970 for more exact representation).

In our analysis we shall not attempt a direct measure of the correlation tensor but rather will perform a straightforward Fourier analysis of the observed zonal eddy velocity component $u'(x)$ in several zonal strips at various latitudes in order to obtain $u'(k)$, where k is the dimensionless wave index which we shall henceforth refer to as the zonal wavenumber. Thus, from world map measurements we obtain,

$$K'(k) = L(k) = \int_k u'^2(k) dk.$$

Again, the method is strictly valid only for continuous waves though the results are meaningful even for a field of isolated eddies.

In isotropic, 3-dimensional turbulence the transfer of energy from one scale to the next takes place by means of the vortex stretching

mechanism, the smaller eddies spinning up in the strain rate field of the larger eddies. Thus, contrary to the deduced direction of $\{K' \cdot \bar{K}\}$ for Jovian eddies, the energy cascade is always direct with energy flowing from large scales to small scales. The characteristic strain rate of an eddy of wavenumber k_i is,

$$s(k_i) = \frac{(k_i E(k_i))^{1/2}}{2\pi/k_i} \quad (3.7)$$

At the largest scale the turbulence is driven by the strain rate of the mean flow (S) and loses energy to smaller scales at a rate ϵ . Thus, on the largest scales $E = (k_i, \epsilon, S)$, which has the nondimensional form,

$$E^* = \frac{E(k_i)}{\epsilon^{3/2} S^{-5/2}} \quad (3.8)$$

Conversely, on the smallest scale (the so-called Kolmogorov microscale) energy cascading down the spectrum at a rate equal to the dissipation rate ϵ is finally "destroyed" by the viscosity ν , and has the non-dimensional form,

$$E^* = \frac{E(k_i)}{\epsilon^{1/4} \nu^{5/4}} \quad (3.9)$$

Note from Equation 3.7 that the strain rate $s(k_i)$ associated with the turbulence increases as k_i increases. The Kolmogorov spectrum, given in

nondimensional form by Equation 3.9, is valid only in the limit as $s(k_i)/S \rightarrow \infty$. On the other hand, the large-scale spectrum (see Equation 3.8) is valid only in the limit as $s(k_i)/k_i^2 \nu \rightarrow \infty$. The spectral region intermediate to the Kolmogorov scale and the large-scale is known as the inertial subrange and represents the region in which both of the above limits apply simultaneously. It can be shown by similarity argument (Tennekes and Lumley, 1972; see page 265) that within this inertial subrange,

$$E(k_i) \propto k_i^{-5/3} . \quad (3.10)$$

3.3 2-Dimensional or Geostrophic Turbulence

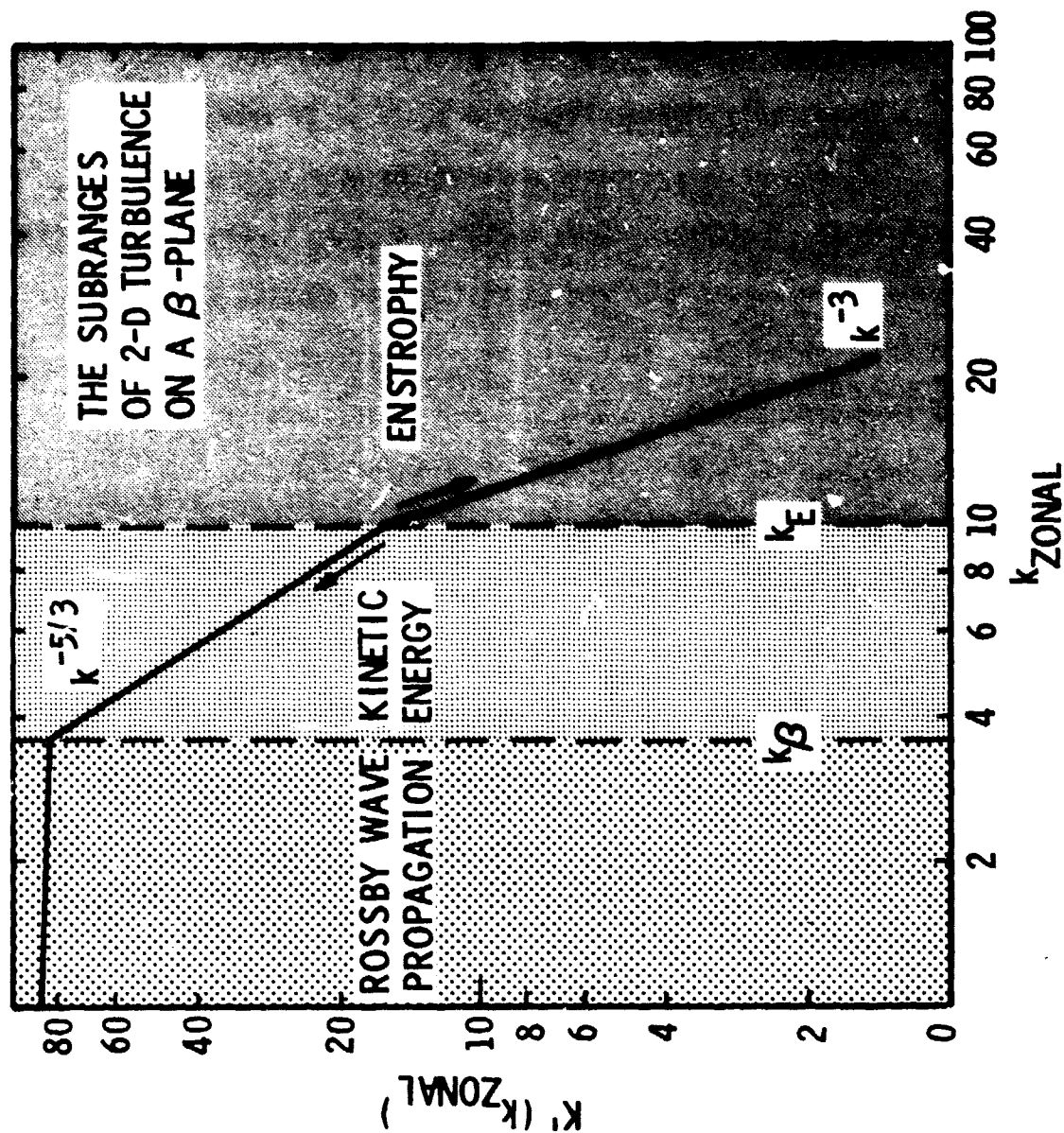
For 3-dimensional turbulence our analysis was restricted only by considerations of energy conservation in the inertial subrange. If the turbulence field is 2-dimensional potential vorticity, as well as energy, is conserved (Fjørtoft, 1953). Conservation of potential vorticity or enstrophy, as mean-squared vorticity is often called, has a pronounced effect on the shape of the kinetic energy power spectrum which becomes by similarity argument (Kraichnan, 1967),

$$E(k_i) \propto k_i^{-3} \quad (3.11)$$

in a region of the inertial subrange over which enstrophy is being transferred. Generally, in 2-dimensional turbulence there are two inertial subranges in which potential vorticity is transferred and the

Figure 3.1. Turbulent transport regimes in a rotating planetary atmosphere. In the turbulent regime kinetic energy (K') input at zonal wavenumber k_E will cascade up to larger scales resulting in a $k^{-5/3}$ power law. Enstrophy (mean squared vorticity) will cascade down to smaller scales resulting in a k^{-3} power law for $k > k_E$. For scales larger than k_β the propagation of Rossby waves interrupts the up-gradient turbulent transport.

ORIGINAL PAGE IS
OF POOR QUALITY



spectrum takes a profile governed by Equation 3.11 and another in which energy is transferred and the spectrum is governed by Equation 3.10 (Kraichnan, 1967; Leith, 1968).

The energy cascade associated with 3-dimensional turbulence is always direct in the sense that energy passes from low wavenumbers to ever higher wavenumbers to be finally dissipated on the Kolmogorov microscale. The energy cascade associated with 2-dimensional turbulence is not as intuitively obvious (see Figure 3.1). If energy is fed into a particular band of "excitation" wavenumbers near $k_i = k_E$, then it can be shown (Kraichnan, 1967) that for $k_i < k_E$ kinetic energy is transferred up the spectrum to smaller and smaller wavenumbers. In this region $E(k_i)$ takes the profile given by Equation 3.10 as in 3-dimensional turbulence. For scales smaller than the excitation wavelength ($k_i > k_E$) enstrophy is transported down the spectrum to larger and larger wavenumbers where it is eventually destroyed by viscosity at scales smaller than those in the inertial subrange. In the enstrophy-transfer subrange $E(k_i)$ takes a profile given by Equation 3.11. The transfer of energy in this enstrophy-transfer subrange and the transfer of enstrophy in the energy-transfer subrange are both zero.

Charney (1971) demonstrates that in a quasi-geostrophic atmosphere (i.e., one governed by Equation 3.1) the large-scale turbulence, which is sometimes referred to as geostrophic turbulence, has an energy spectrum profile governed by enstrophy transfer for wavenumbers greater than k_D . In the terrestrial troposphere

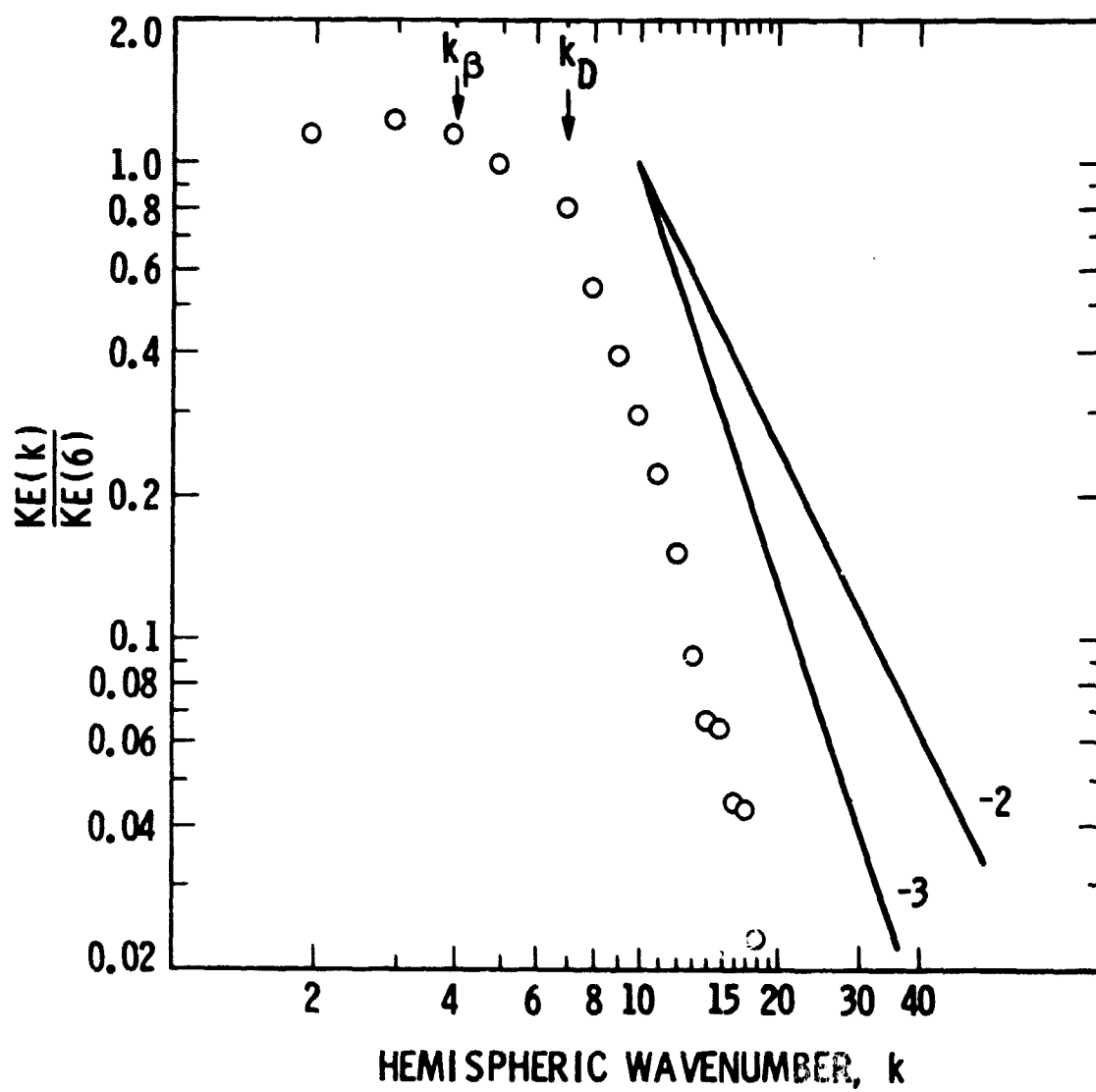
baroclinicity pumps energy into the atmosphere at zonal wavenumbers near $k_E = 7$. Subsequent observational study of the kinetic energy power spectrum of large-scale motions in Earth's atmosphere (Julian et al., 1970) from $k = 1$ to 20, where k is the zonal wavenumber, indicates that the inertial range from about $k = 7$ to 20 does indeed obey the k^{-3} power law as in Equation 3.11 (see Figure 3.2). Thus, in Earth's atmosphere motions on those large scales are basically 2-dimensional or quasi-barotropic due to the fact that enstrophy is conserved. The observed shape of the spectrum for the energy-transfer subrange ($k < 7$) does not, however, obey the $k^{-5/3}$ power law (Equation 3.10). At least two mechanisms are responsible for halting the reverse energy cascade at low wavenumbers in Earth's atmosphere: planetary wave propagation and surface drag at the lower boundary.

Lilly (1971) studies the effects of linear surface drag in a numerically simulated 2-dimensional turbulent field. The effects of surface drag appear to be two-fold:

- a) In the energy-transfer inertial subrange the spectral profile peaks at a wavelength less than the scale of the mean flow and with an amplitude somewhat diminished from that predicted by unimpeded energy transfer.
- b) For large drag and small vorticity transfer rates the spectral profile in the vorticity-transfer subrange exhibits a slope of nearly $k^{-3.7}$ as opposed to k^{-3} .

Figure 3.2. Turbulent kinetic energy power spectrum in Earth's mid-latitude troposphere (from Julian et al., 1970). Values of KE, the turbulent energy, are normalized to the observed value at a zonal or "hemispheric" wavenumber $k = 6$. The Rhines and Rossby deformation wavenumbers are indicated by k_B and k_D respectively. For $k > k_D$ the spectrum seems to obey a k^{-3} power law as anticipated for geostrophic turbulence. Note the diminished slope for $k < k_D$. Large-scale Jovian turbulence occurs in the region $k_B < k < k_D$.

ORIGINAL PAGE IS
OF POOR QUALITY



Rhines (1975) examines the transfer of energy in the large-scale, energy-transfer portion of the subrange for 2-dimensional turbulence on a β -plane. In the $k^{-5/3}$ subrange the transfer of energy to smaller wavenumbers continues unimpeded until the β -restoring force for the increasing length scales begins to dominate even the nonlinear interactions. The timescales for the nonlinear interactions and Rossby wave propagation are equal at a wavenumber given by,

$$k_{\beta} = \sqrt{\beta/2U} \quad (3.12)$$

where,

k_{β} = transition number, or "Rhines" wavenumber

U = typical zonal velocity scale.

Thus, at a wavelength equal to $2\pi/k_{\beta}$ ($\equiv L_{\beta}$) a transition from a turbulent regime ($L < L_{\beta}$) to one of Rossby wave propagation ($L > L_{\beta}$) occurs. The length scale k_{β}^{-1} is often referred to as the Rhines radius. In the turbulent regime the dispersion relation is approximately,

$$\omega \approx kU. \quad (3.13)$$

Thus, flow of energy to smaller wavenumber corresponds to an increase in energy of the lower frequency components. Rossby waves are somewhat unusual in that smaller wavenumbers are associated with higher frequencies according to a dispersion relation like,

$$\omega = \frac{-\beta}{k (1 + m^2/k^2)} \quad (3.14)$$

where,

k = dimensionless zonal wavenumber (or zonal wave index)

m = dimensionless meridional wavenumber (or meridional wave index).

Thus, in an isotropic field the flow of energy to smaller wavenumbers will be impeded by the wavenumber and frequency resonance requirements for wave-wave interactions. Note that according to Equation 3.14 the flow of energy to smaller wavenumbers in the Rossby wave regime is less impeded for very small values of m/k . On the other hand, if m/k is large, kinetic energy will build up at scales near the Rhines radius. Thus, we are apt to find situations in which the eddies, flattened by the β -effect, lead to an end state for the cascade consisting of alternating easterly and westerly jets with width scales given by k_{β}^{-1} and amplitudes constrained by the barotropic stability criterion. Williams (1979b) suggests that such an end state manifests itself on Jupiter.

3.4 Large-Scale Jovian Turbulence

In this section we describe the use of the extended Voyager 2 world map to deduce the spectral profile of the large-scale turbulent motions of the Jovian cloudtops. Conceptionally our analysis is simple and based upon that for Earth's troposphere by Julian et al. (1970). In some regards the actual analysis remains preliminary, and in closing we are compelled to suggest further work.

3.4.1 Measurement of the Turbulent Kinetic Energy Power Spectrum

The excellent data sampling of the Voyager 2 world map (see figure 2.5) suggests that use of a discrete Fourier Transform analysis, which is certainly time-saving as compared to a more rigorous periodogram analysis, would be meaningful. The well-sampled, but nevertheless somewhat uneven, distribution of data points necessitates interpolation to a uniformly spaced grid of points. Based upon typical tiepoint spacing and jet width in the world map, this interpolation was performed within an influence radius ($r = r_i$) about each grid point of $r_i = 2^{\circ}5$. Our analysis is longitudinal, that is we perform a Fourier Transform on the zonal distribution of u' , the eddy zonal velocity component. The value of u' at each grid point in the one dimensional array is taken as the weighted mean of all the actual tiepoints within one influence radius of the grid point. Tiepoints are weighted as r^{-2} .

In order to make use of a 6-bit Fast Fourier Transform (FFT) routine (i.e., one capable of handling 128 samples) we select the longitudinal spacing of grid points as $\Delta x = 2^{\circ}82$. The resulting Nyquist wavelength of the analysis is thus $5^{\circ}64$ or $k = 64$, where k is once again the zonal wavenumber. The FFT routine provides amplitudes for $u'(k)$ for each wavenumber component from $k = 1$ to $k = 64$. The mean value (\bar{u} , represented by $k = 0$) is removed prior to the actual analysis. Squaring the u' amplitudes allows a proportional measure of $K'(k)$, the eddy kinetic energy associated with each resolved wavenumber.

The analysis described above was performed in 13 zonal bins centered on 6 westward and 7 eastward jets. Plots of $u'^2(k)$ in each of these jets are provided as Figures 3.3 through 3.15. In order to smooth-out noise in the analysis individual points plotted in each of these figures represent the mean value of $u'^2(k)$ at four discrete, adjacent wavenumbers. We do not notice any substantial differences between the spectra observed in eastward jets and those observed in westward jets as might be predicted for Green mode baroclinicity (Conrath, Gierasch, and Nath, 1981).

3.4.2 Interpretation of the Jovian Turbulent Spectrum

If the observed cloudtop turbulence is driven by baroclinic forcing we anticipate energy to be fed into the spectrum at k_D , the wavenumber associated with the Rossby deformation radius. Based upon a typical Brunt-Väisälä frequency of $N = 10^{-2} \text{sec}^{-1}$ in the Jovian upper troposphere and a depth scale of $H = 10^4 \text{m}$ (a scale height), we may compute a deformation radius of approximately,

$$L_D = \frac{NH}{f} \sim 10^3 \text{ km}$$

thus,

$$k_D \sim 10^2 .$$

Figure 3.3. Smoothed Jovian turbulent kinetic energy power spectrum ($u'^2(k)$) of westward jet at $+44.5^\circ$ latitude. Units on $u'^2(k)$ are $m^2 \text{ sec}^{-2}$, whereas k_{zonal} is the number of wavelengths fitting around the latitude circle. As in Figures 3.4 through 3.15, k_g is computed according to equation 3.12. In this case somewhat artificially low values for U , the mean zonal velocity within the 5° wide averaging channel were obtained because of the narrowness and weakness of this particular jet.

ORIGINAL PAGE IS
OF POOR QUALITY

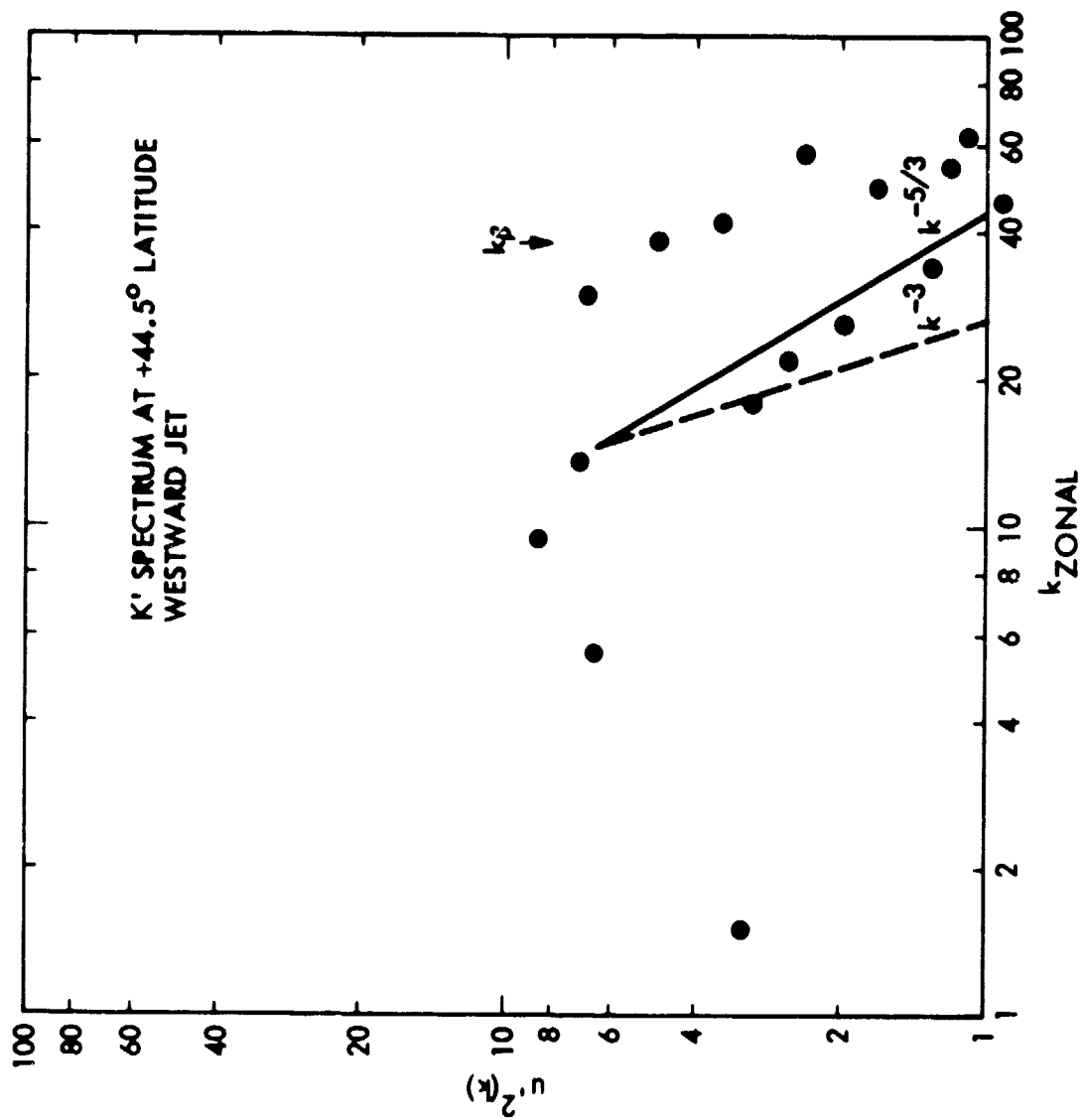


Figure 3.4. Smoothed turbulent kinetic energy power spectrum
 $(u'^2(k))$ of westward jet at +39°5 latitude.

ORIGINAL PAGE IS
OF POOR QUALITY

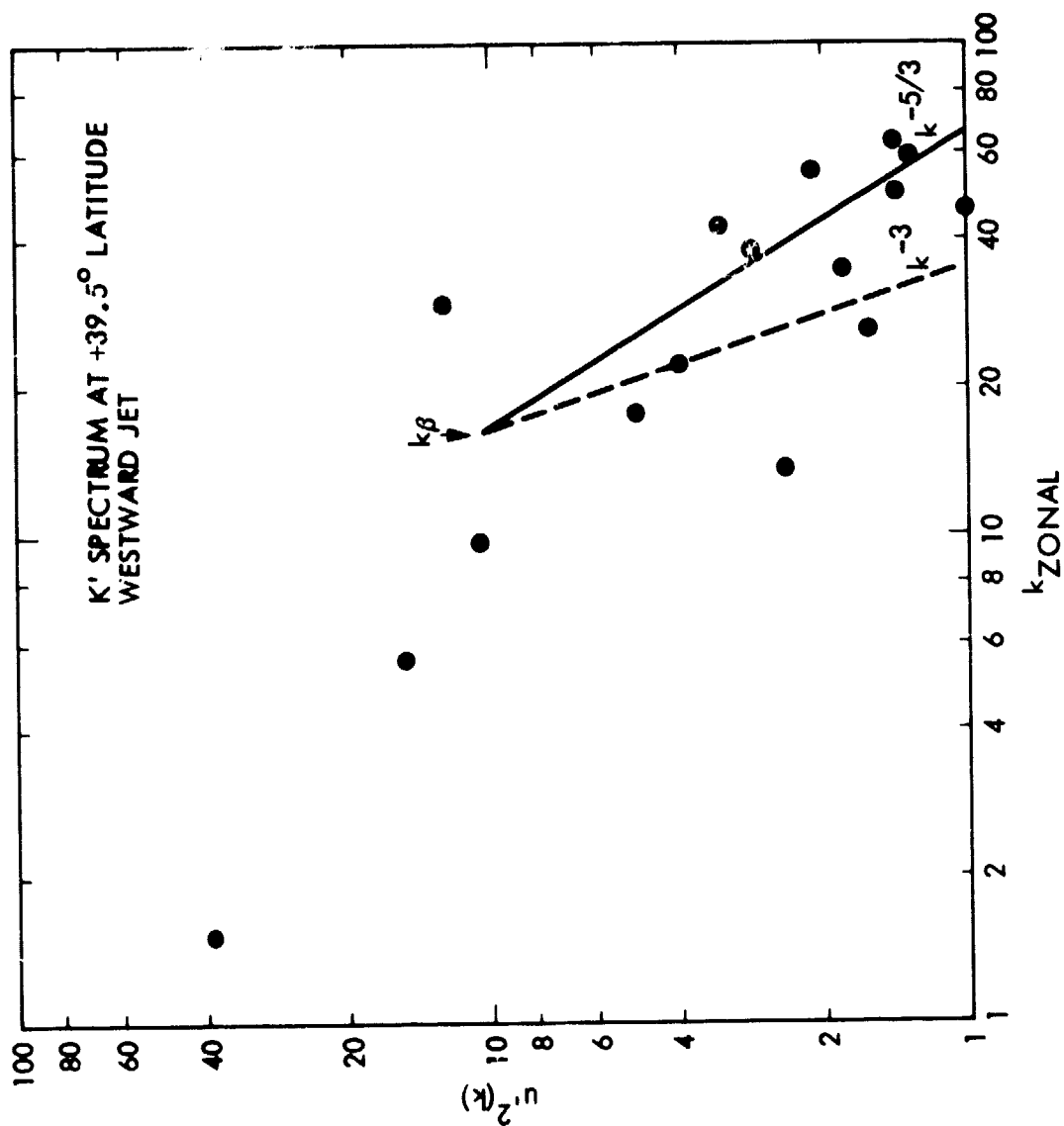


Figure 3.5. Smoothed turbulent kinetic energy power spectrum
($u'^2(k)$) of eastward jet at +35°5 latitude.

ORIGINAL PAGE IS
OF POOR QUALITY

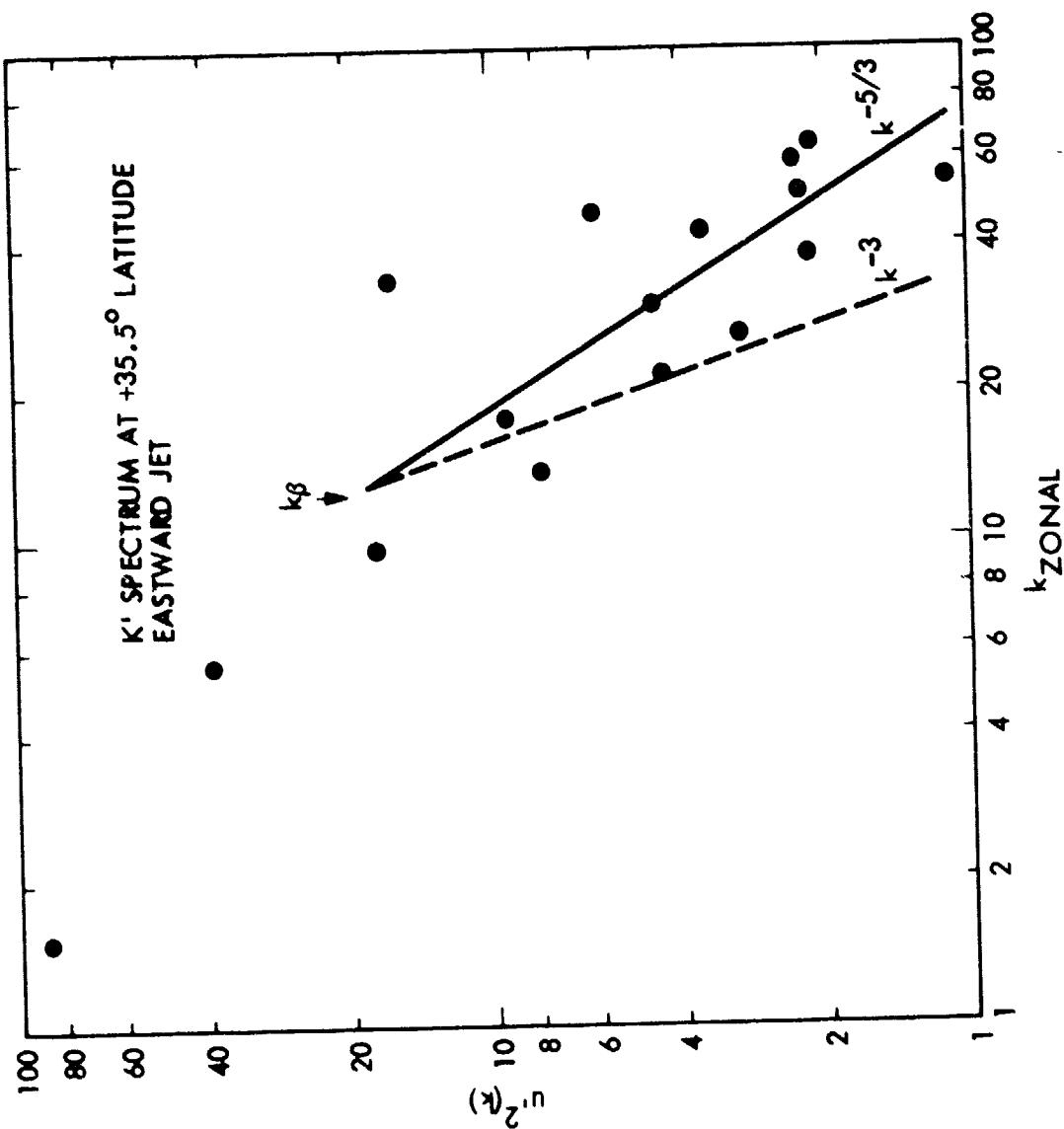


Figure 3.6. Smoothed turbulent kinetic energy power spectrum
 $(u'^2(k))$ of westward jet at +31° latitude.

ORIGINAL PAGE IS
OF POOR QUALITY

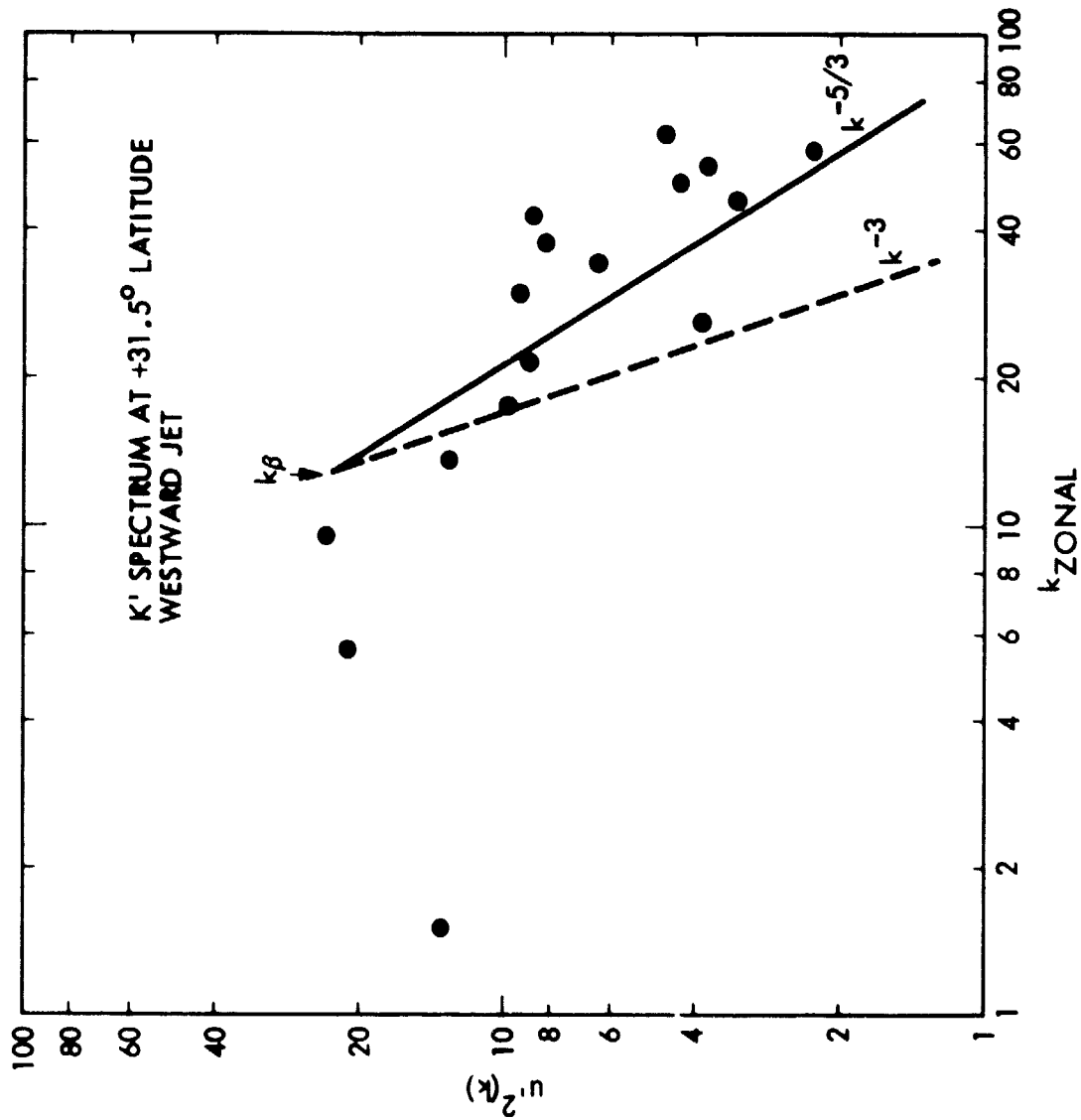


Figure 3.7. Smoothed turbulent kinetic energy power spectrum ($u'^2(k)$) of eastward jet at +23.5 latitude. It is near this latitude (see also Figure 3.8 which follows) that both P' and K' reach a maximum (see Figure 2.6). It is interesting, but highly speculative, to suggest that baroclinic effects are important in this region and lead to an aliased spectrum with an up-turn near the Nyquist wavenumber.

ORIGINAL PAGE IS
OF POOR QUALITY

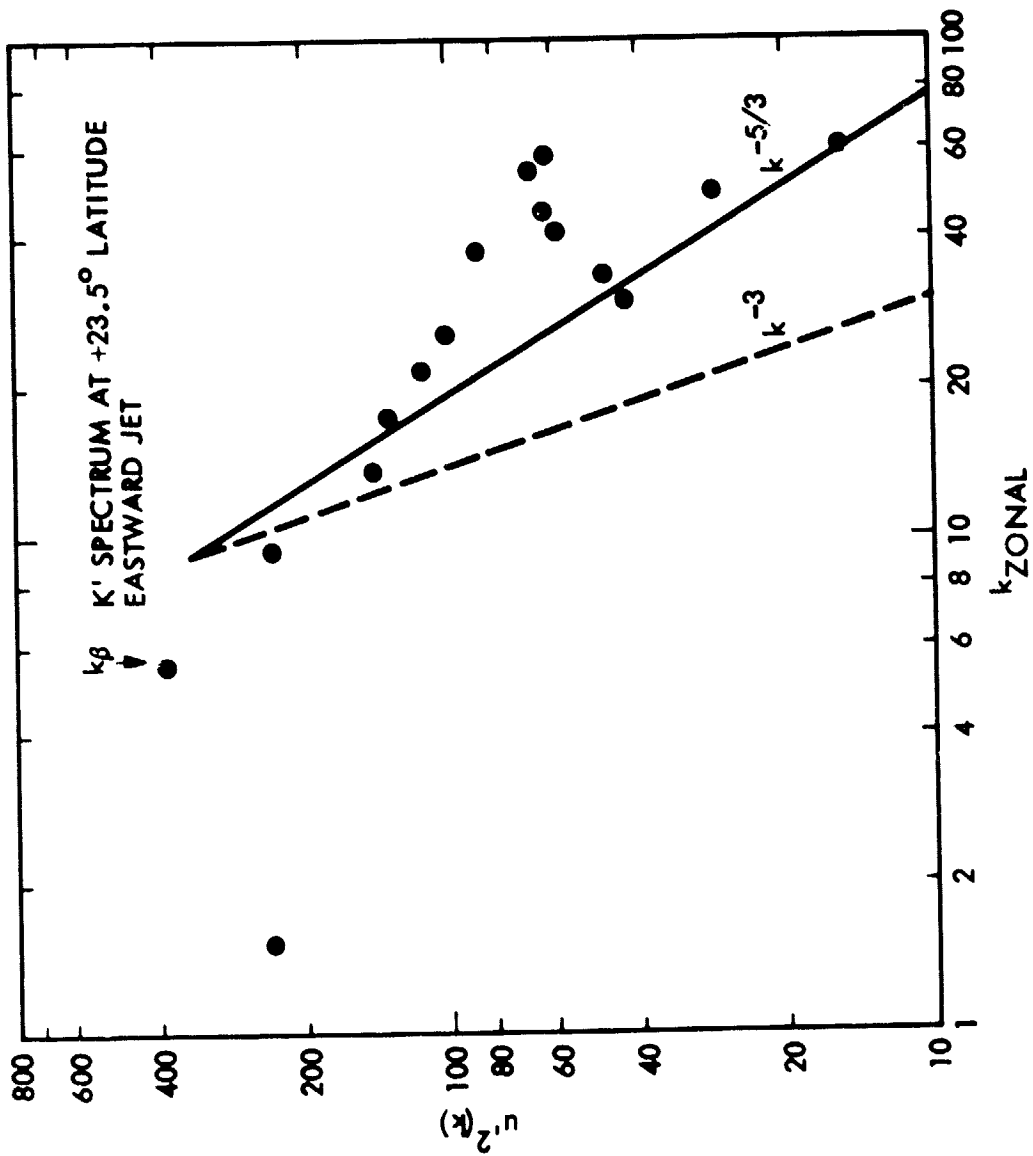


Figure 3.8. Smoothed turbulent kinetic energy power spectrum ($u'^2(k)$) of westward jet at +17°5 latitude. It is near this latitude that both P' and K' reach a maximum (see Figure 2.6). It is interesting, but highly speculative, to suggest that baroclinic effects are important in this region and lead to an aliased spectrum with an up-turn near the Nyquist wavenumber.

ORIGINAL PAGE IS
OF POOR QUALITY.

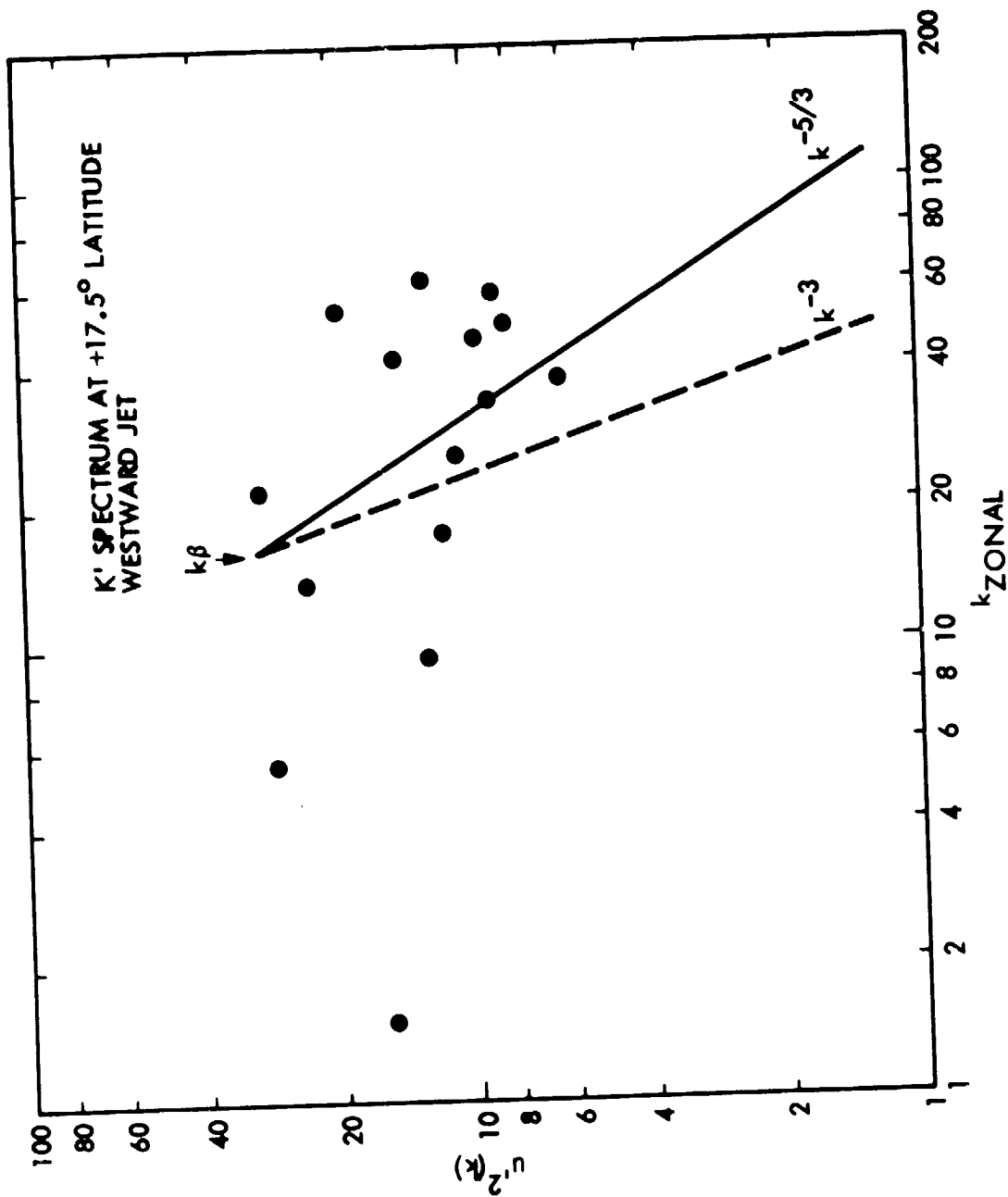


Figure 3.9. Smoothed turbulent kinetic energy power spectrum
 $(u'^2(k))$ of the northern edge of the equatorial
jet at +12°0 latitude.

ORIGINAL PAGE IS
OF POOR QUALITY

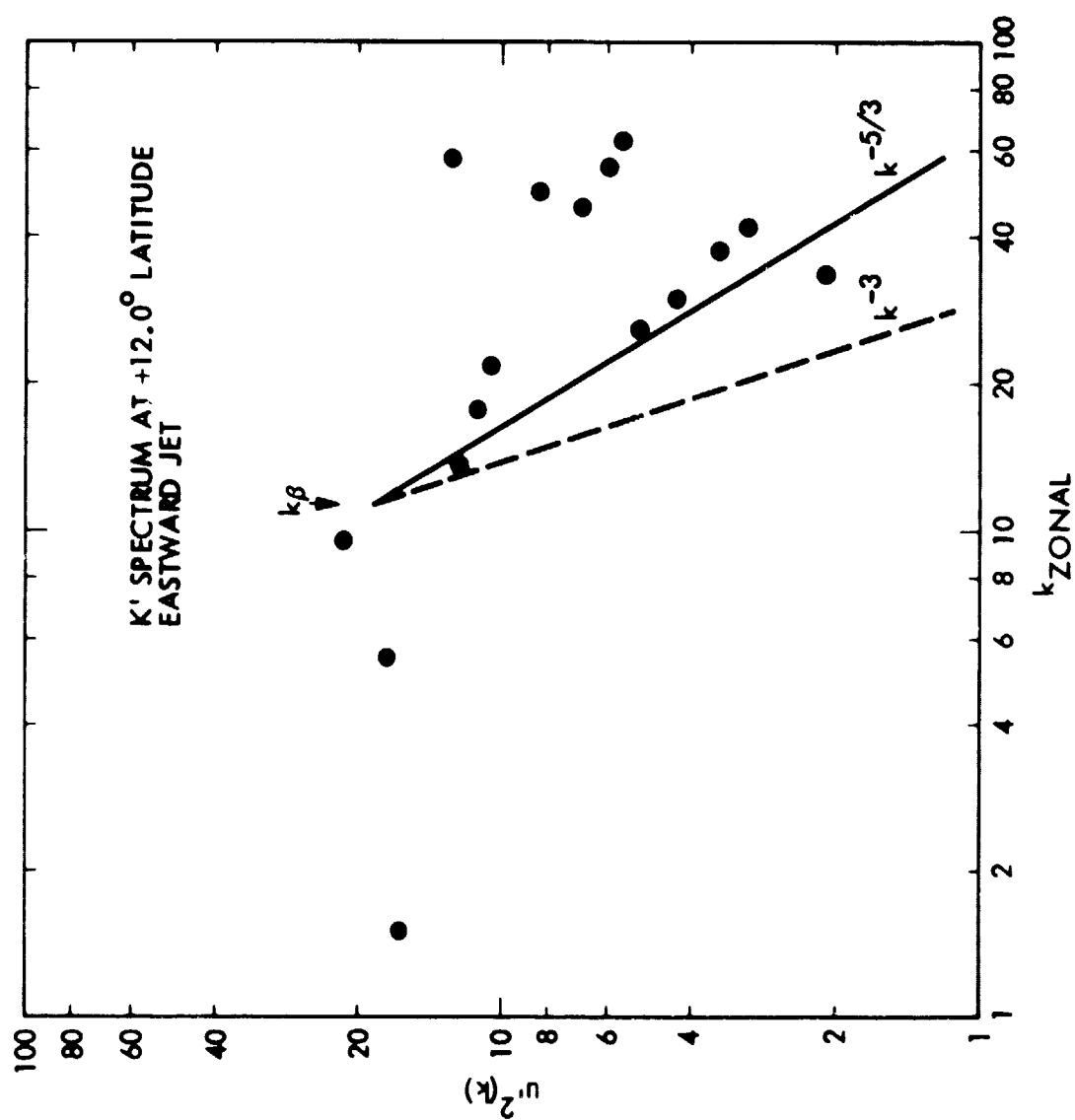


Figure 3.10. Smoothed turbulent kinetic energy power spectrum
 $(u'^2(k))$ of the southern edge of the equatorial
jet at $-12^{\circ}0$ latitude.

ORIGINAL PAGE IS
OF POOR QUALITY

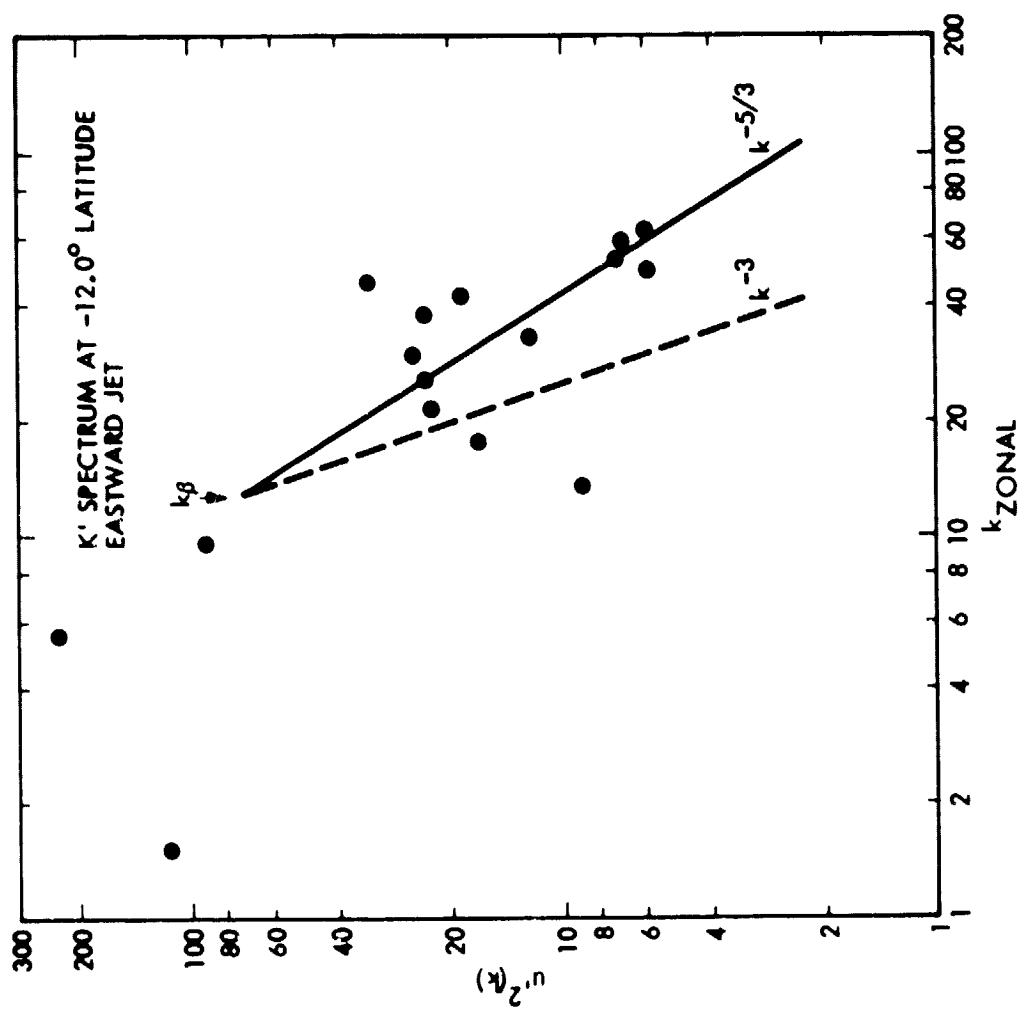


Figure 3.11. Smoothed turbulent kinetic energy power spectrum
 $(u'^2(k))$ of the westward jet at $-19^{\circ}5$ latitude.
It is this jet which runs over the northern edge
of the Great Red Spot.

ORIGINAL PAGE IS
OF PCOR QUALITY

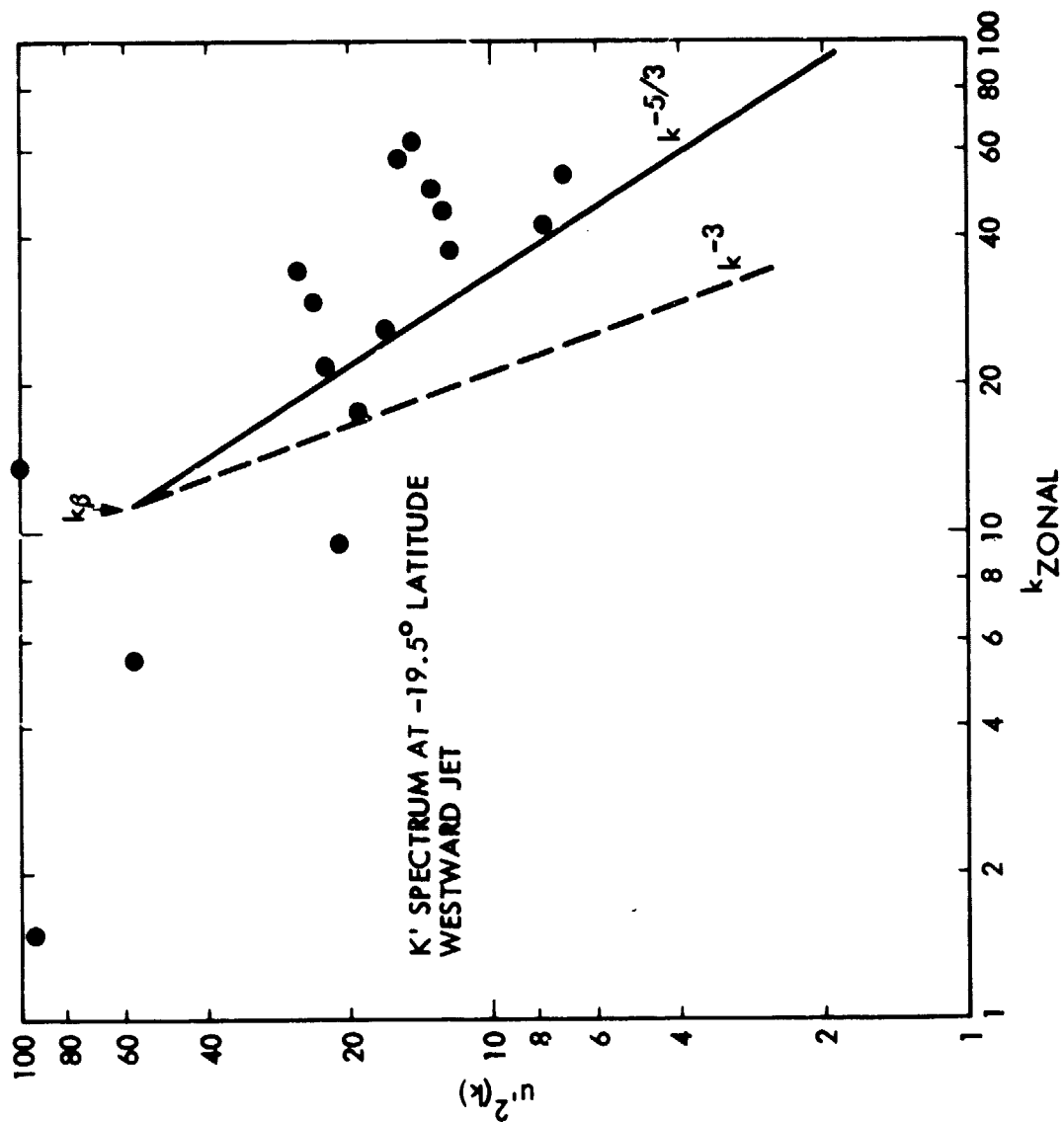


Figure 3.12. Smoothed turbulent kinetic energy power spectrum
 $(u'^2(k))$ of the eastward jet at $-27^{\circ}5$ latitude.

ORIGINAL PAGE IS
OF POOR QUALITY

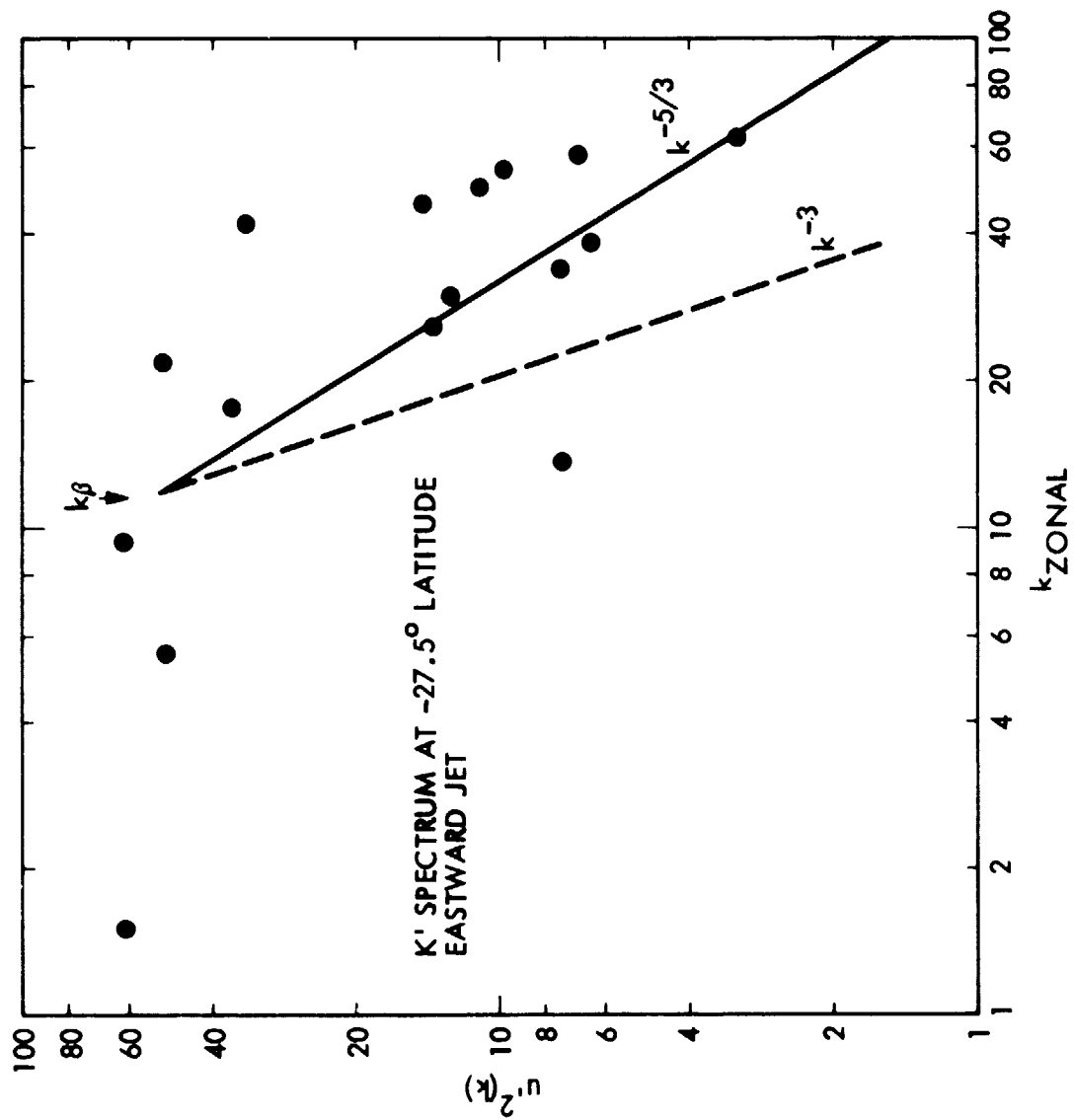


Figure 3.13. Smoothed turbulent kinetic energy power spectrum
 $(u'^2(k))$ of the westward jet at $-32^{\circ}5$ latitude.
It is this jet which runs over the northern edge
of the White Ovals.

ORIGINAL PAGE IS
OF POOR QUALITY

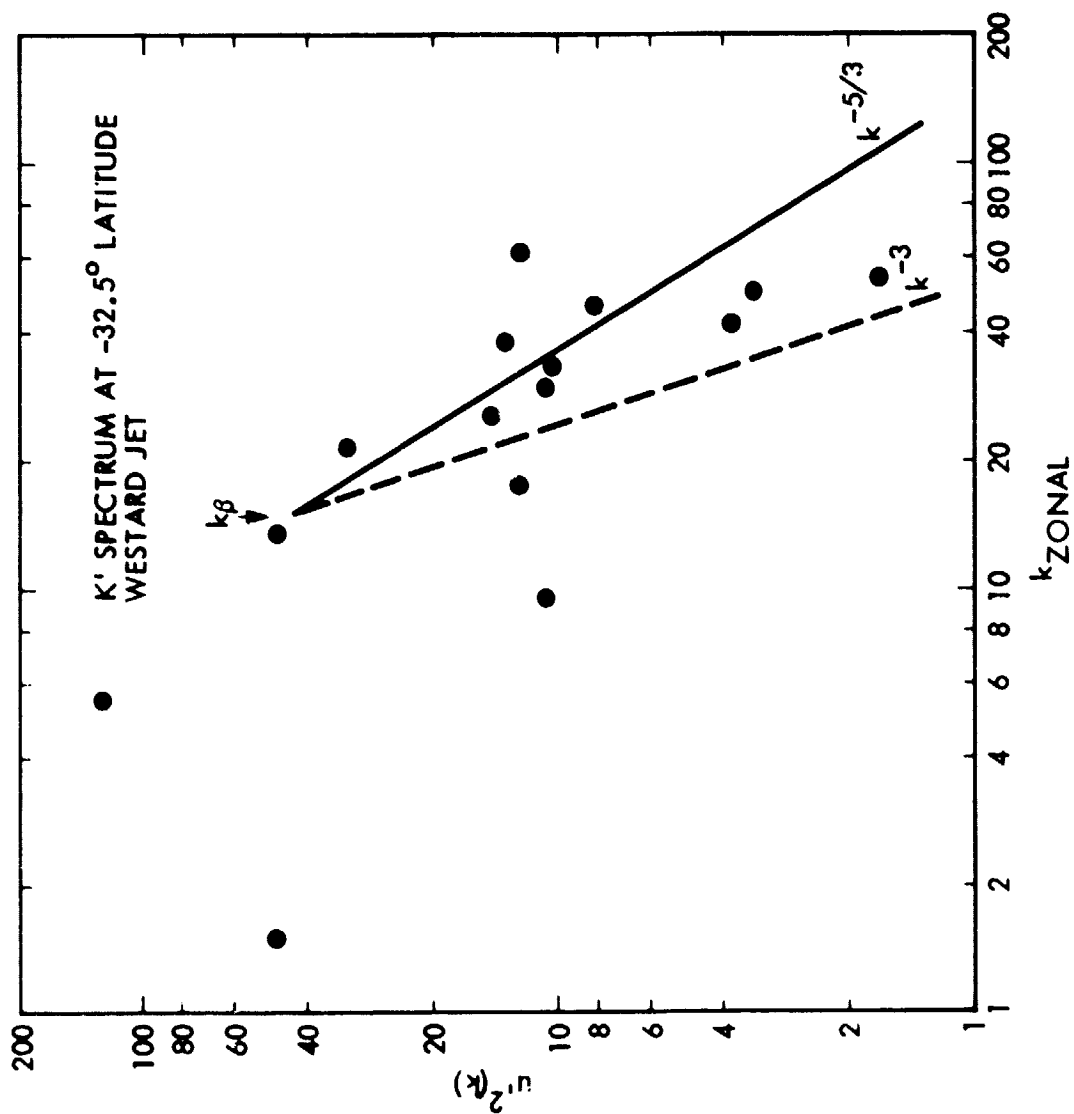


Figure 3.14. Smoothed turbulent kinetic energy power spectrum
($u'^2(k)$) of the eastward jet at -37.5° latitude.
This jet displays one of the best examples of a
 $k^{-5/3}$ power law.

ORIGINAL PAGE IS
OF POOR QUALITY

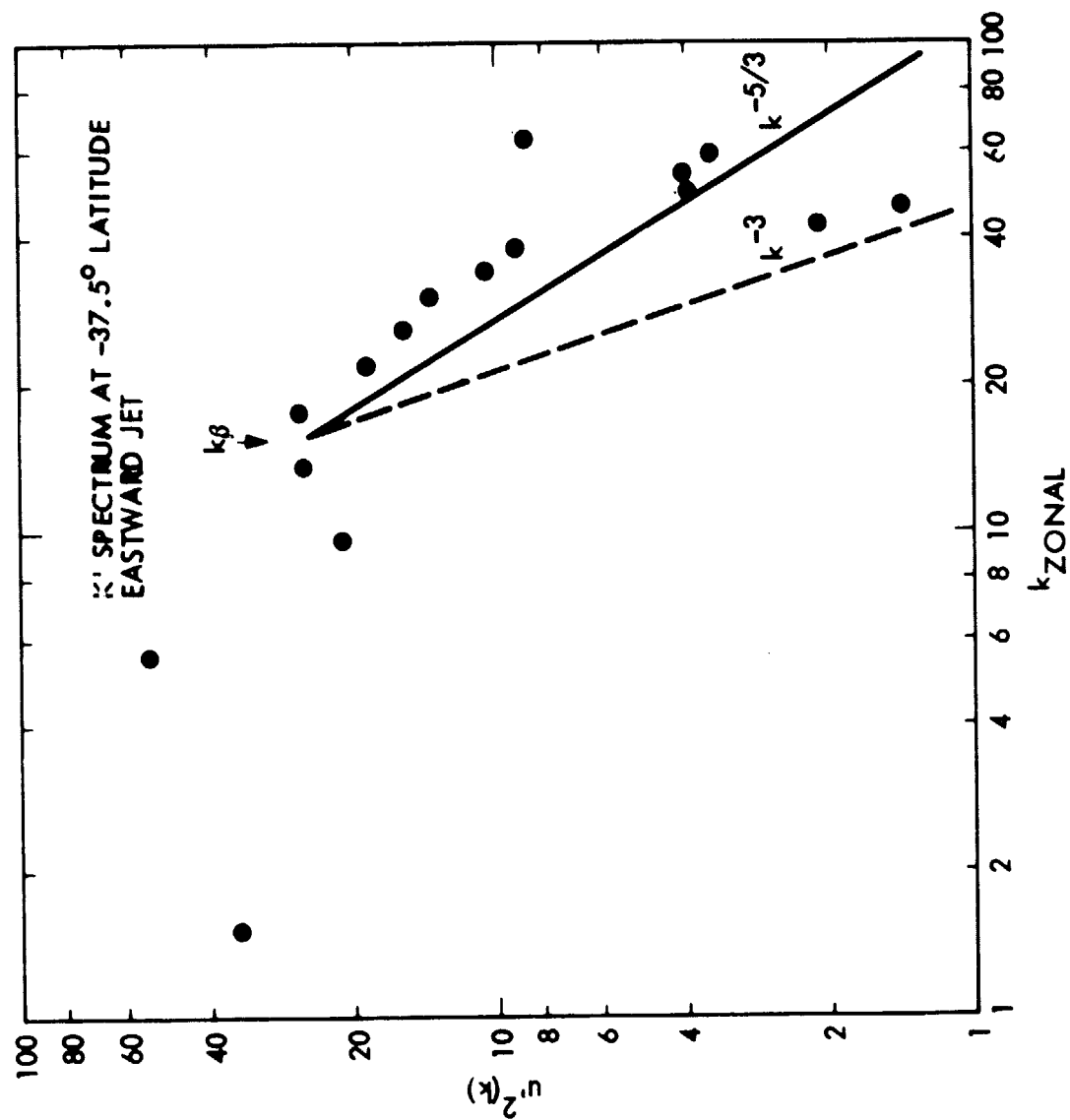
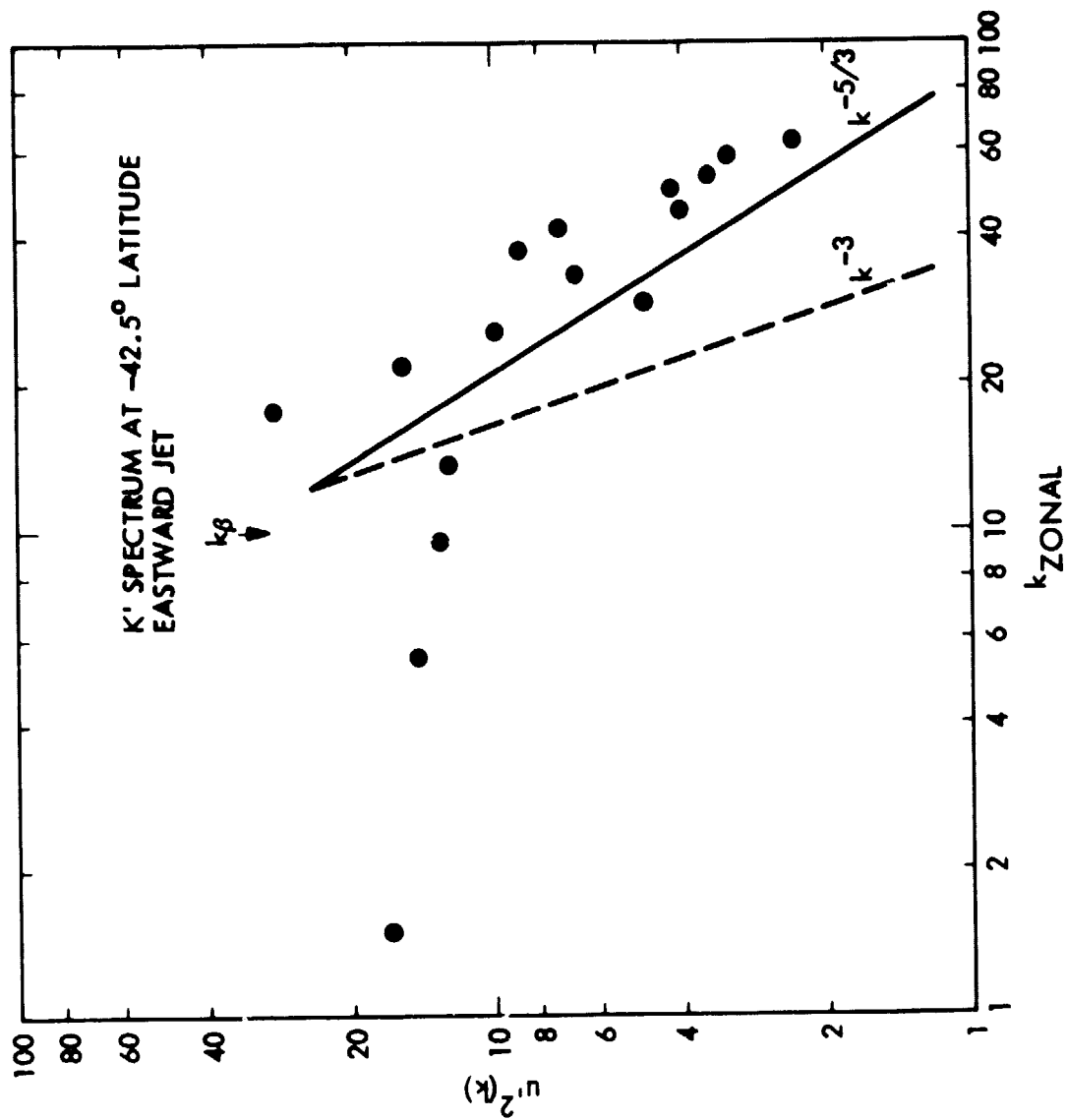


Figure 3.15. Smoothed turbulent kinetic energy power spectrum $(u'^2(k))$ of the eastward jet at $-42^{\circ}5$ latitude. Note the greatly diminished slope of the spectral profile in the Rossby wave propagation region $(k < k_g)$.

ORIGINAL PAGE IS
OF POOR QUALITY



Hence, the wavelength of maximum baroclinic instability is shorter than the resolution of our Fourier analysis. This is likely to have two effects:

- a) If the turbulence is baroclinically driven (i.e., forced at wavenumbers near k_D) our spectral analysis lies in the larger scale energy-transfer subrange for 2-dimensional turbulence. On this basis we might anticipate a $k^{-5/3}$ power law to hold with an up-gradient energy transport.
- b) A peak in $K'(k)$ near k_D could lead to substantial aliasing of our spectral profile leading to upturning of the high frequency end of the spectra.

In Chapter 2 we have verified that the turbulent transfer of kinetic energy proceeds toward increasingly longer wavelengths. As such a reverse cascade does not occur in truly isotropic 3-dimensional turbulence, we conclude that the observed large-scale turbulence must be 2-dimensional (i.e., obeys a potential vorticity equation of the form of Equation 3.1). In the terrestrial troposphere this 2-dimensional nature of large-scale turbulence leads to a k^{-3} power law. This is because terrestrial geostrophic turbulence occurs in the vorticity-transfer subrange (i.e., at wavenumbers higher than k_D). Jovian large-scale turbulence lies in a different regime ($k < k_E \stackrel{?}{=} k_D$),

and we expect the spectrum to obey a $k^{-5/3}$ power law down to wavenumbers ($k = k_g$) associated with the Rhines radius.

It is extremely difficult to discriminate between a k^{-3} and $k^{-5/3}$ power law. However, we have plotted both slopes on each of Figures 3.3 through 3.15. The left end of the linear slopes has been made to coincide with the peak observed in most cases near the Rhines wavenumber (k_g). A careful examination of Figures 3.3 through 3.15 provides us with a fairly firm conviction that the $k^{-5/3}$ power law is indeed being obeyed.

Based upon Equation 3.12 we compute the Rhines wavenumber (k_g) within each jet, where U is taken as the mean zonal velocity within the 5° width of the zonal strip centered on the jet, and mark k_g in each of the spectra presented in Figures 3.3 through 3.15. In many cases we do indeed observe a maximum in $u'^2(k)$ near k_g as predicted by the so-called Rhines effect. In other cases, such as in the eastward jet at $+35.5^\circ$ latitude (see Figure 3.5), $u'^2(k)$ increases down to the scale of the mean flow as anticipated for the barotropically stable end state predicted by Williams (1979b).

In order to demonstrate a statistical significance to our slope analysis we must first demonstrate that $\log(u'^2)$ (taken as dependent variable) and $\log(k)$ (taken as independent variable) possess any meaningful linear correlation. Columns 3 through 6 of Table 3.2 presents the results of linear least squares fits to the form,

$$\log u'^2 = A (\log k) + B . \quad (3.15)$$

Table 3.2. Linear Least Squares Fits to Jet Spectra

Jet Latitude	N	A	B	σ^2	r
-42°5	13	-1.3174	2.8378	0.0018	-0.8811
-37°5	12	-1.6862	3.4841	0.0063	-0.7481
-32°5	12	-1.2609	2.8858	0.0065	-0.6406
-27°5	13	-0.7289	2.2010	0.0078	-0.4440
-19°5	13	-1.0256	2.8059	0.0032	-0.7373
-12°0	13	-0.5182	1.9281	0.0055	-0.3874
+12°0	13	-0.3391	1.3093	0.0047	-0.2838
+17°5	12	-0.1536	1.2763	0.0039	-0.1293
+23°5	14	-1.0069	3.3414	0.0024	-0.8189
+31°5	13	-0.8077	2.0107	0.0021	-0.7350
+35°5	13	-0.9603	2.0576	0.0052	-0.6242
+39°5	12	-1.0874	2.0732	0.0062	-0.5908
+44°5	6	-1.2840	2.3991	0.0094	-0.3638

The four point smoothed data displayed in Figures 3.3 through 3.15 were used for this analysis. The number of degrees of freedom within each jet spectrum is assumed to be $N-2$, where N is the number of smoothed data points for wavenumbers greater than k_g . Wavenumbers less than k_g were excluded from this analysis. The square of the standard deviation is estimated according to,

$$\sigma^2 = \frac{1}{N-2} \sum_{i=1}^N (y_i - A - Bx_i)^2 \quad (3.16)$$

where,

$$\begin{aligned} y_i &= \log(u'^2) \quad \text{at } k = k_i \\ x_i &= \log(k) \quad \text{at } k = k_i. \end{aligned}$$

For 10 degrees of freedom a linear correlation (r) of 0.242 indicates a meaningful linear correlation at the 50% probability level, while $r = 0.549$ indicates a meaningful linear correlation at the 90% level. For most of the jets in our analysis a linear relation between $\log(u'^2)$ and $\log(k)$ is meaningful at better than the 90% confidence level.

The average slope (A) associated with the fits of Table 3.2 is $A = -0.9366$. This corresponds to a power law which decays like $k^{-0.9366}$. There is no turbulent process which yields a power law with decay slower than $k^{-5/3}$. Hence, we might question whether the difference between $A = -0.9366$ and $A = -5/3$ is statistically meaningful in our least squares analysis.

Table 3.3 presents the results of constrained least squares fits to the four point smoothed data for $k > k_p$. For the first fit the slope is constrained to be $A = -5/3$, while for the second fit $A = -3$. In each case only the value of B is allowed to vary. Values of B in Table 3.3 are those giving the best least squares fit with constrained slopes. Again, the standard deviation of the fits is estimated using Equation 3.16. As anticipated values of σ^2 for the $A = -5/3$ fit are substantially smaller than those for the $A = -3$ fit.

We can estimate the uncertainty on the value of A associated with the unconstrained fits of Table 3.2 according to a standard deviation for the slope given by,

$$\sigma_A^2 = \frac{\sigma^2}{\Delta} \sum x_i^2 \quad (3.17)$$

where, σ = standard deviation of unconstrained fits

$$\Delta = N \sum x_i^2 - (\sum x_i)^2.$$

The estimated value of σ_A^2 is displayed as the second column of Table 3.3. Note that the slope of the unconstrained linear fits seems to diminish at latitudes near the equator. The constrained $A = -5/3$ fits nearly duplicate the unconstrained fits at temperate latitudes. Actually, for the jets at -37.5 and $+44.5$ there is no significant difference between the unconstrained fit and the constrained $A = -5/3$ fit, i.e., $-5/3$ lies within the range $A \pm \sigma_A^2$. We conclude that there is little significant difference between the actual unconstrained fits and the constrained fit for $A = -5/3$ at temperate latitudes. On the other

Table 3.3. Linear Least Squares Fits with Constrained Slopes

Jet Latitude	σ_A^2	A	B	σ^2	A	B	σ^2
-42.5	0.0035	-5/3	3.3728	0.0022	-3	5.4153	0.0120
-37.5	0.0186		3.4535	0.0063		5.5406	0.0112
-32.5	0.0192		3.5210	0.0069		5.6082	0.0150
-27.5	0.0152		3.6376	0.0109		5.6801	0.0263
-19.5	0.0062		3.7880	0.0047		5.8305	0.0172
-12.0	0.0007		3.6874	0.0102		5.7299	0.0276
+12.0	0.0091		3.3429	0.0111		5.3855	0.0302
+17.5	0.0115		3.6448	0.0104		5.7319	0.0268
+23.5	0.0030		4.3258	0.0045		6.3151	0.0214
+31.5	0.0041		3.3266	0.0046		5.3691	0.0193
+35.5	0.0101		3.1397	0.0070		5.1822	0.0201
+39.5	0.0183		2.9800	0.0072		5.0671	0.0166
+44.5	0.4500		3.0524	0.0095		5.3288	0.0120

hand, the slope $A = -3$ lies far outside the range of uncertainty in the least squares slope.

The geostrophic constraints, which are responsible for the characteristic 2-dimensional nature of the large-scale turbulence, breakdown near the equator. We might use this tropical departure to explain the breakdown of the $k^{-5/3}$ power law near the equator; however, we have already remarked that these are no turbulent processes which produce a spectrum flatter than $k^{-5/3}$. We suspect two causes for the flatness of the observed spectra:

- a) white noise associated with measurement errors in u'
- b) aliasing from scales unresolved in our analysis.

The former tends to flatten the spectrum more or less uniformly, while the latter would tend to flatten the spectrum near the Nyquist frequency or even cause the high frequency end of the spectrum to turn upward. A very preliminary analysis seems to indicate that in most jets the spectrum is more or less uniformly flatter than a $k^{-5/3}$ profile. In a few cases, however, the overall linear fits worsen with increasing wavenumber (see Figure 3.9 illustrating the spectrum at $+12.0^\circ$ latitude) as we might expect for an aliased spectrum. Such aliasing could be due not only to the presence of baroclinically driven eddies but to wave induced CISK instabilities in Jupiter's tropics as suggested by Maxworthy (1975).

This spectral analysis of the large-scale turbulent motions visible in our world map data set is preliminary. Future work should be carried out to:

- a) use a more strictly applicable periodogram analysis on the unevenly sampled data
- b) definitively establish a statistically more meaningful fit to the $k^{-5/3}$ power law than to the k^{-3} power law
- c) examine the nature of the turbulent spectrum near L_D by using velocity measurements with higher spatial resolution
- d) study the impact on the $K'(k)$ profile of energy input by upward propagating waves so that this forcing mechanism can be contrasted with baroclinicity. Spectral analysis is capable of detecting the signature of wave forcing as suggested by Maxworthy (1975) (see Zangvil and Yanai, 1980).

Nevertheless, we feel that our spectral analysis probably demonstrates the existence of the $k^{-5/3}$, up-gradient energy-transfer subrange of Kraichnan (1967) in a large-scale atmospheric system. As well, the Rhines effect does indeed appear to manifest itself in Jupiter's atmosphere.

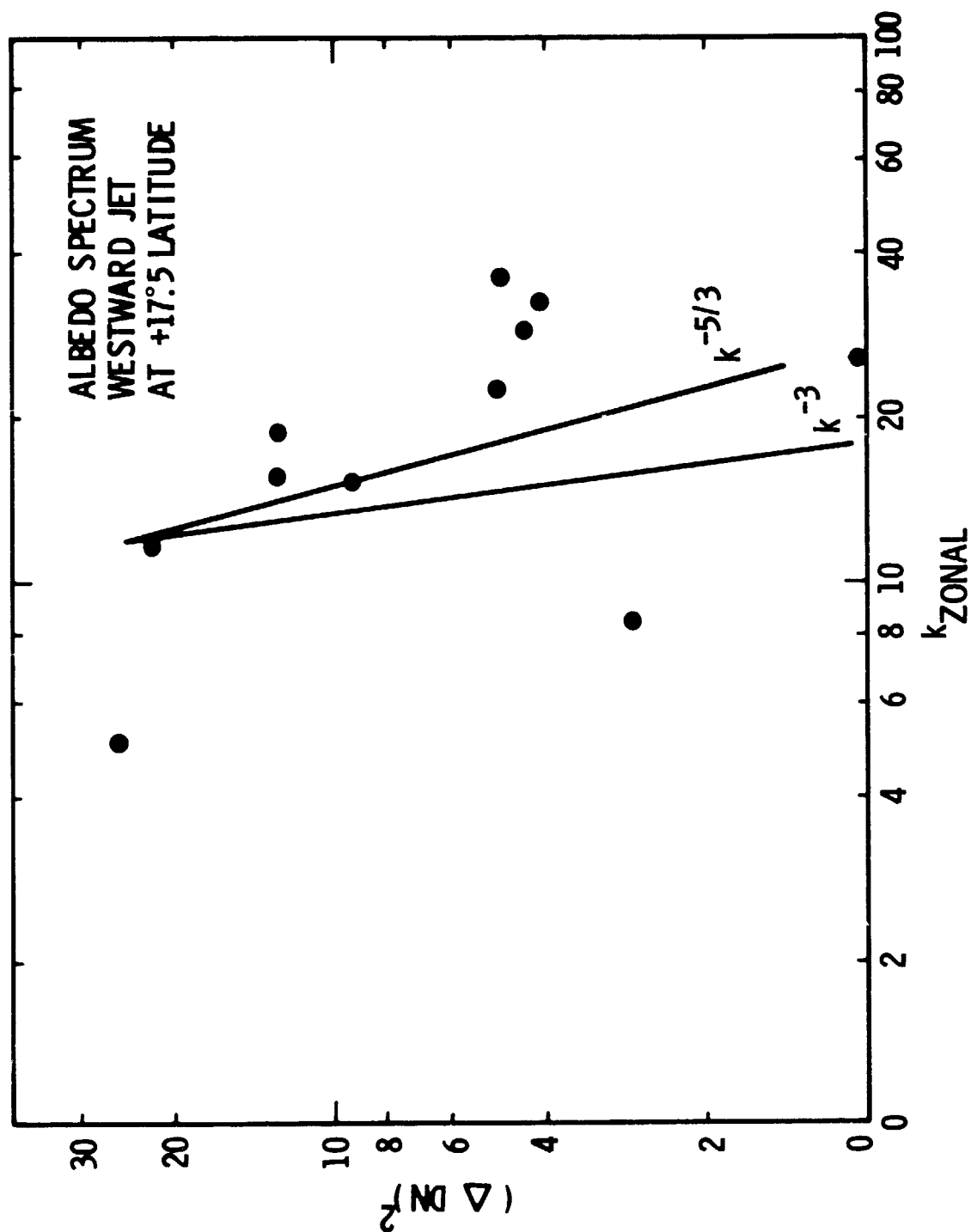
We note that the results of the analysis are consistent with the notion that the observed turbulence is baroclinically forced with energy being transferred upgradient to smaller wavenumbers. We might even speculate that the larger turbulent energy transports observed in Jupiter's atmosphere as compared with Earth's may well be due to the wide range of Jovian eddy scales available to carry out this transport ($k_B < k < k_D$) contrasted with the very limit range of available scales in Earth's troposphere (where $k_B \approx k_D$). The vast expanse of the energy-transfer band of wavenumbers could then effectively isolate the mean zonal flow from variable activity on the baro-

clinic scale with short time constants (i.e., much shorter than the 100 day spin-up period for the mean flow). Produced might be a remarkably steady large-scale mean flow driven by highly variable processes occurring on a much smaller scale.

In closing we point out, as suggested by Williams (1979b), the spectral profile should be evident in the easily observed albedo field of the Jovian cloudtops. Indeed, a longitudinal Fourier analysis of the digitized albedo field of a global mosaic of Jupiter (shown as Figure 3.16) is in accord with our suspected $k^{-5/3}$ power law. Should baroclinicity play a dominant role in driving the cloudtop motions we would expect the albedo field of the cloudtops to become much flatter for scales less than the deformation radius. The fact that this is not always the case (e.g., small features in the South Tropical Zone) may be indicative of mesoscale convection.

Figure 3.16. Albedo power spectrum of the westward jet at +17°5 latitude. The ordinate axis plots a measure of contrast or $(\Delta DN)^2$ where ΔDN is the change from the mean in contrast Digital Number (DN) which codes each of the gray levels in a Voyager image. A global mosaic of 5 narrow-angle frames taken through a green filter were used in the analysis.

ORIGINAL PAGE IS
OF POOR QUALITY



CHAPTER 4. KINEMATICS AND ENERGETICS OF THE GREAT RED SPOT

We turn our attention toward the largest single eddy in the Jovian atmosphere (and for that matter the largest single known eddy in nature) and pose many of the same questions as in the preceding chapters; namely, what is the nature of the flow field of the Great Red Spot (GRS) and what may we subsequently infer about the energetics of this single, large-scale eddy? Both the Great Red Spot and the smaller White Ovals represent eddies of a length scale comparable to the Rhines radius. Therefore, it will be interesting to compare the results of an energy analysis for these Rossby wave-scale eddies with the global analysis which indicated mixing lengths for the up-gradient momentum transport of 10^2 to 10^3 km.

4.1 Introduction

The earliest existing reference to the GRS may well be recorded in Volume 1 (No. 1) of the Philosophical Transactions of the Royal Society of London as a very brief note describing a telescopic observation made by Robert Hooke who "with an excellent twelve-foot telescope observed . . . on the 9th of May, 1664 . . . a small spot in the biggest of the three obscurer belts of Jupiter." There is no way of being certain that this spot, which came to be known as "Hooke's Spot" was in fact the Great Red Spot. Hooke's spot was observed over the next decade by Cassini at the Paris Observatory, but by 1715 had faded from the records and apparently from telescopic view. A feature, which in

description resembles the GRS is mentioned in the literature rather sporadically throughout the 19th Century, including one interesting observation by the Reverend "Hawkeye" Dawes. More or less continuous observational records of the Great Red Spot (or at least the so-called Red Spot Hollow, as the embayment of the South Equatorial Belt caused by the GRS is known) date from late 1878 at which time the GRS seems to have achieved prominence. It has, however, been suggested that the coincidence of this date with the introduction of the first good all reflective telescopes free from chromatic aberrations is more than casual (Reebe, private communication, 1981). In 1882 the GRS began to fade, a waning which was arrested by 1891. However, it is noteworthy that since the late 19th Century the longitudinal extent of the GRS has shrunk monotonically from roughly 40,000 km to 25,000 km. Over the past century numerous records of the drift rate (i.e., phase speed), color, shape, and size of the GRS have been collected by astronomers, both amateur and professional. However, with the single exception of an observation by Reese and Smith (1968), little was known observationally about the nature of the GRS flow field.

The use of temporal sequences of Voyager images allows a detailed view of the flow field of the GRS. We shall base subsequent discussion upon four independent data sets, two taken by each of the Voyager spacecraft and summarized in Table 4.1. All except the data set designated as VGR 1 SET II represent measurements made on frames for which a simultaneously shuttered wide-angle frame was used to fit a map grid to the observed limb of the planet (in all cases the entire planet was visible in the wide-angle frame). The data set designated VGR 1

Table 4.1. Great Red Spot Data Sets

Data	Set	Frame Pairs (FDS Counts)	Spatial Resolution (km/Line Pair)	Time Separation (Hours)	Velocity Resolution (m/sec)
VGR 1	SET I	16268.03 16280.28	95	9.80	3
		16268.03 16280.33	95	9.84	3
		16265.58 16280.28	96	11.76	2
VGR 1	SET II	16341.37 16353.42	43	9.64	1
		16341.45 16353.34	41	9.51	1
		16341.49 16353.30	42	9.45	1
		16341.49 16353.42	42	9.54	1
		16366.12 16366.48	23	0.29	22
		16366.12 16367.00	23	0.70	9
		16367.12 16367.52	23	0.32	20
VGR 2	SET I	20480.09 20492.39	110	9.84	3
VGR 2	SET II	20505.06 20517.32	96	9.81	3
		20517.32 20529.41	90	9.67	3

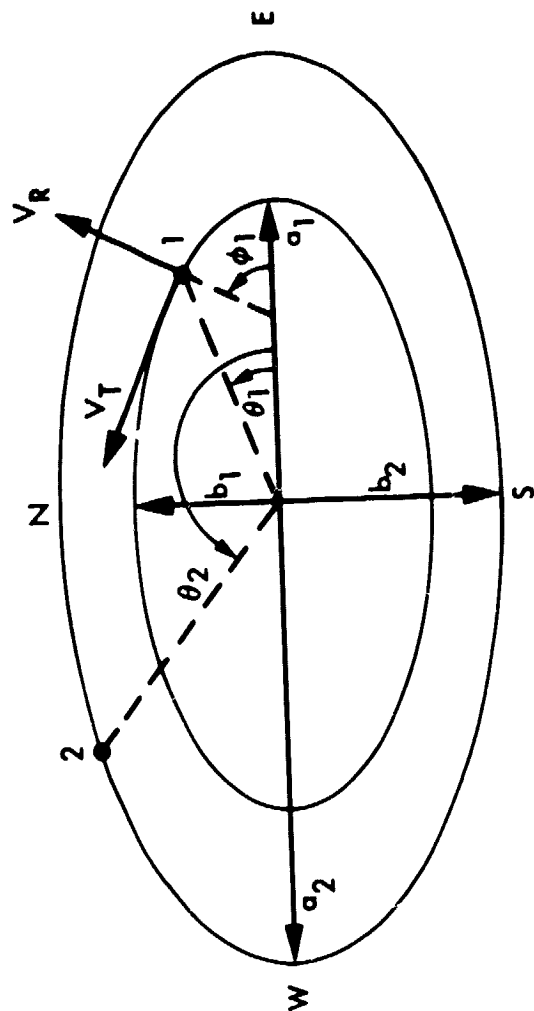
SET II represents the superposition of measurements made on two separate sets of frame pairs: one pair consisting of frames from a 3 x 3 and 3 x 4 narrow-angle frame mosaic of the GRS with a time separation of 9.5 hours and the second pair consisting of frames taken during the Jovian rotation following the 3 x 4 mosaic and having a time separation of 0.5 hour. Only in the frames 16341.37, 16341.45, and 16341.49 was the limb of the planet visible in simultaneously shuttered wide-angle frames. In all later frames the Jovian limb was not visible in the associated wide-angle frame, hence these later narrow-angle frames were essentially "blind." In such a case the AMOS program may be used in a "tiepoint transfer" or "relative navigation" mode, which in this case worked as follows: a frame pair was set up consisting of one frame from the 3 x 3 mosaic and a frame of the GRS taken one rotation before. This pair had accompanying simultaneously shuttered wide-angle frames, hence map grids could be fit to each frame. Several tiepoints were measured in this pair. These tiepoints were then identified in subsequent narrow-angle frames in the 3 x 4 mosaic and were assigned the same velocity as measured in the earlier pair, i.e., the tiepoint was "transferred" to the new frames. The underlying assumption is, of course, that the transferred tiepoint is not undergoing an acceleration, a rather unrealistic assumption for tiepoints in the GRS vortex. Following the transfer of several tiepoints (roughly 20) scattered more or less uniformly across the frame, the logic of the AMOS program is reversed so that the transferred tiepoint coordinates and associated velocities are used as input for the computation of the navigational parameters necessary to fit a map grid to the "blind" frame(s). Fine

tuning of the navigational parameters may be accomplished by removing any unrealistic mean velocities or apparent "shifts" in the resulting flow field. Thus, the data set VGR 1 SET II is likely to have the greatest navigational error associated with it, offsetting the accuracy obtainable with frames of such high spatial resolution. Nevertheless, this data set is interesting as a comparison between present work and earlier collaborative work involving the author and summarized below.

4.2 The Velocity and Vorticity Field of the GRS

Mitchell et al. (1981) present a report on the highest spatial resolution kinematic data set obtained of the GRS and the White Oval BC (see nomenclature of Peek, 1958), i.e., the same data set for the GRS as that we designate VGR 1 SET II. Their approach is to superimpose over both the GRS and White Oval BC a coordinate system of concentric, equal eccentricity ellipses (see their Figure 3, reproduced here as Figure 4.1). The eccentricity is determined by the visual shape of the darker peripheral cloud collar surrounding both features. In the case of the GRS, they take a semi-major axis length (a) of 12.08×10^6 m and a semi-minor axis length (b) of 5.58×10^6 m, giving an eccentricity (ϵ) of 0.887. For the White Oval BC the corresponding dimensions are $a = 4.89 \times 10^6$ m, $b = 2.93 \times 10^6$ m, and $\epsilon = 0.801$. Thus, the position of each measured tiepoint is designated by the semi-major axis length (a) of the ellipse upon which it lies and the azimuthal angle (θ) measured counterclockwise from the eastern semi-major axis (not to be confused with planetographic latitude which we have previously represented by ϕ). We shall reference locations

Figure 4.1. Geometry of concentric ellipses used to define a coordinate system for specifying positions within the Great Red Spot (from Mitchell et al., 1981). The position of point 1 is specified by θ_1 , the angle measured counterclockwise from the eastern semi-major axis to the radius vector associated with point 1, and by a_1 , the semi-major axis length for that ellipse on which point 1 lies. There are no net eddy stresses associated with Mitchell et al.'s completely symmetric analysis.



PRECEDING PAGE BLANK NOT FILMED

within the GRS in this same coordinate system in our discussions. Their concentric ellipses are oriented with the major axis running exactly east-west and the minor axis running exactly north-south. The observed zonal (u) and meridional (v) velocity components of each tie-point are transformed into a velocity component tangential to the ellipse on which the tiepoint lies (V_T) and a component in the direction radially outward from the origin of the concentric ellipses (V_R), all related by the following expression:

$$V_T = -u \sin\phi + v \cos\phi \quad (4.1)$$

$$V_R = u \cos\phi + v \sin\phi \quad (4.2)$$

where,

$$\phi \equiv \tan^{-1} \left[\left(\frac{a}{b} \right)^2 \tan \theta \right]. \quad (4.3)$$

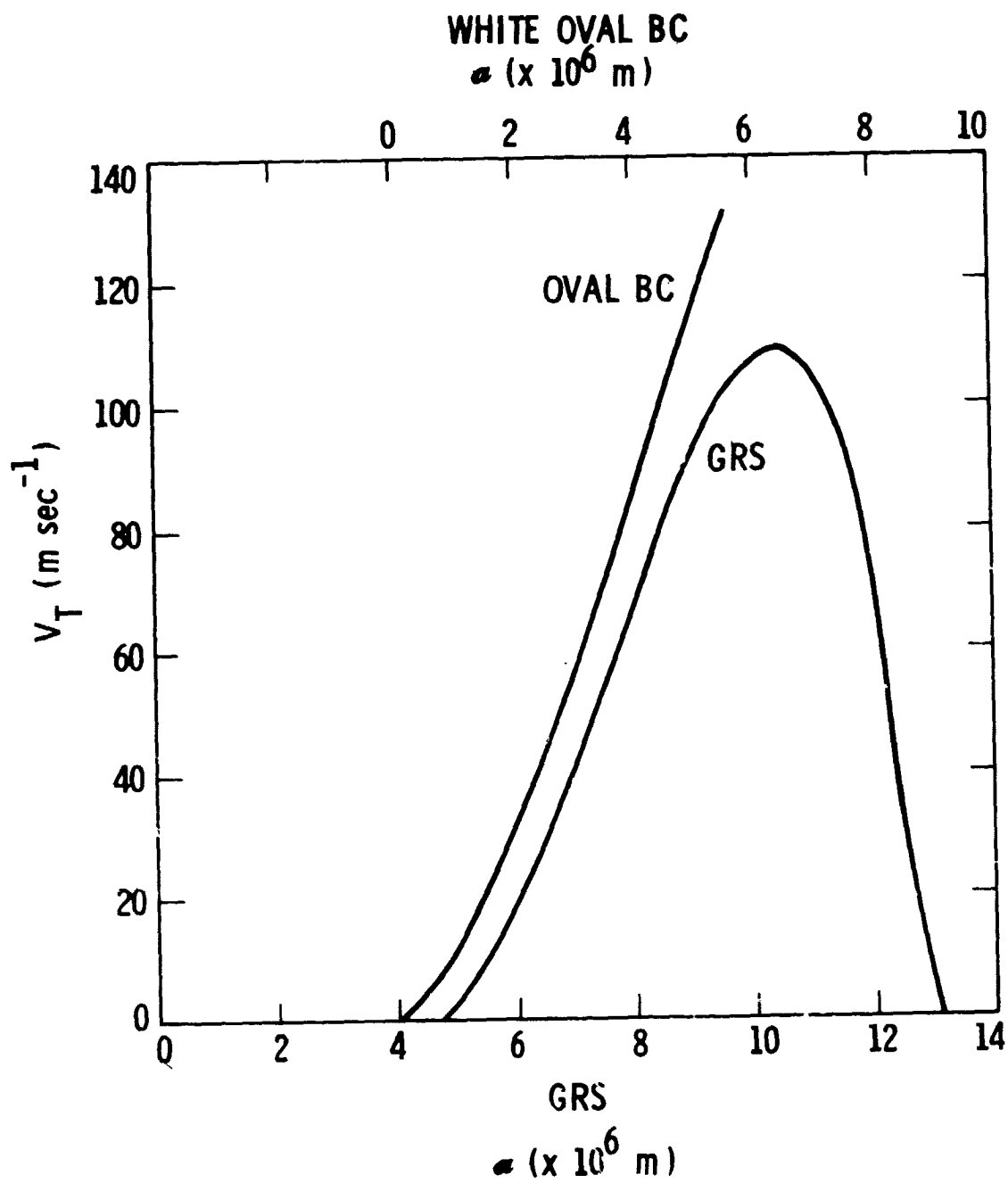
Noting that V_T does not seem to be strongly θ -dependent they least-squares fit the tangential velocity component to a polynomial function of (a) of the form:

$$V_T(a) = C_1 a + C_2 a^2 + C_3 a^3 + C_4 a^4. \quad (4.4)$$

In their discussion Mitchell et al. completely neglect the radial velocity component V_R , noting that it is quite small and possibly θ -dependent as well. Using their polynomial fit we plot $V_T(a)$ in Figure 4.2 which illustrates the striking similarity of V_T for the

Figure 4.2. Profiles of tangential velocity as a function of semi-major axis length within the Great Red Spot (GRS) and White Oval BC. Note the similarity in profiles for the outer portions of the GRS and for the White Oval.

ORIGINAL PAGE IS
OF POOR QUALITY



GRS from $a = 4.2 \times 10^6$ m outward and the White Oval BC. If the inner quiescent portion of the GRS were removed, the profiles of $V_R(a)$ would be nearly identical.

Under the assumption that $V_R \equiv 0$, the vertical component of the relative vorticity (ζ) of the flow along streamlines consisting of concentric ellipses is given by,

$$\zeta(a, \theta) = \frac{a}{b^2 n^3} V_T + \zeta \frac{dV_T}{da} \quad (4.5)$$

where,

$$n \equiv \left[\frac{\cos^2 \theta + \left(\frac{a}{b}\right)^4 \sin^2 \theta}{\cos^2 \theta + \left(\frac{a}{b}\right)^2 \sin^2 \theta} \right]^{1/2}$$

where,

$$b^2 n^3 / a = \text{radius of curvature of a streamline.}$$

For a detailed derivation of Equation (4.5) see the appendix to Mitchell et al. They plot $\zeta(a)$ for fixed values of θ (namely, $\theta = 0^\circ, 30^\circ, 90^\circ$) and note quite similar vorticity profiles for the GRS and White Oval BC (see their Figures 6 and 7). As they neglected the radial component V_R , they only mention that the divergence associated with the flow field is likely to be quite small and probably hidden in the measurement noise. Their flow field consisting of V_T as a simple function of r has no net divergence associated with it;

the convergent flow along the minor axis merely compensates for the divergent flow along the major axis.

We proceed to compare the fields of streamfunction, vorticity, and divergence for our four data sets. The computation of each of these quantities requires that our data field be smoothed, i.e., fit to a grid of evenly spaced points in x (zonal direction, positive eastward) and y (meridional direction, positive northward). This is done using the standard technique of an influence radius (r_i), that is, the value of any scalar quantity (e.g., the zonal and meridional wind component) at each uniform grid point is taken to be the weighted average of all measured values within a circular radius $r = r_i$ of the uniform grid point. All measured values within $r = r_i$ are weighted as $1/r^2$. Figures 4.3, 4.4, 4.5, and 4.6 show the flow field as actually measured for each of our data sets using the AMOS interactive system. Figure 4.7 illustrates an interpolated field of vorticity (units are 10^{-5} sec^{-1}) for the data set VGR2 Set I. Spacing of grid points was taken to be 0.5° in latitude ($\Delta y = 0.5^\circ$) and 3.0° in longitude ($\Delta x = 3.0^\circ$), in versions (a) of each data set and 0.5° in latitude ($\Delta y = 0.5^\circ$) with 1.5° in longitude ($\Delta x = 1.5^\circ$) in versions (b) of each data set. Such a rectangular grid spacing was used so as to preserve resolution in latitude, which is important in our later computations of energy transports, and at the same time produce a field which is not "over interpolated" (i.e., containing more grid points than actual data points). Though grid point spacing is specified in terms of equal intervals in degrees of latitude and longitude (which are not, of course, equal intervals of spatial distance x and y), the actual compu-

Figure 4.3. Plot of tiepoints comprising the GRS data set referred to as VGR1 Set I. As in Figures 4.4 through 4.6, latitudes are planetographic, while longitudes are measured in System III (1967.0), the conventional radio-defined system of longitude. Lengths of vectors are proportional to wind speed. Circles lie at initial observed positions of cloud tracers. Velocities interpolated to an evenly-spaced grid were used in our analysis of net eddy stress.

ORIGINAL PAGE IS
OF POOR QUALITY

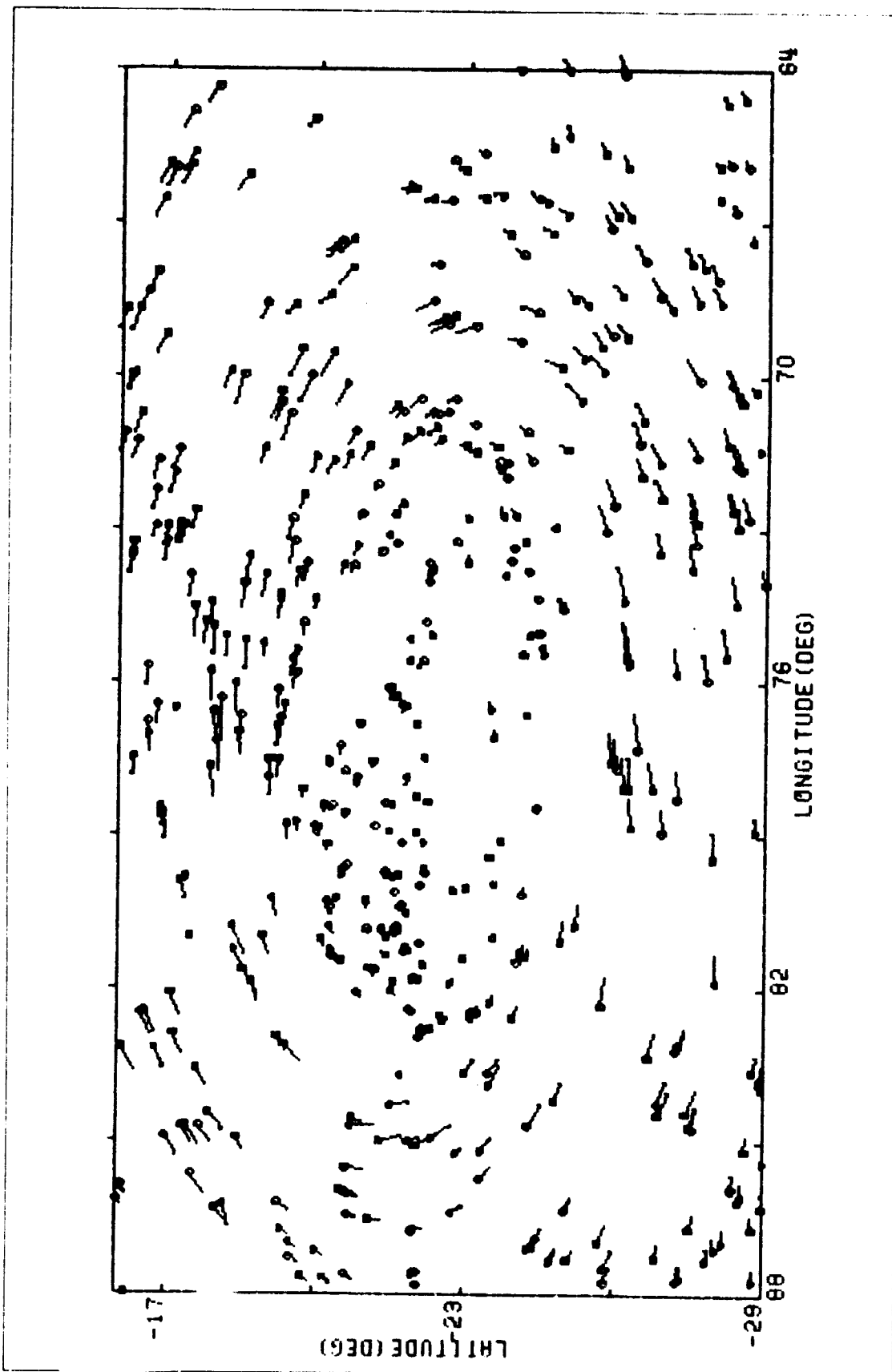


Figure 4.4. Plot of tiepoints comprising the GRS data set referred to as VGR1 Set II.

ORIGINAL PAGE 18
OF POOR QUALITY

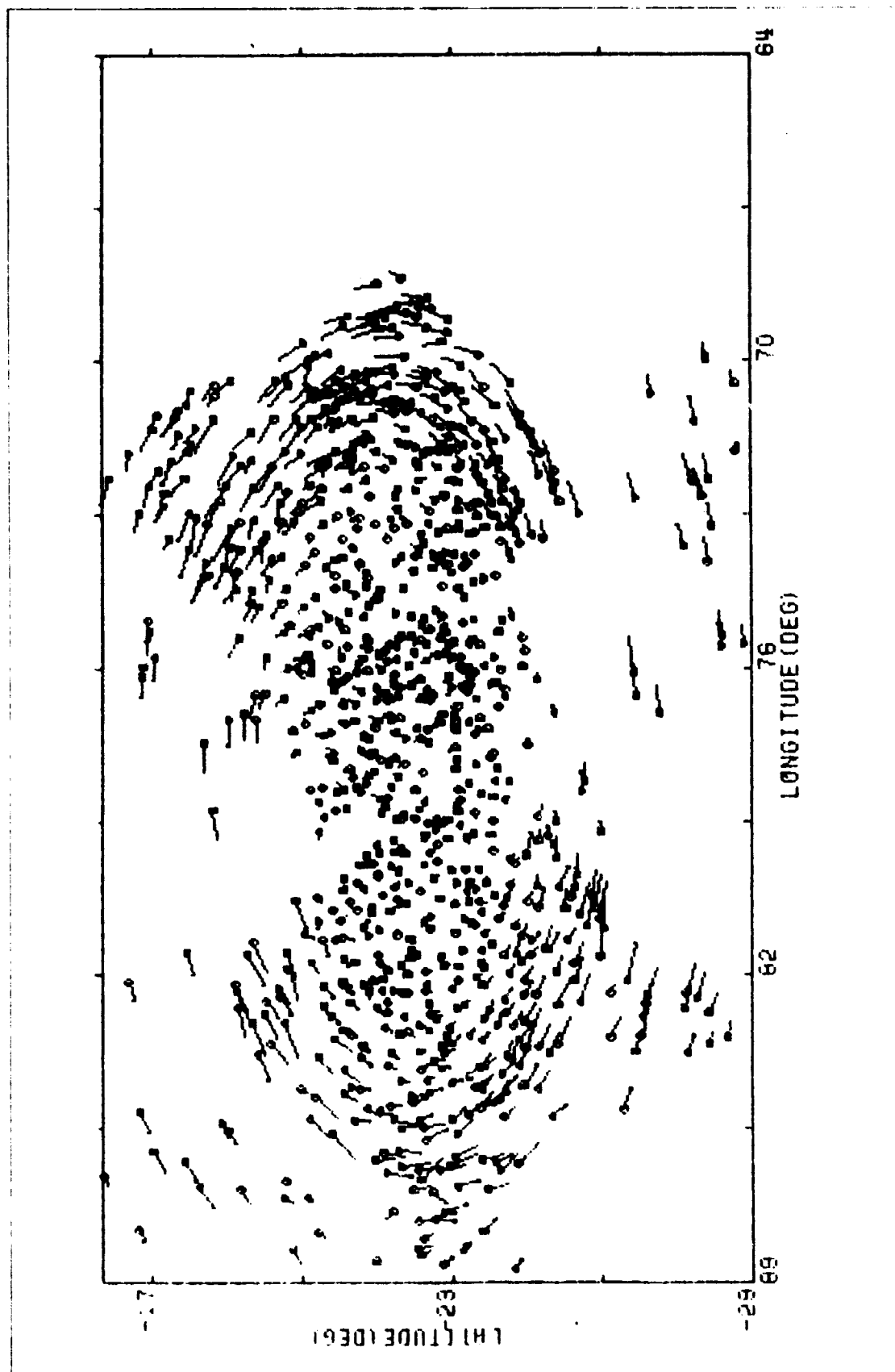


Figure 4.5. Plot of tiepoints comprising the GRS data set referred to as VGR2 Set I.

ORIGINAL PAGE IS
OF POOR QUALITY

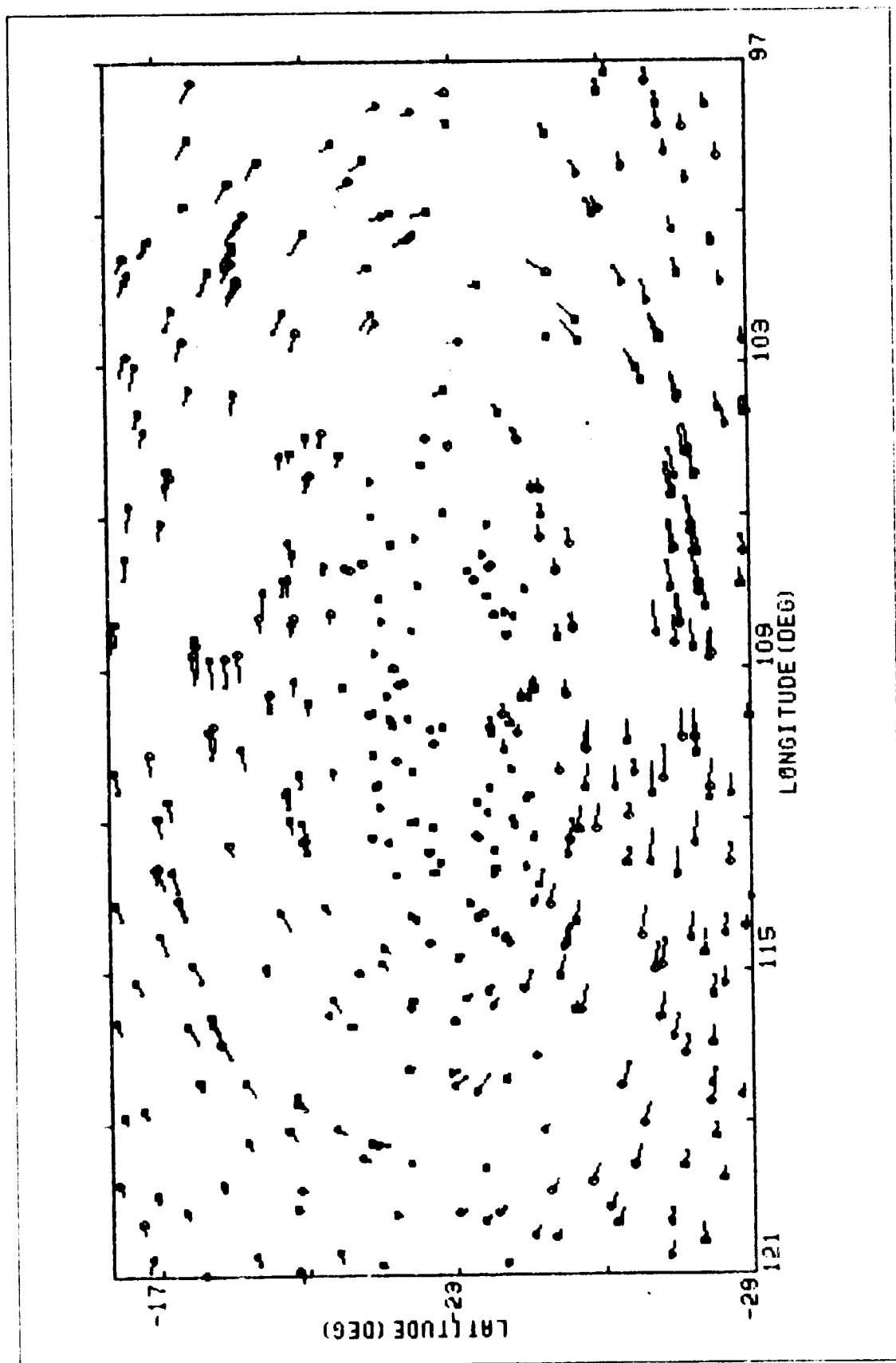


Figure 4.6. Plot of tiepoints comprising the GRS data set referred to as VGR2 Set II.

ORIGINAL PAGE 19
OF POOR QUALITY

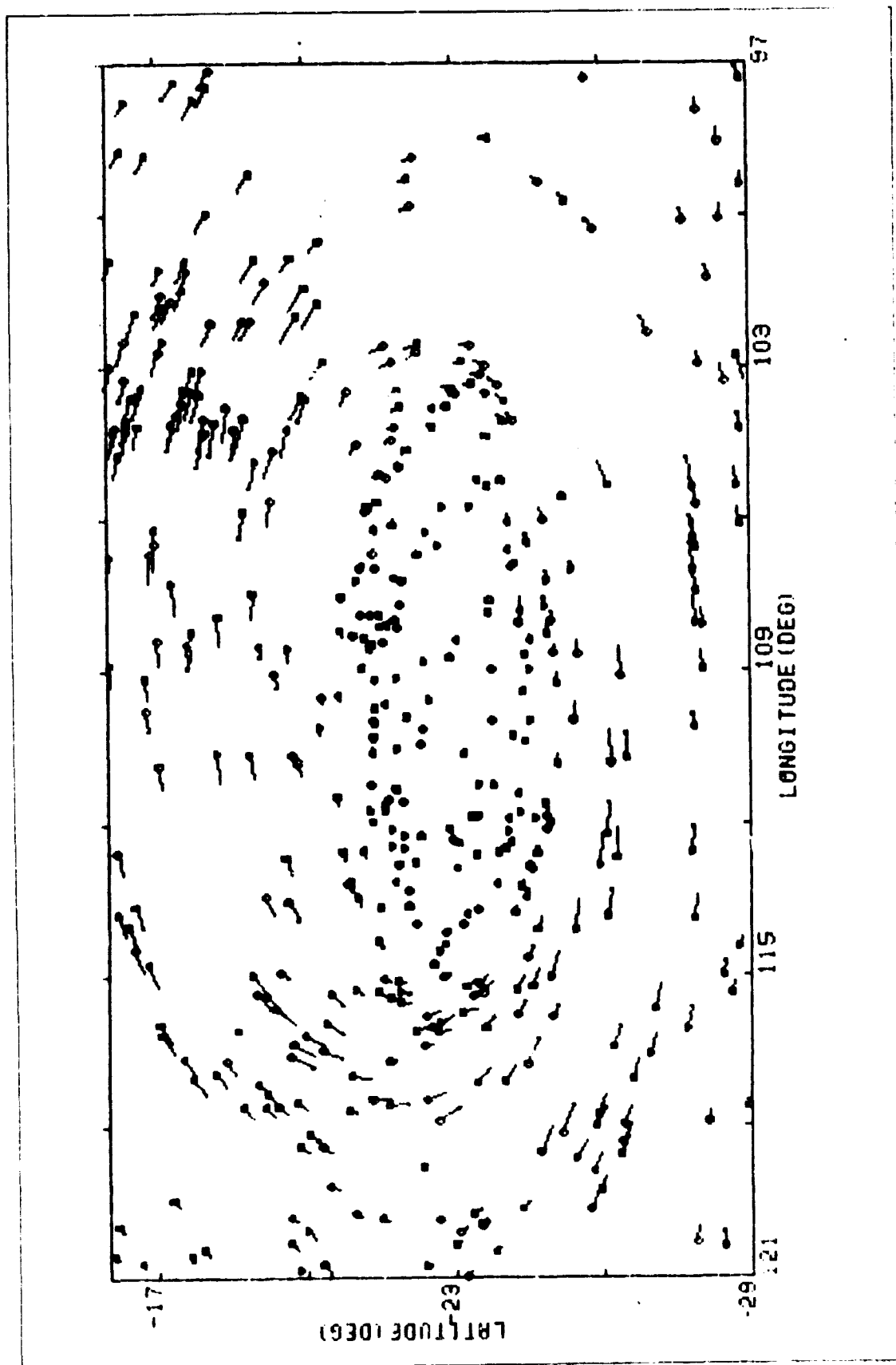
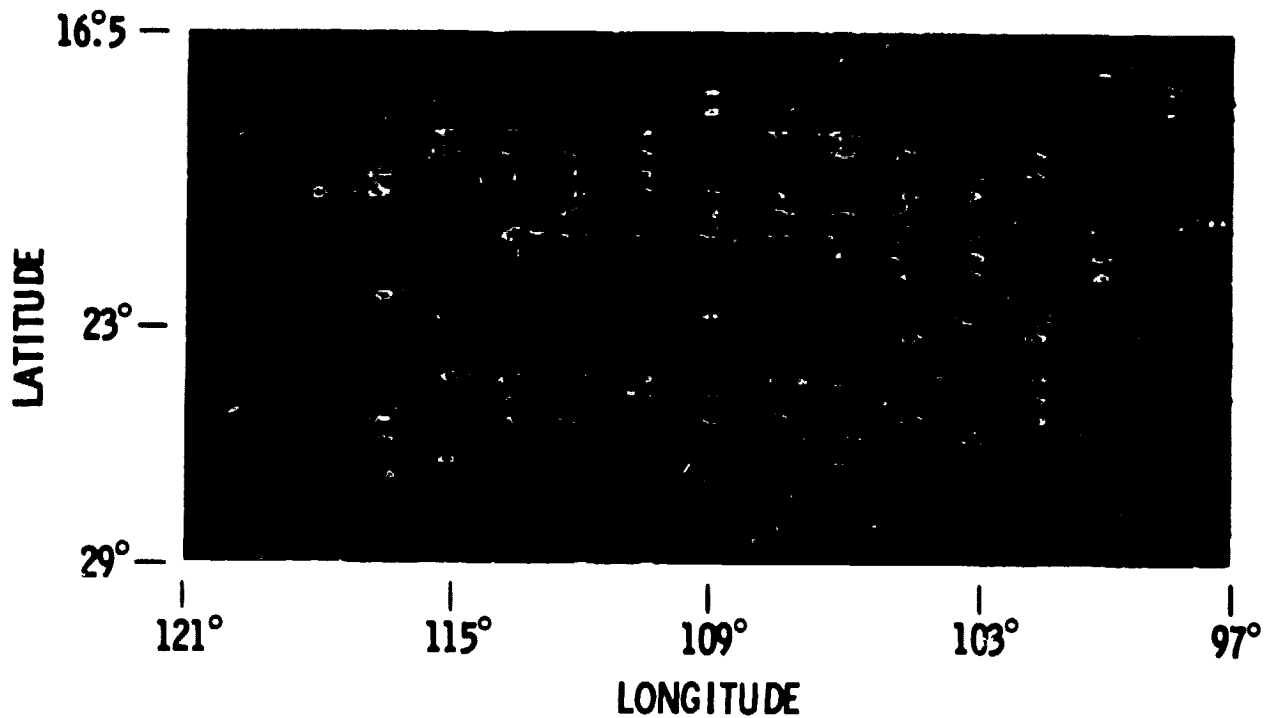


Figure 4.7. Relative vorticity contours computed from the interpolated GRS data set referred to as VGR2 Set I version (b). High level of noise results since relative vorticity is computed as the difference of two finite differenced shears.

ORIGINAL PAGE IS
OF POOR QUALITY



RELATIVE VORTICITY (ζ) CONTOURS

VGR 2 SET I

BRIGHTEST CONTOUR $\rightarrow \zeta = +8 \times 10^{-5} \text{ sec}^{-1}$

DARKEST CONTOUR $\rightarrow \zeta = -2 \times 10^{-5} \text{ sec}^{-1}$

tation of all flow quantities is performed correctly, the curvature of Jupiter having been taken into account. The details of each of our interpolation schemes are summarized in Table 4.2.

Note that the actual spacing of tiepoints (Figures 4.3 through 4.6) is quite uniform, as we would hope, though there is considerable difficulty in identifying tiepoint features in the diffuse and strongly sheared clouds in the outer-peripheral vortex at about $a = 6$ to 8×10^6 m. It is in fact the presence of this peripheral vortex which is the most obvious characteristic of the GRS flow field (see Figure 4.7), rendering a flow field quite unlike that of any terrestrial atmospheric vortex. Figure 4.8 shows the meridional profile of relative vorticity along the minor axis of the GRS, symmetrically averaged about the major axis at -22° latitude for comparison with Mitchell et al. Note that three of the data sets display profiles quite similar to that computed by Mitchell et al. as shown by the smooth curve. The fact that data set VGR 2 SET I seems to show a very atypical profile is understandable when we refer back to Figure 4.5 and notice that it was impossible to identify tiepoints in the peripheral vortex in this data set. The somewhat lower peak relative vorticities displayed in the profiles for the remaining three data sets are probably due to the degraded spatial resolution of our finite grid point spacing which would smooth (i.e., broaden and lower) an actual sharp vorticity peak.

In Figure 4.9 we display the actual finite differenced relative vorticity meridional profile along the minor axis of the GRS in order to look for indications of any north-south asymmetry. Reference to Figure 4.5 indicates that, as previously noted, the absence of data

Table 4.2. GRS Data Sets Interpolation Schemes

Data Set	No. of Actual Tiepoints*	No. of Grid Points	Range in Latitude	Range in Longitude
VGR 1 SET Ia	461	243	-15°0 to -28°0	88°0 to 64°0
SET Ib	461	459	-15°0 to -28°0	88°0 to 64°0
VGR 1 SET IIa	898	243	-15°0 to -28°0	88°0 to 64°0
SET IIb	898	459	-15°0 to -28°0	88°0 to 64°0
VGR 2 SET Ia	384	243	-16°0 to -29°0	121°0 to 97°0
SET IIb	384	459	-16°0 to -29°0	121°0 to 97°0
VGR 2 SET IIa	402	243	-16°0 to -29°0	121°0 to 97°0
SET IIb	402	459	-16°0 to -29°0	121°0 to 97°0

*Up to 10% of the actual tiepoints lie outside the range of the interpolation scheme.

In versions (a): $\Delta x = 3^{\circ}0$ and $\Delta y = 0^{\circ}5$.

In versions (b): $\Delta x = 1^{\circ}5$ and $\Delta y = 0^{\circ}5$.

Figure 4.8. Meridional profile of relative vorticity symmetrically averaged along the minor axis of the Great Red Spot as computed for each of the four data sets used in our analyses and as computed by Mitchell et al. (1981).

ORIGINAL PAGE IS
OF POOR QUALITY

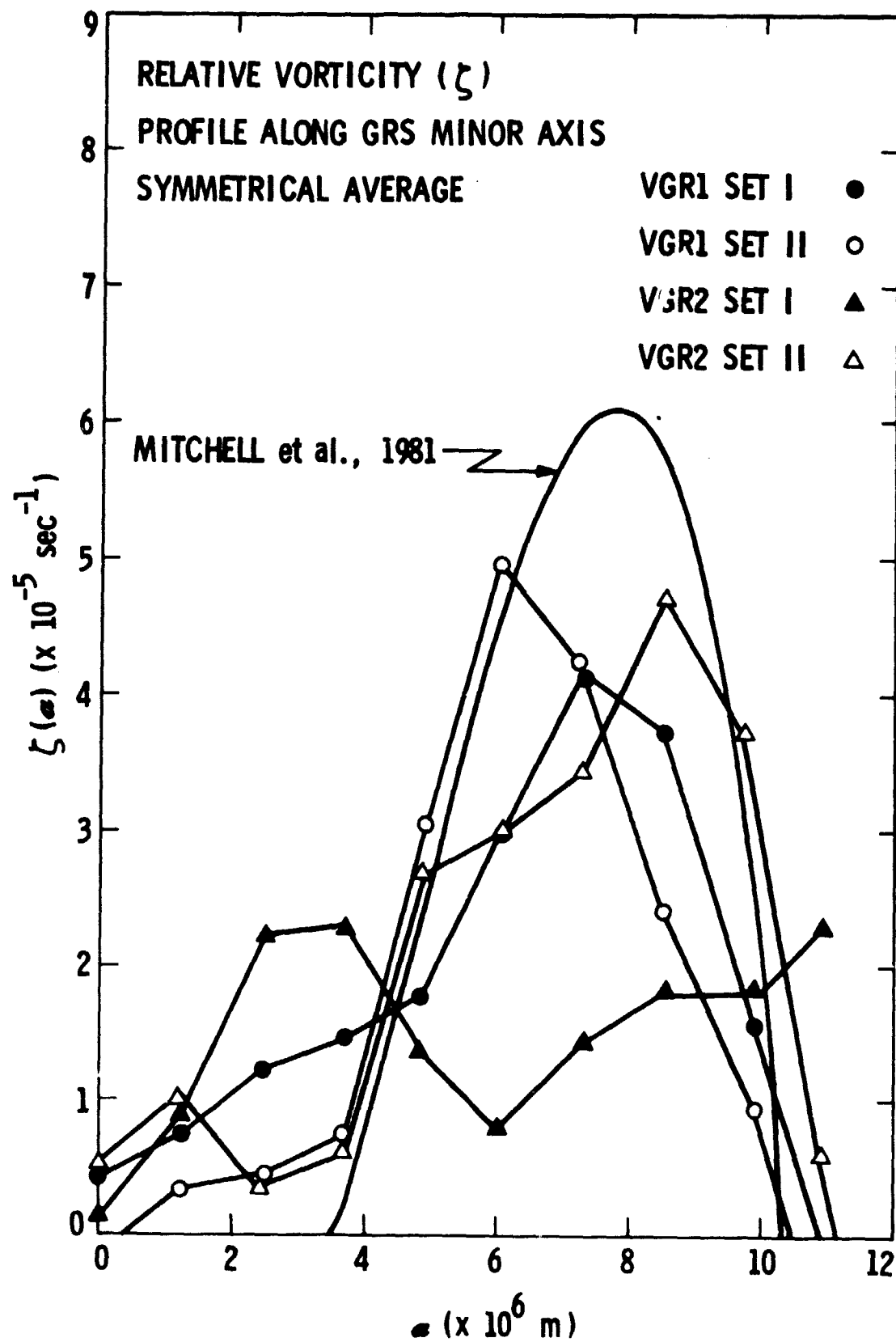
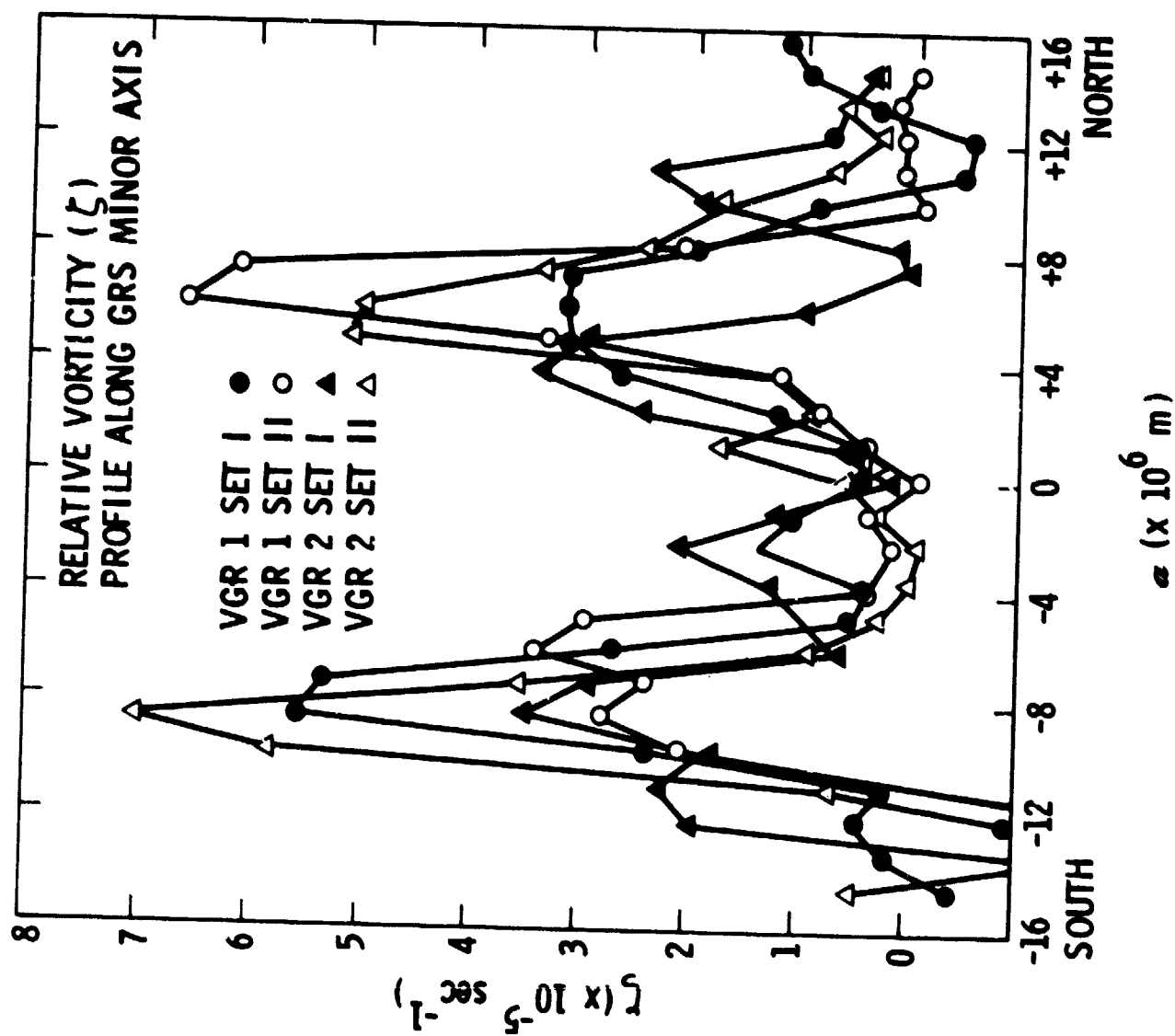


Figure 4.9. Meridional profile of relative vorticity along the minor axis of the Great Red Spot as computed for each of the four data sets used in our analyses.

ORIGINAL PAGE IS
OF POOR QUALITY



points in the peripheral vortex itself explains the lower peak vorticities observed in data set VGR 2 SET I. Reference to Figure 4.4 indicates that our meridional relative vorticity profile for the data set VGR 1 SET II is not likely to be trustworthy at all, as the absence of frame pair coverage along the minor axis of the GRS from about $a = 4 \times 10^6$ m outward makes the computed profile rather meaningless for radii greater than this value. On the other hand, the rather sparse yet uniform sampling of tiepoints evident in the data sets VGR 1 SET I and VGR 2 SET II make them better candidates for uncovering any north-south asymmetry. As seen in Figure 4.9 both of these data sets do display relative vorticity profiles along the minor axis which are markedly asymmetrical with a peak vorticity of about $6.5 \times 10^{-5} \text{ sec}^{-1}$ at $a = -9 \times 10^6$ m (south side) and a lower peak relative vorticity of about $4.0 \times 10^{-5} \text{ sec}^{-1}$ at $a = +5 \times 10^6$ m (north side). The addition of planetary vorticity ($f = 2\Omega \sin\theta$, where $\Omega = 1.76 \times 10^{-4} \text{ sec}^{-1}$ and θ = planetographic latitude) yields the absolute vorticity given by $\zeta + f$ which appears to be more or less conserved at a value of roughly $-8 \times 10^{-5} \text{ sec}^{-1}$ by fluid parcels as they circulate within the GRS.

Using approach movie sequences of Voyager images, the author noticed that smaller, bright vortices produced in Jupiter's so-called F-current, an easterly jet at about -26° latitude, displayed large variations in albedo as they rotated within the GRS after being entrained. The small vortices were observed to substantially brighten as they rounded the northeastern side of the GRS and to dim as they approach the southwestern side. The supposition was that the smaller

vortices were either being vertically stretched or undergoing a wholesale increase in altitude as they moved northward along the eastern edge of the GRS, either case leading to the condensation of more ammonia crystals and hence, an increase in albedo. The opposite effect was presumed to occur on the western side of the GRS. Allison (private communication, 1981) suggests that the observed brightening of these smaller vortices is, in fact, due to vortex-tube stretching governed by the so-called Sverdrup Relation (see Pedlosky, 1979, page 400) which amounts to a restatement of conservation of potential vorticity, i.e.,

$$\frac{d}{dt} \left(\zeta + \frac{f}{D} \right) = 0$$

where,

D = depth scale of the atmosphere

for the appropriate scales of motion. The argument begins with the potential vorticity equation for long waves on a β -plane and in a stratified atmosphere, where for the streamfunction ψ ,

$$\frac{d}{dt} \left[\nabla^2 \psi + \frac{\partial}{\partial z} \left(K^2 \frac{\partial \psi}{\partial z} \right) + \beta y \right] = 0 . \quad (4.6)$$

This is the same as our previous Equation 3.1.

We have seen that this relation expresses a balance in the total time derivative of three terms, which are respectively, the vertical components of relative vorticity, vorticity induced via vortex-tube stretching, and planetary vorticity on a β -plane.

For those scales of motion for which the horizontal Laplacian term may be neglected, i.e., those scales for which dimensionless β given by,

$$\beta^* \approx \frac{L^2}{L_R^2}$$

where, $L_R = (U/\beta_0)^{1/2}$ = stationary Rossby wavelength, is much greater than $O(1)$ and for which,

$$\frac{\beta^*}{K^2} \approx \frac{L_D^2}{L_R^2}$$

where,

$$L_D = ND/f = \text{Rossby deformation radius}$$

is of $O(1)$, we note that the potential vorticity equation reduces to a balance between the second and third term in Equation 4.6. In other words, the balance is between the advection of planetary vorticity and vorticity changes due to stretching. If we estimate the scales of motion for the GRS to be,

$$\beta_0 = \frac{2\Omega}{r_J} \cos \theta \sim 4.6 \times 10^{-12} \text{ m}^{-1} \text{ sec}^{-1}$$

where,

$$U \sim 10^2 \text{ m sec}^{-1}$$

$$L \sim 7 \times 10^6 \text{ m (length scale across semi-minor axis)}$$

$$N \sim 10^2 \text{ sec}^{-1}$$

$$D \sim 10^4 \text{ to } 10^5 \text{ m}$$

$$f \sim 1.3 \times 10^{-4} \text{ sec}^{-1}$$

thus,

$$L_R \sim 4.7 \times 10^6 \text{ m}$$

$$L_D \sim 7.7 \times 10^5 \text{ to } 7.7 \times 10^6 \text{ m}$$

hence,

$$\beta^* \sim 2 \quad = \quad O(1)$$

$$\beta^*/K^2 \sim 30 \text{ to } 3 \quad = \quad O(10) \text{ to } O(1).$$

So, we see that for the smaller entrained F-current vortices the scales of motion associated with their circulation around the GRS do not definitively indicate that the Sverdrup Relation applies. In other words, the advection of relative vorticity may well be of the same order of magnitude as the advection of planetary vorticity. Thus, Equation 4.6 in its complete form represents the appropriate balance. Our present observation that the absolute vorticity appears to be preserved for parcels circulating within the GRS implies that

$$\frac{d}{dt} \left[\nabla^2 \psi + \beta y \right] \equiv 0$$

suggesting by Equation 4.6 that,

$$\frac{d}{dt} \left[\frac{\partial}{\partial z} \left(K^2 \frac{\partial \psi}{\partial z} \right) \right] \equiv 0.$$

Hence, vortex-tube stretching may not be an important process for parcels circulating within the GRS.

4.3 Energetics of the Great Red Spot

Our study of the global energy transport mechanisms operative in the Jovian atmosphere indicated that the up-gradient transport of momentum by eddies smaller than the Rhines radius might be important in the upper troposphere. As pointed out in Chapter 3 we expect the indirect cascade associated with turbulent eddies to be interrupted by the onset of Rossby waves for scales larger than the Rhines radius. In this section we perform an analysis similar to that used on the world-map data sets in order to study the energetics of the Great Red Spot, and White Oval BC, both very large-scale eddies with length scales comparable to or larger than the Rhines radius.

4.3.1 Deduced Energetics for a Closed Momentum Control Volume

Our approach will be to surround the GRS in a closed momentum control volume. The leap of faith from measured inertial forces to energetics is a larger one for a closed momentum control volume than for a global data set. Not only must we contend with the dynamic pressure torque term, but momentum flux terms along the control volume boundaries must be considered as well. Recall that our expression for the time rate of change of mean zonal kinetic energy is given by Equation 2.9. We simplify our task considerably if we make the assumption that the mean meridional velocity may be neglected so that, $\bar{v} \equiv 0$. This is justified by the very small values of observed divergence. Neglecting all vertical motions we have,

$$\frac{\partial \bar{K}}{\partial t} = \{K' \cdot \bar{K}\} + \{p \cdot \bar{K}\} \quad (4.7)$$

where, again,

$$\{K' \cdot \bar{K}\} = + \int_z \int_y \int_x \rho u'v' \frac{d\bar{u}}{dy} dx dy dz - \int_z \int_x \rho [\bar{u}u'v']_y dx dz.$$

We can at best only estimate limits on the pressure torque term; however, the total time rate of change of mean zonal kinetic energy due to eddy stresses is once more given by the familiar correlation between the eddy stress and the ambient meridional shear of the mean zonal wind with the addition of an energy flux convergence term due to momentum transport across the northern and southern boundaries of the control volume. We digress momentarily to discuss the eddy asymmetries which might give rise to eddy-mean flow interactions.

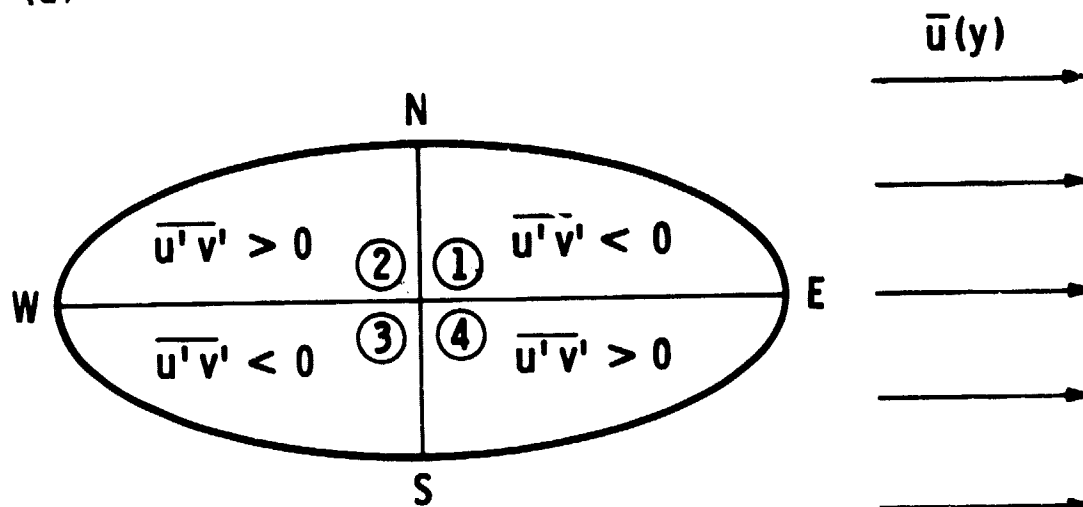
4.3.2 Asymmetry and Eddy Stress

The two essential ingredients for eddy-mean flow interactions are a horizontal shear in the mean flow and appropriate asymmetries in the eddy flow. A symmetric elliptical eddy lying with its major axis oriented perfectly east-west and its minor axis perfectly north-south will not interact energetically with a perfectly zonal mean flow. Reference to Figure 4.10a shows such a non-interacting eddy in an unsheared mean flow. Note that the algebraic sign of the eddy stress given by the product $\overline{u'v'}$ is negative in quadrants 1 and 3 and positive in quadrants 2 and 4. In the case of the GRS, which lies in a negative ambient shear (i.e., $d\bar{u}/dy < 0$, with y increasing northward), this means that if the stresses associated with the odd-numbered quadrants

Figure 4.10. Geometries which lead to net eddy stresses:

- (a) A perfectly symmetric eddy has no associated net stress, the negative stresses of the odd quadrants compensate for the positive stresses of the even quadrants.
- (b) A counterclockwise tilt of the eddy's major axis increases the effective area of the positive stress producing regions (the even quadrants), while diminishing the effective area of the negative stress producing regions (the odd quadrants), leading to positive net eddy stress.

(a)



(b)

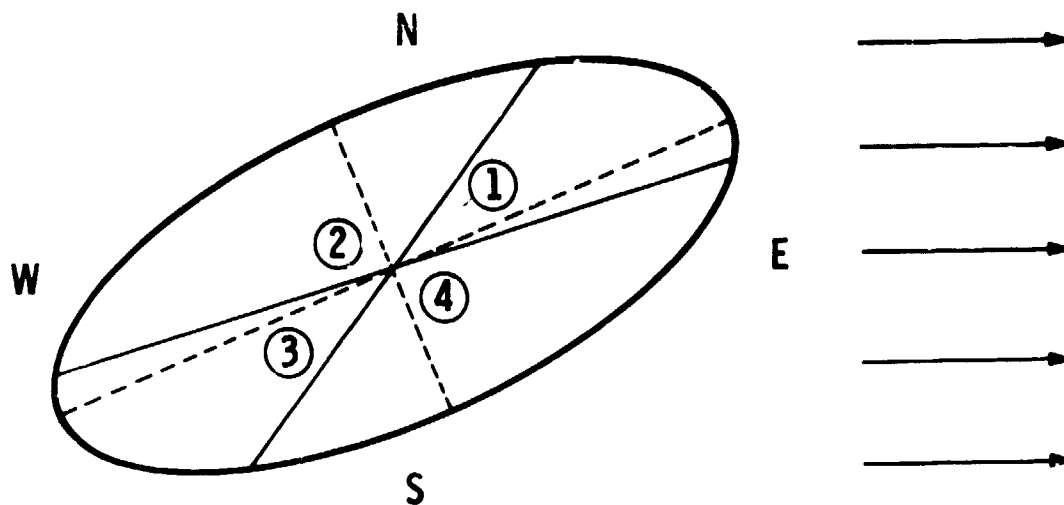
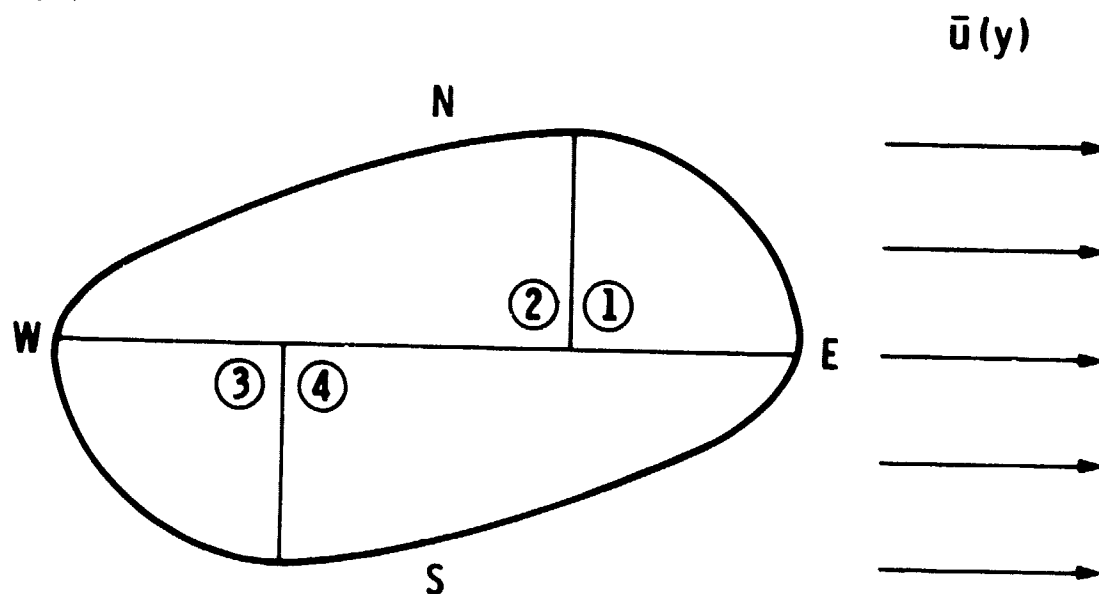


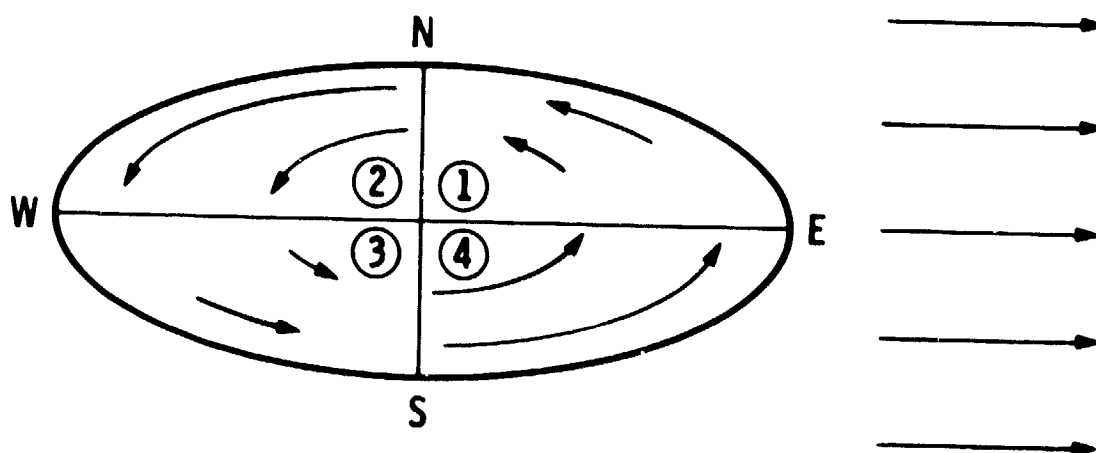
Figure 4.10 continued.

- (c) A geometrical distortion of the eddy which increases the effective area of the positive stress producing regions and diminishes the effective area of the negative stress producing regions.
- (d) An asymmetrical velocity field with higher velocities in the even quadrants leads to the production of net positive eddy stress. Note the associated divergence along the minor axis and convergence along the major axis.

(c)



(d)



exceed in magnitude the stresses associated with the even-numbered quadrants, the mean zonal wind increases in time due to the eddy stresses, i.e., the eddy flow feeds the mean flow. Should the reverse situation occur and the stresses in the even quadrants outweigh the stresses in the odd quadrants, the eddy will barotropically feed off of the mean flow. Using cloudtop measured motions we wish to examine the possibility that the GRS is such a barotropically fed eddy. Thus, we may begin our examination by looking for large-scale asymmetries which maximize the stress contributions from quadrants 2 and 4 while minimizing those from quadrants 1 and 3 and thereby lead to positive net eddy stresses. There are three basic large-scale asymmetries which individually or collectively may provide positive net eddy stresses. These are: a wholesale tilt of the eddy, i.e., a major axis running from southwest to northeast will produce positive net stresses as in Figure 4.10b; a distortion in streamlines such that the effective areas of the even-numbered quadrants (those in which $\overline{u'v'} > 0$) are increased as in Figure 4.10c; and an asymmetry in velocity field with higher velocities in quadrants 2 and 4 as in Figure 4.10d. We briefly discuss a search for direct evidence of these asymmetries.

An asymmetrical velocity field which provides positive net stress will produce a characteristic signature of convergence along the major axis and divergence along the minor axis (see Figure 4.10d). Using the version (a) smoothed velocity fields of our GRS data sets we may compute horizontal divergence as,

$$\bar{\nabla}_h \cdot \bar{\mathbf{V}} = \frac{d\bar{u}}{dx} + \frac{d\bar{v}}{dy}$$

where derivatives are approximated by their centered finite difference equivalents. The results of attempting to deduce divergence fields for our GRS data sets are at best marginal. Typically, divergence is a small quantity and well within the noise level of the finite differencing scheme. An attempt to evaluate the mean divergence (of all four data sets) along the minor axis of the GRS yields $\vec{v}_h \cdot \vec{V} = + 0.07 \times 10^{-5} \text{ sec}^{-1}$ with a standard deviation $\sigma = 0.53 \times 10^{-5} \text{ sec}^{-1}$. A similar evaluation along the major axis of the GRS yields $\vec{v}_h \cdot \vec{V} = + 0.12 \times 10^{-5} \text{ sec}^{-1}$ with $\sigma = 1.03 \times 10^{-5} \text{ sec}^{-1}$. If these results are at all meaningful, which they are probably not, they would indirectly indicate a flow field with a negative net eddy stress contribution. The most important revelation to come out of this analysis is an apparent weak convergence of flow around the outer periphery of the GRS ($a > 12 \times 10^6 \text{ m}$) and a weak divergence of flow within the interior ($a < 12 \times 10^6 \text{ m}$). Noise in our finite difference computation of divergence prevents us from pursuing this matter any further at present.

In an attempt to look for tilting, Mitchell et al. (1981) fit symmetric ellipses to the observed GRS flow allowing the tilt angle between the zonal direction and the major axis to vary as the free parameter. Their results were inconclusive mainly due to problems in identifying feature boundaries for delineation of the flow. However, the plots of GRS tiepoints (Figures 4.3 through 4.6) show a slight, but obvious, wholesale tilt in the orientation of the GRS such that the major axis runs from southwest to northeast.

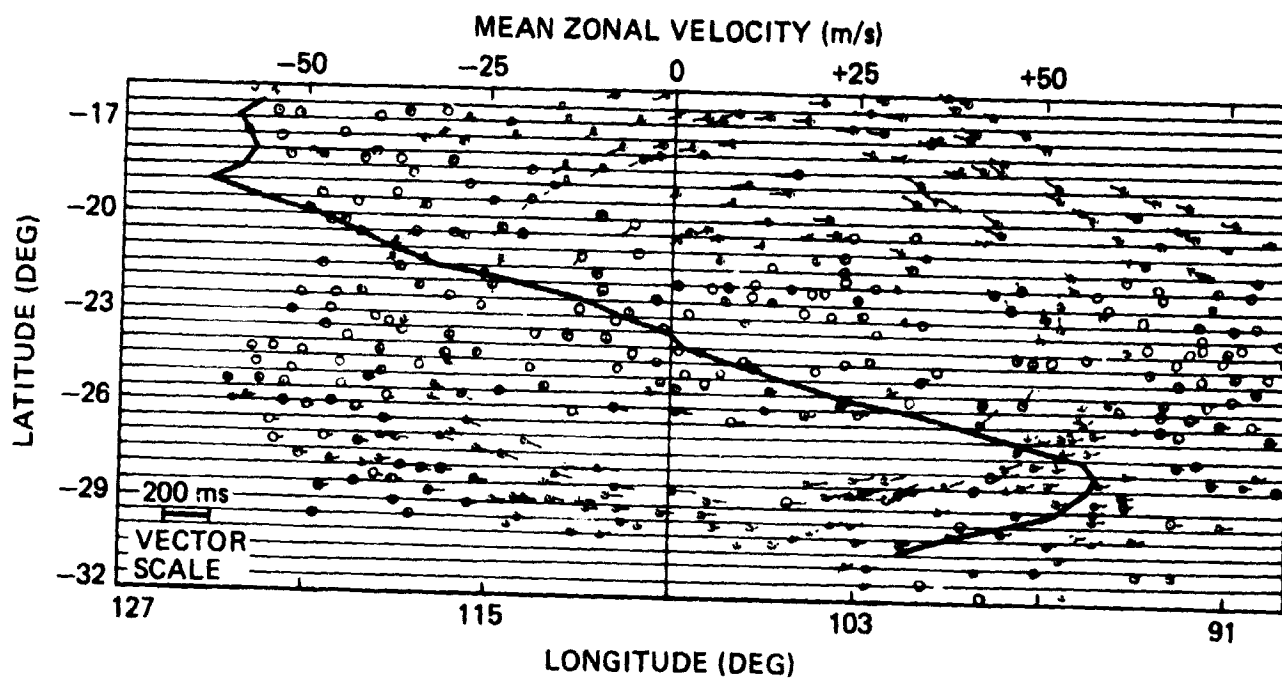
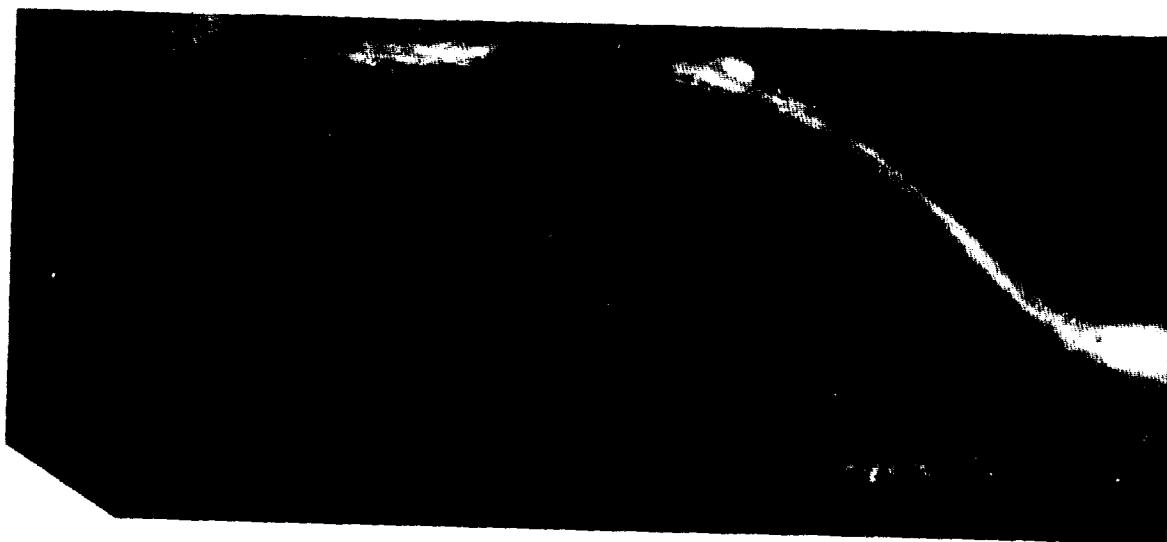
4.3.3 Evaluation of the GRS-Mean Flow Interaction

While an attempt to look for large-scale asymmetries might be intuitively instructive, it does not provide irrefutable evidence of either the algebraic sign or the magnitude of the Red Spot-mean flow interaction. In order to obtain such a measure our approach, as with the "world map" data set, is to divide the data into zonal strips over which averages in x may then be taken. Averaging in y is performed by the summation of zonal strips, while averaging in z still amounts to multiplication by a column density. Figure 4.11 shows a mosaic using some of the frames from data set VGR 2 SET I, as well as an earlier, sparser version of the data set's tiepoints with the zonal averaging bins superimposed.

As we have seen, asymmetries in the eddy field on a quadrant by quadrant basis determine both the algebraic sign and the magnitude of the eddy stress and hence the stress induced momentum transport. Since the marked absence of tiepoints in any one quadrant relative to another will be interpreted as erroneously low averaged velocities (and hence, low eddy stresses) by our zonal averaging scheme, we perform the computation of all kinematic transport terms on the smoothed data sets as earlier described. Using the smoothed flow field, each of the terms in Equation 4.7 becomes in finite difference form:

Figure 4.11. Mosaic of frames used for the Great Red Spot data set VGR2 Set I and latitude averaging bins superimposed upon a measured field of tiepoints. The solid line illustrates the computed profile of $\bar{u}(y)$. In our energetics analysis we use a profile of $\bar{u}(y)$ as computed from the world map data sets.

ORIGINAL PAGE
BLACK AND WHITE PHOTOGRAPH



PRECEDING PAGE BLANK NOT FILMED

$$+ \int_z \int_y \int_x \rho u' v' \frac{d\bar{u}}{dy} dx dy dz = + \frac{\sum_{i=1}^N \rho^* \sum_{j=1}^M \left(u' v' \frac{d\bar{u}}{dy} \right)_{ij}}{N}$$

= eddy stress induced
energy transport

$$- \int_z \int_x \rho [\bar{u} u' v']_y dx dz = - \frac{(\rho^* \bar{u} u' v')_{i=N} - (\rho^* \bar{u} u' v')_{i=1}}{N \Delta y}$$

= kinetic energy flux convergence
associated with flux through the
north (i=N) and south (i=1)
boundaries of the control volume

$$- \int_z \int_y [\bar{u} p]_x dy dz = - \frac{D}{L} \frac{\sum_{i=1}^N (\bar{u} \Delta p)_i}{N}$$

= energy generation
by pressure torque

where,

$\rho^* = 10^4 \text{ kgm/m}^2$ = mass column density of Jovian atmosphere

$\Delta p = p_{\text{EAST}} - p_{\text{WEST}}$ = pressure difference in x across the
control volume

Δy = width of zonal averaging bins

i = index on each zonal bin (y index), increases northward from $i=1$ (southernmost bin) to $i=N$ (northernmost bin)

j = index on longitude (x index), increases westward from $j=1$ (easternmost bin) to $j=M$ (westernmost bin)

$$(\bar{}) = \sum_{j=1}^M ()_j = \text{zonal mean of a quantity}$$

u_{ij} = observed zonal velocity at grid point i, j

$u'_{ij} = u_{ij} - \bar{u}_i$ = zonal component of eddy velocity at grid point i, j

$v_{ij} = v'_{ij}$ = observed meridional component of eddy velocity at grid point i, j

$d\bar{u}/dy = (\bar{u}_{i+1} - \bar{u}_{i-1})/2\Delta y$ = centered finite difference approximation to the meridional shear of mean zonal wind

$D = 10^5 \text{ m}$ = depth scale of Jovian atmosphere over which cloudtop motions represent mean in column

L = length of control volume in x -direction.

Thus, with appropriate assumptions on ρ^* and D , and with the exception of the quantity Δp , we now have a means of relating the observed cloudtop kinematics in an averaging area around the Red Spot to the time rate of change of mean zonal kinetic energy within that area.

Our GRS data sets cover control volumes which are limited to the GRS region in zonal extent (see Figure 4.11). One might, therefore, question the validity of our deduced values of meridional shear and the resulting values of energy transport rates on the basis that the com-

puted mean flow within the control volume and the actual mean flow upon which the GRS is superimposed differ substantially. A comparison of the computed profile of $\bar{u}(y)$ for each of our data sets with a global mean profile through the same latitudes (hence, assumed to represent the true mean flow) indicates fairly close agreement (see Figures 4.12 and 4.13). However, the deduced spin-up times for the GRS differ substantially depending upon which scheme is used. Motions associated with the GRS consist of three components superimposed upon the global mean flow: a meridional flow symmetric about the Red Spot's major axis (v'), zonal perturbations about the computationally determined $\bar{u}(y)$ -profile (u'), and a modified $\bar{u}(y)$ profile with an ambient shear somewhat larger than that determined as the global mean. In order to gauge the effects of the observed stress transports (e.g., estimate "spin-up" times) we must properly compute the total energy associated with the GRS flow as superimposed upon the mean global flow in which the GRS is located. Thus, values presented in Table 4.3 were computed in a scheme using the globally determined values for $\bar{u}(y)$ taken from the final versions of the VGR 1 and VGR 2 world maps.

4.3.4 A Preliminary and Cautious Error Analysis

The first two columns of data in Table 4.3 summarize the results of computing both the eddy stress related kinetic energy transport and the total time rate of change of mean zonal kinetic energy due to eddy stresses in a closed momentum control volume (i.e., transport plus flux convergence) where units are watts m^{-2} . The impact of Table 4.3 is potentially astounding, indicating a GRS which feeds at a rapid rate off of the ambient mean flow. However, before fully embracing a baro-

Figure 4.12. Profiles of $\bar{u}(y)$ as computed from the Voyager 1 world map (connected dots) and as computed within the momentum control volume around the Voyager 1 GRS data sets.

ORIGINAL PAGE IS
OF POOR QUALITY

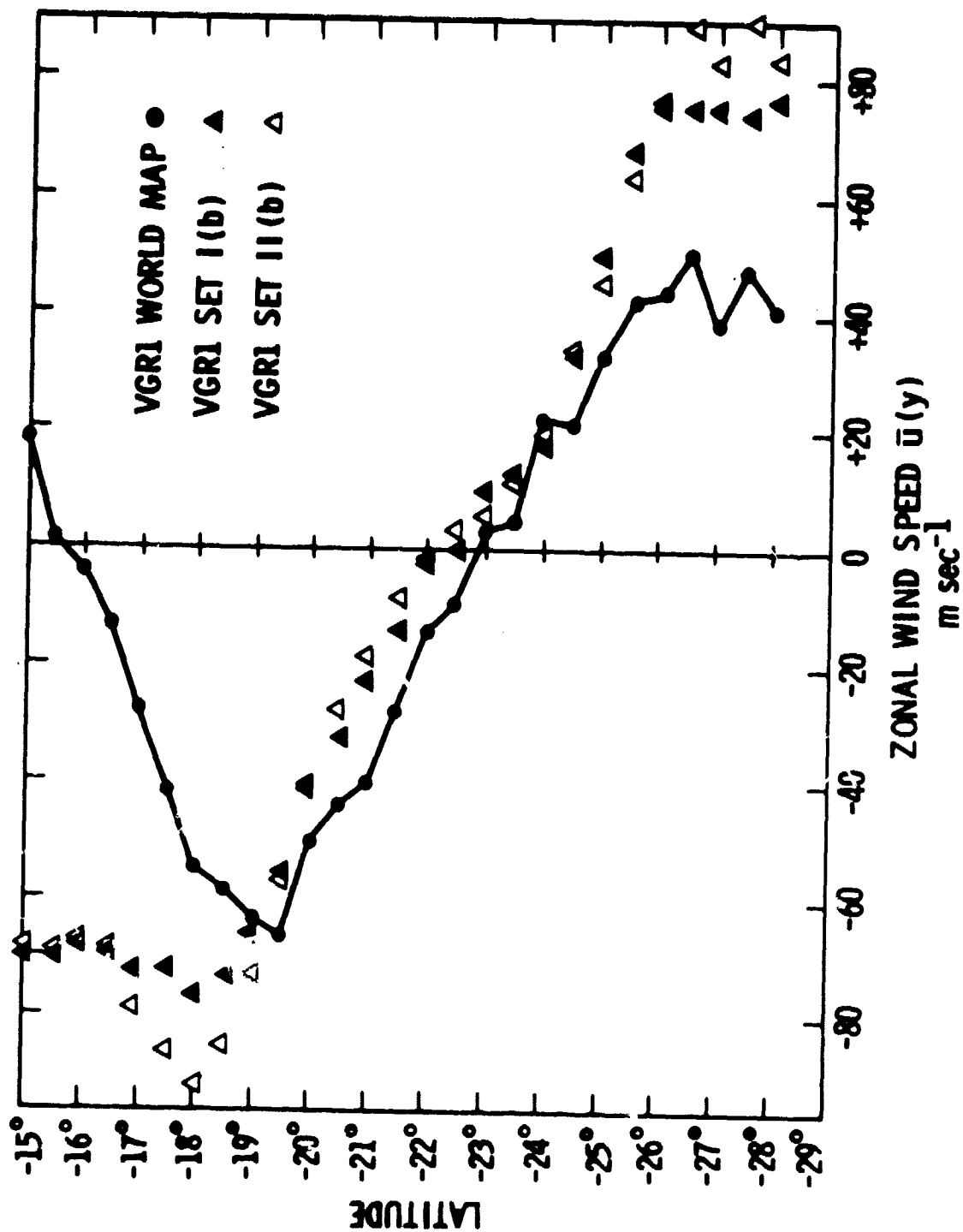


Figure 4.13. Profiles of $\bar{u}(y)$ as computed from the Voyager 2 world map (connected dots) and as computed within the momentum control volume around the Voyager 2 GRS data sets.

ORIGINAL PAGE IS
OF POOR QUALITY

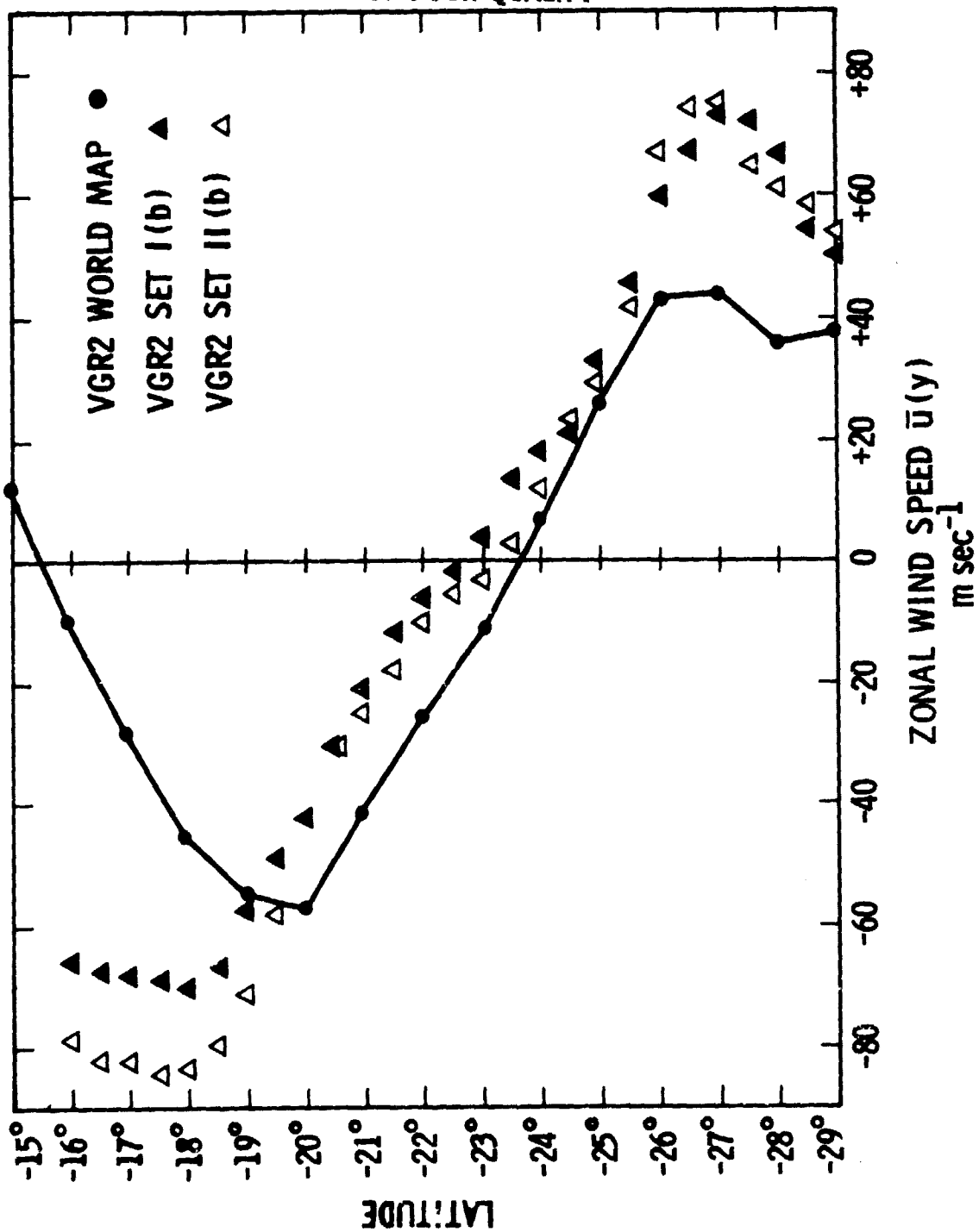


Table 4.3. Computed Energetics of the Great Red Spot

Data Set	Eddy Stress Transport (Watts m ⁻²)	$\{K' \cdot \bar{K}\}$ (Watts m ⁻²)	K' (X10 ²² Watts)	\bar{K} (X10 ²² Watts)	Spin-Up (terrestrial days)
VRG 1 SET Ib	-18.6	-22.9	0.899	0.302	11.22
VGR 1 SET IIb	-29.0	-28.2	0.684	0.302	6.93
VGR 2 SET Ib	-15.6	-17.5	0.435	0.284	7.08
VGR 2 SET IIb	-24.0	-26.2	0.643	0.284	7.00

tropically fed Red Spot (and all the ensuing theoretical repercussions) we must resolve several potential problems relating to our method of analysis: errors associated with uniform grid smoothing, potential error in one of the more sensitive navigational parameters called the "north-angle", and our wholesale neglect of the pressure torque term.

The experiments performed as part of this error analysis were all based upon data sets which use the computationally determined profile of $\bar{u}(y)$ rather than that derived from the world map data sets. This has little effect upon our conclusions.

4.3.4.1 The Effects of Our Smoothing Schemes

Comparison of version (a) and version (b) data sets in Table 4.4 allows a measure of the effects of our smoothing grid. Reference to Table 4.2 indicates that none of the data sets are over-interpolated (i.e., the actual number of tiepoints is always greater than the number of uniform grid points). As seen in Table 4.4 the excellent agreement in computed terms between version (a) and version (b) of our data sets indicates that within reasonable limits changes in grid spacing do not greatly affect our results. We note that VGR 1 SET II is quite under-interpolated in both versions (a) and (b) increasing the likelihood of variance between the two versions. For data set VGR 1 SET II a third interpolation was used with $\Delta x = 1.0$ and $\Delta y = 0.5$, giving a total of 675 uniformly spaced grid points (actual number of tiepoints is somewhat less than 800). The results for this third interpolation are an eddy stress induced energy transport of -30.6 watts/m^2 and a total time rate of change of mean zonal kinetic energy due to eddy stresses (transport plus flux convergence) of -41.8 watts/m^2 . The

Table 4.4. Effects of Smoothing Scheme on Deduced Energetics

Data Set	Eddy Stress Transport (Watts m ⁻²)	$\{K' \cdot \bar{K}\}$ (Watts m ⁻²)
VGR 1 SET Ia	-36.7	-52.1
SET Ib	-37.4	-46.8
VGR 1 SET IIa	-37.8	-56.9
SET IIb	-27.5	-47.6
VGR 2 SET Ia	-18.4	-26.1
SET Ib	-15.5	-22.4
VGR 2 SET IIa	-14.3	-23.5
SET IIb	-16.3	-23.8

results lie between those for versions (a) and (b) of the same data set. Though we are immediately cautious when analyzing VGR 1 SET II, since it contains frame pairs which are navigated in a "relative" sense, there is no obvious reason why such relative navigation would produce noise in our interpolation schemes. Actually, as is obvious in Figure 4.4, the likely causes of such noise are the rather severe data gaps in the peripheral vortex due to lack of frame pair coverage. These data gaps are most pronounced in the northwest and southeast quadrants of the GRS, quadrants for which the eddy stress is positive. Since the ambient mean zonal wind shear is negative, we would anticipate that the contributions made to the eddy stress energy transport term by these two quadrants will be negative. The finer grid interpolation schemes are more readily capable of resolving the peripheral vortex data gaps in these two quadrants, hence the computed energy transport, as well as the total $\{K' \cdot \bar{K}\}$ will tend to be less negative than will be the coarser grid interpolation scheme (i.e., version (a)). Comparisons between VGR 1 SET II version (a) and VGR 1 SET I versions (a) and (b) indicate that this explanation is feasible, and we conclude that for the data set VGR 1 SET II only version (a) (i.e., the coarser grid scheme) is free from the effects of uneven data sampling.

Before leaving the subject of the effects of different interpolation schemes we refer to Table 4.5 which presents the results of changing both Δx and Δy in the smoothing scheme for a somewhat earlier version of data set VGR 2 SET I. In this earlier version there were fewer tiepoints located in the peripheral vortex, leading to

Table 4.5. Various Interpolation Schemes for VGR 2 SET I

Δx (° Longitude)	Δy (° Latitude)	Eddy Stress Transport (Watts m ⁻²)	$\{K' \cdot \bar{K}\}$ (Watts m ⁻²)
0.5	0.5	-11.7	-14.3
0.5	1.0	-11.9	-14.8
1.0	0.5	-11.9	-14.7
1.0	1.0	-12.0	-15.0

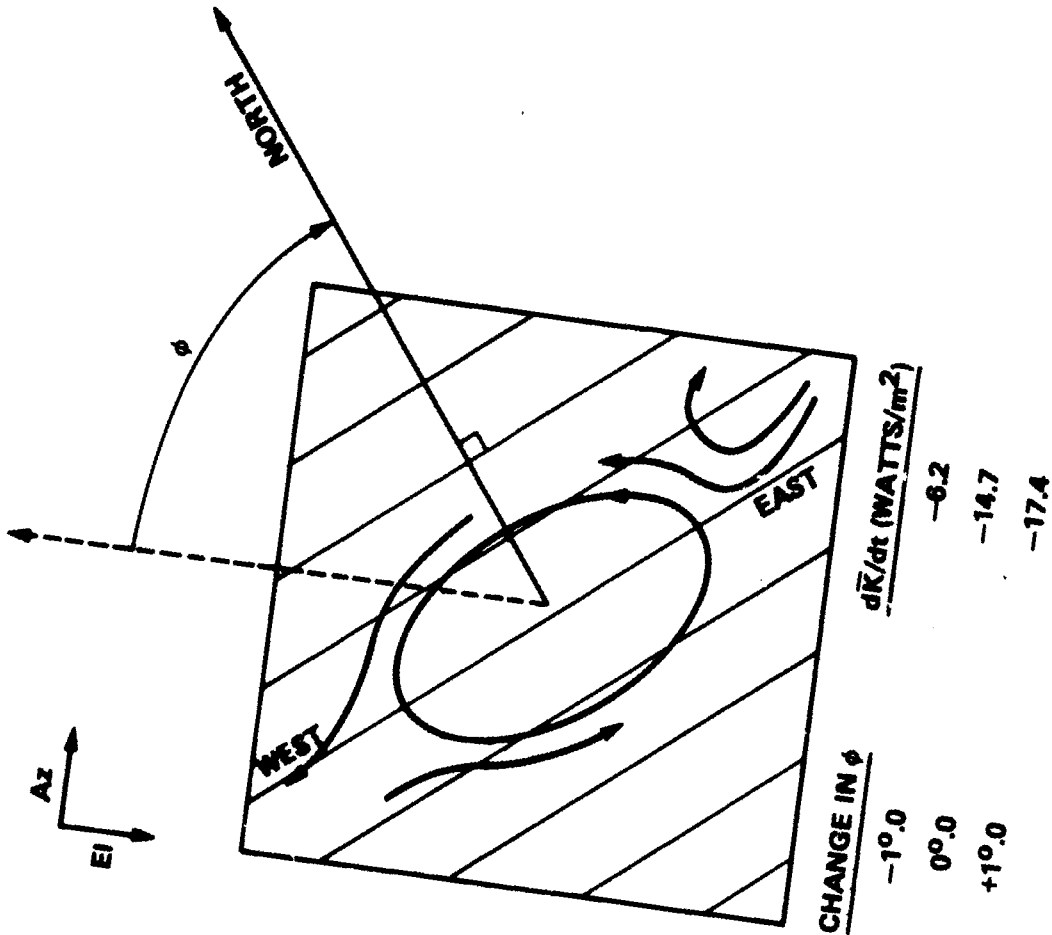
energy transports which are somewhat smaller in magnitude. There is a suggestion that, provided the field remains under-interpolated and the grid spacing is large enough to smooth over data gaps, the magnitude of computed transport and $\{K' \cdot \bar{K}\}$ will diminish slightly with increasingly finer grid spacing (an effect also evident in much of Table 4.4). Though it would be meaningless to conclude anything from this slight effect, one might be tempted to use the trend to argue that the larger scale asymmetries associated with the GRS are those responsible for its ability to feed upon the ambient meridional shear of the zonal wind. It is our conclusion that within the minor limitations discussed above, smoothing of our data introduces little noise into the results and at the same time filters out misleading asymmetries in the data sampling.

4.3.4.2 The Effects of Error in North-Angle

Since even the small tilt of an eddy can have very large effects on the deduced energy transport rates, we must be very cautious that each of the frames used in our GRS data sets is oriented properly, i.e., that we know the direction in each frame to Jupiter's north rotational pole to a high degree of accuracy. The angle measured clockwise from the negative elevation axis to the northward direction in the image plane is known as the north-angle. From Figure 4.14 we readily see how errors in north-angle of only a fraction of a degree might readily translate into drastic errors in deduced energy transport rates (consider that we estimate the overall tilt of the GRS to be about one degree or so). There are three identifiable sources of north-angle error: error in our knowledge of the spacecraft to Jupiter distance,

Figure 4.14. North angle (ϕ) is measured clockwise from the frame's negative elevation axis (see directions of increasing azimuth and elevation denoted at upper left). Small changes in (ϕ) as tabulated beneath the figure result in large changes in deduced energy transport rates in the sense anticipated.

ORIGINAL PAGE IS
OF POOR QUALITY



PRECEDING PAGE BLANK NOT FILMED

of the amount of scan platform twist due to spacecraft limit cycle motion, and of the actual location of Jupiter's north rotational pole.

Error in our knowledge of the radius vector from the spacecraft to Jupiter's center may be as great as ± 100 km. An error this large in range translates into an error of roughly ± 0.1 in north-angle. A typical error in range is only ± 10 km which would translate into a much smaller error in north-angle. The more or less random wobbling motion of the spacecraft about its three axes is known as limit cycle motion. Motion about the spacecraft's roll axis translates (as a function of pointing elevation and azimuth) into an error in north-angle. For cameras pointing directly along the scan platform elevation axis the translation will be direct. Total limit cycle amplitude about the roll axis is ± 0.05 ; hence, in the worse case, limit cycle motion can lead to an error in north-angle of ± 0.05 . Finally, we note that error in our current knowledge of the exact orientation of Jupiter's rotational pole is so small as to lead to a negligible error in north-angle. Thus, in a worst case our knowledge of north-angle has an approximate error of ± 0.1 . But into what sort of error does this translate when we consider energy transport rates?

In order to answer this question we perform an experiment on an earlier version of our data set VGR 2 SET I (the same data set used to generate Table 4.5). The smoothing scheme in use was $\Delta x = 1.0$ and $\Delta y = 0.5$. The value of north-angle used by the AMOS program was purposely incremented by -1.0 , -0.1 , $+0.1$, and $+1.0$ so as to artificially rotate the frame about its center by these amounts. This, of course, has the effect of changing the defined meridional and zonal direc-

tions. The total effect is not quite as conceptually simple as taking a purely zonal flow and then rotating a "tiltable" eddy back and forth about its center. The complicating factors are that the magnitude of the ambient zonal wind shear changes in the tilting process, and that the GRS is not actually located in the center of the frame as suggested by Figure 4.14. The changes in the measured mean flow due to tilting the frame pair are very small and have a negligible effect upon the deduced energy transport rates. However, the change in energy transport rates produced by changes in the eddy stresses are great, and as the center of the GRS is reasonably near the center of both frames in the pair, we may liken the effect to artificially inducing a wholesale tilt of the eddy. Table 4.6 summarizes the results, which do much to build confidence in our supposition that a slight tilt of the GRS plays

Table 4.6. North-Angle Error Analysis

Change in North-Angle (Measured positive clockwise)	$(K' \cdot \bar{K})$ (Watts m^{-2})
+1°0	-6.2
+0°1	-15.4
0°0	-14.7
-0°1	-14.4
-1°0	-17.5

a major role in allowing the eddy to feed upon the mean flow. We note that just as anticipated, tilting the frame pair only one degree in a counterclockwise (clockwise) sense greatly increases (decreases) the rate at which the GRS feeds upon the mean flow. Within the limits of our knowledge of north-angle (± 0.1) the noise associated with our interpolation grid seems to completely mask, and by chance, slightly reverse anticipated changes in the energy transport rates. From these results we may estimate the error on deduced energy transport to be approximately $\pm 0.5 \text{ watts/m}^2$ for a worst case error in north-angle of ± 0.1 .

4.3.4.3 The Pressure Torque Term

We have delayed a discussion of the largest source of a potential misinterpretation of Table 4.3 for last. The pressure torque term, as already noted, is dynamic and is the term initiating motion in our mean zonal kinetic energy equation, the kinematic terms only acting upon the motion once it is initiated. Horizontal pressure gradients, and hence the pressure torque term, are of course unobservable by the Voyager spacecraft. The effects of the torque might, however, be estimated by applying a little dynamic intuition. We begin with a simple estimate of the radial pressure gradient associated with flow around the GRS.

4.3.4.3.1 An Estimate of the Radial Pressure Gradient of the GRS

Noting that Mitchell et al. (1981) estimated the Rossby number (Ro) for tangential flow on the Red Spot's major axis to be 0.36 at a distance $a = 10.5 \times 10^6 \text{ m}$ from the spot's center (where $Ro = V_T \cdot a/b^2 n^3/f$ = ratio of centrifugal to Coriolis acceleration), we

shall assume the tangential flow to be in gradient balance (i.e., balance between centrifugal, Coriolis, and radial pressure gradient accelerations). Hence,

$$-\left(\frac{a}{b}\right)v_T^2 - fv_T = -\frac{1}{\rho} \frac{\partial p}{\partial a} \quad .$$

If the GRS does indeed represent a high pressure center, as seems almost certain (Ingersoll, 1973), then the pressure gradient and centrifugal accelerations acting to the right of a fluid parcel's trajectory are balanced by the Coriolis acceleration to the left (in the southern hemisphere). Thus, use of the appropriate values for our parameters,

$$f = -1.35 \times 10^{-4} \text{ sec}^{-1} \quad \text{at } -22.5 \text{ latitude}$$

$$v_T = 110 \text{ m sec}^{-1} \quad \text{at } a = 10.5 \times 10^6 \text{ m (thus } b = 4.85 \times 10^6 \text{ m)}$$

$$\rho = 9.0 \times 10^{-2} \text{ kg m}^{-3} \quad \text{at } p = 500 \text{ mb (Divine, 1971),}$$

allows us to evaluate the radial pressure gradient as,

$$\frac{\partial p}{\partial a} = -8.51 \times 10^{-4} \text{ newtons m}^{-3} = -8.51 \times 10^6 \text{ mb m}^{-1} \quad .$$

This gradient implies a center to edge (i.e., $a = 10.5 \times 10^6 \text{ m}$) pressure difference of,

$$\Delta p = p]_R = 10.5 \times 10^6 \text{ m} - p]_a = 0 = -89.3 \text{ mb.}$$

This is a fairly typical center to edge pressure difference at the 500 mb level by even terrestrial standards.

4.3.4.3.2 An Estimate of the Ageostrophic Pressure Gradient

An ageostrophic pressure difference maintained across our control volume will give rise to a pressure torque. Thus, as seen before in our computational scheme,

$$(p \cdot K') \approx - \left(\frac{D}{L} \right) \frac{\sum_{i=1}^N (\bar{u} \Delta p)_i}{N}$$

where,

Δp = pressure at the east wall minus pressure at the west wall of our control volume.

Hence, an excess ageostrophic pressure maintained on the west side of the GRS relative to its east side will tend to cancel the energy transport rates inferred from a consideration of the eddy stresses alone.

Use of the VGR 2 global map data set allows a measure of the reasonableness of such a "negating" ageostrophic pressure difference, as follows: Our world map yields a measure of $\bar{\omega}/\omega$ in the zonal "channel" containing the GRS (from roughly -16.5 to -28.5 latitude in width). We may divide this channel into two segments, that

containing the GRS and the remainder of the zonal channel, which we designate as NONGRS. Noting that $\bar{a}K/\bar{a}t$ in this global channel is given exactly by,

$$\begin{aligned} \left[\frac{\partial K}{\partial t} \right]_{\text{CHANNEL}} &= \left[\frac{\text{Area of GRS}}{\text{Area of CHANNEL}} \right] [\{K' \cdot \bar{K}\}]_{\text{GRS}} \\ &+ \left[\frac{\text{Area of NONGRS}}{\text{Area of CHANNEL}} \right] [\{K' \cdot \bar{K}\}]_{\text{NONGRS}} \quad (4.8) \\ &= [0.092] [\{K' \cdot \bar{K}\}]_{\text{GRS}} + [0.908] [\{K' \cdot \bar{K}\}]_{\text{NONGRS}} \end{aligned}$$

where the pressure torque associated with $[\partial \bar{K} / \partial t]_{\text{GRS}}$ and $[\partial \bar{K} / \partial t]_{\text{NONGRS}}$ cancel since,

$$\left[\frac{\partial \bar{K}}{\partial t} \right]_{\text{GRS}} = [\{K' \cdot \bar{K}\}]_{\text{GRS}} + [\{p \cdot K'\}]_{\text{GRS}} \quad (4.9)$$

and,

$$\left[\frac{\partial \bar{K}}{\partial t} \right]_{\text{NONGRS}} = [\{K' \cdot \bar{K}\}]_{\text{NONGRS}} - [\{p \cdot K'\}]_{\text{GRS}} \quad (4.10)$$

We assume that,

$$[\{K' \cdot \bar{K}\}]_{\text{GRS}} \approx -25 \text{ watts m}^{-2}$$

and from our Voyager 2 world map data set that,

$$\left[\frac{\partial \bar{K}}{\partial t} \right]_{\text{CHANNEL}} = +0.99 \text{ watts m}^{-2}.$$

Thus, we obtain from Equation (4.8),

$$\left[\left\{ \bar{K}' \cdot \bar{K} \right\} \right]_{\text{NONGRS}} \approx +3.6 \text{ watts } \bar{m}^2$$

which we note is near the global average energy transport rate.

Now, suppose that the ageostrophic pressure difference (Δp) across the GRS exerts a torque which acts so as to exactly cancel the effects of the GRS stresses, such that $[\partial \bar{K} / \partial t]_{\text{GRS}} = 0$. Equation (4.9) allows an evaluation of this "cancelling" pressure gradient of $\Delta p = -13.5 \times 10^2 \text{ Newtons } \bar{m}^{-2}$ ($= -13.5 \text{ mb}$) where,

$$D = 10^5 \bar{m}$$

$$L = 3.84 \times 10^7 \bar{m} \text{ (the zonal extent of the GRS segment)}$$

$$u = +10 \text{ m sec}^{-1} \text{ (average over the channel width).}$$

Thus, a pressure difference of 13.5 mb maintained across the GRS segment of the channel with higher pressure on the west will negate the effects of the observed GRS stresses.

4.3.4.3.3 The Asymmetry Associated with Ageostrophic Flow

Under the assumption that the GRS represents a normal high pressure center (i.e., one in which the pressure gradient acceleration is larger than the centrifugal acceleration), we have seen that the deduced pressure gradient is $-8.51 \times 10^{-6} \text{ mb } \bar{m}^{-1}$. It initially seems alarming to note that the asymmetric pressure gradient required to cancel the effects of eddy stress in the energy equation is only $-3.52 \times 10^{-7} \text{ mb } \bar{m}^{-1}$ or only about 4% of the symmetric radial pres-

sure gradient. It behooves us to determine how such a pressure differential across the GRS might manifest itself.

If we suppose that the pressure field around the GRS consists of the superposition of the radial, symmetric field of a normal high and a superimposed constant ageostrophic pressure difference maintained from east to west across the GRS control volume so as to cancel the eddy stress effects, we may evaluate the resulting pressure gradient on the eastern half of the GRS as,

$$\begin{aligned} \left[\frac{\partial p}{\partial a} \right]_{\text{EAST}} &= (-8.51 \times 10^{-6} \text{ mb m}^{-1}) + (-0.35 \times 10^{-6} \text{ mb m}^{-1}) \\ &= -8.86 \times 10^{-6} \text{ mb m}^{-1} \end{aligned}$$

and on the western half as,

$$\begin{aligned} \left[\frac{\partial p}{\partial a} \right]_{\text{WEST}} &= (-8.51 \times 10^{-6} \text{ mb m}^{-1}) - (-0.35 \times 10^{-6} \text{ mb m}^{-1}) \\ &= -8.16 \times 10^{-6} \text{ mb m}^{-1}. \end{aligned}$$

Use of the gradient wind balance (though the flow might well be ageostrophic, it should still be gradient, unless unobservable longitudinal asymmetries in the stresses play a major role in the resulting flow) allows us to compute the resulting asymmetry in the tangential velocity field. Once again, assuming that the GRS flow is that of a normal high pressure center, this yields a typical value for the tangential velocity on the eastern side of the Red Spot of,

$$[V_T]_{\text{EAST}} = 123 \text{ m sec}^{-1} \text{ (at } a = 10.5 \times 10^6 \text{ m)}$$

and on the western side of the Red Spot of,

$$[V_T]_{\text{WEST}} = 100 \text{ m sec}^{-1} \text{ (at } a = 10.5 \times 10^6 \text{ m)}.$$

This may be compared with a value $V_T = 110 \text{ m sec}^{-1}$ at $a = 10.5 \times 10^6 \text{ m}$ in Mitchell et al. (1981). Reference to Figures 4.3 through 4.6 clearly demonstrates that even if asymmetries of such a magnitude do exist, observation seems to indicate that it is the tangential flow on the eastern side of the GRS which is somewhat slower. We conclude that there is very little evidence indeed for a pressure differential across the GRS control volume of the magnitude or the algebraic sign necessary to cancel the energetics deduced from our kinematic observations of eddy stress.

4.4 Eddy Stresses Associated with White Oval BC

Based upon a high resolution velocity field of White Oval BC (the same data set used by Mitchell et al.; see their figure 2) we have performed a stress analysis identical to that described in section 4.3.3. One must be cautious with the results as all frames in this set can only be relatively navigated (as in our GRS data set VGR1 SET II). Also, we use the mean profile $\bar{u}(y)$ as defined by the zonal mean within the control volume. This is necessary as the presence of elongated cyclonic regions between each of the three White Ovals makes use of a globally determined profile of $\bar{u}(y)$ risky. We have already remarked on

the dynamic similarity between the flow fields of the GRS and White Oval BC. It is most encouraging that our stress analysis yields results remarkably similar to those for the GRS (in Table 4.3).

The area weighted mean correlation between observed stresses and the computed meridional shear of $\bar{u}(y)$ has a value of -54 watts m^{-2} (where we have once again multiplied by a column density of $\rho^* = 10^4 \text{ kgm m}^{-2}$). Accounting for momentum fluxes along the northern and southern boundaries of the control volume yields,

$$\{K' \cdot \bar{K}\} \simeq -15 \text{ watts m}^2.$$

Thus, it appears that Oval BC (and by inference Ovals FA and DE) may well be maintained by barotropically feeding upon the ambient anti-cyclonic shear of the mean zonal wind. Hence, we suspect that the White Ovals and the GRS may be generically, as well as dynamically, similar. Studies of the flow fields of Ovals FA and DE would be useful in a more complete investigation of our suspicions.

4.5 The Role of Eddy Stresses in Maintaining the GRS

Having discussed at length potential errors in our analysis we may more confidently return to the results summarized in Table 4.3. Comparison of columns four and five in Table 4.3 seems to indicate that the total kinetic energy associated with the GRS flow exceeds the kinetic energy of the ambient mean flow within the enclosed momentum control volume by a factor of two to three (summed over the entire globe the kinetic energy of the mean ambient flow is five to seven

times greater than that associated with the GRS). This excess kinetic energy associated with the GRS is likely, however, to be an over-estimate, since the presumption of Table 4.3 is that both the mean flow and the GRS flow extend through a column of equal atmospheric mass (namely, 10^4 kgm m^{-2}). Comparison of the values for \bar{K} in column five indicates that there has been little change in the overall kinetic energy content of the mean flow between the flyby of VGR 1 and that of VGR 2. This could indicate that the observed role of the eddy stresses in maintaining the flow of the GRS represents a steady state situation. Spin-up times (in the e-folding sense) for the GRS flow may be computed under the assumption that the ratio of $\{K' \cdot \bar{K}\}$ to K' remains constant over the spin-up interval. Values given in column 6 of table 4.3 clearly indicate that if the observed stresses apply throughout an atmospheric column of 10^4 kgm m^{-2} , the GRS would spin-up with a time constant of order 10 terrestrial days.

4.5.1 Nature of the Observed Stresses

Figures 4.15 and 4.16 display the tight negative correlation between the global ambient shear and the GRS stresses for VGR 1 and 2 respectively. The linear least-square fits in the form,

$$\overline{u'v'} = A \frac{d\bar{u}}{dy} + B$$

for each of the data sets are presented in the figures. The actual values of the linear coefficient (A), the intercept (B), the linear correlation coefficient (r), the probability (P) of exceeding r in a

Figure 4.15. Plot of zonal mean eddy stresses ($\overline{u'v'}$) vs. ambient meridional shear of the mean zonal wind ($d\bar{u}/dy$) for the Voyager 1 GRS data sets. Solid lines represent a linear least squares fit to the appropriate data. The slope of such a linear fit is just the eddy viscosity coefficient (K_e).

ORIGINAL PAGE 13
OF POOR QUALITY

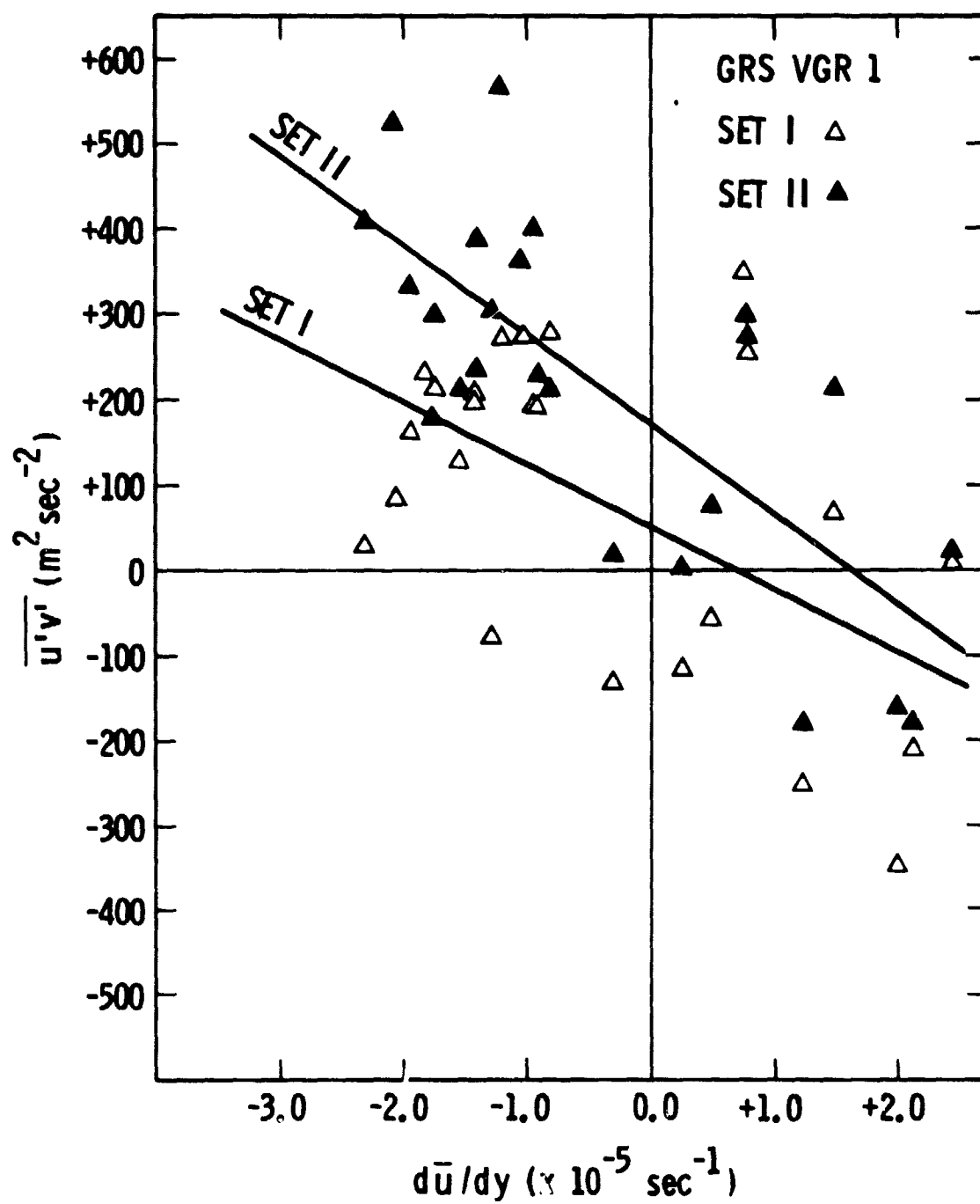
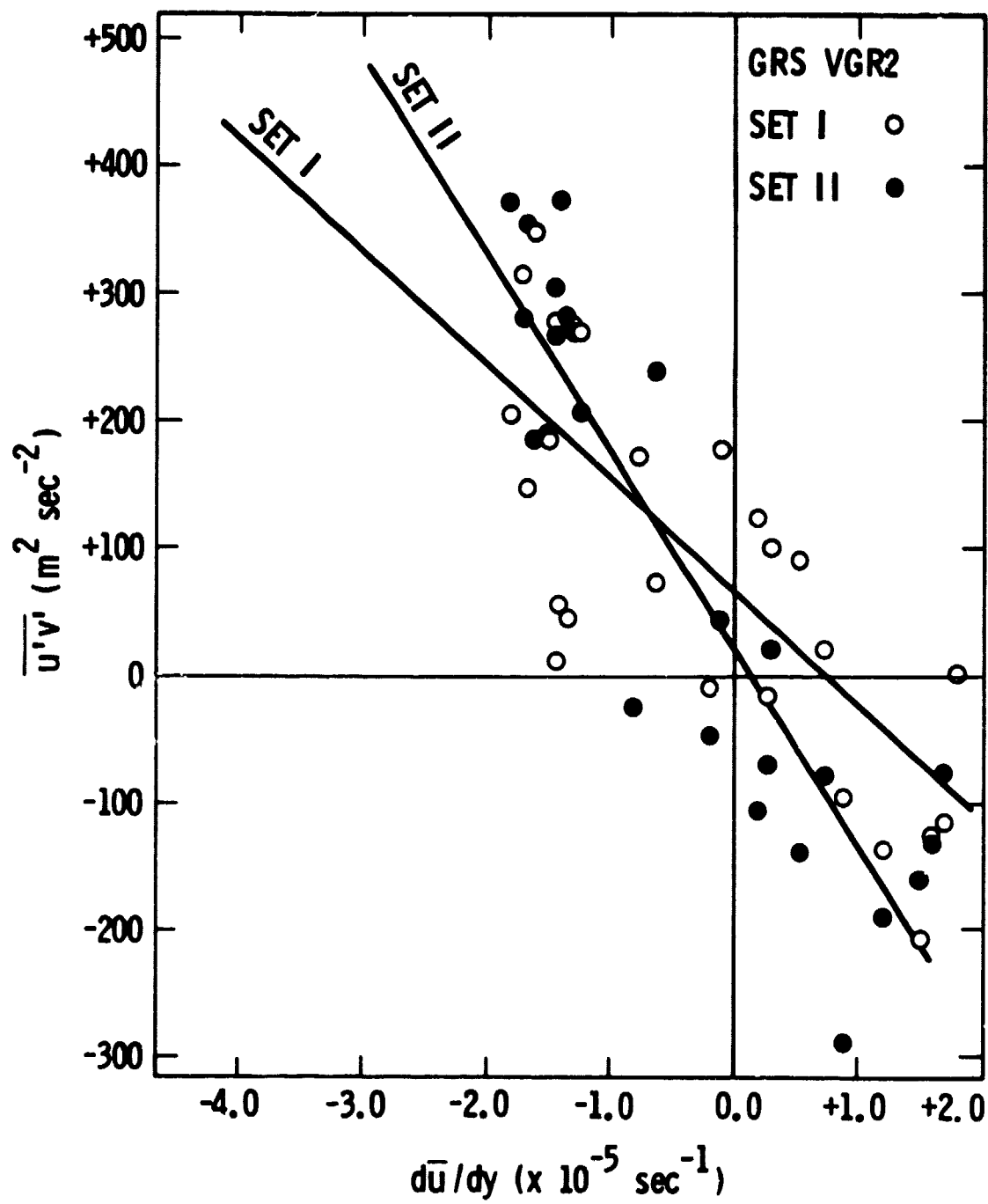


Figure 4.16. Plot of zonal mean eddy stresses ($\overline{u'v'}$) vs. ambient meridional shear of the mean zonal wind ($d\bar{u}/dy$) for the Voyager 2 GRS data sets. Solid lines represent a linear least squares fit to the appropriate data. As previously noted, the slope of such a linear fit is just the eddy viscosity coefficient (K_e).

ORIGINAL PAGE IS
OF POOR QUALITY



random sample of 25 points, the eddy viscosity coefficient (K_e) as determined by the mixing length concept, and the mixing-length (z') where $z' \sim K_e/u'$ for $u' \sim 10 \text{ m sec}^{-1}$ are presented in Table 4.7. The very tight linear correlation between the eddy stresses and the ambient meridional shear of the zonal wind is striking and, as seen from the values for (P), represents a meaningful correlation at the 99.5% level, or generally better, for a random sample of 25 data points (the number of latitude bins in each case). The somewhat looser correlation shown by the data set VGR 1 SET 1 is probably not noteworthy and causes no concern.

The tabulated values of K_e are of interest and when coupled with an estimate of the typical scale of the velocity perturbation (say $u' \sim 10 \text{ m sec}^{-1}$) these values give an estimate of the length scale for the momentum exchange (a sort of mean free path for momentum) provided in the last column. We note that the estimated length scales are very roughly an order of magnitude larger than similarly estimated scales for the globally averaged eddies. This does not confirm, but certainly favors, our hypothesis that it is a slight wholesale tilt of the GRS which allows it to feed barotropically off of the mean zonal flow.

4.5.2 The Barotropic Stability of the Mean Shear

Figure 4.17 presents the observed meridional profiles of $\bar{u}(y)$ for global averages from the Voyager 1 and 2 World Map data sets. Superimposed on the actual profiles is a stability parabola on which $\bar{u}''(y) = \beta$ at -19.5° latitude as computed using Equation 1.10. As already noted in section 1.3.2.4 a shear with curvature greater than

Table 4.7. Great Red Spot Stresses

Data Set	A*	B*	r	P	K_e ($m^2 \text{ sec}^{-1}$)	L' (km)
VGR 1 SET Ib	-73.88	52.11	-0.58	0.005	$+7.39 \times 10^6$	740
VGR 1 SET IIb	-105.90	172.66	-0.77	0.001	$+1.06 \times 10^7$	1060
VGR 2 SET Ib	-89.46	66.80	-0.77	0.001	$+8.95 \times 10^6$	895
VGR 2 SET IIb	-155.607	24.32	-0.90	0.001	$+1.56 \times 10^7$	1560

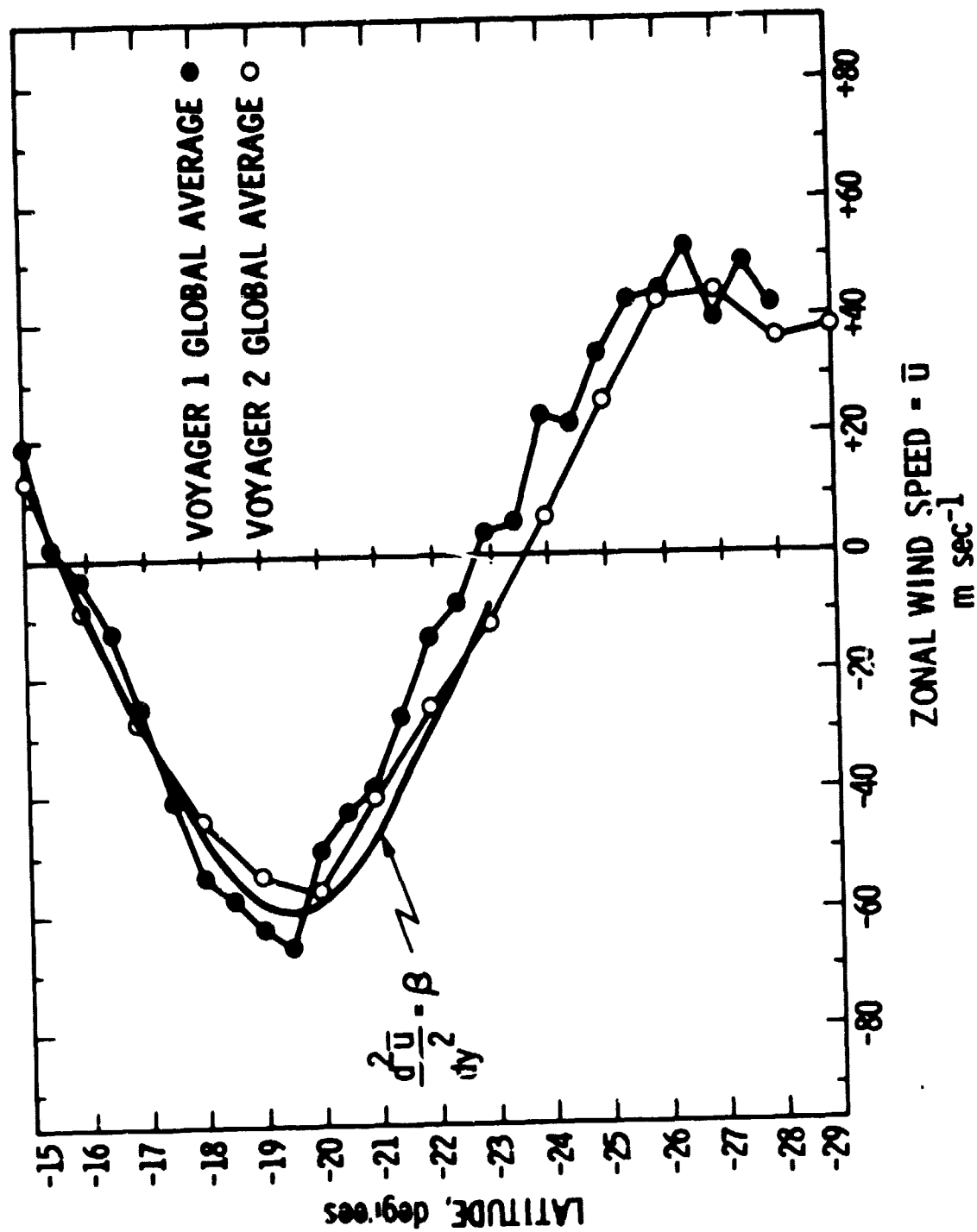
*For the linear least-squares fit of the form,

$$\overline{u'v'} = A \, d\bar{u}/dy + B$$

where, $\overline{u'v'}$ is given in $m^2 \text{ sec}^{-2}$ and $d\bar{u}/dy$ is given in units of $\times 10^{-5} \text{ sec}^{-1}$.

Figure 4.17. Global mean profiles of $\bar{u}(y)$ through the westward jet which runs over the northern edge of the GRS and the region of mean anticyclonic shear in which the GRS is embedded as computed from the world map data sets. The solid parabola represents a locus for which the gradient of the shear vorticity and the gradient of the planetary vorticity are equal ($\theta_0 = -19^\circ 5'$; see equation 1.10).

ORIGINAL PAGE IS
OF POOR QUALITY



that of the stability parabola is likely to be barotropically unstable. A shear with curvature less than that of the stability parabola is likely to be stable. The fact that the profiles of $\bar{u}(y)$ have a curvature almost identical with that of the stability parabola might well be anticipated on the following basis: Suppose that the GRS originated as a turbulent shear region of finite zonal extent (the β -restoring force playing a role analogous to the Brunt-Väisälä frequency in a stratified shear layer). The collapsing mixing layer gives rise to a perturbation (as suggested by Maxworthy, Redekopp and Weidman, 1978) which grows barotropically at the expense of the mean kinetic energy. All the while the barotropic "available" energy represented by the rate at which the actual shear exceeds the barotropically neutral profile decreases. Eventually, the perturbation has attained a considerable magnitude while the mean shear lies very close to a neutrally stable profile. In the steady state the one large eddy feeds at just that rate which maintains the mean shear near neutral stability. The presence of the one large eddy then precludes the growth of any other eddies of similar amplitude within the depleted mean shear. The situation is rather like that of a forest dominated by one huge oak whose spreading branches deplete the forest floor of sunlight and doom those seedlings unfortunate enough to have taken root in the shade.

4.5.3 Theoretical Implication of the Observed Stresses

The Great Red Spot has attracted much theoretical interest during the past century of continuous observation. Some of the earliest ideas were quite bizarre, often involving either volcanic activity beneath the Jovian cloudtops or asteroidal bombardment from above. The first

suggestion that the GRS might be at least a quasi-atmospheric phenomenon was expounded by G. W. Hough in the 1880's when he envisioned the feature as a vast solid body floating raft-like in the liquid oceans with which he believed Jupiter's surface was covered (Hough, 1903). By supposing this liquid ocean to be semi-incandescent Hough even, if only by luck, deduced that the darker GRS was colder than its surroundings. Wildt (1939) and later Peek (1958, pg. 237) picked up the "floating raft" theme. Even within the past decade the notion of a floating solid body has been seriously put forward (Streett, Ringermacher, and Veronis, 1971).

Modern theories for the GRS are summarized in Table 4.8. We have already reviewed several of these models in Section 1.3 and will not repeat the details here. We pass over the Taylor column hypothesis since it now seems unlikely that a true solid-fluid interface exists at the "bottom" of the Jovian atmosphere. We briefly examine those models not previously reviewed.

In a simplistic and qualitative way Kuiper (1972) extended the CISK mechanism of Barcilon and Gierasch (1970) to describe the GRS as a vast shield of cumulus columns towering above the South Tropical Zone and thus rotating somewhat slower than the underlying easterly current, which he likened to the Intertropical Convergence Zone (ITCZ) in Earth's atmosphere. He argued that the divergence at the top of the cumulus towers would result in the anticyclonic vorticity of the shield as a whole. In such a scheme it is the lower level convergence of water vapor and the subsequent release of latent heat which drives the

Table 4.8. Modern Theories for the Great Red Spot

Theory	Reference	Driving Mechanism
Taylor-Proudman Column	Hide, 1961	Stagnant column above surface irregularity
Hurricane	Kuiper, 1972	Conditional Instability of the Second Kind
Free Barotropic Vortex	Ingersoll, 1973	Mechanism not addressed
Convective Instability	Williams & Robinson, 1973	Unstable vertical temperature gradients
Solitary Rossby Wave	Maxworthy & Redekopp, 1976	Forcing not required for nonviscous solution*
Baroclinically Neutral Gyre	Williams, 1979	Baroclinicity of mean field
Green Mode Baroclinic Eddy	Conrath, Gierasch, & Nath, 1981	Baroclinicity of mean field
Internally Heated Baroclinic Vortex	Hide and Read, 1981	Baroclinicity of eddy field
Weakly Stratified Rossby Wave	Ingersoll & Cuong, 1981	Forcing not required for nonviscous solution

*Barotropic forcing has been suggested by Maxworthy, Redekopp, and Weidman (1978) as a mechanism appropriate to the solitary Rossby wave model.

vortex. This vast hurricane model for the GRS has remained popular throughout the past decade. Of particular relevance to our study is a numerical experiment performed by Challa and Pfeffer (1980) in which they examine the role of eddy stresses in the initial development of a terrestrial hurricane. They parameterize eddy fluxes of momentum, as well as water vapor, in a radially symmetric hurricane and find that the stresses can play a significant role in the vortex spin-up process, particularly in these cases where the eddy stresses are strongest near the air-sea interface and result in rapid convergence of momentum (and more importantly water vapor). Their study, coupled with observational evidence of momentum convergence (Black and Anthes, 1971) seems to indicate that the eddy stresses associated with the asymmetric waves in the tropical easterlies play a major role in triggering and perhaps maintaining terrestrial hurricanes. One could envision a situation for the GRS which is not unlike that suggested by Challa and Pfeffer. We note that the very slow divergence within the central portions of the GRS (see Section 4.3.2), if meaningful, could be indicative of interior upwelling and lower level convergence. However, the problem of how one sets up a convergent field in the lower troposphere in the absence of a lower Ekman layer has yet to be fully addressed.

Hide and Read (1981) suggest that the GRS may represent a baroclinic eddy with its own interior heat source. Thus, the perturbation field of temperature and stream function is baroclinic, as opposed to the linear models discussed in Section 1.3.2.2.2 in which the baroclinicity is in the mean field. Voyager IRIS observations indicate

that the GRS may well possess such an interior heat source (Flaser et al., 1981). Future comparison of very high resolution IRIS measured temperature distribution near the GRS and observed distributions of kinetic energy should help gauge the likely importance of the baroclinic mechanism.

It is clear that each of the models which are tied to a specific energy generating mechanism involve transports associated with a vertical velocity field (i.e., both the convective and baroclinic mechanism rely upon vertical motions for the ultimate conversion of P' into K'). Our eddy stress analysis indicates that the GRS is probably maintained as a barotropic instability. The models of Ingersoll (1973), Maxworthy and Redekopp (1976), and Ingersoll and Cuong (1981) are capable of accommodating the barotropic mechanism, though in their present form each model is barotropically neutral. In each case free solutions are obtained to a potential vorticity equation. The analysis of Ingersoll (1973) is purely hydrodynamic in the sense that the effects of stratification are ignored and subsequently the solutions are completely barotropic. The models of Maxworthy and Redekopp (1976) and Ingersoll and Cuong (1981) treat different scales of the stratification parameter K^2 .

CHAPTER 5. THE VERTICAL STRUCTURE OF SOLITARY ROSSBY WAVES

5.1 Solutions to the Quasi-geostrophic Potential Vorticity Equation

Recall the discussion of section 3.1.1 in which we pointed out that the potential vorticity equation is given by equation 3.1 for length scales $L \gtrsim L_D$, i.e., for $K^2 \gtrsim 1$. To first order in Rossby number and for incompressible flow, equation 3.1 becomes the quasi-geostrophic potential vorticity equation given in its nondimensional form by,

$$\left(\frac{\partial}{\partial t} + \psi_y \frac{\partial}{\partial x} - \psi_x \frac{\partial}{\partial y} \right) \left(\nabla^2 + \frac{\partial}{\partial z} \left(K^2 \frac{\partial}{\partial z} \right) \right) \psi + \beta \psi_x = 0 \quad (5.1)$$

where, ψ is the total streamfunction specified by,

$u = + \psi_y$ = nondimensionalized zonal wind speed

$v = - \psi_x$ = nondimensionalized meridional wind speed

$$\nabla^2 () = \frac{\partial^2}{\partial x^2} () + \frac{\partial^2}{\partial y^2} () .$$

For the moment we simply note that the unforced, homogeneous form of the potential vorticity equation given by equation 5.1 is strictly valid only in some time-averaged sense. We require the forcing and dissipation terms which would lie on the right-hand side of the equation to cancel each other such that a steady state flow results for time scales longer than the averaging interval.

Ingersoll and Cuong (1981) set up a two layer numerical model in order to compute $\psi_1(x, y, t)$, the total streamfunction in an upper, weakly stratified layer representing Jupiter's upper troposphere and stratosphere. They assume that the lower layer is adiabatic with a streamfunction $\psi_2 = \int \bar{u}(y) dy$, where $\bar{u}(y)$ is the observed mean zonal wind speed. For large values of k^2 they obtain numerical solutions which are strongly nonlinear. They argue that the existence of solitons in their model is impossible for large values of k^2 . The vortices of Ingersoll and Cuong tend to merge to form new stronger vortices. They suggest that the merging of smaller vortices circulating in the westward current at -12° latitude within the GRS represents such strongly nonlinear interactions. Redekopp (private communication, 1981) has demonstrated that weakly nonlinear solutions are possible in Ingersoll and Cuong's model even for cases where k^2 is large. At present the best test of this model is to examine the validity of its more easily testable weakly nonlinear counterpart, the solitary Rossby wave model of Maxworthy and Redekopp (1976).

The behavior of Ingersoll and Cuong's vortices is quite different from the soliton interactions (i.e., phase shifts and preserved individual identities) manifest by the weakly nonlinear solutions to equation 5.1 first proposed by Maxworthy and Redekopp (1976). Soliton solutions are obtained by a perturbation expansion in ϵ , where ϵ is the disturbance streamfunction nondimensional amplitude specified by,

$$\psi(x, y, z, t) = \int_{y_c}^y \{U(y) - C_0\} dy + \epsilon \psi(x, y, z, t) \quad (5.2)$$

with, C_0 = linear long-wave phase speed for a Rossby Wave in the
observed shear $U(y)$,

$U(y)$ = nondimensional form of $\bar{u}(y)$, the mean zonal speed,

where, $U = C_0$ at $y=y_c$ = "critical layer"

and, Ψ and ψ are respectively the total and the perturbation
streamfunction. The potential vorticity equation for ψ , the pertur-
bation streamfunction becomes,

$$\left[\frac{\partial}{\partial t} + (U - C_0) \frac{\partial}{\partial x} + \epsilon \left(\frac{\partial \psi}{\partial y} \frac{\partial}{\partial x} - \frac{\partial \psi}{\partial x} \frac{\partial}{\partial y} \right) \right] \left[\frac{\partial^2}{\partial x^2} + \frac{\partial^2}{\partial y^2} \right. \quad (5.3)$$

$$\left. + \frac{\partial}{\partial z} \left(K^2 \frac{\partial}{\partial z} \right) \right] \psi + (\beta - U'') \psi_x = 0.$$

Introducing the multiple scales,

$$\xi = \epsilon^{1/2} x \text{ and } \tau = \epsilon^{3/2} t,$$

Maxworthy and Redekopp perform a perturbation expansion in ϵ on ψ
of the form,

$$\psi = \psi^{(1)} + \epsilon \psi^{(2)} + \dots$$

such that $\psi^{(1)}$ satisfies the linearized form of equation 5.3 given by,

$$\left[(U - C_0) \frac{\partial}{\partial \xi} \right] \left[\frac{\partial^2}{\partial y^2} + \frac{\partial}{\partial z} \left(K^2 \frac{\partial}{\partial z} \right) \right] \psi^{(1)} + (\beta - U'') \psi_x^{(1)} = 0. \quad (5.4)$$

We previously noted that the homogeneous form of equation 5.1 is strictly valid in some time-averaged sense. If we explicitly write out the forcing terms on $\psi^{(1)}$, which we assume are present due to the strong barotropic forcing associated with the meridional shear in the mean zonal flow and vertical stress dissipation associated with the vertical shear in the mean flow, the right-hand side of equation 5.4 becomes,

$$+ K_{eH} \frac{d^2 U}{dy^2} - K_{eV} \frac{d^2 U}{dz^2},$$

where we have explicitly written the algebraic sign of the horizontal and vertical eddy viscosity coefficients. In order that we proceed with the unforced form of equation 5.4 we require that the above forcing terms cancel in the steady state case, which presumably applies for the GRS. Thus, in a time-averaged sense we are free to proceed with equation 5.4 and in effect will ignore the strong barotropic feeding of the GRS perturbation.

Maxworthy and Redekopp find that for a continuously stratified atmosphere ($k^2 = k^2(z)$) the solution for $\psi^{(1)}$ may be obtained in the separable form given by,

$$\psi^{(1)} = \sum_n A_n(\xi, \tau) \phi_n(y) Z_n(z) \quad (5.5)$$

where the amplitude $A_n(\xi, \tau)$ is arbitrary to zeroth order, but must satisfy a Korteweg de Vries equation at order ϵ (see Redekopp, 1977).

Substitution of equation 5.5 into equation 5.4 yields the necessary constraints on both the meridional amplitude $\phi_n(y)$, which to lowest order in ϵ must satisfy the barotropic stability equation (see the discussion in section 4.5.2) given by,

$$\phi_n'' - k_n^2 \phi_n + \frac{\beta - U''}{U - C_{0n}} \phi_n = 0 \quad (5.6)$$

with boundary conditions,

$$\phi_n(y_1) = \phi_n(y_2) = 0$$

and the vertical amplitude $Z_n(z)$ which obeys a vertical structure equation with the Boussinesq form,

$$\left(\kappa^2(z) z_n'(z) \right)' + k_n^2 z_n = 0 \quad (5.7)$$

subject to momentarily unspecified boundary conditions.

The intricate coupling of the three amplitudes in the separable solution expressed by equation 5.5 is the eloquent essence of Maxworthy and Redekopp's theory. The meridional amplitude $\phi_n(y)$ couples to the zonal, temporal amplitude $A_n(\xi, \tau)$ either through explicit integral constraints for propagating neutral modes or an explicit solvability condition for regular and singular neutral modes (Redekopp, 1977). The meridional amplitude and the vertical amplitude $z_n(z)$ are coupled through the appropriate choice of eigenvalue k_n .

5.2 Observed Stratification Profiles and Vertical Eigenfunctions

Temperature profiles obtained with Voyager's IRIS allows us to deduce the Brunt-Väisälä frequency ($N(z)$) in Jupiter's upper troposphere and stratosphere. Estimates of L_D can then be obtained for appropriate depth scales (H). Finally, an appropriate scale for κ^2 can be selected for a specified length scale (L). Thus, the IRIS observations of the temperature structure above the GRS and in the ambient unperturbed atmosphere near the GRS (see Flasar et al., 1981 and Conrath et al., 1981) allow us to estimate appropriate forms of $\kappa^2(z)$, enabling us to compute vertical eigenfunctions for equation 5.7 based upon the observed form of $\kappa^2(z)$. The vertical eigenfunction for the lowest eigenvalue (k_1) may be compared to the IRIS measured temperature perturbation observed over the GRS ($T(z)$)

according to the geostrophic balance equation for a hydrostatic atmosphere for which,

$$\frac{\partial \Psi}{\partial z} = - \frac{RT}{f_0}$$

or,

$$Z_n'(z) = -T(z). \quad (5.8)$$

Use of the Bossinesq form of the vertical structure equation (i.e., equation 5.7) is not valid over a number of scale heights. Hence, if we wish to compare eigenfunctions with the observed profile $T(z)$ we must retain compressibility in the model of Maxworthy and Redekopp. Compressibility is easily accommodated if we begin with the appropriate form of equation 5.1 which becomes,

$$\left(\frac{\partial}{\partial t} + v_y \frac{\partial}{\partial x} - v_x \frac{\partial}{\partial y} \right) \left(\frac{\partial^2}{\partial x^2} + \frac{\partial^2}{\partial y^2} + \frac{1}{\rho_0} \frac{\partial}{\partial z} \left(\frac{\rho_0 f_0^2}{N^2} \frac{\partial}{\partial z} \right) \right) \Psi + \beta \frac{\partial \Psi}{\partial x} = 0 \quad (5.9)$$

where z is henceforth given in a log-pressure system as,

$$z = -H \ln(p/p_0)$$

with, $p_0 = 500$ mb

$$H \frac{RT_0}{g} \approx 21.4 \text{ km for the observed cloudtop temperature.}$$

ORIGINAL PAGE IS
OF POOR QUALITY

Subsequent nondimensionalization of equation 5.9, introduction of a perturbation streamfunction as in equation 5.2, and a multiple scale expansion in ϵ leads again to a separable solution of the form given by equation 5.5. Again, $A_n(\xi, \tau)$ is arbitrary up to order ϵ at which it satisfies a KdV equation, and $\phi_n(y)$ satisfies the barotropic stability equation given by equation 5.6. However, the associated vertical structure equation is now given by,

$$\frac{1}{\rho_0} \left(\frac{\rho_0 f_0^2 L^2}{N^2 H^2} P_n' (z) \right)' + k_n^2 P_n(z) = 0 \quad (5.10)$$

where we have replaced the Bossinesq eigenfunction Z_n by its compressible counterpart P_n .

The ideal gas law allows us to write equation 5.10 in the form,

$$P_n'' (z) = \left[\frac{N^2'(z)}{N^2(z)} + \frac{T_0'(z)}{T_0(z)} + 1 \right] P_n' (z) - \left[\frac{N^2(z) H^2}{f_0^2 L^2} \right] k_n^2 P_n(z) = 0 \quad (5.11)$$

where $T_0(z)$ is the temperature distribution of the unperturbed atmosphere ambient to the GRS. The Brunt-Väisälä frequency ($N(z)$) is given by,

$$N^2(z) = \frac{g^2}{RT_0^2} T_0'(z) + \frac{g^2}{c_p T_0}$$

with,

$$N^{2'}(z) = \frac{g^2}{RT_0^2} T_0''(z) - \frac{2g^2}{RT_0^3} (T_0'(z))^2 - \frac{g^2}{c_p T_0^2} T_0'(z).$$

In order to specify $T_0(z)$ we use averaged temperatures at ten pressure levels (ranging from 500 to 30 mb) over the South Equatorial Belt (SEB) which were obtained as part of the IRIS North-South Map data set (Flaser, 1981, private communication). This same data set defined the ambient profile in the presentation by Conrath et al., 1981 of the perturbation temperature profile over the GRS given by $T(z)$, where $T(z)$ is defined as the temperature over the GRS minus the temperature over the SEB. We use least squares fits to the data of the form:

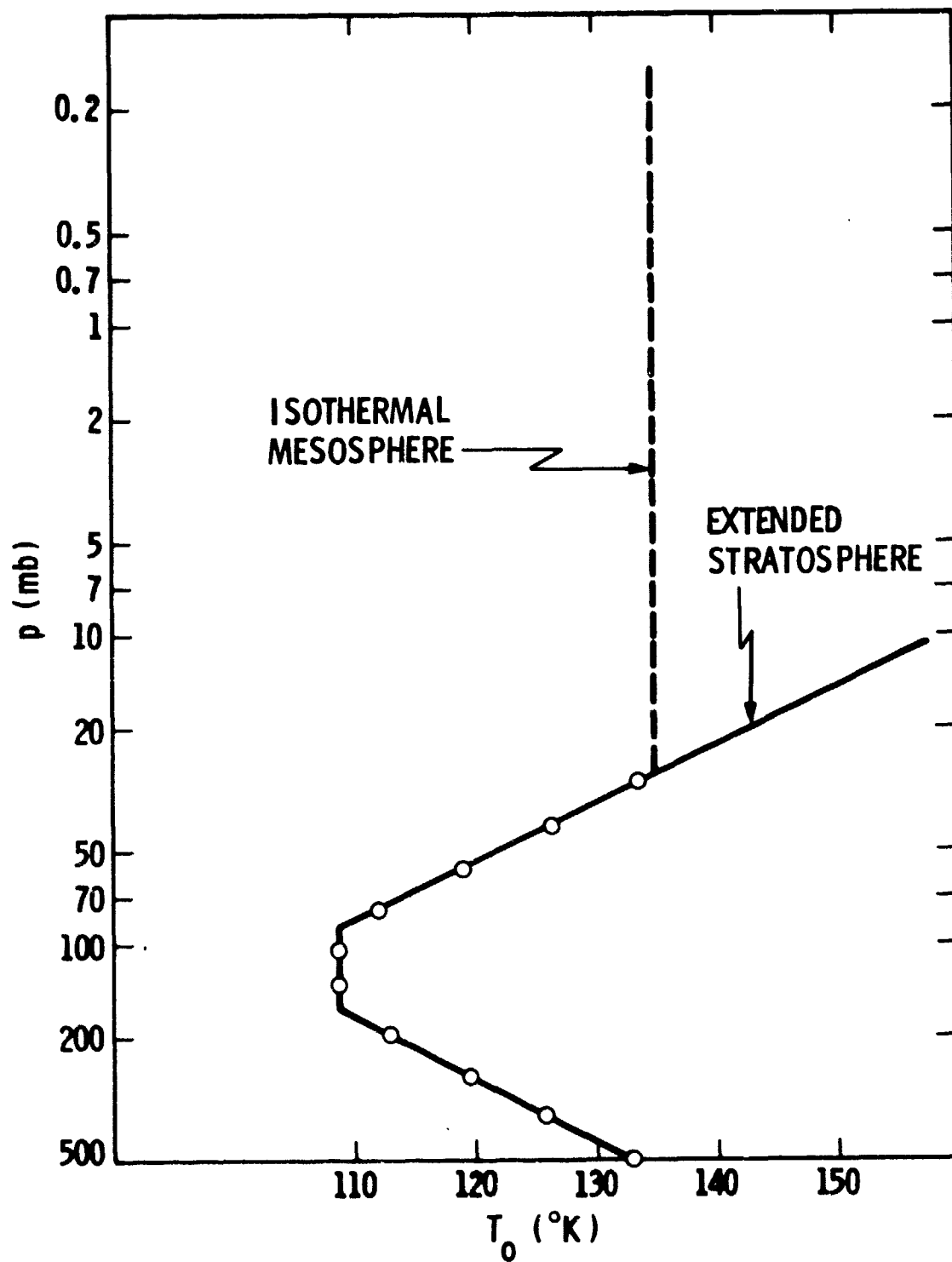
$$\begin{aligned} T_0(z) &= 22.8349 z + 68.9842 && \text{for } z \geq 1.75 \text{ (} p \leq 86.9 \text{mb)} \\ T_0(z) &= 108.7 && \text{for } 1.18 \leq z < 1.75 \text{ (} 86.9 \text{mb} < p \leq 153.6 \text{mb)} \\ T_0(z) &= 132.9107 \exp(-0.1706z) && \text{for } z < 1.18 \text{ (} p > 153.6 \text{mb)} \end{aligned}$$

with $T_0(z)$ in units of $^{\circ}\text{K}$ in order to represent the ambient profile.

Figure 5.1 displays the above fit to the IRIS profile for $T_0(z)$. Equivalent pressure levels at which the IRIS observations apply are indicated. The linear increase in $T_0(z)$ for $z > 2.8$ ($p < 30 \text{mb}$) may seem somewhat unrealistic. Our knowledge of $T_0(z)$ based on IRIS data only goes as high as 30mb. Upper atmospheric temperature profiles obtained using radio occultation data are model dependent upon assumed temperatures at the model's upper boundary located at 10mb (see

Figure 5.1. Profile of zonal mean brightness temperature over the South Equatorial Belt/South Temperate Zone taken from the Voyager 1 north/south map data set. Center of IRIS weighting functions are indicated by open dots. This profile is used to define the ambient stratification of the atmosphere. It is not clear to what level the stratosphere extends.

ORIGINAL PAGE IS
OF POOR QUALITY



Eshleman et al., 1979). If the temperature at 10mb is taken to be 160°K , the resulting profile is basically linear above 90mb or so, corresponding to an extended stratosphere. On the other hand, if the temperature at 10mb is assumed to be 130°K , the atmosphere is basically isothermal from 30mb upward to at least 10mb, corresponding to a mesosphere. Hence, we actually tested two profiles for $T_0(z)$ in our numerical solution, one for which $T_0(z)$ linearly increases above 30mb and another for which $T_0(z)$ becomes isothermal with a value of 137°K at approximately 28mb. There is no significant difference between the resulting eigenfunctions $P_n(z)$ up to at least the 10mb level. Eigenfunctions shown in figure 5.2 were computed using the linearly increasing profile above 30mb.

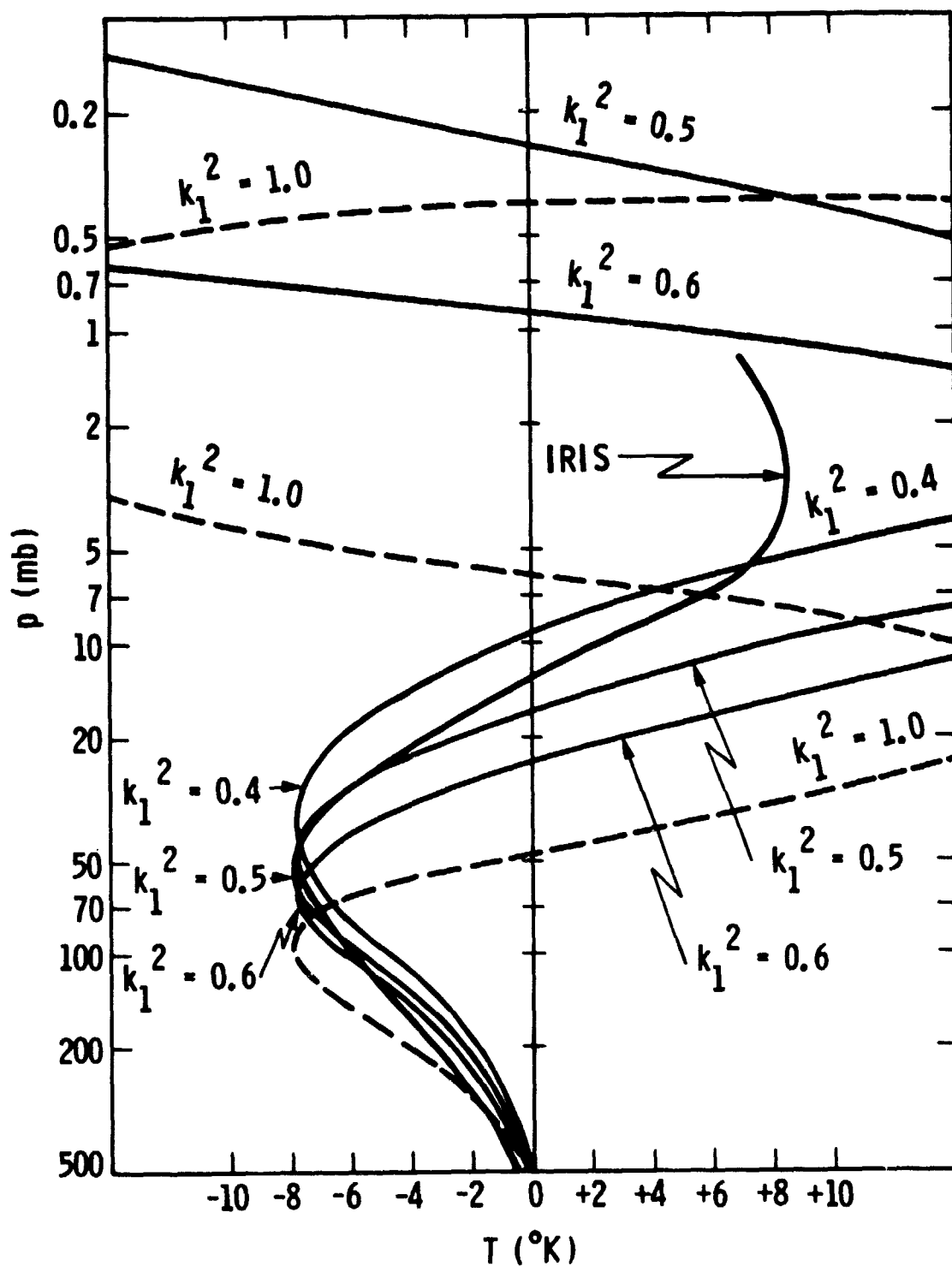
Choosing for the moment to take,

$$P_n'(z) = T(z) = 0 \quad \text{at } z = 0 \quad (5.12)$$

as a lower boundary condition appropriate at the cloudtop level allows numerical solution of equation 5.11 for $P_1(z)$. The lowest eigenvalue k_1 is a free parameter. Use of a fourth order Runge-Kutta scheme to integrate in the direction of increasing z (upward) yields the set of eigenfunctions displayed in figure 5.2. The actual order of magnitude of the eigenvalue k_1 is arbitrary to the extent that the eigenvalue is scaled by the choice of the ratio L^2/L_0^2 . We use equation 5.8 to compare $P_1(z)$ to $T(z)$ over the GRS with $P_1(z)$ normalized to the lower stratospheric minimum observed in $T(z)$.

Figure 5.2. Observed perturbation temperature profile above the Great Red Spot as deduced from high resolution IRIS data sets (see Conrath et al., 1981) and computed perturbation temperature profiles based upon numerical solution of the compressible vertical structure equation (see equation 5.11) for a range of eigenvalues (k_1). Note that $k_1^2 = 0.45$ yields the most realistic result. The computed perturbation temperature profiles have been normalized to the observed minimum in the IRIS profile occurring in the lower stratosphere. Vertical propagation of the solitary Rossby wave readily explains the observed temperature excess above 10 mb.

ORIGINAL PAGE IS
OF POOR QUALITY



We estimate the magnitude of L^2/L_D^2 according to,

$$L \sim 10^3 \text{ to } 10^4 \text{ km}$$

$$H \sim 10 \text{ to } 10^2 \text{ km}$$

$$N^2 \sim 10^{-4} \text{ sec}^{-2}$$

$$f_0^2 \sim 10^{-8} \text{ sec}^{-2}$$

in order to arrive at a scaling of,

$$L^2/L_D^2 \sim 1 \text{ to } 10.$$

Selecting $L^2/L_D^2 \sim 1$ then gives the most likely value for k_1^2 as 0.45 ($k_1 \sim 0.7$). Also shown in figure 5.2 is the eigenfunction associated with $k_1 = 1.0$. In Ingersoll and Cuong's strongly nonlinear numerical model stable solutions exist only for $k_1 > 1.0$. The unrealistic wavelength and nodal positions associated with this eigenvalue indicate that such stable nonlinear solutions suggest an unrealistic vertical structure. However, Ingersoll and Cuong's model can by no means be dismissed on this basis. In the first place their model has only two levels, whereas our eigenfunctions are computed for a continuously stratified atmosphere. Even less definitive is the arbitrary order of magnitude associated with our choice for k_1^2 which scales as L^2/L_D^2 . Thus, the assumption that $L^2 > L_D^2$ results in a corresponding increase in the magnitude of k_1^2 . For example, if $L^2 \sim 10L_D^2$ then the most likely value for k_1^2 becomes 4.5 instead of 0.45.

Howard and Drazin (1964) and Lipps (1965) have obtained solutions to equation 5.6 for mean zonal wind profiles given by $U(y) = \tanh y$ and an eigenvalue given by,

$$c_{01} = -(1-k_1^2)^{1/2}.$$

Our eigenvalue $k_1 = 0.7$ corresponds to the value selected by Maxworthy and Redekopp (1976; see their figure 3) to obtain a solution streamfield bearing remarkable resemblance to the observed GRS flow field.

5.3 Some Conclusions and Suggestions

The results of the previous section suggest that the vertical structure associated with the GRS is remarkably consistent with the solitary Rossby wave description of Maxworthy and Redekopp. Major objections may nevertheless be raised regarding the validity of equation 5.2 (i.e., for $\epsilon \ll 1.0$) and our choice of $L^2/L_D^2 \sim 1$. We have already remarked that ongoing work by Redekopp indicates that weakly nonlinear solutions to equation 5.1 may be obtained for $L^2/L_D^2 > 1$. As well, quasi-linear theory as applied by Maxworthy and Redekopp is in general applicable for perturbations of the same order as the mean field (i.e., for $\epsilon \sim 1$).

The truly definitive test of Maxworthy and Redekopp's model remains to be done. One part of this definitive test is the numerical solution to equation 5.6 for the observed zonal winds $\bar{u}(y) = U(y)$,

which notwithstanding the work of Beaumont (1981), has not been carried out for singular neutral modes for which,

$$\beta - U''(y_c) \neq 0 \text{ and } U_{\min} < C_{on} < U_{\max}.$$

The second part of this definitive test involves a more realistic modeling of the vertical structure associated with the soliton solution. The eigenfunctions shown in figure 5.2 are unrealistic in at least two respects. First, use of a lower boundary condition of the form given by equation 5.12 amounts to the assumption that the ambient and perturbation temperature are equal at the cloudtops. Hence, equation 5.12 by fiat does not allow for a continuation of structure beneath the cloudtops. Under the somewhat unrealistic assumption that the atmosphere is adiabatic beneath the cloudtops (at 500mb) we may treat the cloudtop level as a free interface between a deep adiabatic layer in which the flow is just given by the observed mean zonal flow (following Ingersoll and Cuong, 1981) and a continuously stratified layer above the cloudtops. For such a model the lower boundary condition (applicable at the cloudtops) becomes,

$$P_n'(z) - \alpha^2 P_n(z) = 0 \text{ at } z = 0$$

$$\text{where, } \alpha^2 \equiv \frac{f_0 U_0 L}{gH}. \quad (5.13)$$

It is interesting that we chose to normalize the eigenfunctions by $P_1 = -1.0$ at $z = 0$ in order to obtain the algebraic sign on P'_1 appropriate for comparison with the observed profile $T(z)$. According to equation 5.13, if P_n is negative, then P'_n should be negative, though perhaps small, at $z = 0$. Equation 5.8 then suggests that $T(z) > 0$ at the cloudtop level. This is consistent with the notion that the GRS possess a warm core beneath the cloudtop level. The fact that Conrath et al. present a $T(z)$ which is very slightly negative at the cloudtop level only suggests that a slight shift in their rather arbitrary choice of the axis for $T(z) = 0$ is called for.

The choice of an appropriate lower boundary condition is dependent upon how we model the ambient atmosphere beneath the cloudtops. Such dependence leads us to consider a numerical scheme in which we begin with an isothermal layer in the uppermost stratosphere (i.e., the mesosphere) and integrate downward. Before setting up such a scheme we must consider the growing evanescent behavior of $P_n(z)$. One of the strongest points in favor of the solitary Rossby wave solution is its ability to account for the observed upper stratospheric warming over the GRS as a simple manifestation of the evanescent nature of a vertically propagating, zonally symmetric Rossby wave (notwithstanding the arguments presented by Conrath et al., 1981 which would hold for shorter waves and result in an east-west asymmetry in the isotherms). In fact each of the eigenfunctions in figure 5.1 overshoots the observed warming by a considerable amount. In the Jovian atmosphere infrared cooling to space damps this evanescence so as to produce the

observed profile $T(z)$. Thus, a definitive treatment must model the effects of such cooling. A simple procedure for modeling the damping effects of radiative cooling is to include in our energy equation a diabatic term proportional to the perturbation temperature (Rodgers and Walshaw, 1966) such that,

$$\frac{dT}{dt} - \frac{RT}{c_p} \frac{d \ln p}{dt} = -\alpha_r T \quad (5.14)$$

where $\alpha_r = \alpha_r(T_e) \approx \alpha_r(T_0) = \alpha_r(z)$ is the so-called Newtonian cooling coefficient, and T_e and T_0 represent the radiative equilibrium temperature and the static or ambient temperature. Note that $T_e = T_0$ for an atmosphere in radiative equilibrium. The appropriate quasi-geostrophic vorticity equation now becomes (see Holton, 1975),

$$\begin{aligned} \left(\frac{\partial}{\partial t} + \psi_y \frac{\partial}{\partial x} - \psi_x \frac{\partial}{\partial y} \right) \left(\nabla^2 + \frac{1}{\rho_0} \frac{\partial}{\partial z} \left(\frac{\rho_0 f_0^2}{N^2} \frac{\partial}{\partial z} \right) \right) \psi + \beta \psi_x \\ = - \frac{1}{\rho_0} \frac{\partial}{\partial z} \left(\frac{\rho_0 f_0^2}{N^2} \alpha_r \frac{\partial}{\partial z} \right) \psi. \end{aligned} \quad (5.15)$$

Scaling as does Redekopp (1977) and choosing a nondimensional form for the cooling coefficient scaled by U/L we may proceed to obtain a quasi-linearized solution of the form given by equation 5.5. Again, we find that A_n is arbitrary up to order ϵ at which it satisfies a KdV equation. If we assume that ϕ_n satisfies equation 5.6 and that α_r is $O(1)$, we require a resulting vertical structure equation of the form,

ORIGINAL PAGE IS
OF POOR QUALITY

$$\frac{1}{\rho_0} \left(\frac{\rho_0 f_0^2 L^2}{N^2 H^2} P_n'(z) \right)' + (U - C_{on}) \frac{A_n}{\partial A_n / \partial \xi} \left(\frac{R}{\rho_0 c_p} \right) \left(\frac{\rho_0 f_0^2 L^2}{N^2 H^2} a_r P_n'(z) \right)' + k_n^2 P_n(z) = 0. \quad (5.16)$$

The appearance of the factor $A_n / \partial A_n / \partial \xi$ in equation 5.16 indicates that the presence of Newtonian cooling no longer allows for a truly separable solution (i.e., equation 5.5 is no longer strictly valid). This also means that if we choose to make use of the KdV theory as given by Redekopp (1977) we require cooling at scales of $O(\epsilon^{3/2})$ or smaller, that is the cooling must be "slow".

Gierasch and Goody (1969) estimate a slow cooling rate for the Jovian atmosphere, but whether such a rate is "fast" enough to account for the observed damping of the vertically propagating Rossby wave remains to be seen. Moreover, whether soliton solutions to the KdV equation can exist for cooling rates faster than order $\epsilon^{3/2}$ remains to be demonstrated.

For a periodic wave of the form

$$A_n(\xi, \tau) \sim e^{i\lambda(\xi - ct)}$$

we might replace the ratio,

$$\frac{A_n}{\partial A_n / \partial \xi}$$

by simply $-i\lambda$. Subsequently, for complex eigenfunctions and eigenvalues we could write equations 5.16 as a fourth order system of equations. Obtaining an analytic solution to equations 5.16 within the isothermal lower mesosphere would then allow us to set the eigenfunction in our Runge-Kutta scheme on the proper solution path, namely, that which decays upward. Continuation of the downward integration beneath the cloudtops would allow for reasonable estimates on the depth to which the GRS actually extends. A lack of good estimates for $\alpha_r(z)$ inhibits our further progress. Nevertheless, it is always useful to speculate and suggest approaches to problems whose solution depends upon data which does not yet exist.

CHAPTER 6. SUMMARY

In our investigation we have uncovered the following characteristics of large-scale turbulence in the Jovian atmosphere:

- (a) Using a global data set with double the number of samples used by Beebe et al. (1980) and Ingersoll et al. (1981) we verify the relatively strong up-gradient flux of momentum by eddies. We find that eddies with mixing-lengths of 10^2 to 10^3 km pump kinetic energy into the mean zonal flow at a rate of approximately 2.2×10^{-4} watts kgm^{-1} on a global average. Attempts to quantify transports by means of zonally symmetric stresses are not altogether successful because of the large relative noise associated with mean meridional motions (\bar{v}). However, we find that within the measurement errors associated with \bar{v} , symmetric stress could easily be responsible for the bulk of the cloudtop momentum transport. We find a good correlation between $K'(y)$ and $P'(y)$ suggesting a coupling between the eddy-scale thermodynamics and dynamics like that anticipated for a baroclinic atmosphere. However, there seems to be little correlation between $\bar{K}(y)$ and $\bar{P}(y)$ which could be suggestive of a mean zonal flow ultimately driven by processes different from those associated with the cloudtop stresses.

- (b) An analysis of the kinetic energy power spectrum of the cloudtop turbulent motions suggests that the observed turbulence occurs in a spectral regime in which kinetic energy is flowing up-gradient from much smaller scales. The associated form of the power law is $K'(k) \propto k^{-5/3}$, where k is the zonal wavenumber, as suggested by Kraichnan (1967). Turbulent energy generally peaks at the scale for which Rhines (1975) points out that Rossby wave propagation begins to dominate the field of turbulence.
- (c) A momentum budget analysis of eddies with length scales associated with the Rossby wave regime (e.g., the GRS and White Oval BC) indicates that these eddies feed barotropically upon the ambient meridional shear of the mean zonal wind. Feeding rates associated with these instabilities suggest very short spin-up times, though unobservable pressure torques and vertical structure could easily modify our estimate of a 10 day spin-up time constant. The observed profile of the mean zonal wind ($\bar{u}(y)$) ambient to the GRS closely resembles a barotropically neutral profile suggesting that this observed GRS feeding rate represents a steady state situation in which all of the available barotropic energy associated with the ambient shear has been depleted. Such a barotropic mechanism has been suggested in order to balance viscous effects associated with

vertical eddy stresses in the solitary Rossby wave model of Maxworthy and Redekopp (1976).

- (d) Finally, we use IRIS observations of temperature lapse rates in the atmosphere ambient to the GRS in order to compute a perturbation temperature profile above a solitary Rossby wave. For scales appropriate to the observed stratification and size of the GRS we find that realistic perturbation temperature profiles are generated by a soliton appropriate to the observed ambient shear. However, uncertainties associated with the thermal structure beneath the cloudtops prevent us from making a definitive statement.

In closing, we are lead to suggest that turbulence at scales of 10^2 to 10^3 km is driven by baroclinic effects. The up-gradient transport of turbulent energy results in a turbulent field which peaks at length scales near that at which Rossby wave propagation begins to dominate. The largest scale turbulent motions like the Great Red Spot are maintained as barotropic instabilities with perturbation velocity and temperature fields which can be described by solitary wave theory.

REFERENCES

- ARNASON, G. 1963 The stability of nongeostrophic perturbations in a baroclinic zonal flow. Tellus 15, 205-229.
- BARCILON, A. & GIERASCH, P. 1970 A moist, Hadley cell model for Jupiter's cloud bands. J. Atmos. Sci. 27, 550-560.
- BATCHELOR, G.K. 1953 The Theory of Homogeneous Turbulence. Cambridge University Press.
- BEAUMONT, D.N. 1980 Solitary waves on an unsymmetrical shear flow with applications to Jupiter's Great Red Spot. ICARUS 41, 400-409.
- BEEBE, R.F., INGERSOLL, A.P., HUNT, G.E., MITCHELL, J.L., & MULLER, J.P. 1980 Measurements of wind vectors, eddy momentum transports, and energy conversions in Jupiter's atmosphere from Voyager 1 images. Geophys. Res. Letts. 7, 1-4.
- BLACK, P.G. & ANTHES, R.A. 1971 On the asymmetric structure of the tropical cyclone outflow layer. J. Atmos. Sci. 28, 1348-1366.
- BUSSE, F.H. 1970a Thermal instabilities in rapidly rotating systems. J. Fluid Mech. 44, 441-460.
- BUSSE, F.H. 1970b Differential rotation in stellar convection zones. Astrophys. J. 159, 629-639.

- BUSSE, F. H. 1976 A simple model of convection in the Jovian atmosphere. Icarus 29, 255-260.
- CHALLA, M. & PFEFFER, R.L. 1980 Effects of eddy fluxes of angular momentum on model hurricane development. J. Atmos. Sci. 37, 1603-1618.
- CHANDRASEKHAR, S. 1961 Hydrodynamic and Hydromagnetic Stability. Oxford University Press.
- CHAPMAN, C.R. 1969 Jupiter's zonal winds: variation with latitude. J. Atmos. Sci. 26, 986-990.
- CHARNEY, J.G. 1947 The dynamics of long waves in a baroclinic westerly current. J. Meteor. 4, 135-163.
- CHARNEY, J.G. 1970 Tropical cyclogenesis and the formation of the intertropical convergence zone. Mathematical Problems in the Geophysical Sciences. American Mathematical Society, 355-368.
- CHARNEY, J.G. 1971 Geostrophic turbulence. J. Atmos. Sci. 28, 1087-1095.
- CONRATH, B.J., FLASAR, F.M., PIRRAGLIA, J.A., GIERASCH, P.J., & HUNT, G.E. 1981 Thermal structure and dynamics of the Jovian atmosphere 2. visible cloud features. J. Geophys. Res. 86, 8769-8775.
- CONRATH, B.J., GIERASCH, P.J., & BATH, N. 1981 Stability of zonal flows on Jupiter. Submitted to Icarus.

- DEARDORFF, J.W. 1971 On the magnitude of the subgrid scale eddy coefficient. J. Comput. Phys. 7, 120-133.
- DIVINE, N. 1971 The Planet Jupiter: NASA Space Vehicle Design Criteria. NASA SP-8069. U.S. Government Printing Office.
- DRAZIN, P.G. & HOWARD, L.N. 1966 Hydrodynamic stability of parallel flow of inviscid fluid. Advanc. Appl. Mech. 9, 1-89.
- EADY, E.T. 1949 Long waves and cyclone waves. Tellus 1, 32-52.
- ESHLEMAN, V.R. et al. 1979 Radio science with Voyager 1 at Jupiter: preliminary profiles of the atmosphere and ionosphere. Science 204, 976-978.
- FERREL, W. 1889 A Popular Treatise on the Winds. Wiley.
- FJORTOFT, R. 1953 On the changes in the spectral distribution of kinetic energy for two-dimensional, nondivergent flow. Tellus 5, 225-230.
- FLASAR, FM., CONRATH, B.J., PIRRAGLIA, J.A., CLARK, P.C., FRENCH, R.G. & GIERASCH, P.J. 1981 Thermal structure and dynamics of the Jovian atmosphere 1. The Great Red Spot. J. Geophys. Res. 86, 8759-8767.
- GAUTIER, D. & COURTIN, R. 1979 Atmospheric thermal structure of the planets. Icarus 39, 28-45.
- GIERASCH, P.J. & GOODY, R.M. 1969 Radiative time constants in the atmosphere of Jupiter. J. Atmos. Sci. 26, 979-980.

- GIERASCH, P.J., INGERSOLL, A.P., & WILLIAMS, R.T. 1973 Radiative instability of a cloudy planetary atmosphere. Icarus 19, 473-481.
- GIERASCH, P.J., INGERSOLL, A.P., & POLLARD, D. 1979 Baroclinic instabilities in Jupiter's zonal flow. Icarus 40, 205-212.
- GIERASCH, P.J. & STONE, P.H. 1968 A mechanism for Jupiter's equatorial acceleration. J. Atmos. Sci. 25, 1169-1170.
- GREEN, J.S.A. 1960 A problem in baroclinic stability. Quart. J. Roy. Meteor. Soc. 86, 237-251.
- GREENSPAN, H.P. 1968 The Theory of Rotating Fluids. Cambridge University Press.
- HADLEY, G. 1735 Concerning the cause of the general trade-winds. Phil. Trans. Roy. Soc. 29, 58-62.
- HALLEY, E. 1686 An historical account of the trade winds, and monsoons, observable in the seas between and near the tropicks; with an attempt to assign the phisical cause of the said winds. Phil. Trans. Roy. Soc. 16, 153-168.
- HANEL, R. et al. 1977 The Voyager infrared spectroscopy and radiometry investigation. Space Sci. Rev. 21, 129-157.
- HANEL, R. et al. 1979 Infrared observations of the Jovian system from Voyager 1. Science 204, 972-976.

HANEL, R.A., CONRATH, B.J., HERATH, L.W., KUNDE, V.G., & PIRRAGLIA, J.A.

1981 Albedo, internal heat, and energy balance of Jupiter:
preliminary results of the Voyager infrared investigation.

J. Geophys. Res. 86, 8705-8712.

HESS, S.L. & PANOFSKY, H.A. 1951 The atmospheres of the other planets.

Compendium of Meteorology. American Meteorological Society,
391-398.

HIDE, R. 1961 Origin of Jupiter's Great Red Spot. Nature 190, 895.

HIDE, R. & READ, P.L. 1981 Stable baroclinic eddies in the laboratory
and in Jupiter's atmosphere. Paper presented to the Royal
Astronomical Society, Meeting of April, 1981 at Cambridge
University.

HOLTON, J.R. 1972 An Introduction to Dynamic Meteorology. Academic
Press.

HOLTON, J.R. 1975 The Dynamic Meteorology of the Stratosphere and
Mesosphere. American Meteorological Society.

HOUGH, G.W. 1903 Address to the American Association for the Advance-
ment of Science. Proc. Amer. Assoc. Advan. Sci. 52.

HOWARD, L.N. & DRAZIN, P.G. 1964 On instability of parallel flow of
inviscid fluid in a rotating system with variable Coriolis
parameter. J. Math. & Phys. 43, 83-99.

- INGERSOLL, A.P. 1973 Jupiter's Great Red Spot: a free atmospheric vortex? Science 182, 1346-1348.
- INGERSOLL, A.P., BEEBE, R.F., COLLINS, S.A., HUNT, G.E., MITCHELL, J.L., MULLER, J.P., SMITH, B.A., & TERRILE, R.J. 1979 Zonal velocity and texture in the Jovian atmosphere inferred from Voyager images. Nature 280, 773-775.
- INGERSOLL, A.P., BEEBE, R.F., MITCHELL, J.L., GARNEAU, G.W., YAGI, G.M., & MULLER, J.P. 1980 Interaction of eddies and mean zonal flow on Jupiter as inferred from Voyager 1 and 2 images. J. Geophys. Res. 86, 8733-8743.
- INGERSOLL, A.P. & CUONG, P.G. 1980 Numerical model of long-lived Jovian vortices. Paper submitted to J. Atmos. Sci.
- INGERSOLL, A.P. & CUZZI, J.N. 1969 Dynamics of Jupiter's cloud bands. J. Atmos. Sci. 26, 981-985.
- INGERSOLL, A.P. & POLLARD, D. 1981 Relation between interior winds and surface winds on Jupiter and Saturn. Paper submitted to Nature.
- JEFFREYS, H. 1926 On the dynamics of geostrophic winds. Quart. J. Roy. Meteor. Soc. 52, 85-104.
- JULIAN, P.R., WASHINGTON, W.M., HEMBREE, L., & RIDLEY, C. 1970 On the spectral distribution of large-scale atmospheric kinetic energy. J. Atmos. Sci. 27, 376-387.

KRAICHNAN, R.H. 1967 Inertial ranges in two-dimensional turbulence.

Phys. Fluids 10, 1417- 1423.

KUO, H.L. 1951 Vorticity transfer as related to the development of the general circulation. J. Meteor. 8, 307-315.

KUO, H.L. 1952 Three dimensional disturbances in a baroclinic zonal current. J. Meteor. 9, 260-278.

KUIPER, G.P. 1972 Lunar and Planetary Laboratory studies of Jupiter-II. Sky and Telescope 43, 75-81.

LEITH, C.E. 1968 Diffusion approximation for two-dimensional turbulence. Phys. Fluids 11, 671-674.

LILLY, D.K. 1971 Numerical simulation of developing and decaying two-dimensional turbulence. J. Fluid Mech. 45, 395-415.

LINDZEN, R.S. 1971 Equatorial planetary waves in shear: part I. J. Atmos. Sci. 28, 609-622.

LIPPS, F.B. 1965 The stability of an asymmetric zonal current in the atmosphere, J. Fluid Mech. 21, 225-239.

LORENZ, E.N. 1955 Available potential energy and the maintenance of the general circulation. Tellus 7, 157-167.

LORENZ, E.N. 1967 The Nature and Theory of the General Circulation of the Atmosphere. World Meteorological Organization.

LUMLEY, J.L 1970 Stochastic Tools in Turbulence. Academic Press.

- McINTYRE, M.E. 1972 Baroclinic instability of an idealized model of the polar night jet. Quart. J. Roy. Meteor. Soc. 98, 165-174.
- MAXWORTHY, T. 1973 A review of Jovian atmospheric dynamics. Planet. Space Sci. 21, 623-641.
- MAXWORTHY, T. 1975 A wave driven model of the Jovian equatorial jet. Planet. Space Sci. 23, 1223-1233.
- MAXWORTHY, T. & REDEKOPP, L.G. 1976 A solitary Rossby wave theory of the Great Red Spot and other features in the Jovian atmosphere. Icarus 29, 261-271.
- MAXWORTHY, T., REDEKOPP, L.G., & WEIDMAN, P.D. 1978 On the production and interaction of planetary solitary waves: applications to the Jovian atmosphere. Icarus 33, 388-409.
- MITCHELL, J.L., BEEBE, R.F., INGERSOLL, A.P., & GARNEAU, G.W. 1981 Flow fields within Jupiter's Great Red Spot and White Oval BC. J. Geophys. Res. 86, 8751-8757.
- OORT, A.H. 1964 On estimates of the atmospheric energy cycle. Mon. Weather Rev. 92, 483-493.
- PEDLOSKY, J. 1979 Geophysical Fluid Dynamics. Springer-Verlag.
- PEEK, B.M. 1958 The Planet Jupiter. Faber and Faber.

- PHILLIPS, N.A. 1954 Energy transformations and meridional circulations associated with simple baroclinic waves in a two-level, quasi-geostrophic model. Tellus 6, 273-286.
- PHILLIPS, N.A. 1956 The general circulation of the atmosphere: a numerical experiment. Quart. J. Roy. Meteor. Soc. 82, 123-164.
- PODOLAK, M. & CAMERON, A.G.W. 1974 Models of the giant planets. Icarus 22, 123-148.
- PRIESTLEY, C.H.B. 1959 Turbulent Transfer in the Lower Atmosphere University of Chicago Press.
- REDEKOPP, L.G. 1977 On the theory of solitary Rossby waves. J. Fluid Mech. 82, 725-745.
- REYNOLDS, O. 1895 On the dynamical theory of incompressible viscous fluids and the determination of the criterion. Phil. Trans. Roy. Soc. A 186, 123.
- REESE, E.J. & SMITH, B.A. 1968 Evidence of vorticity in the Great Red Spot of Jupiter. Icarus 9, 474-486.
- RHINES, P.B. 1975 Waves and turbulence on a beta-plane. J. Fluid Mech. 69, 417-443.
- ROBERTS, P.H. 1968 On the thermal instability of a rotating fluid sphere containing heat sources. Phil. Trans. Roy. Soc. A 163, 93-117.

- RODGERS, C.D. & WALSHAW, C.D. 1966 The computation of infrared cooling rate in planetary atmospheres. Quart. J. Roy. Meteor. Soc. 92, 67-92.
- SMITH, B.A. et al. 1977 Voyager imaging experiment. Space Sci. Rev. 21, 103-127.
- SMITH, B.A. et al. 1981 Encounter with Saturn: Voyager 1 imaging science results. Science 212, 163-191.
- SNYDER, L. 1979 Television optics for the Voyager mission to Jupiter and Saturn. Proc. Soc. Photo-optical Inst. Eng. 183, 274-282.
- STARR, V.P. & WHITE, R.M. 1951 A hemispherical study of the atmospheric angular-momentum balance. Quart. J. Roy. Meteor. Soc., 77, 215-225.
- STONE, P.H. 1966 On non-geostrophic baroclinic stability. J. Atmos. Sci. 23, 390-400.
- STONE, P.H. 1967 An application of baroclinic stability theory to the dynamics of the Jovian atmosphere. J. Atmos. Sci. 24, 642-652.
- STONE, P.H. 1971 The symmetric baroclinic instability of an equatorial current. Geophys. Fluid Dyn. 2, 147-164.

- STONE, P.H. 1972 A simplified radiative-dynamical model for the static stability of rotating atmospheres. J. Atmos. Sci. 29, 405-418.
- STONE, P.H. 1976 The meteorology of the Jovian atmosphere. Jupiter. University of Arizona Press, 586-618.
- STREETT, W.B., RINGERMACHER, H.I., & VERONIS, G. 1971 On the structure and motions of Jupiter's Red Spot. Icarus 14, 319-342.
- TENNEKES, H. & LUMLEY, J.L. 1972 A First Course in Turbulence. Massachusetts Institute of Technology Press.
- THOMSON, J. 1857 Grand currents of atmospheric circulation. Address to the British Assoc. Meeting, Dublin.
- WEST, R.A. & TOMASKO, M.G. 1980 Spatially resolved methane band photometry of Jupiter. Icarus 41, 278-292.
- WHITE, R.M. 1949 The role of mountains in the angular-momentum balance of the atmosphere. J. Meteor. 6, 353-355.
- WILDT, R. 1939 Address to the American Philosophical Society. Proc. Amer. Phil. Soc. 81, 135.
- WILLIAMS, G.P. 1979a Planetary circulations: 2. The Jovian quasi-geostrophic regime. J. Atmos. Sci. 36, 932-968.
- WILLIAMS, G.P. 1979b Planetary Circulations: 1. barotropic representation of Jovian and terrestrial turbulence. J. Atmos. Sci. 35, 1399-1426.

- WILLIAMS, G.P. & ROBINSON, J.B. 1973 Dynamics of a convectively unstable atmosphere: Jupiter? J. Atmos. Sci. 30, 684-717.
- YAGI, G.M., LORRE, J.J., & JEPSEN, P.L. 1978 Dynamic feature analysis for Voyager at the Image Processing Laboratory. Proc. Conf. on Atmospheric Environment of Aerospace Systems and Applied Meteorology. American Meteorological Society, 110-117.
- ZANGVIL, A. & YANAI, M. 1980 Upper tropospheric waves in the tropics. Part I: dynamical analysis in the wavenumber-frequency domain. J. Atmos. Sci. 37, 283-298.